

**ÉCOLE DOCTORALE SCIENCES DE LA TERRE ET DE L'ENVIRONNEMENT**

**[ EOST - IPGS / KIT ]**

**THÈSE** présentée par :

**Xavier KINNAERT**

soutenue le : **16 septembre 2016**

pour obtenir le grade de : **Docteur de l'université de Strasbourg**

Discipline/ Spécialité : **Géophysique - Sismologie**

**Data processing of induced seismicity :  
estimation of errors and of their impact on  
geothermal reservoir models**

**THÈSE dirigée par :**

**Mr. ACHAUER Ulrich**  
**Mr. KOHL Thomas**

Physicien Dr., Université de Strasbourg, *IPGS*  
Professeur Dr., KIT, Karlsruhe

**RAPPORTEURS:**

**Mr. RITTER Joachim**  
**Mr. FISCHER Tomás**

PD Dr., GPI, Karlsruhe  
Professeur Dr., Charles University, Prague

---

**AUTRES MEMBRES DU JURY :**

**Mr. SCHMITTBUHL Jean**  
**Mr. GENTER Albert**  
**Mr. SCHILLING Frank**

Directeur de recherches Dr., EOST (Examineur)  
Dr., Directeur général adjoint d'ES-Géothermie (Examineur)  
Professeur Dr., KIT, Karlsruhe (Président du jury)



# DATA PROCESSING OF INDUCED-SEISMICITY: ESTIMATION OF ERRORS AND OF THEIR IMPACT ON GEOHERMAL RESERVOIR MODELS

Zur Erlangung des akademischen Grades eines  
DOKTORS DER NATURWISSENSCHAFTEN

von der Fakultät

Bauingenieur-, Geo- und Umweltwissenschaften  
des Karlsruher Instituts für Technologie (KIT)

genehmigte

DISSERTATION

von

Xavier Kinnaert, M.Sc.

aus Strasbourg

Tag der mündlichen

Prüfung: 16. September 2016

Referent: Prof. Dr. Thomas Kohl (KIT)

Korreferent: Prof. Dr. Ulrich Achauer (IPGS, Uds)

Karlsruhe 2016



## Zusammenfassung

Die korrekte Lokalisierung von induzierter Seismizität und den dazugehörigen Herdflächenlösungen sind sehr wichtige Parameter. So werden zum Beispiel die Verteilung der Erdbeben und die Orientierung ihrer Herdflächenlösungen dazu benutzt um in der Tiefe liegende Reservoirs zu lokalisieren und abzubilden. In dieser Doktorarbeit wird eine Technik vorgeschlagen um die methodisch bedingten Fehler zu quantifizieren. Mit dieser Methode werden die verschiedenen Fehlerquellen, die Unsicherheiten und die Fehler im Modell getrennt. Die Technik wird für die geothermischen Felder in Soultz und in Rittershoffen benutzt um den Einfluss verschiedener Parameter (Annahmen) auf die Lokalisierung der induzierten Seismizität zu bestimmen. Es wurde festgestellt, dass Bohrlochseismometer und eine gute azimutale Verteilung der seismischen Stationen die Unbestimmtheiten verkleinern. Die Geschwindigkeitsunbestimmtheiten, die durch eine Gauss-Verteilung mit 5% Fehler dargestellt werden, vervielfachen die Lokalisierungsungenauigkeiten um einen Faktor 2 bis 3. Eine ungenaue Kenntnis des Untergrunds oder die verwendete vereinfachte Darstellung der Geschwindigkeitsverhältnisse im Untergrund (notwendig um die synthetischen Rechnungen durchführen zu können) führen zu anisotropen Abweichungen und Fehlern in der Herdtiefe von bis zu 10%. Diese können die Interpretationen des Untergrunds deutlich verfälschen. Ein "calibration shot" kann diese Fehler korrigieren. Leider können die Fehler für die Herdflächenlösungen nicht in derselben Weise korrigiert werden. Es erscheint daher als keine gute Idee, ein Reservoir nur über die Lokalisierung von Erdbeben zu bestimmen. Eine Kombination mehrerer seismischer Methoden scheint angezeigt. Die hier besprochene Methode kann als Grundlage dienen für die Erkundung anderer (geothermischer) Reservoirs. Eine gute *a priori* Kenntnis über den Untergrund bleibt dabei unabdingbar.

**Schlüsselwörter:** Unbestimmtheiten, Ungenauigkeiten, induzierte Seismizität, seismische Lokalisierung, Herdflächenlösung

## Abstract

Induced seismicity location and focal mechanisms are commonly used to image the sub-surface design in reservoirs among other tasks. In this Ph.D. the inaccuracies and uncertainties on earthquake location and focal mechanisms are quantified using a three-step method. The technique is applied to the geothermal sites of Soultz and Rittershoffen to investigate the effect of several criteria on the earthquake location. A good azimuthal seismic coverage and the use of seismic down-hole sensors seriously decrease the location uncertainty. On the contrary, velocity model uncertainties, represented by a 5% Gaussian distribution of the velocity model around the reference model, will multiply location uncertainties by a factor of 2 to 3. An incorrect knowledge of the sub-surface or the simplifications performed before the earthquake location can lead to biases of 10% of the vertical distance separating the source and the stations with a non-isotropic spatial distribution. Hence the sub-surface design may be distorted in the interpretations. To prevent from that fact, the calibration shot method was proved to be efficient. The study on focal mechanism errors seems to lead to different conclusions. Obviously, the angular bias may be increased by neglecting the fault in the velocity. But, it may also be the same as or even smaller than the bias calculated for the case simulating a perfect knowledge of the medium of propagation. Furthermore a better seismic coverage always leads to smaller angular biases. Hence, it is worth advising to use more than only earthquake location in order to image a reservoir. Other geothermal sites and reservoirs may benefit from the method developed here.

**Key words:** uncertainties, inaccuracies, induced seismicity, earthquake location, focal mechanism

## Résumé

La localisation de séismes induits ainsi que les mécanismes au foyer associés sont des outils fréquemment utilisés afin, entre autres, d'imager la structure d'un réservoir. Cette thèse présente une technique permettant de quantifier les erreurs associées à ces deux paramètres. Par cette méthode, incertitudes et imprécisions sont distinguées. La méthode a été appliquée aux sites de Soultz et de Rittershoffen pour étudier l'impact de plusieurs critères sur la localisation de la sismicité induite. Ainsi, il a été montré que l'utilisation de capteurs installés profondément dans des puits et qu'une bonne couverture sismique azimutale réduit sérieusement les incertitudes de localisation. Les incertitudes du modèle de vitesse, représentées par une distribution gaussienne des modèles avec un écart de 5% autour du modèle de référence, multiplient les incertitudes de localisation par un facteur 2 à 3. Des simplifications utilisées pour le calcul ou une mauvaise connaissance du milieu peuvent mener à des imprécisions de l'ordre de 10% spatialement non isotropes. Ainsi, les structures du sous-sol peuvent être déformées dans les interprétations. L'application d'un tir de calibration peut néanmoins corriger ce fait en grande partie. L'étude d'erreurs associées aux mécanismes au foyer ne semble cependant pas conduire aux mêmes conclusions. Le biais angulaire peut certes être augmenté par l'omission de la faille dans le modèle de vitesse, mais dans plusieurs cas il est le même que dans le cas idéal voire diminué. En outre, une meilleure couverture sismique améliorerait toujours le mécanisme au foyer obtenu. Ainsi, il n'est pas conseillé d'imager un réservoir en n'utilisant que la localisation de séismes, mais une combinaison de plusieurs paramètres sismiques pourrait s'avérer efficace. La méthode appliquée dans le cadre de cette thèse pourra servir pour d'autres sites à condition d'en avoir une bonne connaissance *a priori*.

**Mots clés :** imprécisions, incertitudes, sismicité induite, localisation de séisme, mécanisme au foyer

# Acknowledgments

Before introducing the content of the Ph.D. thesis, I would like to thank some people, organizations and companies. Firstly, I am very thankful to Professors Ulrich Achauer and Thomas Kohl who kindly accepted to supervise this PhD project. Thanks a lot to the different organizations including the KIT, EnBW, the CNRS and the LabEx “G-Eau-Thermie profonde” which provided the funding necessary for this Ph.D. Many thanks go as well to the “DFH-UFA” which paid roughly all travel expenses related to this Ph. D.

Emmanuel, I am very glad that we met around 4 years ago (already!) and I would like to thank you for the help, the multiple advices and hence the time you spent for me. I guess I won't be able to thank you as much as you deserve. David, it was a great pleasure to discuss with you during work-times as well as during our sport sessions.

Many people have contributed to help me accomplishing the presented work and I would like to thank all those who spent a bit of their time explaining me the different codes I needed to use to perform the studies. I am especially grateful to Prof. Thomas Bohlen, Laura Gassner and Tilman Metz and to Olivier Lengliné with whom I spent several hours discussing and exchanged many e-mails. During those four years, I had the opportunity to introduce my work at both several conferences but also internal seminars. Hence, thank you very much to all members of the “Seismo-Seminar” and the “Café LabEx” for the fruitful discussions and advices provided each time I gave a talk. Among you, I will give a special thanks to PD Joachim Ritter who is the source of this Ph.D. topic. Furthermore I was also very pleased to work in a team regrouping many different research domains related to the geothermal reservoir. Even though it was sometimes a bit difficult to understand the discussions since the topics and used language were not mine, all in all it was very interesting and I learned many things from each discussion (either new German word or new scientific knowledge from various topics).

Of course I would like to thank Mrs Silke Schlichting, and the other secretaries for the time we spent together to understand and solve the “administrative” issues.

Obviously, one need some rest and fun/relaxing times when working as a Ph.D. student. For that, it was very kind from Hubert Heitz to accept and introduce me to his orchestra. Therefore, thanks a lot Hubert, “Bleib Gesund” and please continue to head the Collegium Musicum in the same motivating mood as you use to do. Many thanks also go to all the

members of this orchestra. For the fun-times, I would like to thank the two “Indonesian workers” of our team: David and Yodha. I was really happy to have you as good partners to practice several sports to refresh my mind. I am also very glad to have such friends in my parents’ town (they will recognise themselves) who always try to make me fun and with whom I can have serious discussions too.

Last and not least, I am very happy and grateful for being born in our family. Hence “The hugest thank (it won’t be enough either) Maman, Papa and Christine” for listening to me, bearing my stress-crises and not switching off skype during those times. Thank you for letting me the opportunity to study all those years, for all your advices in many domains and for your support. Furthermore thank you very much to my grand-parents and uncle for the same “stress-reason” as well as the fruitful scientific and musical discussions.

Finally thank you for opening this manuscript. I hope you will read it and find something interesting for your taste.



# Table of content

Acknowledgments.....	7
<b>1 Introduction .....</b>	<b>21</b>
<b>1.1 Context .....</b>	<b>21</b>
<b>1.2 Aim of the Ph. D. ....</b>	<b>24</b>
<b>1.3 Plan of the manuscript.....</b>	<b>24</b>
<b>FIRST PART .....</b>	<b>26</b>
<b>2 Theory .....</b>	<b>28</b>
<b>2.1 Inverse Problem.....</b>	<b>28</b>
<b>2.2 Earthquake location.....</b>	<b>35</b>
<b>2.3 Determination of earthquake focal mechanism.....</b>	<b>42</b>
<b>2.4 Seismic waveforms modelling .....</b>	<b>50</b>
<b>3 Geological settings: the Upper Rhine Graben (URG).....</b>	<b>56</b>
<b>3.1 Brief history of the URG.....</b>	<b>56</b>
<b>3.2 Temperature anomalies in the URG.....</b>	<b>58</b>
<b>3.3 Geothermal sites in the URG.....</b>	<b>59</b>
<b>SECOND PART .....</b>	<b>63</b>
<b>4 The combination of surface and down-hole seismic networks for earthquake location at the Soultz-sous-Forêts geothermal site (France) .....</b>	<b>67</b>
<b>Abstract.....</b>	<b>67</b>
<b>4.1 Introduction .....</b>	<b>68</b>
<b>4.2 Methodology .....</b>	<b>70</b>
<b>4.3 The Soultz-sous-Forêts geothermal site.....</b>	<b>70</b>
<b>4.4 Results and discussion.....</b>	<b>74</b>
<b>4.5 Conclusion and outlooks .....</b>	<b>84</b>
<b>Acknowledgment .....</b>	<b>86</b>
<b>References .....</b>	<b>86</b>

<b>5</b>	<b>Modelling earthquake location errors at a reservoir scale: a case study in the Upper Rhine Graben</b>	88
	Abstract	88
5.1	Introduction	89
5.2	Methodology	92
5.3	Case study: Rittershoffen geothermal field	96
5.4	Results and discussions	100
5.5	Conclusions and outlook	122
	Acknowledgments	124
	References	124
	<b>THIRD PART</b>	126
<b>6</b>	<b>Modelling focal mechanism errors of seismicity induced at Rittershoffen geothermal field (Alsace, France)</b>	131
	Abstract	131
6.1	Introduction	132
6.2	Methodology	133
6.3	The Rittershoffen geothermal site	134
6.4	Results and Discussion	137
6.5	Conclusion	141
	References	142
	Acknowledgment	142
	<b>FOURTH PART</b>	140
<b>7</b>	<b>Discussion, conclusion</b>	144
7.1	Gaussian distribution of the hypocentre PDF	144
7.2	Impact of a calibration shot on earthquake location	145
7.3	Impact of the seismic coverage on focal mechanisms	147
7.4	Impact of the use of amplitude ratios S/P on focal mechanisms	152
7.5	Main discussion and conclusion	153
<b>8</b>	<b>Outlooks</b>	157
<b>9</b>	<b>References</b>	159

Fehler! Textmarke nicht definiert.

<b>APPENDICES</b> .....	165
<b>10 Modelling seismic event location errors at the reservoir scale: application to the geothermal site of Soultz-sous-Forêts (Alsace, France)</b> .....	172
<b>Abstract</b> .....	172
<b>10.1 Introduction</b> .....	173
<b>10.2 Methodology</b> .....	174
<b>10.3 The Soultz-sous-Forêts geothermal site</b> .....	175
<b>10.4 Results and discussion</b> .....	178
<b>10.5 Conclusion and outlooks</b> .....	184
<b>Acknowledgment</b> .....	185
<b>References</b> .....	185

# List of figures

## In the introduction

Figure 1-1: Diagram of predictions until 2050 showing the evolution of the world energy consumption and its distribution among the different kind of energy sources (IEA, 2011). On this graph, the width of the bands account for the uncertainties: it gives the range of possible values for the use of each energy source. A further increase of the use of renewable energies is expected. Among them, geothermal energy technologies are expected to be developed to reach an amount of about 20 EJ of production per year for Heating and a bit more than 5 EJ per year to be converted in electrical power. .... 22

Figure 1-2 : Schematic explanation of the EGS principle used in industry. .... 23

## In the first part

Figure 2-1: Schematic representation of the method proposed by Tarantola concerning the different states of information and their combination. The horizontal axes called “m” represent the model space whereas the vertical axes, called “d” account for the data space. The function  $g(m)$  introduces the theory relating both. For this example, it is assumed to be perfect. The probability densities for the a-priori model and for the observations are represented by  $\rho_M$  and  $\rho_D$  respectively. On those diagrams  $\mathbf{m}_{prior}$  is the preferred model used a-priori and  $\mathbf{d}_{obs}$  the most probable observation. The blue star accounts for the best fit model according to the data set. The grey horizontal (vertical) grey zone is the domain of acceptable data (parameters) values according to the associated uncertainties. .... 33

Figure 2-2: Schematic of the global method developed to get local earthquake location uncertainties and inaccuracies.(picture adapted from Gaucher et al(2016))..... 41

Figure 2-3: Representation of the 3 angles defining a fracture on a fault. (picture from Stein and Wysession (2009)). .... 43

Figure 2-4 : Beach-ball representing the three basic focal mechanisms. The P and T indicators accounts for “compressional” and “tensional” zones respectively. Here, the lower hemisphere of the focal sphere is represented..... 43

Figure 2-5 : Radiation diagram for P- (left), SV- (middle) and SH- (right) waves for a Double-couple (DC) source. Red and blue patterns indicate dilatation and compression zones respectively. (picture adapted from Šílený and Milev (2008)) ..... 45

Figure 2-6 : Schematic geometrical distribution of a standard staggered grid like in SOFI3D (Bohlen *et al.*, 2012)..... 53

Figure 3-1 : -left: localisation of the URG in the ECRIS formation. –Right: temperature anomalies in the URG with the different geothermal sites developed, under development or stopped in the area (modified from Bailleux *et al.* (2013)). ..... 57

Figure 3-2 : -Temperature profile in the URG (from Bailleux *et al.* (2013)) ..... 59

**In the second part**

Figure 4-1: Geometry of the seismic networks monitoring during the stimulation of the well GPK2 in June-July 2000. The filled triangles stand for 3C-sensors whereas the empty symbols stand for vertical sensors. Red and green triangles show the position of the down-hole and surface sensors respectively. The projections of the synthetic (crosses) and real (dots) seismic clouds (Cuenot, 2009) are plotted. The blue arrows show the Xc and Yc axes used in this study, which correspond to a rotation of the original geographic system according to the main distribution of the seismic cloud. Easting and northing are given relative to GPK1 wellhead. .... 72

Figure 4-2: Reference P- (black curve) and S-wave (grey curve) velocity profiles as described by Cuenot (2009, p115). The shallower dashed line delimits the top of the deep injection zone during the GPK2 stimulation and the deeper dashed line delimits the bottom of GPK2..... 73

Figure 4-3 : Sections of the location uncertainties computed with the combination of the surface and the down-hole seismic networks. The variation at a given depth (bottom panel), Xc position (top right panel) and Yc position (top left panel) are presented. The colorbar defines the range of uncertainties and is common to all plots showing them.... 76

Figure 4-4: Location uncertainties obtained with the down-hole network (left panel) and with the surface network (right panel). The distribution of uncertainties at Xc=-250 m (top), Yc=-375 m (middle) and at 4500 m depth (bottom) is shown with the colour scale of Figure 4-3. .... 77

Figure 4-5 : Box-plots of the location inaccuracy along the Yc (top left), Xc (top right) and depth (bottom) axes. The coordinates are given with respect to the GPK1 wellhead but in the cloud system. The box-plots are formed by the median (full disk) the first and third

quartiles (crosses) and the range (dashed line). The perpendicular dashed line accounts for the mesh size used for the location process.....	79
Figure 4-6: Box-plots of the location inaccuracy along $X_c$ (top), $Y_c$ (middle) and depth (bottom) computed using the down-hole network (left) and the surface network (right). The “picked” arrival-times were rounded at 10 ms before locating. Symbols are described in caption of Figure 4-5.....	81
Figure 4-7: Spatial distribution of the initial and relocated synthetic sources computed with the combined network (top), the down-hole network (middle) and the surface network (bottom). The perturbed (lower) velocity zone is shown in grey. The results are shown for the sources originally on north-south vertical plane (left), east-west vertical plane (right). On each plane, each blue dot shows the projection of one relocation position and the associated red line shows the displacement to be applied to move to the event initial position.....	82
Figure 5-1: Schematic of the multi-step approach applied to model earthquake location errors. ....	94
Figure 5-2: General view of the Upper Rhine Graben and of the deep geothermal fields (red circles) close to Rittershoffen (black circle). ....	96
Figure 5-3: Vertical cross-section of the geological structure between Soultz-sous-Forêts and Rittershoffen geothermal fields. (Adapted from GeORG Project Team (2015)).....	97
Figure 5-4: Map of the seismic network deployed at Rittershoffen. The Soultz-sous-Forêts permanent stations (blue squares), the Rittershoffen permanent stations (red squares) and the temporary stations (green triangles) are shown as well as GRT1 wellhead (red crossed circle). Station E3316 (reversed green triangle) was unavailable during the period of interest and is used only in sub-section 5.4.3. The largest rectangle delimits the velocity model zone used in this study. The smallest rectangle delimits the area in which the seismic sources are simulated; the two segments are the projections of the vertical sections of simulated sources. The projection of the zone with perturbed velocity (see sub-section 5.4.2.1) is shown as a grey circle. All coordinates are in Lambert II extended system.....	99
Figure 5-5: Profiles of the reference P-wave (blue curve) and S-wave (black curve) velocities at Rittershoffen overlaying the 150 random profiles for the P-wave (red curves) and the S-wave (green curves) velocities (see sub-section 5.4.2.1 for details). The bottom depth of the well GRT1 (horizontal dashed line) and the upper depth of the injection zone (horizontal dotted-dashed line) are also shown.....	100

Figure 5-6: 3D view of the relocation uncertainties at 68.3% (dark blue) and 99.7% (light blue) confidence levels of 27 sources distributed around GRT1 well (red curve). Part of the seismic stations is also displayed (grey cones). ..... 102

Figure 5-7: Horizontal section of the location uncertainty at 2414 m. The stations above the location zone are displayed (white triangles) as well as the GRT1 well trajectory (black curve)..... 103

Figure 5-8: Boxplots of the location uncertainties as a function of latitude (top left), longitude (top right) and depth (bottom left). The uncertainties median (points), 25<sup>th</sup> and 75<sup>th</sup> percentiles (crosses), and range (dotted segment) are shown. The 10-m relocation-mesh size is displayed (grey dashed-line) as reference. .... 104

Figure 5-9: Boxplots of the depth (top-left), the horizontal (top-right) and the total (bottom left) location inaccuracies of the synthetic earthquakes as a function of the latitude, and location inaccuracies as a function of depth (bottom right). On this last subplot, the 1D velocity profile is shown in grey. The relocations were computed by NLL using the P- and S-waves arrivals rounded at the closest 10 ms. For details on the symbols see Figure 5-8..... 106

Figure 5-10: 3D view of the relocation uncertainties at 68.3% confidence levels for the 81 sources distributed every 300 m in the E-W vertical plane (light grey) and in the N-S vertical plane (dark grey) around GRT1 well (red curve). Part of the seismic stations is also displayed (grey cones) and the initial 1D velocity model is shown as a N-S vertical section..... 109

Figure 5-11: Vertical section at 2 m North (left) and 215 m West (right) of the largest location uncertainty interpolated on a 10-m mesh. The GRT1 well trajectory is displayed (black curve)..... 109

Figure 5-12: Projection of the initial locations and of the relocations of the synthetic earthquake hypocentres for the vertical E-W plane (left) and for the vertical N-S plane (right). The relocated hypocentres (blue points) should be shifted along the red line to come back to their nitial location. The shadowed area represents the perturbed velocity zone. .... 111

Figure 5-13: Boxplots of the relocation inaccuracies for the seismic sources located on the E-W vertical plane (left column) and on the N-S vertical plane (right column). The horizontal (top row), vertical (middle row) and total (bottom row) relocation inaccuracies as a function of the event depth are presented. The vertical grey lines at +/- 20 m indicate the mesh-size of the relocation model, the 1D velocity profile is also displayed as a grey curve. For details on the symbols see Figure 5-8. .... 112

Figure 5-14: 3D view of the relocation of the synthetic events initially located on the horizontal plane and along the fault (top) and on the N-S and E-W vertical plane (bottom). The initial locations were on the grey planes whereas the relocations are on the coloured planes. The colour scale is associated with the largest uncertainty value which varies between 50 m and 250 m. The location of the fault is shown by the brown plane (bottom)..... 116

Figure 5-15: Boxplots of the horizontal (left column) and vertical (right column) inaccuracies for the horizontal plane along East (top row) and along North (middle row) and for the N-S vertical plane along depth (bottom row). For details on the symbols see Figure 5-8. .... 117

Figure 5-16: Horizontal section of the location uncertainty at 2414 m using the 16-station network. The stations above the location zone are displayed (white triangles) as well as the GRT1 well trajectory (black curve). Same display as Figure 5-7. .... 119

Figure 5-17: 3D view of the relocation, by the 16-station network, of the synthetic events initially located on the horizontal plane and along the fault (top) and on the N-S and E-W vertical plane (bottom). The initial locations were on the grey planes whereas the relocations are on the coloured planes. The colour scale is associated with the largest uncertainty value which varies between 50 m and 250 m. The location of the fault is shown by the brown plane (bottom). Same display as Figure 5-14. .... 121

**In the third part**

Figure 6-1: P- (red) and S- (blue) reference velocity profiles. The black stars indicate the depths of the synthetic sources..... 135

Figure 6-2: Geometry of the seismic networks monitoring seismicity at Rittershoffen geothermal field. The Net15 seismic network (green triangles) monitored the stimulations of GRT1 well in 2013. The Net16 network contains all stations from Net15 and an additional temporary station, E3316 (red triangle). The whole Net41 seismic network was installed before the drilling of GRT2 in 2014 and consists of the Net16 with the additional stations represented by blue triangles. The GRT1 well-head (red crossed circle), is also displayed. All coordinates are given in Lambert II extended system. .... 136

Figure 6-3: Upper view of the beachball of the best focal mechanism for the central source. Solution obtained in the 1D reference velocity model, from P-wave polarities on Net41. The white lines show all acceptable FMs. The circles show the polarities observed at the different seismic stations according to their azimuth and take-off angles: green for undetermined, blue for positive, orange for negative..... 137



Figure 6-4: Boxplot representation (Tukey, 1977) of the angular inaccuracy (in degrees) of the slip vector of the acceptable focal mechanisms obtained using P-wave polarities measured on Net15. Each boxplot shows the inaccuracies for one source. The first three correspond to the shallowest sources and the last three to the deepest ones. For each triplet, the northern source is shown first. Each boxplot shows the median (full disk), the first and third quartiles (crosses) and the range (dashed line) of the angular discrepancies between both fault plan normals. The angular inaccuracy for the mean normal vector is shown by the unfilled disk and the number of FMs used to perform the statistics is written above each boxplot. .... 138

Figure 6-5: Polar representation of strike and dip angles for all acceptable FMs. The mean and the original fault planes solutions are represented by the red and green squares respectively. Rows of the table correspond to source depth whereas columns correspond to source latitude (north-left, south-right). .... 139

Figure 6-6: Angular inaccuracy (in degrees) of the slips of the acceptable fault plane solutions, which were determined by the P-wave polarities measured on Net15 in the 3D to 1D velocity model. See Figure 6-4 for symbol details..... 140

Figure 6-7: Upper view of the beachball of the best focal mechanism for the central source. Solution determined by the P-wave polarities and amplitude ratios measured on Net15 in the 3D to 1D velocity model. Same representation as in Figure 6-3 ..... 141

**In the fourth part**

Figure 7-1 : Differences between locations performed with the grid-search method and expected location assuming a Gaussian distribution of the PDF. The boxplots are formed with the median value (red line), the first and third quartiles (extrema of the blue boxes) and the UIF and LIF (extrema of the vertical dashed lines). Outliers are represented by red crosses. The dashed gray line corresponds to the mesh size used for the location process..... 144

Figure 7-2 : Distribution of uncertainties and inaccuracies obtained after applying the station correction during the inversion process. Results for sources initially placed along the fault, on a horizontal plane, on a N-S vertical plane and on a E-W vertical plane are shown. .... 146

Figure 7-3: The angular inaccuracy for focal mechanisms obtained with Net15 (top) and Net41 (bottom) is presented as boxplots. The median (black disk), the first and third quartiles (crosses) and the range (dashed line) form the boxplot. The focal mechanism inaccuracy associated with the mean vector is shown (white disk) and the number of

focal mechanisms used to carry out the statistics is written near the associated boxplot. The results are shown for the ideal case (left panels) and when the fault was omitted in the model (right panels)..... 148

Figure 7-4: Polar representation of the set of fault planes associated with the acceptable focal mechanisms obtained by HASH software (blue dots) from polarities of the Net41. Each circle corresponds to a dip interval whereas each section to a 30° interval of azimuth. The initial (green square) fault plane is displayed as well as the fault plane associated with the mean slip vector (red square). ..... 150

Figure 7-5: Same figure as Figure 7-4 but for FMs obtained when the fault is omitted in the inversion process. .... 151

Figure 7-6 : The angular inaccuracy for focal mechanisms obtained with Net15 (top) and Net41 (bottom) is presented as boxplots. The median (black disk), the first and third quartiles (crosses) and the range (dashed line) form the boxplot. The focal mechanism inaccuracy associated with the mean vector is shown (white disk) and the number of focal mechanisms used to carry out the statistics is written near the associated boxplot. The results are shown for the ideal case when using (right panels) or not (left panels) the amplitudes ratios in the inversion..... 153

**In the appendices**

Figure 10-1: Reference P- (red curve) and S-wave (green curve) velocity profiles as described by Cuenot (2009, p.115). The shallower dashed line delimits the top of the deep injection zone during the GPK2 stimulation and the deeper dashed line delimits the bottom of GPK2..... 176

Figure 10-2: Geometry of the seismic networks monitoring during the stimulation of the well GPK2 in June-July 2000. The filled triangles stand for 3C-sensors whereas the empty symbols stand for mono-component geophones. Red and green triangles show the position of the down-hole and surface sensors respectively. The projections of the synthetic (crosses) and real (dots) seismic clouds (Cuenot, 2009) are also represented. The blue arrows show the Xc and Yc axes used in this study, which correspond to a rotation of the original geographic system according to the main distribution of the seismic cloud. Easting and Northing are given relative to GPK1 well-head. .... 177

Figure 10-3 : Boxplots of the location uncertainties computed with the combination of the surface and the down-hole seismic networks. The variation with depth (bottom panel), along Xc (top right panel) and along Yc (top left panel) are presented. The boxplots

show the range of values (dashed lines), the first and third quartile (crosses) and the median (disk)..... 180

Figure 10-4: Uncertainties obtained with the down-hole network (left panel) and with the surface network (right panel). Boxplots symbols are the same as in Figure 10-3. .... 180

Figure 10-5 : Box-plots of the location inaccuracy along depth. The box-plots are formed like in Figure 10-3. The perpendicular dashed line accounts for the mesh size used for the location process. .... 182

Figure 10-6: Boxplots showing total inaccuracies for location computed with the combined network (top panels) and the down-hole network alone (bottom) with data from a synthetic modelling in a profile with a LVZ. The locations were carried out in the reference velocity model. The location were computed for sources on vertical-Yc plane (left), vertical-Xc plane (right) and horizontal plane (not shown). The perpendicular grey-line accounts for the mesh size used for the location and the shadowed zone corresponds to the simulated injection zone. The symbols concerning the boxplots are described in Figure 10-3..... 183



# 1 Introduction

## 1.1 Context

### 1.1.1 Geothermal energy

Since the number of human being keeps on increasing, the amount of energy needed to supply everybody is becoming huge and a real challenge to address. Hence, in order to replace part of fossil energies, development of renewable energies like wind, solar energy or geothermal energy began several decades ago. However the productivity of these new kinds of energy remains lower than the one of fossil fuels and therefore, improvement in this field is still required. The IEA report [IEA, 2011] foresaw a production of more than 250 EJ per year for the whole energy storage, and a production of 20 to 25 EJ per year ( $\approx 0.5510^{16}$  Wt.h) in 2050 for both use of geothermal energy – heat and electrical power – as shown in the Figure 1-1.

The term “geothermal” originates from a combination of the two Greek words GEO and THERM, which respectively mean EARTH and HEAT. Therefore, by definition, geothermal energy is a source of energy generated and stored in the Earth. Different causes can create geothermal heat as for example radiogenic decay [Kohl *et al.*, 1995]. Furthermore, sharp contrasts in the geothermal gradient are created by the combination of thermal convection movements in the asthenosphere and thermal conduction in the lithosphere. Like other renewable energies and unlike fossil energies, the direct impact of the use of geothermal energy on our planet is very low. For example it does not reject any “greenhouse gas” in the atmosphere. Furthermore and compared to other renewable energies, geothermal energy has the advantage of not being weather dependant, which makes it available the whole year long and therefore an attractive alternative energy. Two kinds of geothermal energy exist. In the case of the shallow geothermal energy, wells may be drilled down to  $\sim 400$  m. Consequently the temperature reached in the subsurface is not high enough to produce electrical power and is mainly used to heat private houses. On the contrary, with the deep geothermal energy, a temperature usually higher than  $150^{\circ}\text{C}$  is reached and the heat extracted can be used either for heating buildings or to provide electrical power. This work will be focused on deep geothermal energy. Several places in the world present conventional geothermal energy sources, for example in the proximity of active volcanoes in Iceland or in Chile. In these

areas, the heat is easily accessible from the Earth’s surface or at least in the very near sub-surface and can be easily extracted. However from a worldwide perspective, these places are anomalies and the geothermal resources are typically distributed at larger depth. Hence, to access this energy, several technologies are developed all over the Earth. Wells are drilled, deepened or reused and several processes like the EGS systems (see sub-section 1.1.2) were developed to reach, extract, convert and use this underground energy.

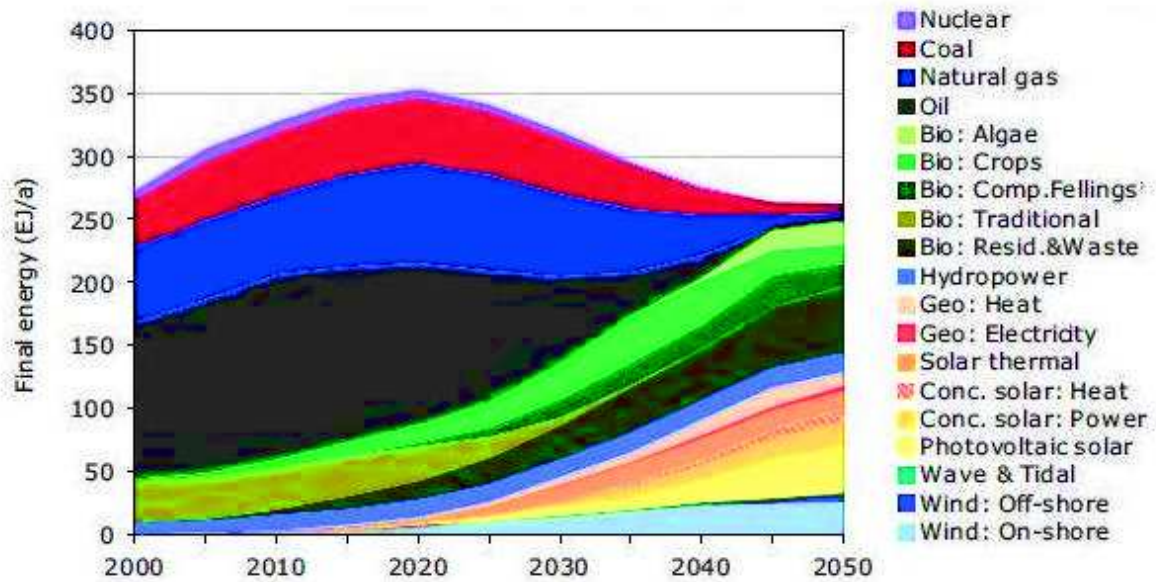


Figure 1-1: Diagram of predictions until 2050 showing the evolution of the world energy consumption and its distribution among the different kind of energy sources [IEA, 2011]. On this graph, the width of the bands account for the uncertainties: it gives the range of possible values for the use of each energy source. A further increase of the use of renewable energies is expected. Among them, geothermal energy technologies are expected to be developed to reach an amount of about 20 EJ of production per year for Heating and a bit more than 5 EJ per year to be converted in electrical power.

### 1.1.2 HDR/EGS systems

According to the different situations and accessibilities to the geothermal energy several technologies were developed. Among those technologies, one can refer to the Hot Dry Rock (HDR) and to the Enhanced (or Engineered) Geothermal Systems (EGS) methods. Compared to the HDR technique, which uses hydraulic fracturing to create fractures in the sub-surface to form a good network for fluid propagation, the EGS takes advantage of the existing content in fractures of the sub-surface. To choose between HDR and EGS one commonly looks at the permeability of the initial sub-surface. The exploitation principle is shown in Figure 1-2. Cold water is injected in a first well – also called “injector well” – down to a system of fractures in the sub-surface. While propagating in the fracture network, the fluid is heated by friction with the surrounding rocks until reaching a second well (the production well). Rocks and fractures together form the so-called “geothermal reservoir”. The hot fluid is pumped in the production

well and it then moved through the Heat Exchanger where its heat is extracted. An improvement of the connectivity between the fractures in the reservoir and/or between the wells and the reservoir is often necessary, explaining the term “enhanced” in the name EGS. Chemical and/or thermal and/or hydraulic stimulations are the common ways used to this improvement. In the case of a successful stimulation, the deep reservoir can be exploited and one can extract the heat from the hot natural brine from a power plant at surface. The natural brine is then reinjected into the reservoir at a lower temperature [ES Geothermie].

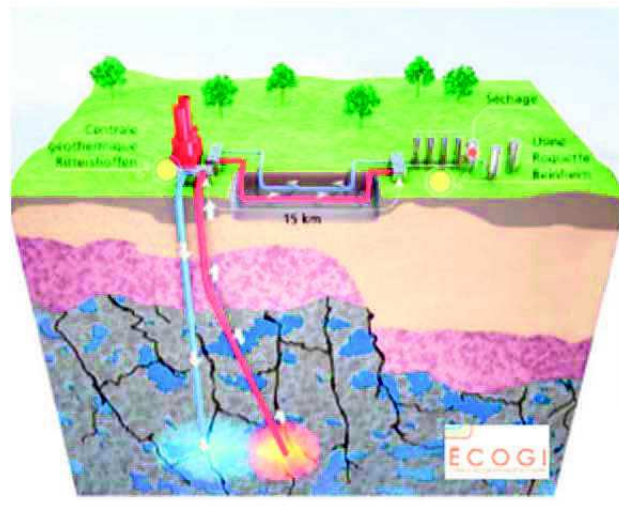


Figure 1-2 : Schematic explanation of the EGS principle used in industry.

The first HDR was developed in the 1970’s in Fenton Hill (USA). The success of the experiment led other countries all over the world to try it. To give a few examples, Australian people created an EGS in the Hunter Valley whereas European people developed geothermal energy production in Rosemanove (Cornwall, UK), in Bad Urach (Germany), in Le Mayet de Montagne (France) or in Fjällbacka (Sweden). Still in Europe, many geothermal sites were installed in the Upper Rhine Graben (URG), a geological region extending from North Switzerland to Frankfurt (Germany) and briefly described in chapter 3. The first geothermal site in the URG was developed in Soultz-sous-Forêts (France) and is used as a pilot site in this region. The measurements and experiments performed there enabled the development of other geothermal fields in areas such as Basel, Riehen (Switzerland), in Landau, Insheim and Bruchsal (Germany) and newly in Rittershoffen, a village located in the proximity of Soultz-sous-Forêts.

Due to a modification of the stress field in the sub-surface during the propagation of water, seismicity may be induced during the stimulation of or circulation tests in the fracture networks of an EGS. The term “induced seismicity” is commonly used to define the whole set of the earthquakes due to these operations and more generally to human activity. This induced

seismicity is used for many different purposes. For example, faults and fractures geometry and orientation in reservoirs were obtained from induced earthquakes location and focal mechanisms [Sausse *et al.*, 2010; Frietsch *et al.*, 2015]. The seismic risk zones may be defined by an accurate study of earthquake location and magnitude among other parameters [Bromley and Majer, 2012; Gaucher, 2016; Gaucher *et al.*, 2015; Giardini, 2009]. To interpret the results in a reliable manner, it is necessary to quantify the errors associated with these seismic parameters (earthquake location, focal mechanism,...).

Two notions are grouped in the term “error”. The uncertainties can be defined as the range of acceptable values for a given result. For example, if we ask several persons to measure the dimensions of an object, they may provide different results. The uncertainty may then be defined by the range of the different values obtained. In many domains the uncertainties are provided with the result. On the contrary, the inaccuracy is a bias. It defines how far the obtained result is from the reality and cannot be determined without *a priori* knowledge. In our previous example, the inaccuracy is the difference between the real size of the object and the size measured by a badly calibrated ruler. An inaccurate but precise measure will lead to misinterpret the result whereas an accurate but uncertain measure may lead to loose interpretation. According to those definitions, it is far better to obtain accurate and uncertain results than inaccurate but certain ones. The term “data processing” covers all ways to pass from the raw dataset into the parameters we are looking for.

## **1.2 Aim of the Ph. D.**

The global goal of the study can be divided into several steps. The first and main aim of the Ph.D. is to quantify the errors associated with travel-times-earthquake-location using body waves. The propagation of those errors into the determination of the focal mechanism errors is then investigated. The methodology was developed for the local scale of a reservoir. The final aim is to quantify the impact of those errors on the interpretations of geosciences results. For example, the deformation of structures and their orientation change will be discussed.

## **1.3 Plan of the manuscript**

The manuscript is based on a cumulative dissertation of several studies performed during the Ph.D. Before the studies themselves, some important notions are introduced for a better understanding of the manuscript (chapter 2). In this chapter a small explanation about the earthquake location and the methods to process it (section 2.2) is preceded by a brief introduction to the inverse problem theory (section 2.1). Several methods will be introduced

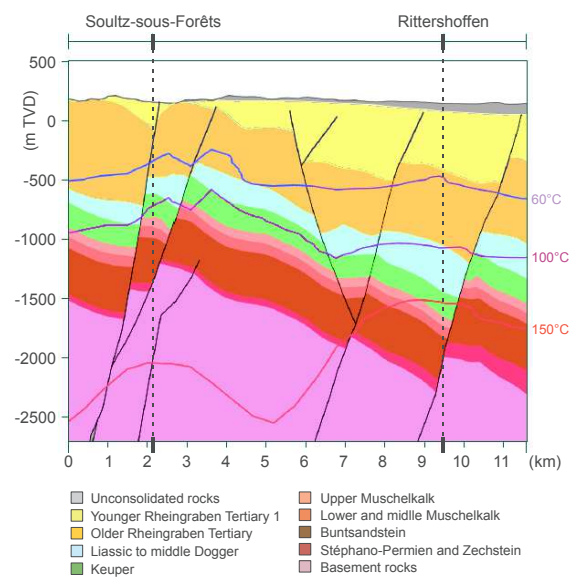


and the method applied to carry out the location uncertainties and inaccuracies will be described. In section 2.3, the notion of focal mechanism is explained and several methods to get them are briefly described as well as the method chosen to model the focal mechanism uncertainties and inaccuracies. Both earthquake location and focal mechanisms are carried out by solving inverse problems. In a last section, some methods to create waveforms are summarized with the encountered difficulties, drawbacks. Then, the geological context is described and the two geothermal sites used for our investigation are presented (chapter 3). The second part of the manuscript consists in the main topic of the Ph.D.: the quantification of inaccuracies and uncertainties associated with the earthquake location. The impact of several parameters are investigated and discussed. The main text is contained in two papers forming one chapter each. The content in chapter 5 was submitted to Pure and Applied Geophysics [Kinnaert *et al.*, *submitted*]. This is an application of the methodology to the geothermal site of Soultz-sous-Forêts for which the impact of down-hole sensors on earthquake location is investigated. In chapter 6, which content was published in JGI [Kinnaert *et al.*, 2016], the possible location errors at the geothermal site of Rittershoffen are investigated. In a third part initial results for the focal mechanism uncertainty and inaccuracy are carried out and discussed for the stimulation of GRT1 at Rittershoffen. In chapter 7, several assumptions done during our processing flow are discussed as well possible working perspectives before concluding. Chapter 8 provides more general outlooks to the performed work.



# FIRST PART:

## Theory and geothermal settings



Vertical cross-section of the geological structure between Soultz-sous-Forêts and Rittershoffen geothermal fields  
(Adapted from GeORG Project Team (2015)).

## 2 Theory

As explained in the Introduction part, the aim of this PhD is to model expected errors on event location and focal mechanisms for induced earthquakes occurring at the scale of a (geothermal) reservoir. In this section, the concept of event location and different methods used to perform it will be introduced (section 2.2). The concept of location error will be explained. Then, the concepts of focal mechanism and moment tensor will be discussed (section 2.3), focusing on the concept of Double-Couple sources [Nakano, 1923; Shearer, 2009] since this is the kind of earthquakes we used for the study. A discussion about the definition of the focal mechanism error will be included in that sub-section. In section 2.4 the creation of waveforms using different methods is discussed focusing on the finite difference (FD) method because this is the one used in our study. But, since the earthquake location and focal mechanism are inverse problem solutions, notions about it and some (common) techniques to solve it are firstly introduced (section 2.1).

### 2.1 Inverse Problem

#### 2.1.1 Definitions, setting the inverse problem

The “inverse problem” designs all situations in which we are looking for the causes of a phenomenon knowing its consequences. These consequences are commonly called “data” or “observations” [Jaynes, 2003; Tarantola, 2005]. In a general sense, solving an inverse problem means finding a model approximating the reality according to a chosen uncertainty (quality) and to a set of observations. In a mathematical sense, solving this type of problem is the equivalent of a comparison between results obtained by a theoretical function and the observations. The aim is to find the set of parameters (the model,  $\mathbf{m}$  in equation 2-1) which fit the best with the observation set ( $\mathbf{d}$  in equation 2-1) according to predefined properties (stored in function  $g$  or matrix  $\mathbf{G}$ ) [Tarantola, 2005; Ramm, 2006] and acceptable uncertainties (term  $\mathbf{e}$  in equation 2-1).

$$\mathbf{G} \cdot \mathbf{m} + \mathbf{e} = g(\mathbf{m}) = \mathbf{d} \quad 2-1$$

In a general way, the inverse problem is divided into three parts: the *a priori* information, the *a posteriori* information, and the theory. This *a priori* information contains always the set of observations and sometimes an *a priori* solution (the *a priori* model). On the contrary, the

different solutions belong to the *a posteriori* information. The theory is only the mathematical part relating all observations to a model (derivatives, constants for multiplications, ...).

The mathematical concept of the “well given problem” was derived from a definition proposed by *Hadamard* [1902]. According to him, the mathematical models representing the physical observations should have a unique existing solution and this solution should depend continuously on the data (equivalently, the theoretical function should be continuous). Nonetheless, inverse problems are generally not “well given problems”: for example, they often suffer from the presence of uncertainties in the data set. In that case there is no model to explain correctly the whole set of observations with the associated uncertainties. Hence, instead of looking for an exact solution, we search the model which fits the best with the observations. Nevertheless, since the solution is not exact anymore, several models can fit with the observations and *a priori* information should help to find the best.

To set the inverse problem two kinds of formulations are possible: the linear formulation and the non-linear formulation. In the linear formulation all terms of the equation are given by a vector or a matrix like in equation 2-2. In that equation,  $\mathbf{d}$  is a vector containing all observations whereas the vector  $\mathbf{m}$  is the set of unknown parameters. The matrix  $\mathbf{G}$  contains the physical and mathematical properties of the problem (of the *a-priori* model) and  $\mathbf{e}$  is a vector containing the error associated with the data.

$$\mathbf{G} \cdot \mathbf{m} + \mathbf{e} = \mathbf{d} \quad 2-2$$

In the non-linear formulation, the different part of the equation cannot be described by tensors. The observations are given as the result of a function of the parameters (right terms in equation 2-1).

Now that we know what it is, let us consider some existing methods to solve the inverse problem.

### 2.1.2 Solving an inverse problem

In most cases, solving an inverse problem means looking for the minimization of a cost-function. This way can be used either for a linear or a non-linear formulation of the inverse problem. If the number of independent data is higher than the number of parameters to be determined, the system is overdetermined and the set of equations to be solved becomes inconsistent due to errors in the data. A common way to solve this kind of system is a least-square estimation. On the contrary, some problems are underdetermined: the number of independent data is lower than the number of parameters to be determined, leading to infinity of possible solutions. One way to solve these problems is the minimum norm solution (in the

case of linear problems). But most often, the inverse problem is both overdetermined for some parameter(s) and underdetermined for other one(s). Hence, none of the two previous methods (least squares and minimum norm) can be used to estimate the model. The problem is said to be ill-conditioned.

### 2.1.2.1 Solving linear inverse problems

In that case, the forward problem can be simply written as in equation 2-2 [Snieder and Trampert, 2000; Tarantola, 2005]. However, in many papers, the error vector  $\mathbf{e}$  is directly taken into account in the data vector and hence does not appear explicitly in the formula. Denoting by  $\mathbf{m}_e$  the estimated model, it can always be calculated by equation 2-3 in which  $\mathbf{G}^g$  is linked to the “generalized inverse” of matrix  $\mathbf{G}$  [Snieder and Trampert, 2000].

$$\mathbf{m}_e = \mathbf{G}^{-g} \mathbf{d} \quad 2-3$$

Replacing  $\mathbf{d}$  in 2-3 by its value in 2-2, the term corresponding to the “kernel resolution” appears. It is defined as

$$\mathbf{R} = \mathbf{G}^{-g} \mathbf{G} \quad 2-4$$

In the case of a perfect resolution, this term is equal to the identity matrix ( $\mathbf{R}=\mathbf{I}$ ).

In geophysics, linear methods are often used to solve inverse problems. Furthermore, the matrix  $\mathbf{G}$  set in the formulation (equation 2-1) is always rectangular. Hence the generalized inverse method is necessary to solve the inverse problem. A particular solution from the generalized inverse for overdetermined problems with linear method is the least-square process. The solution is given by equation 2-5 [Strang, 1988]. The subscripts -1 and T are associated with the inverse and transpose operation respectively.

$$\mathbf{m}_e = (\mathbf{G}^T \mathbf{G})^{-1} \mathbf{G}^T \mathbf{d} \quad 2-5$$

To solve underdetermined problems with linear method one can use the Lagrange multipliers [Menke, 2012]. By this method, the estimated model is expressed by

$$\mathbf{m}_e = \mathbf{G}^T (\mathbf{G} \mathbf{G}^T)^{-1} \mathbf{d} \quad 2-6$$

The damped least squares method [Levenberg, 1944] like expressed in the right part of 2-7 is a possible solution for ill-conditioned problem which are linearly formulated. The left part of the same equation is the damped version of the minimum norm solution. The matrix  $\mathbf{I}$  is the identity matrix and the symbol  $\gamma$  represents the damping factor.

$$\mathbf{m}_e = (\mathbf{G}^T \mathbf{G} + \gamma \mathbf{I})^{-1} \mathbf{G}^T \mathbf{d} = \mathbf{G}^T (\mathbf{G}^T \mathbf{G} + \gamma \mathbf{I})^{-1} \mathbf{d} \quad 2-7$$

The method of the generalized inverse is associated with the Singular Value Decomposition (SVD) of matrix  $\mathbf{G}$  [Jackson, 1972; Wiggins, 1972; Lee and Stewart, 1981], which is itself based on the Lanczos decomposition [Lanczos, 1961]. Including matrix of weights for both

data ( $\mathbf{W}_d$ ) and parameters ( $\mathbf{W}_m$ ) the system of equations to be solved becomes [Snieder and Trampert, 2000]:

$$\begin{bmatrix} \mathbf{W}_d^{1/2} \mathbf{G} \\ \sqrt{\gamma} \mathbf{W}_m^{1/2} \end{bmatrix} \mathbf{m} = \begin{bmatrix} \mathbf{W}_d^{1/2} \mathbf{d} \\ \mathbf{0} \end{bmatrix} \quad 2-8$$

The SVD method can be seen as a generalisation of the eigenvalue-eigenvectors decomposition of square matrices to non-square matrices. Setting  $\mathbf{G}_{ex} = \begin{bmatrix} \mathbf{W}_d^{1/2} \mathbf{G} \\ \sqrt{\gamma} \mathbf{W}_m^{1/2} \end{bmatrix}$  and

$\mathbf{d}_{ex} = \begin{bmatrix} \mathbf{W}_d^{1/2} \mathbf{d} \\ \mathbf{0} \end{bmatrix}$ , equation 2-8 becomes

$$\mathbf{G}_{ex} \mathbf{m} = \mathbf{d}_{ex} \quad 2-9$$

The relations given in equation 2-10 link both types of inverse problems according to their eigenvalues and eigenvectors.

$$\mathbf{G}_{ex} \mathbf{v}_{(n)} = \lambda_n \mathbf{u}_{(n)} \quad 2-10$$

$$\mathbf{G}_{ex}^T \mathbf{u}_{(n)} = \lambda_n \mathbf{v}_{(n)}$$

By multiplying the first line by  $\mathbf{G}_{ex}^T$  and the second by  $\mathbf{G}_{ex}$  and then replacing, we define  $\mathbf{u}_{(n)}$  and  $\mathbf{v}_{(n)}$  as being the eigenvectors of  $\mathbf{G}_{ex} \mathbf{G}_{ex}^T$  and  $\mathbf{G}_{ex}^T \mathbf{G}_{ex}$  respectively. They are associated with the same non-zero eigenvalues  $\lambda_n^2$ . The square root of the eigenvalue,  $\lambda_n$ , is called the singular value of  $\mathbf{G}_{ex}$ . Eigenvectors  $\mathbf{u}_{(n)}$  and  $\mathbf{v}_{(n)}$  are often organized in matrices  $\mathbf{U}$  and  $\mathbf{V}$  for which they constitute the columns. Matrices  $\mathbf{U}$  and  $\mathbf{V}$  can then be arranged such that they can be divided into two part: the part associated with non-zeros eigenvalues ( $\mathbf{U}_p$  and  $\mathbf{V}_p$ ) and the part to complete for the zeros eigenvalues ( $\mathbf{U}_0$  and  $\mathbf{V}_0$ ). This leads to equation 2-11. The singular values  $\lambda_i$  in matrix  $\Sigma$  are sorted in decreasing order.

$$\mathbf{G}_{ex} = [\mathbf{U}_p \quad \mathbf{U}_0] \begin{bmatrix} \Sigma & \mathbf{0} \\ \mathbf{0} & \mathbf{0} \end{bmatrix} \begin{bmatrix} \mathbf{V}_p^T \\ \mathbf{V}_0^T \end{bmatrix} \quad 2-11$$

$$\Sigma = \begin{bmatrix} \lambda_1 & 0 & \dots & 0 \\ 0 & \lambda_2 & 0 & \dots \\ 0 & 0 & & \lambda_p \end{bmatrix}$$

The solution for vector  $\mathbf{m}$  can then be written like in equation 2-12 in which  $\Sigma^{-1}$  is the inverse of  $\Sigma$ .

$$\mathbf{m} = \mathbf{V}_p \Sigma^{-1} \mathbf{U}_p^T \mathbf{d} = \sum_{n=1}^p \left( \frac{1}{\lambda_n} \mathbf{v}_{(n)} (\mathbf{u}_{(n)} \cdot \mathbf{d}) \right) \quad 2-12$$

Nevertheless, this method is quite time consuming [Nolet, 1985]. Hence other methods were developed to solve the inverse problem but keeping in mind the necessity of the resolution matrix [Zhang and McMechan, 1995][Deal and Nolet, 1996]. The method is based on the

LSQR developed by *Christopher C. Paige and Michael A. Saunders* [1982] who themselves improved the conjugate gradient (CG) method [*Hestenes and Stiefel*, 1952] with some similarities to the pre-cited generalised inverse method based on the SVD [*Spakman and Nolet*, 1988]. The method begins with the reduction of matrix **G** into a bidiagonal form by the Householder transformation [*G. Golub and W. Kahan*, 1965; *Householder*, 1955]. Then a QR algorithm is used to find the singular value of the obtained bidiagonal matrix.

### 2.1.2.2 Solving non-linear inverse problems

Any inverse problem can also be solved by probabilistic approach. To use the probabilities all parts of the inverse problem (data and model) are represented using probability density functions (PDF). The PDF is the function used to describe a continuous probability distribution of a random variable X. The graph of the PDF is continuous at least over the domain (the continuous range) of the random variable X which is itself continuous. The area delimited by the curve of the PDF and the x-axis including the whole domain is equivalent to the probability of finding the solution in the whole domain which is of course equal to 1. The chance of obtaining a probability between a and b for the random variable X is thus equal to the area under the curve between x=a and x=b. Mathematically, it is the same as solving equation 2-13 in which P() stands for the probability and f(x) is the so-called PDF [*Jeffreys*, 1939; *Jaynes*, 2003; *Tarantola*, 2005].

$$P(A \leq X \leq B) = \int_A^B f(x)dx \quad 2-13$$

One way to estimate the *a posteriori* PDF is based on the Bayes theorem [*Bayes*, 1958] and the theory of conditional probabilities [*Drilleau et al.*, 2013]. *Tarantola* [2005] proposed to consider the a-posteriori probability density as being the combinations of the “state of information” of the inverse problem. In that representation, the observations are introduced by the probability density  $\rho_D(\mathbf{d})$  where **d** accounts for a vector of data belonging to the data space D. This data probability density can be represented by a Gaussian law centred on the most probable observation  $\mathbf{d}_{\text{obs}}$  with a standard deviation equal to the measure uncertainty. The knowledge of the a-priori model is taken into account by the density  $\rho_M(\mathbf{m})$  of a vector of parameter **m** in the model space M (also called parameter space). This density can be modelled by a Gaussian law too but this time it is centred on the preferred model  $\mathbf{m}_{\text{prior}}$  and its standard deviation is defined accordingly to how much we trust the model. The theory is represented by the function g relating data and models by the equation  $g(\mathbf{m})=\mathbf{d}$ . The likelihood function L(**m**) is a probability density belonging to the model space which



describes how much a model  $\mathbf{m}$  can explain the data  $\mathbf{d}$ . It is proportional to  $\rho_D(g(\mathbf{m}))$ . The a-posteriori probability density in the model space, called  $\sigma_M(\mathbf{m})$  is given by the product between the likelihood function and the probability density of the a-priori model. The whole method is schematically represented on Figure 2-1.

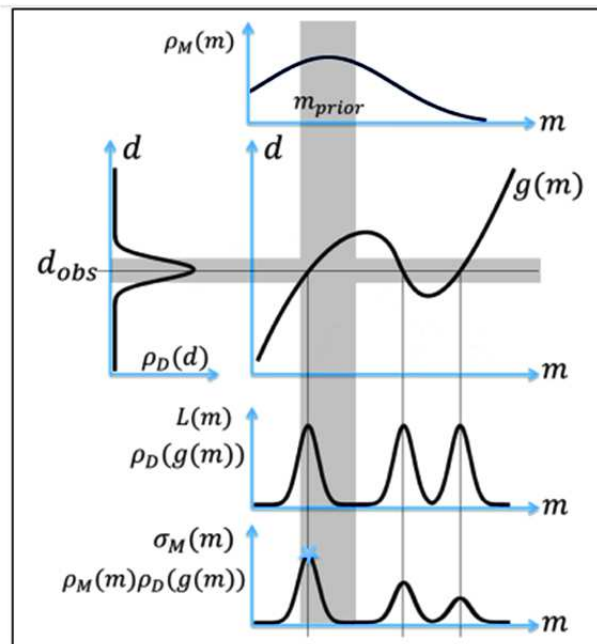


Figure 2-1: Schematic representation of the method proposed by Tarantola concerning the different states of information and their combination. The horizontal axes called “m” represent the model space whereas the vertical axes, called “d” account for the data space. The function  $g(m)$  introduces the theory relating both. For this example, it is assumed to be perfect. The probability densities for the a-priori model and for the observations are represented by  $\rho_M$  and  $\rho_D$  respectively. On those diagrams  $m_{prior}$  is the preferred model used a-priori and  $d_{obs}$  the most probable observation. The blue star accounts for the best fit model according to the data set. The grey horizontal (vertical) grey zone is the domain of acceptable data (parameters) values according to the associated uncertainties.

Depending on the complexity of the theory (function  $g$ ), the formulation of the inverse problem may be not linear. Therefore the methods described previously in sub-section 2.1.2.1 cannot be directly used. Nevertheless, the non-linear problems can sometimes be linearized, and the solution can be computed as previously described [Tarantola and Valette, 1982]. Since the linear approximation is only locally valuable, the inversion has to be repeated iteratively in order to get a local maximum of the a-posteriori probability density. The “gradient method” is another method to solve the non-linear inverse problem. Nonetheless, this method is strongly dependent on the initial model and can be locked in a local maximum. If too many sets of model parameters solve the inverse problem, the methods presented above cannot be used anymore. The a-posteriori PDF should be entirely estimated. To reach this goal, several techniques were developed. The most basic one is the Grid-Search method which looks for the solution over the whole model space. In that technique, the model space is discretized into a grid. The finer the grid is, the more precise the result can be. Nevertheless, the mesh dimensions and number in the grid as well as the number of parameters to be

determined will directly constrain the computing time and memory necessary for the calcul. *Godano* [2009] expected 11,793,600 iterations to explore the whole set of all three angles defining a fault plane by step of 1°. Hence, it was mandatory to create other methods for solving non-linear inverse problems.

Among the other methods, several are based on the Monte-Carlo [*Metropolis and Ulam*, 1949; *Metropolis et al.*, 1953; *Mosegaard and Tarantola*, 1995] exploration. The model space (parameter space), assumed to be discrete and finished, is sampled. Several models are generated according to a random walk in that model space. The random walk is often defined by the Markov chains [*Gilks*, 2005]. This means that the set of parameters checked at step n+1 depends only on the set of parameters checked at step n. The iteration in the random exploration for the Monte-Carlo simulation may be described as follow. For one state  $X_n = i$  in the Markov chain, one set of parameters ( $m_i$ ) is assumed to be the solution of the inverse problem. The state  $X_{n+1} = j$  corresponds to the set of parameters  $m_j$ , which is obtained by a random perturbation, taken in an interval  $I = [-dm; +dm]$ , of the parameters of  $m_i$ . Then the theoretical data (observations) are calculated by using equation 2-1 and the cost function giving the difference between observed data and theoretical data is calculated, like in many other methods, by an  $L_p$ -norm

$$S_j = \frac{1}{p} \sum_i \frac{|d_i - g_i(m_j)|^p}{\sigma_i^p} \quad 2-14$$

In this equation,  $\sigma$  is the uncertainty associated with the observed data  $d$ . The  $p$  is the order of the norm. For a first-order norm,  $L_1$ ,  $\sigma$  is evaluated after Laplace distribution whereas it follows a gaussian distribution for  $L_2$ . The cost-function  $S_j$  for  $X_{n+1}=j$  is compared to the cost-function  $S_i$  for  $X_{n+1}=i$ . If the inequation  $S_j \leq S_i$  is verified,  $m_j$  is used as the current solution of the problem. Else the acceptance or rejection of  $m_j$  as the current solution is defined according to a probability law,  $P(i \rightarrow j)$ , depending on the used algorithm. For the pure Monte-Carlo algorithm,

$$P(i \rightarrow j) = 0 \quad 2-15$$

Nevertheless, using this method, the process may be blocked in a local minimum. Therefore, other algorithms were developed based on the basic principle of this Monte-Carlo method.

The algorithm proposed by *Metropolis et al.* [1953] works the same way as the pure Monte-Carlo method instead that the probability law is defined by

$$P(i \rightarrow j) = e^{-(S_j - S_i)} \quad 2-16$$

By this technique, the region of the global minimum is usually correctly determined. Nonetheless, the algorithm is not optimal for having a finer location of this absolute minimum.

The method was then improved including the simulated annealing for the computation [Kirkpatrick *et al.*, 1983; Billings, 1994]. The technique is based on an analogy with thermodynamics. The colder a crystal is, the more difficult it is for a molecule to get out of it. In analogy, it describes the capacity of the exploration to get out of a local minimum and continue its walk in the model space. This means that the state  $m_j$  should be accepted but for a cost-function  $S_j > S_i$  associated with the state  $m_i$ . Defining by  $T_{n+1}$  the “temperature”, which controls the decrease of the probability at step  $n+1$  in the process, the probability law in the simulated annealing algorithm is written as

$$P(i \rightarrow j) = e^{-\left(\frac{S_j - S_i}{T_{n+1}}\right)}; T_{n+1} = aT_n \quad 2-17$$

In that algorithm, the probability of acceptance is strong for the first iterations and then decreases for each iteration. Hence, the first iterations define a rough location of the minimum of the cost-function. This means that many “bad” configurations  $m$  are accepted in order to cover a large part of the model space. Then, step by step, focus is made on the best region (with the absolute minimum of the cost-function) and the algorithm does not allow the exploration outside this focusing region.

For both earthquake location (section 2.2) and focal mechanism determination (section 2.3), the errors can be distinguished into inaccuracies and uncertainties. The uncertainties are usually due to uncertainties on observations and are included in the inverse problem formulation. Those can be related to “doubt”. On the contrary, the inaccuracies are commonly related to all missing conditions in the inverse problem either because of a lack of knowledge or to simplify the formulation (for example when using linear formulation of the inverse problem).

## 2.2 Earthquake location

### 2.2.1 Definition

Earthquake location is the solution of a non-linear inverse problem [Tarantola Albert, 2005] investigated for ages [Geiger, 1912; Flinn, 1965; Wittlinger *et al.*, 1993; Billings, 1994; Husen and Hardebeck, 2010]. Looking for an earthquake hypocentre means that the parameters in vector  $\mathbf{m}$  of equation 2-1 are the East, North, and depth coordinates of the

earthquake as well as its origin time. Assuming those are independent parameters, we hence need 4 different observations to get a unique solution for the location. Commonly, the  $d$  in equation 2-1 is filled with observed arrival-times (on seismograms) recorded at different seismic stations. The function  $g$  or matrix  $G$  contains the mathematical formulation of the physic of the problem. It can for example consist in partial derivative of the arrival-times relatively to the different parameters of the searched model. Earthquake location is a primary task in many seismological studies since several other earthquake characteristics like the focal mechanism are derived from it.

To locate hypocentres, most of the automated techniques are based on the time residual minimisation. This means that the differences (the residuals) between observed (also called picked) and theoretical (or computed for given parameters) arrival-times are calculated and compared. The minimum residual indicates the location of the hypocentre. The Geiger algorithm [Geiger, 1912] is a common one to linearize the inverse problem. P- and S-wave first onsets are mostly used. A rough overview of the methods using arrival-times as input data can be seen in [Thurber and Rabinowitz, 2000]. If the P- first onset can usually be correctly determined, it is not the case for later phases, even S-waves. Those methods can be divided into two classes: the absolute location methods and the relative location method. Earthquake location of both types is very sensitive to several parameters, particularly the velocity model representing the propagation medium [Michelini and Lomax, 2004; Gritto et al., 2008; Husen and Hardebeck, 2010; Gesret et al., 2015]. Moreover, the precision of the picked arrival-times is of primary importance [Gharti et al., 2010].

If one use a Bayesian formulation of the solution, the PDF describing the earthquake location at position  $\mathbf{X}$  is given by equation 2-18 [Tarantola, 2005].

$$PDF(\mathbf{X}) = K \cdot \exp \left\{ -\frac{1}{2} \left( [\tilde{\mathbf{T}}_{obs} - \tilde{\mathbf{T}}_{calc}(\mathbf{X})]^t \cdot \mathbf{C}^{-1} \cdot [\tilde{\mathbf{T}}_{obs} - \tilde{\mathbf{T}}_{calc}(\mathbf{X})] \right) \right\} \quad 2-18$$

The underscripts “Calc” and “Obs” account for calculated (computed from given theory) and observed (picked) respectively. The superscripts “t” and “-1” means that the affected vector or matrix is transposed or inversed respectively. The symbol “~” above the vectors  $\mathbf{T}$  (of arrival-times) means that their weighted mean has been deleted from each of their values. The matrix  $\mathbf{C}^{-1}$  contains all weights.

As explained before in a more general sense, the errors resulting from earthquake locations procedures are divided into two classes: location uncertainty and location inaccuracy [Tarantola, 2005]. The first one usually results from uncertainties in the data used in the inverse problem (typically arrival-times uncertainties) whereas the seconds result from inconsistencies in the input parameters (typically an incorrect velocity model). Both can be

determined but the conditions to get the inaccuracies are far more restrictive. The data uncertainties are represented by the symbol “e” in equation 2-1.

## 2.2.2 Absolute location methods

The absolute methods locate each event separately. The equations are solved for one event at a time according to the chosen method and limiting conditions (e.g. thresholds,...) used for computation. Some techniques are now available to take errors in inputs (travel-times errors) and to provide earthquake location with its associated uncertainty [Sambridge and Kennett, 1986; Moser *et al.*, 1992; Wittlinger *et al.*, 1993; Lomax *et al.*, 2000; Husen *et al.*, 2003]. The cited examples deal with probabilistic techniques applied to the non-linear formulation of the earthquake location problem since we chose one of them. Nonetheless the equivalent exist for the linear formulation of the problem [Lahr, John, C., 1999]. The method to derive the uncertainty is often based on the one proposed by Pavlis [1986].

If the inverse problem is set in a linear formulation, its solution can be calculated by software like HYPO71 [Lee and Lahr, 1975] or HYPOELLIPSE [Lahr, John, C., 1999]. The linear methods appear to provide good enough results for simple layered models, but they cannot deal with strongly heterogeneous medium [Lomax *et al.*, 2000]. In this case, the inverse problem is set in a non-linear formulation and can be solved using the grid-search and the Monte-Carlo methods [Press, 1968; Hammersley, 2013; Sen and Stoffa, 2013] for example. Those methods allow the calculation of the whole probability density function (PDF) representing the event location and its uncertainty. Nevertheless they are quite time consuming if we need to use model grids containing many nodes (either for its dimension or because we need a fine cell). To overcome this problematic, Lomax *et al.* [2000] propose a Metropolis-Gibbs algorithm [Metropolis *et al.*, 1953] but using global sampling. This Metropolis-Gibbs sampler is comparable to the simulated annealing [Kirkpatrick *et al.*, 1983; Billings, 1994] using a constant “temperature” parameter. The Metropolis-Gibbs algorithm deals with a random walk in the space of solutions (coordinates x, y, z). The nearby trials moves of the walk are accepted or rejected according to the PDF evaluated by computing the forward problem. Due to the random walk, the Metropolis-Gibbs improved method should work out correct earthquake location even if the volume of the whole PDF obtained is small compared to the volume of the initial searching region [Lomax *et al.*, 2000]. This method is also known in the NonLinLoc software as the OctTree method [Lomax, 2011].

### 2.2.3 Relative location methods

The relative location methods are based on a hypothesis concerning distances. If the distance separating the hypocentre of two seismic sources is very small compared to the distance separating them from the recording station, the rays arriving at the station from both sources is assumed to propagate the same way instead in the very proximity of the sources. Therefore, considering that the events have the same origin-time, the delay observed on the seismograms recorded at the common station is due to the spatial separation of the two events. The idea was developed in the 1980's by the introduction of the concept of the doublet [Poupinet *et al.*, 1985] and multiplet [Poupinet *et al.*, 1984] which were proved to be efficient and to give more accurate results than single event location methods [Poupinet *et al.*, 1985]. The multiplet is thus defined as a group of (micro-)seismic events providing similar waveforms but occurring at different times. The technique was used successfully at different scales [Poupinet *et al.*, 1984; Gaucher *et al.*, 1998; Moriya *et al.*, 2002].

Among the relative location methods, one can cite the master-slave location technique [Ito, 1985; Frémont and Malone, 1987] and the double-difference (DD) technique [Waldhauser and Ellsworth, 2000]. In the master-slave (or master-event) approach, all events (the slaves) are located according to the position of a single event (the master-event) which is assumed to be very accurately located [Frémont and Malone, 1987; Deichmann and Garcia-Fernandez, 1992]. An important limit of the method is the extension of the seismic cloud compared to the distance separating this cloud and the seismic sensors. This may be prevented by determining cross-correlation time-delay for the pairs of events and then combining those time-delays in a linear system solved by the least-square method [Fréchet, 1985; Klein, 1994].

The advantage of the DD method is the multiplicity of possibility to create couple of earthquakes. Each source can be located relatively to any other provided that the distance separating them is very small compared to the distance to the seismic station. For a linear formulation of the inverse problem, equation 2-2 becomes equation 2-19 where the subscripts “i” and “j” indicate the seismic events and the underscript “k” the common seismic station. The superscript “cal” and “obs” account for the calculated (after some theory) and observed (picked) arrival-times respectively. The values in  $dr_k^{ij}$  are the so-called “double-differences”. The main drawback of the method is the need of initial earthquake locations.

$$\frac{\partial t_k^i}{\partial m} \Delta m^i - \frac{\partial t_k^j}{\partial m} \Delta m^j = dr_k^{ij} \quad 2-19$$

$$dr_k^{ij} = (t_k^i - t_k^j)^{obs} - (t_k^i - t_k^j)^{cal}$$

Uncertainties on locations obtained by those relative methods can be derived by the technique of *Pavlis* [1992].

## **2.2.4 Several other absolute location methods**

### **2.2.4.1 Polarization method**

The techniques using the onset arrival-times are the most common way to locate hypocentres. Nonetheless, the information can be not sufficient if the seismic coverage is not appropriated. Hence other techniques were developed. Some of them are based on the direction of the arrival-times (DOA) either using a single-station [*Magotra et al.*, 1987; *Christoffersson et al.*, 1988; *Frohlich and Pulliam*, 1999] or for seismic arrays [*Jepsen and Kennett*, 1990; *Wax et al.*, 1996]. Two different main ways exist to determine the DOA. One uses the distribution of the seismic energy over the sensor components [*Aster et al.*, 1990; *Frohlich and Pulliam*, 1999]. The second kind deals with the apparent velocity of the waves observed over the seismic array or antenna [*Schweitzer et al.*, 2011]. Most of the methods using DOA are based on the covariance matrix around the P-wave arrival proposed by *Flinn* [1965]. The azimuth and inclination of the corresponding seismic ray at the station are determined according to this matrix [*Aster et al.*, 1990; *Kinscher et al.*, 2015].

Because the topic is subject to many investigations [*Gaucher et al.*, in prep] and is not useful for our work, we will stop here the discussion about it.

### **2.2.4.2 Full waveform method**

The method belongs to the Kirchhof-migration based location techniques [*Menke*, 1999]. The full waveforms obtained at different station, are exploited to locate the earthquake. The technique uses calculated arrival-times delay between two stations for the same source for a set of given properties for the sub-surface (velocity model, ...). The waveforms from the different sensors are then “time-shifted” according to the delays and stacked (addition of the signal amplitudes from the different stations). The constructive and negative interferences lead to higher signal-to-noise ratio. The location is obtained according to the time associated with the maximum of the stack and time-delays between the different stations [*Kao and Shan*, 2004; *Ekström*, 2006; *Grigoli et al.*, 2013; *Zeng et al.*, 2014]. Among those techniques, one can distinguish the Source-Scanning algorithm [*Kao and Shan*, 2004; *Kao and Shan*, 2007] which is based on the stacking of the absolute amplitudes of normalized seismograms provided by the different stations. The stacking can also be done on signal envelope either for P-wave only [*Baker et al.*, 2005] or for both P- and S-waves [*Gharti et al.*, 2010; *Zeng et al.*, 2014]. Some other studies used the amplitudes of the STA/LTA ratio [*Withers et al.*, 1999;

*Drew et al.*, 2013; *Grigoli et al.*, 2013] or of the kurtosis [*Maggi and Michelini*, 2010; *Langet et al.*, 2014] instead of the signal amplitude.

Other techniques in the full waveforms category use time-reversed seismograms as virtual sources [*McMechan*, 1982]. In that case, the original source is considered to be a point where the maximum energy focuses and the wavefield is back-propagated from each virtual source to this original one. The observations are time-reversed and used as limits as the reverse modelling is computed [*Gajewski and Tessmer*, 2005].

It was decided to locate the induced earthquakes by absolute method because it is a first step. We used a non-linear formulation of the inverse problem and a grid-search method in a Bayesian approach to be able to compute the whole PDF of the earthquake location in some complex models. Having the whole PDF helps to quantify the location uncertainty.

### **2.2.5 Proposed methodology to get earthquake location error**

As explained before, errors can be divided into two main kinds: uncertainty and inaccuracy. In the case of earthquake hypocentres, uncertainties are quite often discussed whichever the scale is: for tele-seismic events as well as for local events. On the other hand, location biases (inaccuracies) were often not taken into account in the previous studies. Usually they are not worked out because of a lack of a-priori knowledge concerning the sub-surface. The a-priori knowledge of the sub-surface allows the determination of the ray path. Hence the waveforms recorded at the different sensors and the travel-times needed to reach them from the hypocentre are computable. Therefore we can create a basis of event locations.

Here we developed a methodology to get both location uncertainty and location inaccuracy for earthquakes occurring at a local scale such as geothermal reservoirs in our examples. This method can be divided into three main steps: a synthetic modelling step, a location step and a comparison step. A schematic representation of the methodology is shown in Figure 2-2.

In the synthetic modelling step a seismic cloud is firstly created. Earthquake locations are then defined either in a coordinate system relatively to a chosen point or in absolute coordinate depending on the studies. Positions of seismic sensors are also defined in the same coordinates system. This synthetic network is created with the locations of real sensors. Then the body-waves (P- and S-waves) travel-times between each earthquake forming the synthetic cloud and each station of the seismic network are computed. Those calculations are performed using the eikonal solver developed by *Podvin and Lecomte* [1991]. This method combines the Huygen's principle with a finite-difference approximation method in order to compute seismic waves' travel-times in any kind of velocity model (3D as well as 1D). The hypotheses



made in this step are assumed to be representative of the reality. Hence, the obtained travel-times are then used as the observed ones for the next steps.

In the second step, also called “location step”, some modifications are applied to the hypotheses used in the prior synthetic modelling step. By the way, we mimic the common biases and uncertainties introduced when processing seismic inversions for earthquake location. For example, picking uncertainties are added to the travel-times. The choice of the velocity model used during this inversion process to locate the earthquake depends on the knowledge of the sub-surface. The use of a 1D velocity model instead of a 3D model is a common practice when the sub-surface is poorly known or in order to simplify the inversion process of earthquake location. By using the NonLinLoc code [Lomax, 2011] with a grid-search method, the earthquake locations are worked out as well as their probability density function (PDF). This PDF provides the uncertainty of the location associated with a given confidence level [Lomax et al., 2000], here of 68,3%. The uncertainty is defined as the half-length of its longest axis, assuming that this PDF is Gaussian and hence is represented by an ellipsoid.

Finally, in the last step called the comparison step, the locations outputs from the inversion step are compared to the locations input in the synthetic modelling step. The inaccuracy is defined as the discrepancy between both locations. Global inaccuracy as well as vertical and horizontal inaccuracies can be worked out by the methodology.

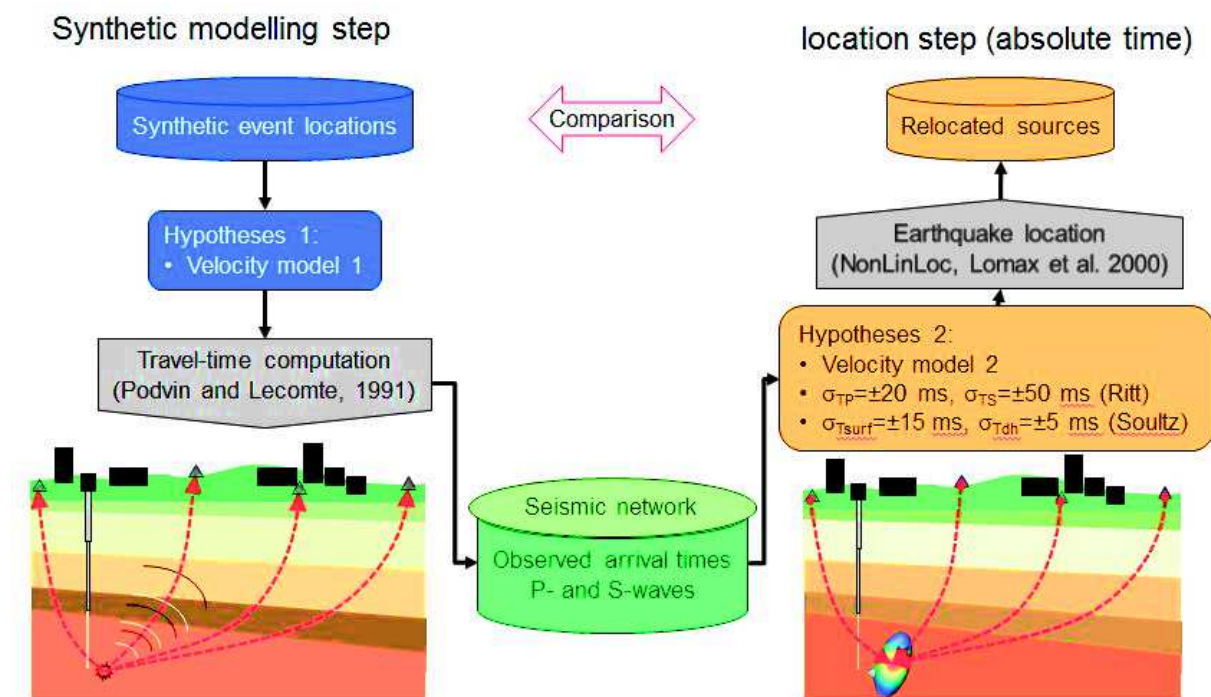


Figure 2-2: Schematic of the global method developed to get local earthquake location uncertainties and inaccuracies. (picture adapted from Gaucher et al. [2016])

After applying this methodology to determine hypocentre uncertainties and inaccuracies, different ways were then used to represent and interpret them. For example, statistics using boxplots [Tukey, 1977] were nicely representative for inaccuracies evolution in depth in a 1D velocity model. Some maps were also computed to get a better piece of information concerning the spatial distribution of these errors.

The methodology introduced in this section was applied for two different geothermal fields: Soultz-sous-Forêts (chapter 4) and Rittershoffen (chapter 5). Nevertheless, it could be applied to any other site, geothermal or not, as long as they are local ones. The major drawback of this methodology is the requirement of a sufficient *a priori* knowledge concerning the sub-surface.

## **2.3 Determination of earthquake focal mechanism**

### **2.3.1 Definitions**

The expression “focal mechanism” designs a geometrical or mathematical representation of the way the energy of an earthquake is released, distributed at its hypocentre (the point where the earthquake occurs, its focus) [Brumbaugh, 1979]. The rupture one can observe on a fault, a fracture, is also called “fault mechanism” in several references. Since it refers to a plane, it can be defined by two angles. A third angle is added to define the movement on the plane. The strike (or azimuth) is the angle made by the horizontal line separating the hypocentre and the North and the fault plane. It is counted clockwise and therefore has values in the range 0-360°. The dip angle characterizes the slope of the fault plane according to the surface of the Earth. Hence a 90°-angle fault plane dips vertically. The third and last angle defining a focal mechanism is the rake, the slip direction of the hanging wall relative to the foot wall on the fault plane. It is define from the horizontal of the plane in the direction of the azimuth. The strike and dip angles defining a rupture on a fault are also used to describe a fault plane (Figure 2-3).

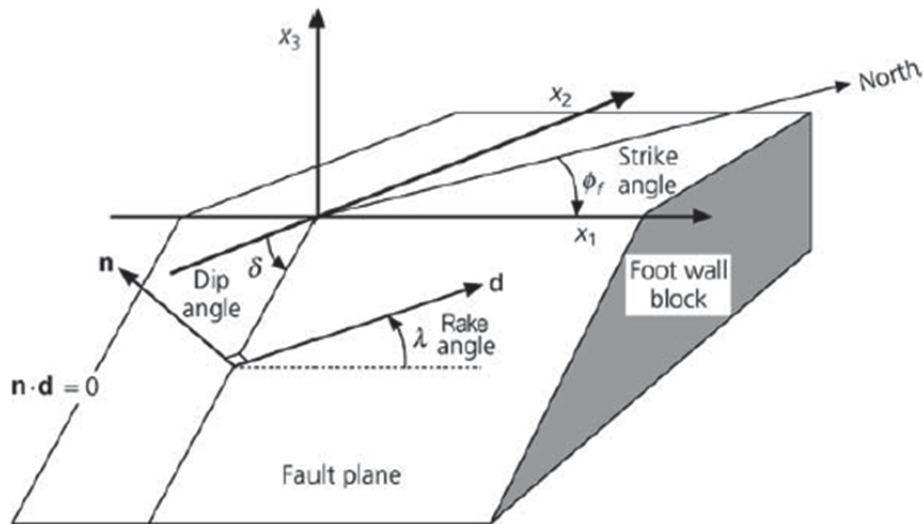


Figure 2-3: Representation of the 3 angles defining a fracture on a fault. (picture from *Stein and Wysession* [2009])

In many studies, the focal mechanisms are assumed to be representable by a pure double-couple (DC) [Nakano, 1923; Rutledge and Phillips, 2002; Li et al., 2011a]. The structure of this model is formed by two orthogonal planes usually called “fault plane” and “auxiliary plane”. If the “fault plane” is commonly assumed to represent the geological structures observed on the field, it cannot in reality be distinguished from the “mindly” auxiliary plane and the software used to compute the focal mechanism do not distinguish between both either. Three basic kinds of fault rupture exist. For the pure strike-slip mode, the two blocks slip laterally from each other either in a right- or left-lateral direction. In that case, the rake angle is equal to zero and the fault dips vertically whereas the azimuth can take all possible values. For the thrust-faulting mode, the hanging wall slips topward whereas the foot wall-block slips downward. In that configuration the rake angle is  $90^\circ$  whereas it is  $-90^\circ$  (or  $270^\circ$ ) for the last faulting mode, namely the normal-faulting mode. For the last two cases the dip is usually around  $30^\circ$  and  $60^\circ$  respectively.

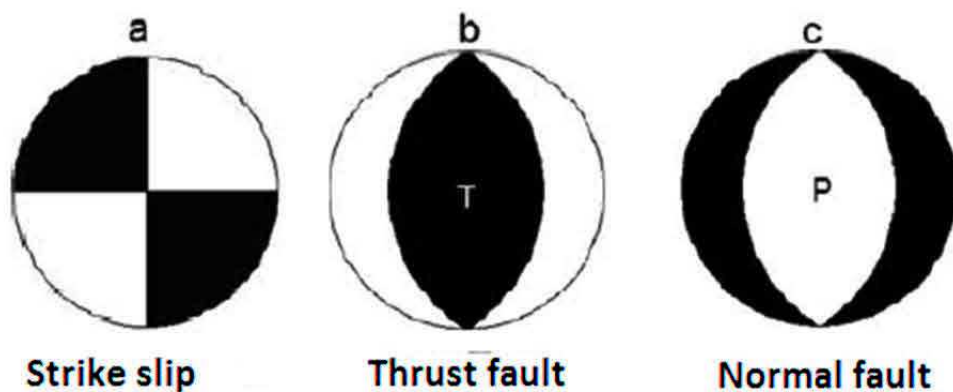


Figure 2-4 : Beach-ball representing the three basic focal mechanisms. The P and T indicators accounts for “compressional” and “tensional” zones respectively. Here, the lower hemisphere of the focal sphere is represented.

Mathematically, the focal mechanism of an earthquake can be represented by a second-order tensor of 9 components (a 3x3 matrix) called the “moment tensor” [Aki and Richards, 2009; Stein and Wysession, 2009]. According to the definition of the strike, dip and rake angles (Figure 2-3), the different components of this moment tensor, called  $\mathbf{M}$  can be defined by equations 2-20 [Aki and Richards, 2009]. This tensor becomes often symmetric because in many cases no rotation of the mass involved in a fracturing process occurs. Hence, only 6 independent components define the moment tensor.

$$M_0 = \mu SD \quad 2-20$$

$$M_{11} = -M_0(\sin(\delta) \cos(\lambda) \sin(2\phi) + \sin(2\delta) \sin(\lambda) \sin^2(\phi))$$

$$M_{12} = M_0(\sin(\delta) \cos(\lambda) \cos(2\phi) + 0.5 \sin(2\delta) \sin(\lambda) \sin(2\phi))$$

$$M_{13} = -M_0(\cos(\delta) \cos(\lambda) \cos(\phi) + \cos(2\delta) \sin(\lambda) \sin(\phi))$$

$$M_{22} = M_0(\sin(\delta) \cos(\lambda) \sin(2\phi) - \sin(2\delta) \sin(\lambda) \cos^2(\phi))$$

$$M_{23} = -M_0(\cos(\delta) \cos(\lambda) \sin(\phi) + \cos(2\delta) \sin(\lambda) \cos(\phi))$$

$$M_{33} = M_0 \sin(2\delta) \sin(\lambda)$$

In the first equation,  $\mu$  is the shear modulus; S the surface affected on the fault by the rupture and D the displacement on the fault. In this study, we focus on sources represented by DC. Nevertheless, even if DC is commonly assumed to be a good representation, one has to mention the possibility of having non-DC content in the source, like CLVD (Compensated Linear Vector Dipole) and tensile component [Aki and Richards, 2009].

Many parameters can affect the error on focal mechanism. The number of stations providing the observations is of course a serious candidate. If only a few stations provides acceptable observations, a modification in one of the observation can lead to serious inconsistency [Zollo and Bernard, 1991; Rabinowitz and Hofstetter, 1992]. The station coverage furnishing the observations can also strongly impact on the focal mechanism uncertainties [Vallina, 1999]; [Zollo and Bernard, 1991; Rabinowitz and Hofstetter, 1992] as well as the uncertainties on P-waves polarities and earthquake locations [Hardebeck and Shearer, 2002]. The signal to noise ratio (SNR) can have a strong impact on results provided by methods using the wave amplitude(s) [Hardebeck and Shearer, 2003].

### 2.3.2 Use of focal mechanisms

The focal mechanisms of earthquake were mainly used for the identification and mapping of the fault. The obtained fault design allows, according to some hypotheses, to estimate the stress field at a global scale [Heidbach et al., 2004], which is a crucial parameter in the understanding of tectonics and seismicity, especially in intraplate regions [Zoback, 1992] or more locally, the crustal stress field from small ( $M < 4$ ) earthquakes. Several methods were

developed to get the stress field from seismic data either directly from the data provided by the seismograms [Rivera and Cisternas, 1990] or by a succession of two inversion with the first one resulting in the focal mechanism or moment tensor of the earthquake [Angelier, 1984; Gephart, 1990]. Some researchers even created methods using a simultaneous inversion to get both focal mechanism and stress tensor [Loohuis and van Eck, 1996]. Because stress fields and their determination are not the scope of this study, we do not introduce the theory behind it.

### 2.3.3 Determination of focal mechanism

Determining the focal mechanism of a seismic event is also solving an inverse problem. The observations in  $d$  are commonly the wave polarities and/or the wave amplitudes of the signal. The searched parameters in  $m$  can be the strike, dip and rake angles or the components of the moment tensor for example. To better understand the different methods, one should remind that the motion of the soil due to P-wave is parallel to the P-wave propagation. On the contrary, S-waves induce a soil motion perpendicular to their propagation, either transverse (SH waves) or perpendicular to the plane wave (SV). Hence stations located on the nodal or on the auxiliary plane describing the focal mechanism do not record P-wave and for the same distance source-to-station, the amplitude ratios SV/P and SH/P are higher than for other stations. Therefore, by combining amplitude ratios from several sensors, expecting a good seismic coverage, one can determine the focal mechanism of a seismic source. Several papers show also the possibility to determine the focal mechanism with few sensors [Godano *et al.*, 2009a] but they improved the basic technique.

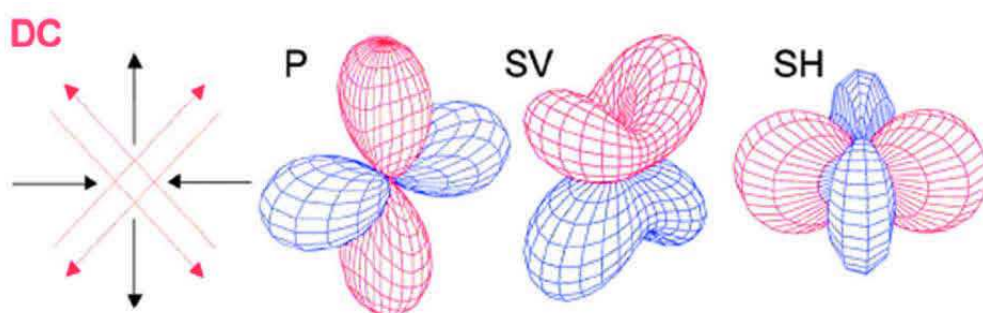


Figure 2-5 : Radiation diagram for P- (left), SV- (middle) and SH- (right) waves for a Double-couple (DC) source. Red and blue patterns indicate dilatation and compression zones respectively. (picture adapted from Šílený and Milev [2008])

#### 2.3.3.1 P-waves polarity method

The most common method applied to determine the focal mechanism of an earthquake, which is also one of the firstly developed, uses the P-wave first motion polarities seen on the records

provided by several seismic stations [Nakano, 1923; Byerly, 1926; Brumbaugh, 1979]. The method consists in finding the best fitting between trials of nodal planes and the set of observations projected on the focal sphere according to the orientation of the ray when it leaves the source [Reasenber and Oppenheimer, 1985]; [Hardebeck and Shearer, 2002; Snoke, 2003]. In the FPFIT package software [Reasenber and Oppenheimer, 1985], all possible strike, dip and rake angles are tested by grid-search to find the best-fitting focal mechanism. For an obtained focal mechanism, the misfit is defined as the number of polarities which are inconsistent with the prediction given by the drawn quadrant (the positive polarities in the extensional part and the negative polarities in the compressional part). The inconsistencies are weighted according to the distance from the nodal plane and the quality of the observation. In the package software HASH [Hardebeck and Shearer, 2002], the possibility to take into account errors in earthquake location and in velocity model exists by defining or calculating the uncertainties on the azimuth and the dip of the take-off angles. This software works out a set of acceptable focal mechanisms according to the expected error rate and then provides the preferred solution defined as the average of the acceptable set. This average is calculated iteratively after removing the outliers in the set of acceptable focal mechanisms. These outliers are defined to be out of a chosen angle around the preferred mechanism.

### 2.3.3.2 S-wave polarization method

P-waves are not the only one used for the determination of focal mechanism. S-waves and more specifically their polarizations are also utilized at this aim [Brumbaugh, 1979; Natale et al., 1991]. In fact, S-waves vibrate in the plane transverse to the ray path. The polarization of the S-wave can be described by the angle defined between the S-wave propagation direction (the vertical plane containing the ray) and the direction of the S-wave movement. This angle is called the angle of polarization, can be denoted by  $\varepsilon$  and defined by the trigonometric expression 2-21 where SH and SV define the amplitude of the vibration of S-waves. The amplitude of SH is measured in the horizontal plane with the wavefront but in the direction perpendicular to the propagation vector. The SV amplitude is obtained from the measure in the direction perpendicular to the wave propagation and to the wavefront. The three vectors form an orthogonal three-axes system.

$$\tan(\varepsilon) = \frac{SH}{SV} \quad 2-21$$

Since  $\varepsilon$  is constant along the whole seismic ray [Båth, 1961], The S-wave motion can be reconstructed in the focal region provided that SV and SH can be determined from the ground movement recorded at the seismic station

### 2.3.3.3 Amplitude and amplitude ratio methods

To complete the polarity method, new ones were developed. One of the most common is about the amplitude of direct P- and S-waves and/or their ratio [Rau *et al.*, 1996; Hardebeck and Shearer, 2003; Snoke, 2003; Godano *et al.*, 2009b]. If the choice is made to use only the direct P- and S-waves amplitudes, one can combine these absolute amplitude values with their polarity (the sign of the amplitude), which add a piece of information. Nonetheless, the method presents a serious drawback since wave amplitudes are particularly affected by a mismodelling of the Earth structure as well as the site effects or the instrumental response [Julian and Foulger, 1996]. To decrease the impact of these parameters, one can use the amplitude ratios SV/P, SH/P and SV/SH but then we lose the piece of information provided by the polarity of the amplitude and the polarity of the P-wave is required to compute.

### 2.3.3.4 Other methods, combinations

Due to the lack of data for small magnitude events, and to the errors associated with the concerned earthquake locations, other methods than the simple use of P-wave polarities were developed. A Bayesian approach was computed to determine focal mechanism in volcanic area [Natale, 1994]. In that method, the probability density function (PDF) is graphically represented for the whole space where the source parameters are defined by the method of Zollo and Bernard [1989]. To determine the PDF, either P-waves polarities S-waves polarization or S/P amplitude ratios of direct waves can be used. Another Bayesian approach was developed to determine focal mechanism with the help of the distribution of the Matrix Fisher [Walsh *et al.*, 2009]. As written by the authors, it was initially developed for P-waves polarities but can be extended to other kind of data necessary to retrieve focal mechanisms.

Several combination of the different pre-cited techniques were also applied many times [Zollo and Bernard, 1991]. The most common combination uses both P-wave polarities and S, P amplitudes or S/P amplitude ratios [Rabinowitz and Hofstetter, 1992; Hardebeck and Shearer, 2003].

### Waveforms methods

Other methods compare full waveforms obtained by the seismic receptors to synthesized waveforms computed for known focal mechanisms [Zhao and Helmberger, 1994; Dreger *et al.*, 1998; Tan and Helmberger, 2007] for example). This method was firstly used on waveforms obtained for low-frequency signals, meaning at global or regional scale. It was then improved to deal with high-frequency waveforms [Julià *et al.*, 2009; Li *et al.*, 2011a; Li *et al.*, 2011b]. The waveform inversion method was successfully used on micro-earthquake signals recorded for events occurring in Brazil [Carvalho *et al.*, 2016], and in the Dobra Voda

(Slovakia) [Fojtková et al., 2010] for example. In this waveform inversion, implemented in the ISOLA software [Sokos and Zahradník, 2008], the moment tensor is calculated using the least-squares method whereas the hypocenter position and time are defined by a grid-search method [Sokos and Zahradník, 2008; Sokos and Zahradník, 2013]. In that software the source is approximated by a single point-source and the moment rate-time is assumed to be known whereas the inversion is performed in the time-domain. To represent the Earth response, the software uses Green's functions calculated in a 1D velocity model and created by a discrete-wavenumber method including the near-, the intermediate-, and the far-field components [Bouchon, 2003; Bouchon, 1981; Coutant, 1990]. The formulation of the inverse problem is done according to the one of [Kikuchi and Kanamori, 1991].

In our study, the software HASH is used because it can deal with amplitude ratio and define the focal mechanism uncertainties. Furthermore, it uses a non-linear formulation of the inverse problem which allows the use of complex models. Moreover, the software takes into account observation uncertainties.

### 2.3.4 Proposed methodology to model seismic focal mechanism errors at the reservoir scale

In a first step observations are created for a given focal mechanism. In fact, synthetic waveforms are computed for given sources and at different monitoring stations with the software SOFI3D [Bohlen, 2002; Bohlen et al., 2012]. The source function is represented by a Ricker because it is widely used in the seismological community [Gholamy and Kreinovich, 2014].

$$r(\tau) = (1 - \tau^2)e^{-\tau^2} \tag{2-22}$$

$$\tau = \frac{\pi(t - \frac{1.5}{f_c} - t_d)}{\frac{1}{f_c}}$$

In the formula of the Ricker wavelet (equation 2-22), symbols  $f_c$  and  $t_d$  are the corner frequency and source duration respectively. To prevent from reflection at boundaries of the model, The Perfectly Matched Layer of Komatitsch and Martin [2007] is used. The velocity in the boundaries is taken as the highest velocity in the reference velocity model.

P-wave polarities and body wave amplitudes are derived from the obtained waveforms. The amplitudes are read on the computed global amplitude trace. This is only the square root of the sum of the squares of the signals from each component of the station.



$$Amp = \sqrt{amp_x^2 + amp_y^2 + amp_z^2} \quad 2-23$$

The amplitudes for P- and S-waves are the maximum on the Amp trace in given windows along abscise. This window is obviously different for P- and S-waves but also for each event and for each sensor and was defined manually.

In the same time, the take-off angles from that source is calculated for the different stations by the finite differences technique developed by *Podvin and Lecomte* [1991].

In the second step, the observations are inverted to compute the focal mechanism, maybe after modification of some hypotheses. In the last step, the slip vector of the obtained focal mechanism is compared to the slip vector of the initial mechanism to get the angular inaccuracy. To get the coordinates of the slip vectors from the strike ( $\phi$ ), dip ( $\delta$ ) and rake ( $\lambda$ ) angles, the formula given in equation 2-24 are used [*Aki and Richards*, 2009].

$$\begin{aligned} x &= \cos(\lambda) \sin(\phi) \\ y &= \cos(\lambda) \cos(\phi) \\ z &= -\sin(\lambda) \sin(\delta) \end{aligned} \quad 2-24$$

Then the norms of the slip vectors are computed. The angular inaccuracy is derived from the scalar product of the slip vector obtained with the output from HASH with each of the four vectors defining the initial focal mechanism (FM). We have two vectors, one in each sense of the direction, for both the slip on the fault and auxiliary planes defining the FM. The minimum of the four angular misfits between the vectors defining the initial FM and the vector defined by the obtained FM from HASH is considered as the angular inaccuracy. The formula to compare two slip vectors is given in equation 2-25.

$$Inacang = \arccos\left(\frac{(x_{slip1} * x_{slip2} + y_{slip1} * y_{slip2} + z_{slip1} * z_{slip2})}{norm_{slip1} * norm_{slip2}}\right) \quad 2-25$$

The uncertainty may be carried out by the software used to compute the focal mechanism or by the range of the acceptable solutions if the distribution of the acceptable FM is Gaussian. The results are shown as boxplots [*Tukey*, 1977], as beachballs [*Aki and Richards*, 2009; *Stein and Wysession*, 2009] or in a polar description of the distribution of all acceptable FMs.

In the following paper, focal mechanism inaccuracies and uncertainties are investigated for a simulation according to the stimulation of well GRT1 at the geothermal site of Rittershoffen. This site was chosen because the focal mechanisms are under computation and hence the task could be simplified by the present study.

## 2.4 Seismic waveforms modelling

Any waveform modelling, which is a direct problem (in opposition to inverse problem like earthquake location and focal mechanism determination), aims at solving the set of equations derived from the conservation of momentum and given by [Aki and Richards, 2009; Lay and Wallace, 1995]

$$\rho\left(\frac{dv_i}{dt} + v_i\nabla v_i\right) = -\frac{\partial p_{ij}}{\partial x_j} + f_i \quad 2-26$$

In this equation,  $f$  accounts for the external forces (in Newtons),  $p$  for the stress (in MPa),  $v$  is the velocity (in m/s) and  $\rho$  the density (in  $\text{kg/m}^3$ ). In the physics, this equation is satisfied for any volume, filled either by solid, liquid or gas. For our study, it will be used to describe the behaviour of a fault in a geothermal reservoir. Assuming an elastic propagation medium leads to a solution like

$$p_{ij} = \lambda\theta\delta_{ij} + 2\mu\epsilon_{ij} \quad 2-27$$

The  $\lambda$  and  $\mu$  correspond to the Lamé parameters whereas the deformation (unitless) tensor is represented by  $\epsilon_{ij} = \left(\frac{\partial u_i}{\partial x_j} + \frac{\partial u_j}{\partial x_i}\right)$  and the symbol  $\theta$  accounts for the cubic dilatation which is calculated by the trace of the deformation tensor. The symbol  $\delta$  represents the Kronecker-delta function (which is equal to 0 if  $i$  and  $j$  are different or to 1 in the case of an equality of both subscripts).

Different numerical methods exist to model synthetic waveforms. Among them one can cite the finite element method [Bao *et al.*, 1998], the spectral element [Komatitsch and Tromp, 1999; Komatitsch *et al.*, 2000] and the finite difference [Virieux, 1986; Levander, 1988].

The finite element techniques are based on the subdivision of the problem domain into many sub-domains, each represented by several equations belonging to the initial problem. The procedure may be introduced as a special case of the Galerkin method to discretize the continuous operator which might be a differential operator. At that aim, the weak formulation of the equations is used. This formulation allows the transfer of some concepts in linear algebra in order to solve partial differential equations (among other).

The spectral element method was introduced by Patera [1984] as a special formulation of the finite element method. This technique uses high degree piecewise polynomials to solve partial differential equations.

## 2.4.1 The Finite-Difference method

### 2.4.1.1 Finite differences: global definitions and explanations

The finite-difference (FD) method is commonly used for the numerical differentiation operation. In this sub-section we will explain its development in 1D but the procedure is similar in 2D and 3D.

Three kinds of FD exist: the forward FD, the backward FD and the central FD. Let us also remind that the derivative of a function is a representation of its local slope. Calling  $h$  the step on the  $x$ -axis before and after  $x=c$ , we can use the Taylor series around  $c$  given in equation 2-28 to obtain an approximation of the derivative of function  $f$  at point  $c$ . This is the forward formulation.

$$f(c+h) = f(c) + hf'(c) + \frac{h^2}{2!}f''(c) + \frac{h^3}{3!}f'''(c) + \dots \quad 2-28$$

In that equation, the symbol "!" accounts for the factorial of the number (for example  $3!=3*2*1=6$ ) whereas  $f'$ ,  $f''$ ,  $f'''$  are the first, second and third derivative of function  $f$  respectively. Extracting  $f'(c)$  from equation 2-28 and after some simplifications, we obtain

$$f'(c) = \frac{f(c+h) - f(c)}{h} - \frac{h}{2!}f''(c) - \frac{h^2}{3!}f'''(c) - \dots \quad 2-29$$

By assuming a first order error on  $h$  represented by  $0(h)$ , we get

$$f'(x)|_{x=c} = \frac{f(c+h) - f(c)}{h} + 0(h) \quad 2-30$$

Omitting the error given by  $0(h)$  and assuming that  $h$  is a step along a given axis, the forward finite-difference operator may be written as

$$f'(x)|_{x=c} = \frac{f(c+dh) - f(c)}{dh} = D^+ \quad 2-31$$

To approximate higher order derivatives, one need more steps along the  $x$ -axis. For example for the calculation of the approximation of a second-order derivative, the initial Taylor expansion is given by equation 2-32.

$$f(c+2h) = f(c) + 2hf'(c) + \frac{4h^2}{2!}f''(c) + \frac{4h^3}{3!}f'''(c) + \dots \quad 2-32$$

By subtracting two times equation 2-28 from equation 2-32 and then extracting  $f''(c)$  from the result, one gets

$$f''(x)|_{x=c} = \frac{f(c+2h) - 2f(c+h) + f(c)}{h^2} + 0(h) \quad 2-33$$

Denoting  $\Delta_F^n f(c)$ , the  $n^{\text{th}}$  order forward FD of function  $f$  at point  $x=c$ , we get  $f'(x)|_{x=c} = \Delta_F f(c)/h$ ,  $f''(x)|_{x=c} = \Delta_F^2 f(c)/h^2$  and using the recursive relation

$$\Delta_F^n f(c) = \Delta_F(\Delta_F^{n-1} f(c)) \quad 2-34$$

We get the approximate derivative

$$\frac{d^n f}{dx^n} \Big|_{x=c} = \frac{\Delta_F^n f(c)}{h^n} + 0(h) \quad 2-35$$

Up to there, we only consider first order errors ( $0(h)$ ) in the calculation of the FD. Nevertheless, it is possible to deal with higher order for those errors by including more terms in the Taylor series. Remembering equations 2-32 and after simplifications one gets for the second order derivative of function  $f$

$$f''(x) \Big|_{x=c} = \frac{f(c+2h) - 2f(c+h) + f(c)}{h^2} - hf'''(c) + \dots \quad 2-36$$

Now replacing 2-36 into 2-29, we obtain

$$\begin{aligned} f'(x) \Big|_{x=c} &= \frac{f(c+h) - f(c)}{h} - \frac{f(c+2h) - 2f(c+h) + f(c)}{2h} + \frac{h^2}{3} + \dots \quad 2-37 \\ &= \frac{-f(c+2h) + 4f(c+h) - 3f(c)}{2h} + 0^2(h) \end{aligned}$$

The term  $0^2(h)$  in equation 2-37 is the second order error in  $h$ . More generally, to get an error of order  $k$  in  $h$  for the first derivative, one need to replace until the  $k^{\text{th}}$  order derivative in the Taylor expression, which means dealing with the  $k^{(\text{th}+1)}$  derivative order term.

Until now focus was only on forward FD operator. For that type, we need the value of the function  $f$  for steps after the point  $x=c$ . Nonetheless, two other kinds of FD operator exist: the backward FD operators and the central FD operators. For the backward operators, only the value of  $f$  associated with values of  $x$  lower or equal to  $c$  are needed. In this type of FD operator,  $h$  is replaced by  $-h$  in equation 2-28 and the  $D^+$  becomes  $D^-$  in equation 2-31. On the contrary, to create the central FD operators, we need both equations 2-28 and its equivalent for backward operator. By subtracting the second from the first and then extracting the term  $f'(c)$ , we get

$$\begin{aligned} f'(c) &= \frac{f(c+h) - f(c-h)}{2h} - \frac{h^2}{6} f'''(c) - \dots \quad 2-38 \\ &= \frac{f(c+h) - f(c-h)}{2h} + 0^2(h) \end{aligned}$$

We can note that the error provided in equation 2-38 is already a second-order error in  $h$ . This is the advantage of central FD: they are more accurate than the two other types for the same derivative order. Nevertheless, to compute this kind of finite-differences, one need to know how the function evolve before and after the considered point.

In our study, the finite-differences are computed to create synthetic seismograms. These waveforms are then used to get the P-wave polarities and the amplitudes of P-waves and S-waves signals in order to compute the focal mechanism.

### 2.4.1.2 The finite-difference method used here

The method used for this work is an improvement of the finite difference approach firstly described by *Virieux* [1984; 1986] and *Levander* [1988] and implemented in the SOFI3D software [*Bohlen, 2002*].

To solve equations 2-26 and 2-27 (or its equivalent in the case of a visco-elastic medium of propagation), one can use a spatial and a temporal discretisation. Velocities, stresses, Lamé parameters and density are calculated at each node of the so-formed grid for each time step. At this aim, the partial derivatives are replaced by the so-called “finite-differences”. For example, the derivative of a function  $y$  after a variable  $x$  is given by the forward operator

$$D_x^+ = \frac{y(i+1) - y(i)}{dh} \quad 2-39$$

Or the backward operator

$$D_x^- = \frac{y(i) - y(i-1)}{dh} \quad 2-40$$

Those are first order finite-differences. In order to use more than one spatial step ( $dh$ ) in the finite differences (equivalent of higher order finite differences), the SOFI3D software places the variables (velocity, stress,...) on a Standard Staggered Grid (SSG) [*Bohlen and Saenger, 2006*]. The SSG is a discretized representation of the different parameters included in the forward problem to define the model. A geometrical representation is introduced in Figure 2-6. The density ( $\rho$ ) is arithmetically averaged and the Lamé parameters ( $\lambda$  and  $\mu$ ) harmonically averaged to satisfy the stability of the Standard Staggered Grid. The components of the velocity vector ( $v_x$ ,  $v_y$  and  $v_z$ ) are positioned in the middle of a mesh boarder-line in the corresponding direction whereas the Lamé parameters, the density and the diagonal components of the stress tensor are placed on the node. The other components of the stress tensor are located in the middle of the face with which they are associated.

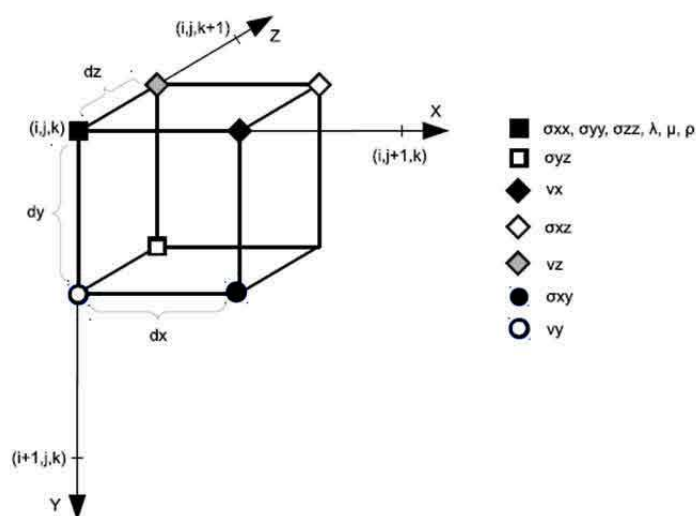


Figure 2-6 : Schematic geometrical distribution of a standard staggered grid like in SOFI3D [*Bohlen et al., 2012*]

## Computing criteria

To prevent the computation to abort, one should check numerical artefacts and instabilities. The length of the mesh ( $dh$ ) forming the discretized models should verify the grid dispersion criteria [MOCZO *et al.*, 2001] given in equation 2-41 for focus on P- and S-waves.

$$dh \leq \frac{\lambda_{min}}{n} = \frac{v_{s min}}{nf_{max}} \quad 2-41$$

In that equation  $\lambda_{min}$  is the minimum wavelength of the signal,  $v_{s min}$  the minimum S-wave velocity according to the modelled propagation medium and  $f_{max}$  the highest frequency of the source signal. The coefficient  $n$  is related to the order of the FD and to its type (Holberg or Taylor). To avoid the Courant instability [Courant *et al.*, 1928], temporal analogy of the spatial grid dispersion, the time step,  $dt$ , must verify the criteria given by equation 2-42.

$$dt \leq \frac{dh}{hv_{p max}\sqrt{3}} \quad 2-42$$

Coefficient  $h$  depends on the FD order and type (Holberg or Taylor) but is different from the coefficient  $n$  in equation 2-41.  $v_{p max}$  accounts for the maximum P-wave velocity in the propagation medium and  $dh$  is the mesh size, which maximum is calculated by equation 2-41.

### 2.4.1.3 Boundary conditions

Contrarily to the Earth which looks infinite when working at a local scale, created (synthetic) models have boundaries and conditions must be specified to define these boundaries in modelling calculations. SOFI3D can deal with two kinds of boundary conditions defined in its input parameters. The Dirichlet boundary condition [Cheng and Cheng, 2005] specifies parameter values at the extremity of the model. Even if those values are often set to 0, this boundary condition presents a major drawback in our case: it does not take an infinite full space into account and let seismic wave reflections occur at the boundaries. Hence, the signals recorded by at least the station near the extremities of the model can be complicated by the reflections. Another option is proposed in the SOFI3D software to get rid of the reflection: the absorbing boundary condition.

To absorb the waves at the boundaries of the synthetic model, Cerjan *et al.* [1985] developed an exponential damping based on the width of the boundary. This boundary is described as an enlargement of the model by a few grid nodes (FW) in each of the spatial directions in which a damping coefficient defined by equation 2-43 is applied. The idea is that the waves are damped in the boundary and cannot come back into the model or if they do they do not significantly affect the signal because they are too strongly attenuated.

$$damp = e^{-a^2x^2}; \quad a = \sqrt{\frac{-\log(amp)}{FW}}; \quad amp = 0.92 \quad 2-43$$

Nonetheless, the reflections are not completely deleted by this kind of absorbing boundary. Therefore another more suitable absorbing boundary condition was implemented in SOFI3D software: the Perfectly Matched Layers (PML) or Convolutional Perfectly Matched Layers (CPML) [Komatitsch and Tromp, 2003; Komatitsch and Martin, 2007]. The method was used for the first time for electromagnetic waves [Berenger, 1994] and then accommodated for acoustic and seismic waves [Chew and Liu, 1996; Liu and Tao, 1997; Komatitsch and Tromp, 2003; Diaz and Joly, 2006]. The main drawback of this method is that it solves exact wave equations only, which can be problematic in the case of the finite-differences method. Hence, before applying this boundary condition, the waves obtained by the FD method in SOFI3D are softened by a damping function  $dam$  defined by

$$dam = -v_{PML} \frac{\log(\alpha)}{L} \quad 2-44$$

In that equation,  $L$  is the thickness of the absorbing boundary,  $v_{PML}$  the P-wave velocity in the boundary and  $\alpha = 1 * 10^{-4}$ .

The major drawback with the classical PML method remains in the behaviour of waves arriving at the model boundaries with a grazing incidence. For those waves, the reflection coefficient can become very large [Winton and Rappaport, 2000]. Hence, the classical PML is less efficient for models with thin mesh slices or for sources located near the model boundaries [Collino and Monk, 1998]. To get rid of this fact, the transformation of the complex coordinates are modified in order to use a butterworth filter [Kuzuoglu and Mittra, 1996] in order to attenuate the energy of waves arriving with grazing incidence whereas the other waves are very less affected by the filter. The method is called the convolutional-PML (CPML). The drawback of this method is a splitting of the equations and thus an increase in computing memory. Hence, Komatitsch and Martin [2007] introduced an unsplit CPML based on the initial CPML but in which the equations of elasto-dynamic are not split anymore. This CPML boundary condition is implemented in SOFI3D [Bohlen et al., 2012]. The CPML method was chosen for our study because it has the advantages of preventing boundary reflections of waves without needing too much enlargement in the dimensions of the used model, which is interesting for spending computing time and memory. One can also use this advantage to calculate with smaller meshes and thus higher sources frequencies (e.g. equation 2-41).

# 3 Geological settings: the Upper Rhine Graben (URG)

## 3.1 Brief history of the URG

Our studies are applied on two geothermal sites located in the western part of the Upper Rhine Graben (URG). The URG is a geological structure composed of an extensive rift. The URG belongs to the European Cenozoic Rift System (also called ECRIS) and was partly formed in response to the Alpine orogeny [Ziegler, 1992; Dèzes *et al.*, 2004]. The ECRIS is an 1100 km long system of rifts extending from the Mediterranean to the North Sea [Ziegler, 1992]. This succession of rifts occurred as a result of intraplate stresses during Eocene period and is still active [Ziegler and Dèzes, 2007]. The rifts align roughly East-North-East/West-South-West (ENE-WSW) in the ECRIS structure. The URG is an approximately 300 km long rift extending from the North of Switzerland, near Basel, to the town of Frankfurt (Germany). According to Pribnow and Schnellschmidt [2000], it is about 30 to 40 km wide (Figure 3-1). The stress state in the URG varied over the geological periods. Particularly in the Tertiary Era, the URG underwent some modifications of its main stress field [Edel *et al.*, 2007; Larroque *et al.*, 1987; Bergerat, 1985]. During the Late Eocene, the URG was subject to a compression with the  $\sigma_1$  stress axis oriented North-South. In the Oligocene, the  $\sigma_3$  stress axis was oriented East-West and the URG was under extension process [Bergerat, 1985; Villemin and Bergerat, 1987]. A left lateral transcurrent displacement is the result of a NW-SE striking  $\sigma_1$  stress axis [Illies, 1978; Bergerat, 1985; Laubscher, 1992; Schumacher, 2002; Rotstein *et al.*, 2005] since the Late Miocene. This is suggested to correspond to the second (in time) main deformation phase whereas the first was controlled by a WSW-ENE oriented  $\sigma_3$ , orthogonal to the average rift axis [Illies, 1978; Schumacher, 2002].

The main structural trends in the URG already existed when the rifting began in the Cenozoic Era [Schumacher, 2002]. This will be referred to, as in the pre-cited paper, the pre-rift setting. During this period, the central European segment of the Variscan belt (which was located between Paris basin and the Bohemian Massif) presented a striking structural grain oriented NE to ENE. Another specification in the URG is the NNE oriented sinistral fault zones which are probably related to dyke swarms and intrusive bodies occurring during Late Carboniferous to Permian. Referring to its boarder faults, the structure may result from a sinistrally



transtensive kinematics oriented NW-SE to NNE-SSW with a NE-SW to E-W oriented extension [Plenefisch and Bonjer, 1997; Lopes-Cardozo and Behrmann, 2006]. Rotstein and Schaming [2011] suggest that the observed structures result in the first order from uplifts and erosion along the boundaries of the URG, represented by the Vosges and the Black Forest, but also in the centre of the URG.

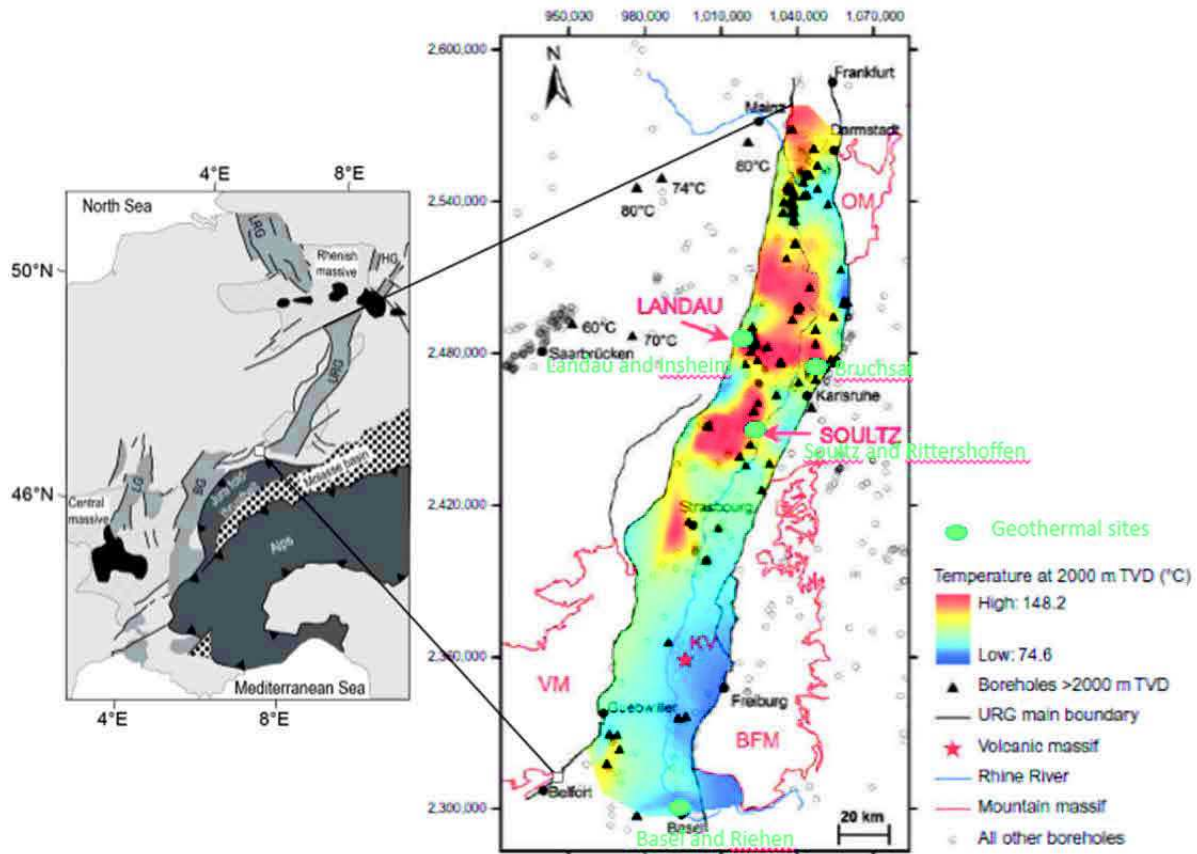


Figure 3-1 : -left: localisation of the URG in the ECRIS formation. –Right: temperature anomalies in the URG with the different geothermal sites developed, under development or stopped in the area (modified from Bailleux *et al.* [2013]).

This complicated geological history resulted in a structure of tilted and shifted blocs –also called horst- with many faults and fractures. This structure is nowadays known as the URG. Only few natural seismic events were felt by the population in the region during the last hundredths of years. Seismic events present quite low magnitudes (always  $M_l < 4$ ) and their recurrence time is quite long. The investigations on the seismic pattern in the region showed strong lateral variation of the seismogenic zone in the crust [Bonjer *et al.*, 1984] with maximum focal depth varying between 12-13 km in the graben and 20-22 km on the eastern borderfault of the URG, near the Black-Forest. In that zone, the shallowest 10-km-thick layer was shown to be seismically inactive [Gelbke, 1978]. Some reflection and refraction seismic surveys helped to the determination of the structures in that region [Wentzel and Brun, 1991; Gajewski and Prodehl, 1987; Mayer *et al.*, 1997]. A combination of different methods at

different scales was compiled to image the actual structures in the lithosphere of the Southern Rhine Graben and to confirm the previous results [Lopes-Cardozo and Granet, 2005].

### 3.2 Temperature anomalies in the URG

The URG presents high temperature anomalies referring to the common temperature gradient of 3K/100m. Those anomalies are well studied and described both at 800 m depth [Pribnow and Schellschmidt, 2000] and at 2000 m depth [Agemar *et al.*, 2012; Bailleux *et al.*, 2013]. The map showing the temperature distribution obtained by those authors is shown in Figure 3-1 (right). On that map, several zones with temperatures higher than 140 °C are seen in the northern part from Soultz. On the contrary, there is no high temperature zone at 2000 m depth in the southern part of the URG except at the extreme south-western part. However, even there, the temperature is still lower than that in the northern part. On this figure, one can also notice that the higher temperatures are mainly found in the west side of the URG. At 800 m depth, the highest temperature, 120 °C was reached at Soultz-sous-Forêt (Soultz) [Pribnow and Schellschmidt, 2000]. This highest temperature anomaly partly explains the choice of this site for being a pilot site to develop geothermal energy in the region.

The temperature gradient (Figure 3-2) obtained by Bailleux *et al* [2013] is very high in the upper sedimentary layers (up to ~1 km) with a mean value of about 120 °C/km. This conductive regime can be defined by the thermal conductivity and diffusivity of the rocks as well as their heat capacity and the radiogenic heat production [Clauser and Villingier, 1990; Person and Garven, 1992]. In a second depth interval, the gradient decreases to a mean value of about 25 °C/km, due to convection. The slope of the temperature profile then increases again at ~3500 m depth but the reached value is lower than in the upper part. The depth of the gradient abrupt change was determined to range between 1100 and 1400 m [Dose, 2006]. The temperature gradients multiplied by the depths intervals associated together and also with the temperature at the shallowest sedimentary layer lead to temperatures between 75°C and 150°C in the whole URG at a depth of 2000 m (Figure 3-2).

This type of curve and temperature evolution can be seen in many places in the URG [Agemar *et al.*, 2012] and is one of the reasons for the development of geothermal energy in this region. Some of the geothermal sites are presented in the following paragraphs and their locations are shown in Figure 3-1.

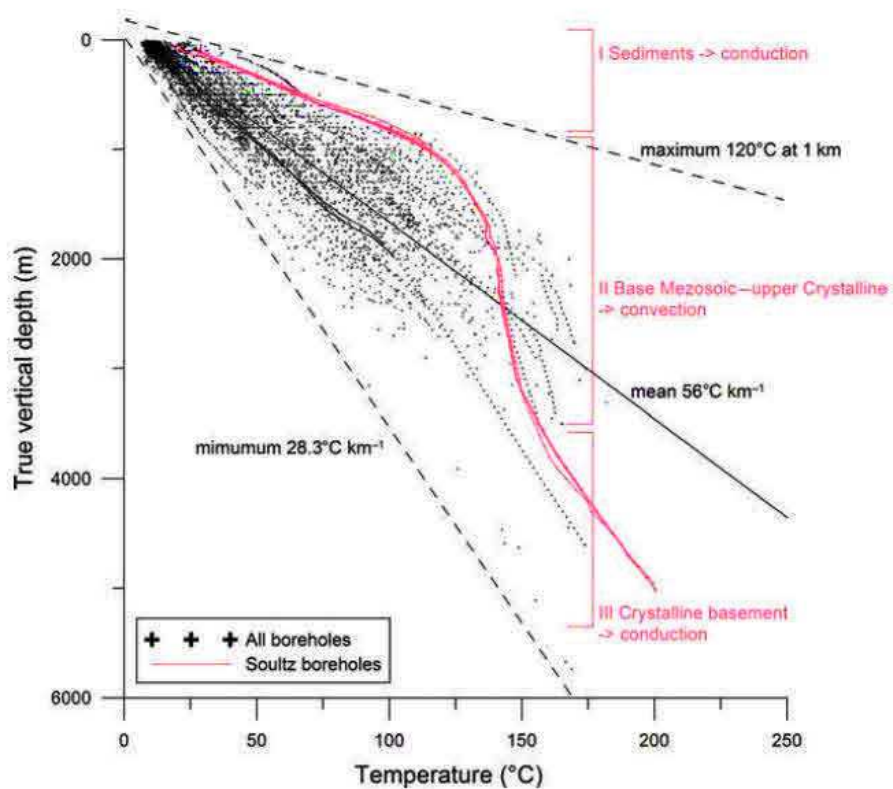


Figure 3-2 : -Temperature profile in the URG (from Bailleux *et al* [2013])

### 3.3 Geothermal sites in the URG

#### 3.3.1 Soultz-sous-Forêts

The first geothermal site research project in the area was developed at Soultz-sous-Forêt (Soultz), about 50 km north from Strasbourg. The Soultz site is a so-called Enhanced (or Engineered) Geothermal System (EGS). This means the presence of fractured rocks in the sub-surface before human activity. The low natural permeability of the rocks leads to a poor hydraulic connection between the fractures. In order to improve the circulation of the fluids in the fractured rocks, various techniques like hydraulic or chemical stimulations were applied. Four deep wells were drilled between 1990 and 2005, and three of them down to 5000 m or deeper, in order to develop two deep reservoirs within the granite at 3500 and 5000 m depth respectively [Baumgärtner *et al.*, 1996; Baria *et al.*, 1999; Gérard *et al.*, 2006]. In the deepest reservoir, the temperature transmitted to the circulating fluid can reach about 200 °C [Genter *et al.*, 2010]. The investigations at Soultz cover roughly the whole domain of geosciences. Geology, fluid geochemistry, hydraulics, temperature estimations, geomechanics and micro-seismicity were studied from data such as logs and cuttings extracted from the wells, salinity of the fluids, pressure measurement, stress estimation, and induced seismicity for example.

Some of these data were provided from drilling or during the stimulation circulation tests whereas other measurements were done during quiet periods to be used as reference.

The Soultz research project began in 1986 [*Gérard and Kappelmeyer, 1987*]. In the late 1980s and the very beginning of 1990s an ancient well was cored (EPS1) whereas the first of the four deep wells (GPK1) was drilled firstly down to about 2000 m. In the 1990s, GPK1 was deepened to 3600 m and GPK2 was drilled down to roughly the same depth. Hydraulic stimulations of both wells were performed to improve the fluid circulation and circulation tests were done. During the very late 1990s and the first half of the 2000s two other wells (GPK3 and GPK4) were drilled deeper than 5000 m and GPK2 was deepened to a similar depth. Hydraulic stimulations were done for each of the three wells and some complementary chemical stimulations were carried out.

At Soultz, the top of the crystalline basement is located around 1400 m depth [*Genter et al., 2010*]. The horst and graben structure of the site was known before the geothermal project began due to oil investigations [*Schnaebeler, 1948*]. *Dezayes et al* [2010] and *Sausse et al* [2010] did 3D analysis to image the spatial distribution of the fracture and faults zones and other structures visible in the reservoir. The maximum horizontal principal stress was found to be about  $N169^{\circ}E \pm 14^{\circ}$  whereas the principal stress magnitudes may be calculated as functions of depth [*Valley and Evans, 2007*] and the minimum horizontal stress could be estimated from the maximum pressure reached at the casing shoes of the well during the hydraulic stimulations [*Bérard and Cornet, 2003*]. Among the other studies, some focused on the fluid geochemistry [*Sanjuan et al., 2010; Aquilina et al., 1997*] and others on the radioactivity of the components [*Stussi et al., 2002*] but many focused on induced seismicity recorded during the stimulations [*Charléty et al., 2007; Cuenot et al., 2006; Cuenot et al., 2008; Dorbath et al., 2009*]. The final aim of all those studies on microseismicity is to image the reservoir at a large scale since this is the only possible way to do it. Furthermore, many tests were performed there like the stimulation at low rate.

The results and the methods developed at Soultz were applied to other deep geothermal sites in the URG. Thus, Soultz fullfills its role of pilot site. Part of our study will focus on the earthquakes induced during the GPK2 deep stimulation.

### **3.3.2 Rittershoffen: geothermal for industrial process heat utilization**

Seven km to the east of Soultz, the Rittershoffen geothermal field is under development. This site should be the first deep EGS to produce geothermal heat for industrial use [*Maurer et al., 2015*]. For that site, a doublet of wells was drilled in 2012 and 2014. A maximum depth of 2500 m was reached. The main part of the manuscript will focus on results obtained for this

geothermal site. The geographical proximity of Soultz and Rittershoffen is not reflected in the geological structure of both geothermal sites. The same geological layers are observed but with different thicknesses. Actually, if we consider the typical graben-horst structure of the URG, we can see that both sites do not belong to the same “tilted bloc” [GeORG Project Team, 2015]. At Rittershoffen, the granitic basement is covered by about 2000 m of Mesozoic and Cenozoic sediments whereas the top of the granite was reached at about 1400 m depth at Soultz. At Rittershoffen, a temperature of 165 °C was reached at 1800 m depth [Baujard et al., 2014]. According to the necessary temperatures for the two projects, the temperature gradients and the structures, the targeted reservoir at Rittershoffen is formed by the Triassic sandstones and Paleozoic granite whereas only the granite constitutes the two reservoirs at Soultz. The doublet of wells targets the normal fault delimiting two tilted blocks below Rittershoffen. The targeted normal fault is approximately oriented NS and dips 60°W with a vertical shift of 200 m. To improve the connectivity between the first well GRT1 and the reservoir, several stimulations were done in 2013 [Baujard et al., 2014] and induced seismicity. The corresponding seismic cloud was oriented N-S to NNE-SSW, extending 2 km long, 1 km wide and 2 km in depth [Maurer et al., 2015]. No stimulation was necessary for the second well GRT2 drilled in 2014 since its connectivity to the reservoir was already acceptable for geothermal performance.

### 3.3.3 Other geothermal sites

Several geothermal sites were also developed in the German side of the Upper Rhine Graben. They are here briefly introduced but not well described since the study does not focus on them. Landau is located NW from Karlsruhe, still in Germany. The geothermal system consists of two wells drilled down to 3300 m and 3170 m depth ending in the shallow granite. The power plant ran successfully from 2007 to 2014 May 14<sup>th</sup>. However, due to felt seismicity and surface fracture and deformation, the power plant was stopped [Heimlich et al., 2015]. The local magnitude of the induced seismicity recorded ranges between -1 and 2.7 at depth from 3500 to 5000 m [Expertengruppe, 2010; Grund et al., 2016]. A geothermal water temperature of about 160°C was measured at depth [Agemar et al., 2012]. This is the hottest geothermal fluid exploited in the German part of the URG. Locally small and moderate seismicity was recorded [Ritter et al., 2009; Ritter, 2011]. The first stimulation and circulation tests carried out in the early 2006 induced seismicity with local magnitude  $M_L < 1$  [Plenkens et al., 2013; Schindler et al., 2010]. Due to the power plant exploitation, induced earthquakes occurred between 2000 and 6000 m depth [Groos et al., 2013]. The focal mechanisms were

studied and showed a general orientation NNW-SSE in agreement with the URG [Gäßner *et al.*, 2014].

About 5 km SE from Landau, the Insheim geothermal field has been in activity since April 2009 [Baumgärtner and Lerch, 2013]. Contrary to the case of the pair Soultz-Rittershoffen, the structure does not strongly differ between the geothermal sites of Landau and Insheim. Both reservoirs were developed at the interface between the sediments and the granite like in Rittershoffen. Induced seismicity at Landau and Insheim was (is) recorded by about 30 stations in a surface area of 20 by 20 km<sup>2</sup>. By a cross-correlation algorithm [Plenkers *et al.*, 2013], 1363 and 619 induced earthquakes were detected between 2006 and 2013 at Landau and Insheim respectively [Groos *et al.*, 2013].

A new project also started near Frankfurt, in Gross-Gerau. The drilling of the first well began in late March 2016. It is planned to reach 3500 to 4000 m depth where a temperature around 170°C was estimated according to a geothermal gradient of 5.6°C/100m [Agemar *et al.*, 2012]. In this area of the URG, sediments are the age of the Permo-Carboniferous Saar-Nahe-Basin. These are mainly clastic continental sediments of alluvial fans, braided and meandering rivers, deltaic and lacustrine formation [Wenke *et al.*, 2010; Korsch and Schäfer, 1995]. This project aims at providing electricity to about 20000 people living in the surroundings.

In Bruchsal, located about 30 km North from Karlsruhe, a high temperature gradient of about 50°C/km is observed [Herzberger *et al.*, 2010]. The project started in the mid 1980's with the drilling of a doublet of wells down to 2000 and 2500 m depth. At these depths, water temperature reaches about 120°C when extracted from the Buntsandstein, Rotliegend and Zechstein sedimentary layers covering the granitic crystalline basement. The reservoir, which is located between 1700 and 2500 m depth [Hauber, 1993; Meixner *et al.*, 2016], may be divided into several blocks separated by normal faults [Herzberger *et al.*, 2010; Meixner, 2010]. Contrarily to the other sites presented above, its reservoir consists only in sedimentary formations. The highest temperature observed in Bruchsal is about 130°C. No mechanical or chemical stimulation was necessary in this hydrothermal system before running the power plant.

A new EGS was developed in Switzerland, in the city of Basel. In December 2006, massive water volume was injected at around 5000 m depth in a first well [Häring *et al.*, 2008]. Seismic sensors installed at depth comprised between 300 and 2750 m recorded the induced seismicity. The project stopped when an earthquake of magnitude  $M_L=3.4$  was recorded [Deichmann and Giardini, 2009].

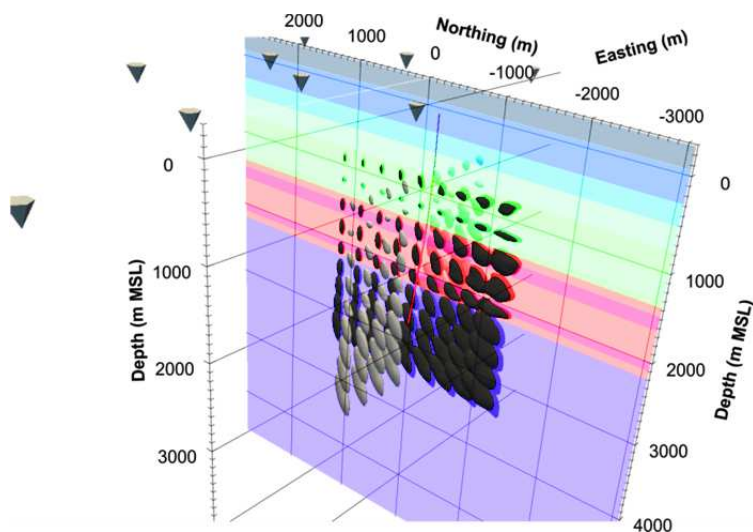
As written above, many micro-earthquakes can occur during stimulations and circulation tests periods. In the following we looked at the reliability on event location (chapters 4 and 5) for this kind of experiment.





## SECOND PART:

### Earthquake location errors



3D view of the relocation uncertainties at 68.3% confidence levels for sources simulated at Rittershoffen geothermal reservoir

This part consists in two papers relating the results of the investigations on micro-earthquakes location errors. The first paper (chapter 4) is a case study on synthetic data simulating the stimulation of the well GPK2 in 2000 at Soultz-sous-Forêts. The major point of this work is the impact of the down-hole network on the earthquake location. In the second paper (chapter 5), location errors are investigated for the geothermal site of Rittershoffen [*Kinnaert et al.*, 2016] mainly focusing on the impact of the velocity model on the earthquake locations.

# 4 The combination of surface and down-hole seismic networks for earthquake location at the Soultz-sous-Forêts geothermal site (France)

X. Kinnaert<sup>1,2\*</sup>, E. Gaucher<sup>1</sup>, T. Kohl<sup>1</sup> and U. Achauer<sup>2</sup>

<sup>1</sup>: Division of Geothermal Research, Institute of Applied Geosciences, Karlsruhe Institute of Technology, Adenauerring 20b, Geb 50.40., D-76131 Karlsruhe, Germany.

<sup>2</sup>: EOST-IPGS UMR7516, 5 rue René Descartes, F-67000 Strasbourg, France.

\*Corresponding author: Email: xavier.kinnaert@kit.edu, Phone: +49 721 608 45223, Fax: +49 721 608 45228.

**Abbreviated title:** Location inaccuracies and uncertainties at Soultz

## Abstract

Using induced seismicity in seismological methods is of primary interest to image fractured reservoirs for a hydrogeological characterization or to mitigate seismic hazard. This requires an accurate earthquake location and is nowadays an important seismological task in reservoir engineering. The determination of the hypocentres depends strongly on the propagation medium and the monitoring seismic network. In this work, location uncertainties and location inaccuracies are modelled to investigate the impact of several parameters: the picking precision and accuracy, the seismic network and the velocity perturbation due to water injection.

The quantification of uncertainties and inaccuracies is achieved by a three-step approach. In a first step, travel-times of body-waves between synthetic earthquake hypocentres and seismic receiver positions are calculated with a velocity model representing the real geology. In a second step the arrival-times obtained (picked) under these conditions are used in a formulation of the inverse problem to relocate these synthetic events. The final step consists in comparing the relocations with the initial locations. Performing detailed synthetic tests allows changing initial model hypotheses - e.g. by varying the velocity model or the picking

accuracy - to account for the lack of knowledge or the simplifications commonly made for computation.

The method is applied to the geothermal site of Soultz-sous-Forêts, which is located in the Upper Rhine Graben (France) and was subject to detailed scientific investigations. We focus on a massive water injection in 2000 performed to enhance the productivity of the well GPK2 in the granitic basement at approximately 5 km depth, producing more than 7'000 induced - earthquakes recorded by down-hole and surface seismic networks. Herein, we specifically quantify the location error from the joint or the separate use of the down-hole and surface network. Besides the description of the usual location uncertainties, the impact of the picking time precision at  $\pm 10$  ms given in the input catalogue is investigated. The velocity model is modified to mimic possible effects of a massive water injection and its impact on earthquake hypocentres.

It is shown that the down-hole network at Soultz is more favourable to decrease the location uncertainty compared to the surface network due to its increased coverage at depth. Adequate optimization methods of local seismic networks to increase earthquake location capabilities are clearly more advantageous for improved reservoir engineering. Characterizing the uncertainty in locating flow paths in fractured geothermal reservoirs from induced seismic data can become an important economic issue. Further application of the proposed methodology to operating project in the same setting of the Upper Rhine Graben like Rittershoffen, Landau, or Insheim can also lead to optimized monitoring.

**Key words:** Location inaccuracy; Location uncertainty; Down-hole monitoring; Seismic coverage; Soultz; EGS.

## 4.1 Introduction

Local seismic monitoring of the exploitation of engineered deep sub-surface reservoirs, such as geothermal reservoirs or oil and gas reservoirs, is now common practice. The value brought by such observation tool has been proven several times both for reservoir description and seismic hazard mitigation. However, it strongly depends on the quantity of recorded earthquakes, their location quality and the reliability of other source parameters (e.g. magnitude, seismic moment, focal mechanism). For example, the recording of only few micro-earthquakes at the Groß-Schönebeck (Germany) research geothermal site prevented from describing its sub-surface away from the main boreholes and the large location uncertainties does not facilitate the interpretation of the few results (Kwiatek *et al.*, 2010). On the contrary, the Soultz-sous-Forêts geothermal site (France), at similar depths and for similar

stress amplitudes (Gaucher, 2013), benefited from numerous micro-earthquakes to highlight major faults and fractures in the deep reservoir (Sausse *et al.*, 2010) and to describe the hydro-mechanical behaviour of the latter (Cornet *et al.*, 2007; Kohl and Mégel, 2007; Held *et al.*, 2014). Besides the quantity of induced earthquakes, the quality of their location is also of importance for reliable interpretation of the results. In Unterhaching geothermal field (Germany), velocity model uncertainties may vary the depth of the induced seismicity by 800 to 1000 m (Megies and Wassermann, 2014), which makes difficult its interpretation in terms of physical processes at its origin. Recently, Kinnaert *et al.* (2016) showed that the seismicity recorded at  $\sim 3$  km depth at the Rittershoffen geothermal field (France) may be displaced by several hundreds of meters depending on the integration of a normal fault within the velocity model (or not). These few examples illustrate that locating earthquakes, even at a local scale, remains uncertain and biased. Unless specific operations such as active tomography or calibration shots may be carried out to minimize or remove the location inaccuracies (Bardainne and Gaucher, 2010; Gaucher *et al.*, 2016), prior quantification of the possible range of expected location errors at a given site remains a useful tool to anticipate and to assess the results interpretation.

We propose to investigate the effect of several parameters which may affect the location of the seismicity which has been recorded at the Soultz-sous-Forêts geothermal site (France). This site benefited from surface and down-hole seismic monitoring during the development of its reservoirs. Therefore, it is possible to analyse the variation of the earthquake hypocentres and of the location errors as a function of the network used or their combination. The addition of surface stations to improve the seismic coverage at the nearby Rittershoffen geothermal site was shown to decrease the location uncertainties (Kinnaert *et al.*, 2016) but also to increase the location bias in the case of an inadequate velocity model (Gaucher *et al.*, 2016). Therefore, one can wonder if the use of a down-hole network at Soultz leads to similar conclusions.

For this study, we follow the procedure proposed by Kinnaert *et al.* (2016) to quantify location inaccuracies and uncertainties and we briefly describe it. To follow, the Soultz geothermal site is presented with the seismicity recorded during the major stimulation of the well GPK2 (in 2000), which is of interest. Then, the impact of the different networks on location uncertainties is quantified. Further, picked arrival time precision of the reference seismological catalogue and the location bias it leads to is also investigated as a function of the network. At last, the velocity model is perturbed to mimic the possible impact of the

massive water injection. For each case, the consequences on the sub-surface interpretation of the results are discussed.

## 4.2 Methodology

In order to estimate the seismic event location uncertainties and inaccuracies, we follow the method proposed by Kinnaert *et al.* (2016). It consists of three steps: 1) the modelling of seismic travel-times between synthetic locations and networks, 2) the use of the modelled travel-times as observation times and the perturbation of the initial modelling assumptions before relocation of the synthetic events, and 3) the comparison of the original and relocated hypocentres. The hypotheses that are assumed to represent the reality of the Earth during the synthetic modelling step are modified before the relocations. Those changes are supposed to represent usual uncertainties or/and inaccuracies encountered during the processing of real seismological data.

Standard numerical codes are used within the procedure. The seismic travel-times are computed using the finite-difference code of Podvin and Lecomte (1991), which is implemented in the NonLinLoc software (Lomax, 2011). This non-linear location package is applied both for the synthetic modelling and the relocation steps. It was chosen for the reasons mentioned by Kinnaert *et al.* (2016): 1) it keeps the non-linearity of the location inverse problem, 2) it allows the user performing calculations in 3D structures by applying the Bayesian formalism proposed by Tarantola and Valette (1982) and the methodology of Wittlinger *et al.* (1993), and 3) the complete probability density function (PDF) of the event hypocentre may be available by applying the grid-search method implemented in the code. The location uncertainties can be fully described by the spatial distribution of the PDF. However, for simplicity, they are defined here as the half-length of the longest axis of the 68.3 % confidence level, assuming a Gaussian posterior distribution (Lomax *et al.*, 2009). The horizontal, vertical and total inaccuracies are obtained by comparing the hypocentre position after (re-)location with the initial synthetic hypocentre of the source.

## 4.3 The Soultz-sous-Forêts geothermal site

### 4.3.1 Geological settings

The Soultz-sous-Forêts geothermal site is located in the Upper Rhine Graben (URG), in the north-eastern part of France. The geological and structural settings of the shallow sub-surface

in the URG are well known due to earlier investigations from the oil industry (Schnaebelé, 1948). Several seismic reflexion and refraction profiles were acquired and processed in the region. They provided relatively good knowledge of the sedimentary cover in the Soultz area and highlighted the numerous horst and grabens typical of the URG (Wentzel and Brun, 1991). Nonetheless, below the sedimentary cover, in the crystalline basement the geological structure is less clear (e.g. Place *et al.*, 2010).

Because of the presence of fracture networks in the sub-surface and thermal anomalies (Bailleux *et al.*, 2013), the URG is suitable for geothermal energy development. Besides Soultz, several deep geothermal sites exist such as Rittershoffen (France), Landau, Insheim, Bruchsal (all in Germany) or are under development like Gross-Gerau and a site in the proximity of Trebur (Germany).

At Soultz, two main reservoirs have been developed at around 3500 m and 5000 m depth in the granitic basement. In the deepest reservoir, temperature reaches about 200°C (Baumgärtner *et al.*, 2000). The Paleozoic granitic basement is overlaid by about 1400 m of sediments from tertiary and quaternary eras (Genter *et al.*, 2010). Those granites are highly fractured.

### **4.3.2 Seismicity induced in 2000**

The deep geothermal research project of Soultz started in 1986 (Gérard and Kappelmeyer, 1987). The first well, GPK1, was initially drilled down to about 2000 m and later deepened to about 3500 m. Three other wells were then drilled down to a depth of 5000 m in the 1990's and 2000's (Genter *et al.*, 2010; Cuenot, 2009). In order to improve the geothermal fluid circulation in the fracture network, chemical and/or hydraulic and/or thermal stimulations were performed (Schill *et al.*, submitted). The stimulations and circulation test, which induced micro-seismicity (e.g. Cuenot *et al.*, 2008; Charléty *et al.*, 2006; Gaucher, 1998), were monitored by various seismic networks. The latter were composed of surface seismometers and deep down-hole accelerometers. The down-hole network recorded generally about 3 times more induced earthquakes than the surface network (Charléty *et al.*, 2007; Baria *et al.*, 2000; Dyer, 2001).

This paper is focused on the seismicity induced by the stimulation of the well GPK2, which was carried out in June-July 2000. The seismic records obtained during this stimulation and the associated catalogues were used several times (Dyer, 2001; Cuenot *et al.*, 2008; Calò *et al.*, 2011), mainly for deep reservoir description purposes. The first hypocentre locations were

obtained by Dyer *et al* (2001), using the down-hole network only. Cuenot *et al* (2008) were the first to combine the data from the surface and the down-hole networks to locate the induced seismicity. They located about 7200 events (Figure 4-1) following their selection criteria which, among others, required the joint use of 3 down-hole seismic wave arrival picks and 5 surface picks. The events were located in the granite, between 4000 and 5500 m depth (Charl  ty *et al.*, 2007; Cuenot *et al.*, 2008; Dorbath *et al.*, 2009). Along its major axis oriented  $\sim 30^\circ W$ , the seismic cloud extends over  $\sim 2.5$  km and  $\sim 1.5$  km in the transverse direction. The earthquake catalogue resulting from the work of Cuenot *et al.* (2008) as well as the associated picks is used as a reference database in our present study. Cal   *et al.* (2011) applied a double-difference tomography using the same catalogue.

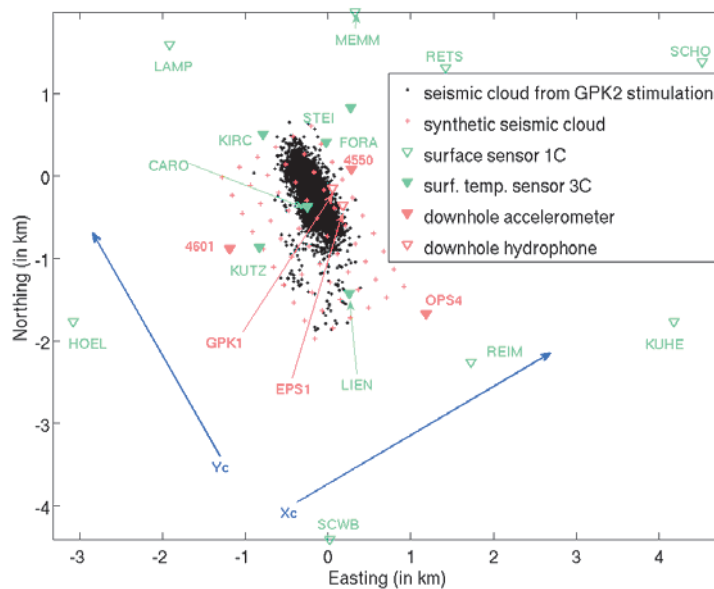


Figure 4-1: Geometry of the seismic networks monitoring during the stimulation of the well GPK2 in June-July 2000. The filled triangles stand for 3C-sensors whereas the empty symbols stand for vertical sensors. Red and green triangles show the position of the down-hole and surface sensors respectively. The projections of the synthetic (crosses) and real (dots) seismic clouds (Cuenot, 2009) are plotted. The blue arrows show the  $X_c$  and  $Y_c$  axes used in this study, which correspond to a rotation of the original geographic system according to the main distribution of the seismic cloud. Easting and northing are given relative to GPK1 wellhead.

### 4.3.3 Reference velocity model

The velocity model we take as a reference is the model used by Cuenot *et al.* (2008). This is a flat layered model with increasing velocity as a function of depth (Figure 4-2). The P-waves propagate at  $\sim 1800$  m/s in the shallowest sedimentary layer and their velocity increases up to  $\sim 5800$  m/s at the top of the non-altered granitic layer which is located at  $\sim 1700$  m depth. The largest velocity contrast is observed at the sediment-altered granite interface, close to 1400 m depth. The S-wave velocity ranges from 860 m/s in the shallow sedimentary layer to  $\sim 3300$



m/s in the non-altered granitic basement. The  $V_p/V_s$  ratio is not constant over depth and varies between 1.75 in the granite and 2.15 for the shallowest sedimentary layer.

In this work, this model is always used to relocate the synthetic sources.

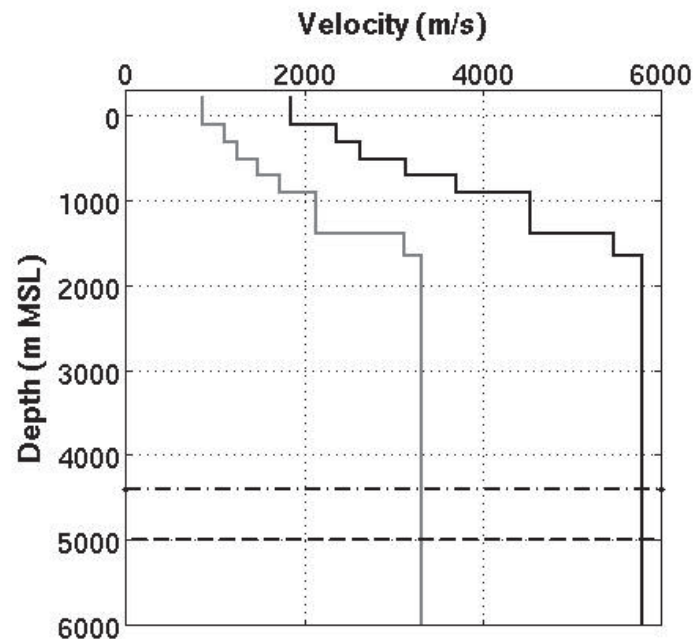


Figure 4-2: Reference P- (black curve) and S-wave (grey curve) velocity profiles as described by Cuenot (2009, p115). The shallower dashed line delimits the top of the deep injection zone during the GPK2 stimulation and the deeper dashed line delimits the bottom of GPK2.

#### 4.3.4 Seismic monitoring networks

The seismic networks which recorded the seismicity induced during the GPK2 stimulation in June-July 2000 were of two types: a down-hole network and a surface network. Cuenot *et al.* (2008) used the associated records to create the reference picking catalogue and to locate the induced earthquakes. Three accelerometers with 4 components (in wells 4550, 4601 and OPS4 at ~1500 m depth) and 2 hydrophones (in wells EPS1 and GPK1 at ~2000 m and ~3500 m depth respectively) constitute the down-hole network. Signals from these sensors were sampled at 2000 Hz (Dyer, 2001). Among those down-hole sensors, the EPS1 sensor is not used in this study for consistency with the lack of (reliable) picking at this station shown in the reference catalogue. The surface seismic network deployed before the stimulation was composed of eight vertical component seismometers and nine 3C-seismometers. However, to be still consistent with the reference catalogue, the three 3C-seismometers of the ReNaSS (Réseau National de Surveillance Sismique) network were not used. The eight vertical stations used a sampling frequency of 184.6 Hz whereas the 3C-stations applied a sampling frequency of 150 Hz. One can note that one of the surface 3C-sensor (CARO) was installed near the GPK1 wellhead and thus right above the induced seismic cloud.

To investigate the effect of the network design and coverage at Soultz, we use three network combinations to locate the hypocentres. Locations are computed with the observations from the down-hole sensors alone (red triangles in Figure 4-1) but without using the data provided by EPS1 as mentioned (i.e. four stations in total). A network composed of the surface sensors alone (green triangles on Figure 4-1) gives a second set of hypocentres (i.e. 14 stations in total). The third network used here is simply the combination of both previous networks and is called the “combined network” in the following.

### **4.3.5 Synthetic event hypocentres**

To investigate the location errors, a synthetic seismic cloud (red crosses on Figure 4-1) was created in accordance with the real seismicity (black dots) induced by the GPK2 stimulation. In the rotated system described by  $X_c$  and  $Y_c$  axes on Figure 4-1, the synthetic sources are distributed every 125 m (only one source on two is shown by the red crosses on Figure 4-1) in each direction between -1125 and 125 m along  $X_c$  and between -1625 and 625 m along  $Y_c$ . All coordinates are referenced to the GPK1 wellhead in a system rotated 30° anti-clockwise. The real seismic events mainly cover the north-east quarter of the synthetic event zone. Hence, we will focus our interpretations on this part.

Either all sources in the 3D grid will be used in the following sections or a subset on three orthogonal planes: two vertical planes and one horizontal plane. The extension of these planes is similar to the extension of the 3D grid and they all cut the well at the mid-point of the GPK2 open-hole section. Therefore, the horizontal plane is located close to 4529 m depth, the vertical plane oriented along  $X_c$  is close to 234 m south of GPK1 and the one oriented along  $Y_c$  is close to 311 m west of GPK1, in the rotated coordinate system.

All depths given in this paper are true vertical depth from mean sea level (TVD MSL) unless specified differently. The reference system is also the rotated coordinate system defined by the  $X_c$ ,  $Y_c$  and the vertical directions.

## **4.4 Results and discussion**

### **4.4.1 Location uncertainties**

To quantify location uncertainties, the only modification done between the synthetic modelling step and the location step is the addition of picking uncertainties to the travel-times. Any other assumptions concerning the sub-surface are left unchanged. Hence, we used

the reference layered velocity model, which is discretized on a 12.5 m mesh for both steps. The picking uncertainties for the down-hole stations and for the surface stations are set to  $\pm 5$  ms and  $\pm 15$  ms respectively (pers. Com. N. Cuenot, 2015). As observed on the seismograms, the P- and S-waves uncertainties are taken similar. All sources of the 3D grid are relocated using the three network configurations previously described: surface network, down-hole network, and combined network. The combined network, which is used in the reference catalogue, is taken as a reference in our discussion and the results from the other seismic networks are compared to its results.

Obviously, no location inaccuracy is noted for any of the tested seismic network. In Figure 4-3 the distribution of the location uncertainties is presented for three sections: a vertical section at  $X_c = -250$  m, a vertical section at  $Y_c = -375$  m and a horizontal section at 4500 m depth. As shown, the location uncertainty obtained from the combined network increases almost linearly with increasing depth. An increase of the location uncertainty along increasing values of  $X_c$  is seen. The thickness of the layer associated with the lowest uncertainty is lower for the higher values of  $X_c$  than for its lower values. The other layers seem to keep the same thicknesses along the whole axis. The uncertainty is more symmetrically distributed along the  $Y_c$  axis. From a centre  $\sim 500$  m “south” of GPK1, the uncertainty increases both to the north and to the south but reaches values slightly larger in the south.

To better quantify the results, statistical analysis of the spatial distribution of the uncertainties was performed (results not shown). From about 52 m at 4000 m depth, the median location uncertainty reaches about 73 m at 5500 m and the maximum reaches 77 m in the deepest part. Furthermore, the range of uncertainties and the interquartile range (third quartile minus first quartile:  $Q_3 - Q_1$ ) do not vary significantly with depth. On the other hand, such an evolution is not seen along the  $X_c$  and  $Y_c$  axes. The location uncertainty increases to the north and to the south along  $Y_c$  from a point located about 500 m southward from GPK1, which roughly corresponds to the latitude of the injection point in GPK2. It reaches a median value of 64 m in the southern part and 65 m in the northern part. The third quartile does not exceed 71 m uncertainty and is even lower than 67 m at the inflexion point. Along the  $X_c$  axis, a very small increase is noted with median values from 61 m in the western part to 64 m in the eastern part of the synthetic cloud. In the north-east part of the synthetic cloud, where most of the induced seismicity was located (Figure 4-1), the absolute locations can exhibit uncertainties with a median between 65 m and 77 m and a maximum  $Q_3$  of about 70-75 m depending on the source depth. The modelled uncertainties are a bit smaller than the 80 m horizontal and 100 m

vertical means provided by Cuenot *et al.* (2008), who are at the origin of the reference catalogue, but are clearly of the order.

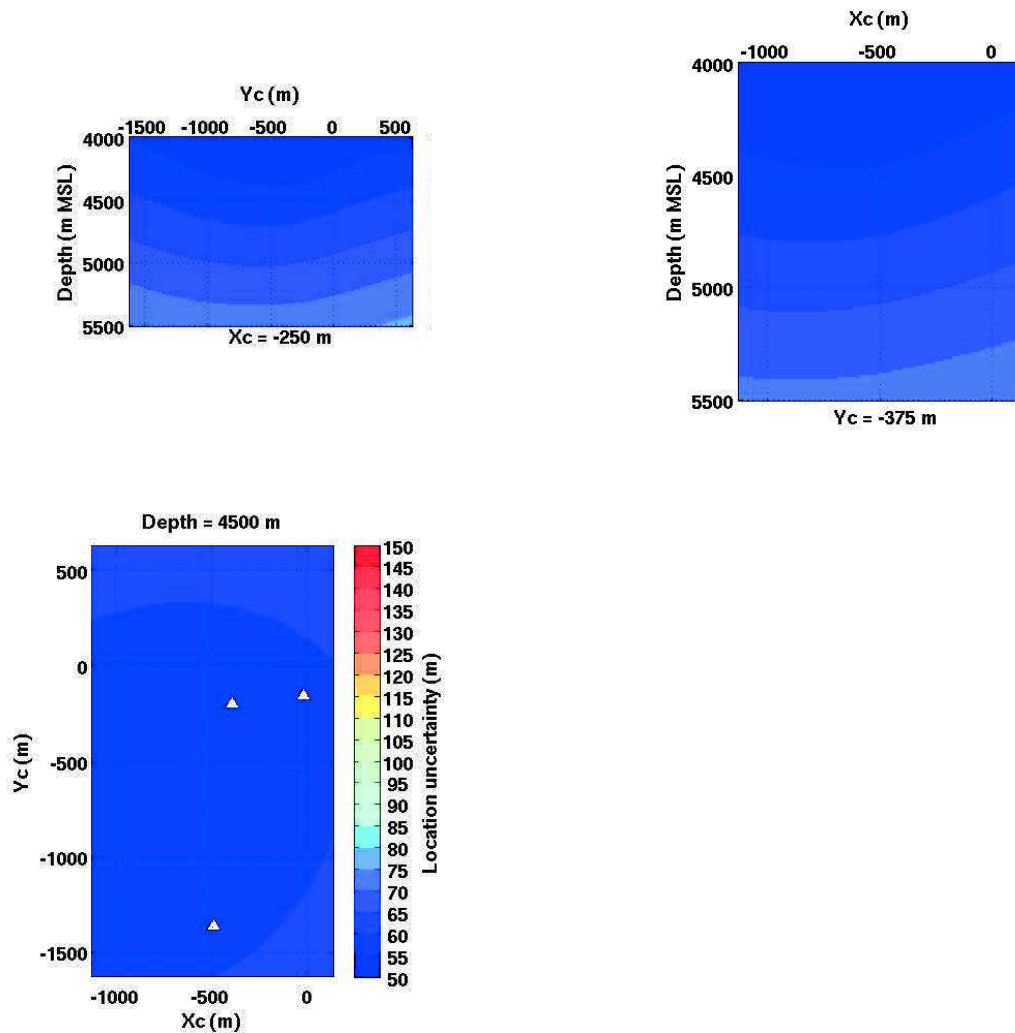


Figure 4-3 : Sections of the location uncertainties computed with the combination of the surface and the down-hole seismic networks. The variation at a given depth (bottom panel), Xc position (top right panel) and Yc position (top left panel) are presented. The colorbar defines the range of uncertainties and is common to all plots showing them.

As shown in Figure 4-4, locating the events with the down-hole network only or with the surface network only leads to larger uncertainties than with both networks. Locating using the down-hole network increases the hypocentres uncertainties by 12 to 23 m (median value) with a maximum increase of  $\sim 30$  m. This leads to location uncertainties of the order of 65 to 90 m as a median value and a maximum uncertainty of about 105 m (left panel of Figure 4-4). The relative proximity of the deep sensors from the seismicity and the associated relatively small picking uncertainties ( $\pm 5$  ms) provide locations that are quite precise. On the contrary, locations determined from the surface network alone have larger uncertainties. The median value can be increased by 55 to 75 m. This means a total median location uncertainty of  $\sim 150$  m in the worst case (right panel of Figure 4-4). The uncertainty variations between the down-

hole network and the combined network are smaller than those obtained between the surface network and the combined network, both in amplitude and spatial distribution. This suggests that the down-hole network strongly influence the location uncertainties of the combined network. The increase of uncertainty between locations performed with the surface network and with the combined network is stronger in the southern than in the northern part of the seismic cloud. The opposite effect is obtained between the down-hole network and the combined network locations (top of Figure 4-4).

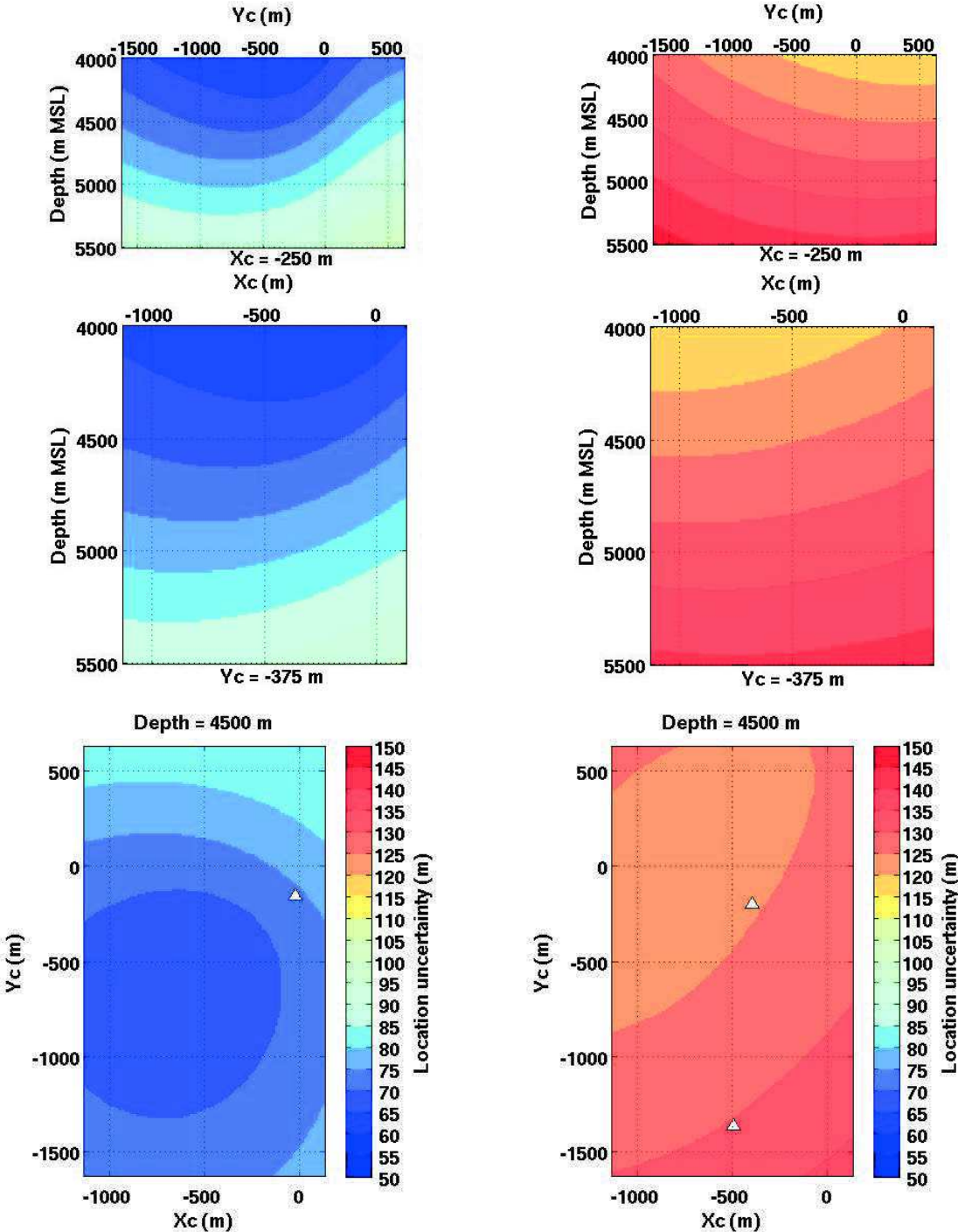


Figure 4-4: Location uncertainties obtained with the down-hole network (left panel) and with the surface network (right panel). The distribution of uncertainties at  $X_c = -250$  m (top),  $Y_c = -375$  m (middle) and at 4500 m depth (bottom) is shown with the colour scale of Figure 4-3.

Compared to the location uncertainties obtained by the combined network, those obtained by the surface network or by the down-hole network have a larger range with depth. As shown in Figure 4-4, the down-hole network better constrains the location uncertainties in the south direction along  $Y_c$  while the surface network better constrains the location uncertainties in the north along  $Y_c$ . With a smaller extent, the down-hole network better constrains the location uncertainties to the west along  $X_c$ , while the surface network better constrains uncertainties to the east along  $X_c$ . Finally, one can see that the down-hole network provides better depth control of the event hypocentres, especially for the shallower earthquakes.

To conclude, this study quantifies the value of adding the Soultz down-hole network to the surface network in order to better determine the micro-earthquake hypocentres. It shows that the combination of both networks decreases by a factor of two the location uncertainty compared to those which would be obtained from the surface network only. The highest uncertainties are found in the north-east part of the synthetic seismic cloud, which also corresponds to the highest density of the real seismic cloud.

#### **4.4.2 Location errors due to observed-time inaccuracies**

Many seismological catalogues and seismological processing toolboxes are limited to arrival-time picking accuracy of 10 ms. This was proven to lead to location inaccuracies at the scale of the geothermal site of Rittershoffen located 7 km to the east of Soultz (Kinnaert *et al.*, 2016). We investigate here the possible effects at Soultz, where the induced seismicity is located  $\sim 2$  times deeper than at Rittershoffen. The reference picking catalogue used in this study and in many other studies has such 10 ms picking accuracy. To reproduce picking time inaccuracy, we rounded at 10 ms the travel-times from the modelling step prior to location. All sources of the 3D grid are used and we perform the location with each of the three considered networks. Both the synthetic modelling and the location were computed in the reference velocity model.

In Figure 4-5 and Figure 4-6, the location inaccuracies are quantified using boxplots (Tukey, 1977) displaying the median, the first and third quartiles, and the range of the considered dataset.

The picking accuracy has negligible impact on the location uncertainty, which has spatial and amplitude distributions similar to the ideal case described in the previous sub-section. However, location inaccuracies are observed, mainly in the horizontal plane, for all tested networks, although they remain smaller than the uncertainties. The absolute values of the first

and third quartiles of the vertical inaccuracies are usually smaller than or equal to 12.5 m, the mesh size used for the location process. The accuracy of the event origin time is within  $\pm 0.5$  ms from expectation, for every direction and for each of the three tested networks.

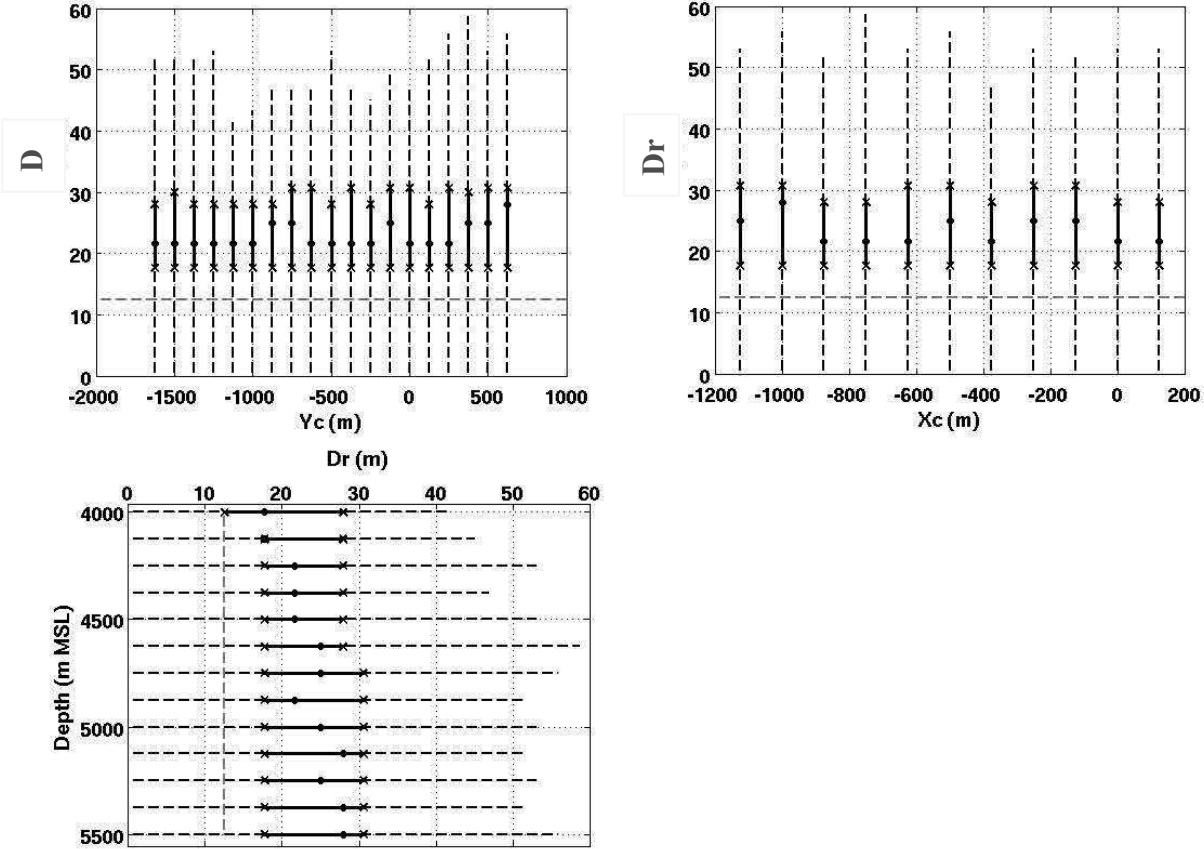


Figure 4-5 : Box-plots of the location inaccuracy along the Yc (top left), Xc (top right) and depth (bottom) axes. The coordinates are given with respect to the GPK1 wellhead but in the cloud system. The box-plots are formed by the median (full disk) the first and third quartiles (crosses) and the range (dashed line). The perpendicular dashed line accounts for the mesh size used for the location process.

With the combined network, the relocated hypocentres have inaccuracies of the order of 15 to 30 m as median values with the smallest inaccuracies in the eastern and the southern part of the synthetic seismic cloud, and for the shallowest events (Figure 4-5). The more inaccurate locations show a total bias of about 60 m. The median of the horizontal inaccuracies ranges mainly between 17 and 18 m. A higher value of 25 m was found for the northern and deepest planes. The third quartile varies between 25 m (in the shallowest part) and 30 m (for the deepest locations), and a maximum horizontal inaccuracy of about 55 m is seen for the deepest sources.

The location using the down-hole network alone leads, in general, to hypocentre inaccuracies with median between 30 and 40 m (Figure 4-6) and variations, which are similar for the horizontal inaccuracies. Median horizontal inaccuracies of 20 to 30 m are observed but do not exhibit specific spatial distribution. A bias up to 90-95 m exists for the less accurate locations

at depth and in the north part of the synthetic cloud. The shallowest sources are the most accurate locations. The third quartile, which ranges between 30 and 40 m, increases, like the median, with depth and in both south and north from a point situated 1000 m in the south of GPK1. A maximum horizontal bias of about 90 m is seen for the deepest sources. Hence, performing event location using the down-hole network alone multiplies the uncertainties and inaccuracies by a factor of about 1.5 in comparison with the results obtained with the combined network.

The hypocentre biases obtained by locating with the surface network alone (right panels in Figure 4-6) are lower than those obtained for the combined network. Median inaccuracies smaller than 20 m are found in all directions of the synthetic cloud, the third quartile value does not exceed 30 m and a maximum bias of about 50 m is observed for the deepest sources and close to the cloud centre.

These results may be explained from the position of the different networks relative to the source initial locations. The travel-time needed for the P- and S-waves to reach the down-hole network is shorter than for the surface network. Hence, rounding at 10 ms has a larger impact on the observed times of the down-hole network which brings larger inaccuracies in the location. Consequently, combining the down-hole and surface networks leads to larger location inaccuracies than with the surface network alone, but smaller ones than with the down-hole network alone.

Travel-times residuals were calculated for each source location at each seismic sensor and for both P- and S-waves. The sum of the residuals (for one source but for all stations together) usually varies between 1 and 4 ms depending on the position of the seismic source relatively to the stations, the phase and the network used for the location. Nonetheless, they remain smaller than 5 ms and are not significant with regards to the 10 ms rounding. Furthermore, the derived station corrections (at each station for the whole set of sources, we worked out the average of the travel-time residuals) between 1 and 50  $\mu$ s according to the phase, to the station and to the network used for the location. Those values cannot be used to identify any issue with the pickings or correct from the input inaccuracy.

To conclude, using input travel-times rounded at the nearest 10 ms mainly leads to horizontal location inaccuracies. Nevertheless, those biases are still smaller or equal to the location uncertainties. The down-hole network, which leads to the largest biases, up to 50 m, may increase the location inaccuracy by about 30 m compared to the combined network.



According to these results, the GPK2 reference catalogue is not suitable for locating only with the down-hole network at Soultz.

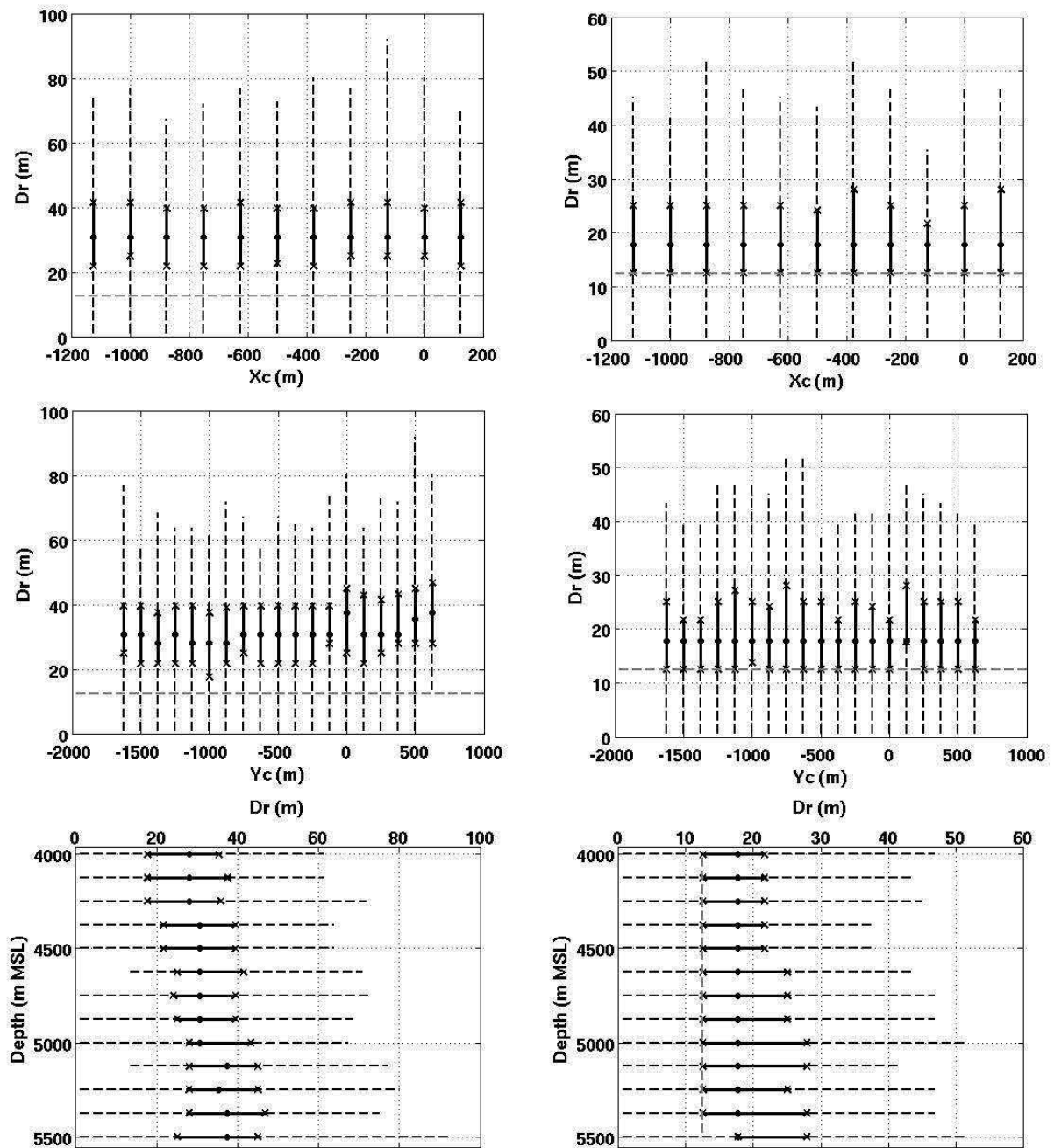


Figure 4-6: Box-plots of the location inaccuracy along  $X_c$  (top),  $Y_c$  (middle) and depth (bottom) computed using the down-hole network (left) and the surface network (right). The “picked” arrival-times were rounded at 10 ms before locating. Symbols are described in caption of Figure 4-5.

#### 4.4.3 Location errors in a perturbed velocity model

The impact on seismological observations of massive fluid injection or fluid circulation in underground reservoirs is of primary interest. We investigate whether the location of the Soultz seismicity using the seismic networks would be sensitive to a velocity decrease at the depth of the water injection in GPK2. To model the effect of the fluid injection in GPK2, we

reproduce the synthetic test performed by Calò *et al.* (2011). Between 4030 and 5030 m depth, in a radius of 375 m around GPK2, the P-wave and S-wave velocities are decreased by 10% and 5% respectively. The synthetic observation times are computed in this perturbed velocity model, but the event locations are still computed in the reference velocity. The synthetic sources are distributed on the three orthogonal planes crossing GPK2 at the middle of the open-hole section.

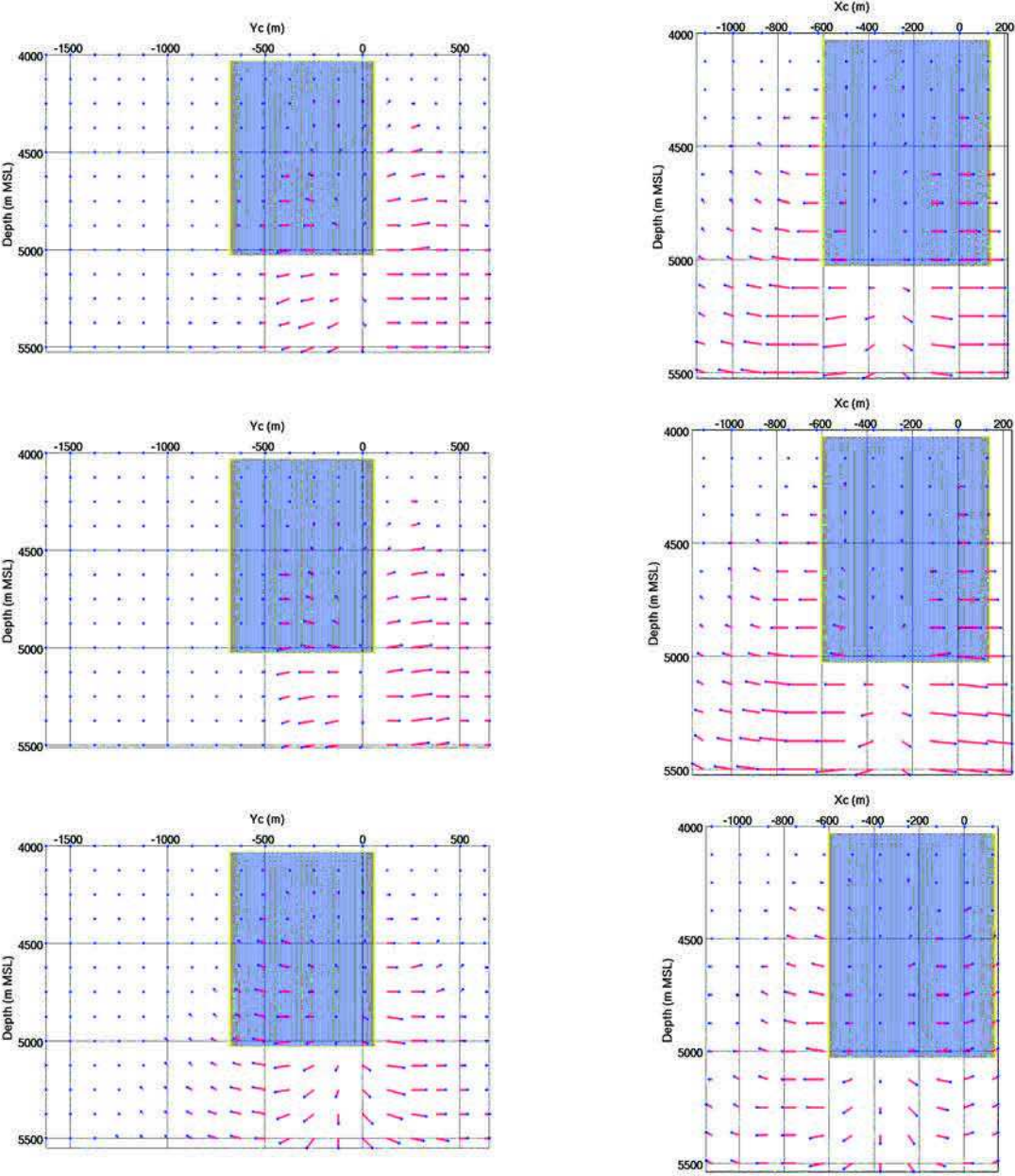


Figure 4-7: Spatial distribution of the initial and relocated synthetic sources computed with the combined network (top), the down-hole network (middle) and the surface network (bottom). The perturbed (lower) velocity zone is shown in grey. The results are shown for the sources originally on north-south vertical plane (left), east-west vertical plane (right). On each plane, each blue dot shows the projection of one relocation position and the associated red line shows the displacement to be applied to move to the event initial position.

No significant modification of the location uncertainty, in amplitude or in spatial distribution, is observed compared to the ideal case described in sub-section 4.4.1. Figure 4-7 shows the

results associated to the location inaccuracies for the three network configurations. In all cases, the events shallower than the perturbed zone are relocated at their original position. In the perturbed zone or deeper, the combined network leads to significant decrease of location accuracy (Figure 4-7 top panels), which is mainly horizontal (the vertical bias is always smaller than one grid-cell). The bias increases through the injection zone and reaches about 100 m of median horizontal value at its bottom for sources situated on the vertical-Xc plane. However, a maximum horizontal bias of ~150 m can be observed for these sources. For the sources distributed on the vertical-Yc plane, the median horizontal inaccuracy can reach 75 m in depth and the maximum is ~90 m. For the same sources but without the observations from the down-hole network, a median horizontal inaccuracy of 30 m can be reached and a maximum of 70 m. Considering the horizontal plane of sources distributed at ~4500 m depth, the effect of the low velocity zone is to move the events away from their initial position from a point located ~125 m to the west and 250 m to the south. When the extreme values are taken into account, the inaccuracies can be two times larger than the uncertainties for the combined network, leading to bias of about 150 m with uncertainties of about 75 m. At the deepest part of Xc-vertical plane, the combined network leads to ~110 m inaccuracy, about 1.4 times the uncertainty. Interestingly, the origin times of the events are as accurate as for the ideal case.

The locations performed using the down-hole and the surface network separately are also biased if the injection zone is not taken into account during the location process. The down-hole network leads to median horizontal inaccuracy up to 125 m along depth with a maximum of 195 m for the sources on the vertical-Xc plane (but only 15 m median with 100 m maximum for the sources on the vertical-Yc plane). On these vertical planes, the inaccuracy can reach 90 m as median value along the Xc and Yc axes. Nonetheless, maximum inaccuracy is far smaller for sources on the vertical-Yc plane than for sources on the vertical-Xc plane: they reach about 200 m in the latter and 100 m in the former (Figure 4-7 middle panels). The inaccuracy distribution can be partly explained by the design of the down-hole network and is close to the distribution observed for the combined network. The inaccuracies of about 50-100 m might be slightly larger than the ~80 m of location uncertainty. Nevertheless, median inaccuracy of about 130 m, which is about 1.3 times the 95 m of the location uncertainty, can be observed in the deepest part of the Xc-vertical plane of sources.

For the surface network (Figure 4-7 bottom panels), a median horizontal inaccuracy of ~70 m is reached at the bottom of the stimulated zone for sources positioned on the vertical-Xc plane. This median reaches about 40 m for sources on the vertical-Yc plane. The observed maximum horizontal inaccuracies reach 110 m and 100 m respectively. Regarding the

distribution along the  $X_c$  and the  $Y_c$  axes, an increase of the horizontal and total inaccuracies is observed from each side toward the stimulated zone. Median global inaccuracy of 70 and 80 m are seen for sources positioned along the  $Y_c$  and  $X_c$  axes respectively. The distribution of the location inaccuracies is different from that of both other networks. For the surface network, the inaccuracies look symmetrically distributed from a plane at  $X_c \sim -100$  m. Furthermore, the vertical inaccuracy for sources deeper than 5000 m is larger and inaccuracies are still observed in the south of the simulated injection zone. Moreover, using this network alone leads to location inaccuracy of the same order or smaller than the location uncertainty.

Residuals were also calculated for this study for each source of each plane. As expected the values vary with the seismic phase and to the position of the source relatively to the station in the perturbed velocity model, but they also vary according to the seismic network used for location. However, they are all smaller than 1 ms. Therefore, the impact of the velocity model changes is almost invisible from this time residual perspective despite it generates bias in the locations.

To conclude, not taking into account the low velocity zone leads to noticeable location inaccuracies but usually not large enough to be correctly differentiated from the location uncertainties if we consider the median values, except for the deepest sources in the  $X_c$ -vertical plane. Only the largest inaccuracies may be larger than uncertainties of the associated hypocentre for locations performed by the combined network and by the down-hole network, but not for location computed by the surface network (due to the larger location uncertainties). The distribution of the observed location inaccuracies are is not isotropic. Furthermore, the strong impact of the down-hole sensors on the location is once more emphasized by the similarity of the values and spatial distribution of the location inaccuracies obtained for the combined network and for the down-hole network.

## 4.5 Conclusion and outlooks

In this paper, we mainly focused on the impact of several seismic network configurations on earthquake location errors, discriminating uncertainty from inaccuracy. The methodology was applied to a synthetic data-set representative of the seismicity induced during the massive stimulation of the GPK2 well at Soultz-sous-Forêts, in 2000. The combination of a surface and a down-hole network provides the most certain hypocentre locations, of the order of 55 m to 75 m in the denser part of the seismic cloud. This result is compatible with the estimates from Cuenot *et al.* (2008), however, we show that the uncertainty is not homogeneously

distributed in space, is larger at the NE than at the SW and increases with depth. The implementation of the down-hole network allows decreasing by a factor of two the location uncertainties compared to those which would be obtained from the surface network only.

The use of P- and S-wave arrival-times rounded at 10 ms, as written in the existing catalogue of observations, leads to location inaccuracy up to 20-30 m for locations computed with the combined network. The picking inaccuracy generates stronger bias for sources which are deep or in the north-east part of the seismic cloud. Nevertheless, the location inaccuracies remain smaller by a factor of 3 than the location uncertainties and may be considered as negligible. The rounding effect induces location inaccuracies 50% larger with the down-hole network than with the surface network. Even if the location inaccuracy will remain smaller than the uncertainty, it is recommended not to locate sources using rounded travel-times catalogue at the nearest 10 ms and the down-hole network alone. Therefore the down-hole network is useful to diminish the location uncertainty but leads to stronger location bias compared to the other two tested networks.

The impact on event location of a P- and S-wave velocity decrease of 10 % and 5 % respectively in a low-velocity cylinder centred on the middle of the open-hole section of GPK2 was investigated. It was supposed to represent the effect due to the massive water injection carried out to stimulate the well in 2000. This does neither affect significantly the location uncertainty nor the vertical accuracy. Nevertheless, the horizontal location accuracy can be strongly affected, up to 200 m as a maximum. Unfortunately, larger location inaccuracies than uncertainties are observed for some sources in the deepest western part of the synthetic cloud, where part of the real seismic cloud was located. This means that for those sources, bias larger than 100 m should be expected for the combined network. This value is compared with the 75 m of uncertainty. In that case, the real hypocentre will not be included in the  $1-\sigma$  confidence level. On the other hand, sources located on a plane at ~4500 m depth and on a  $Y_c$ -vertical plane do not bring to similar conclusions since the inaccuracies are always smaller than or the same order as the location uncertainties.

All those conclusions are suitable for absolute location methods. Nevertheless, the improvement or deterioration brought by relative location methods should also be investigated since the latter become routinely used to locate earthquakes. The proposed methodology could be used in similar reservoir monitoring contexts to characterize the capabilities of the existing or expected seismicity in terms of reservoir description.

## Acknowledgment

This work was conducted in the framework of the excellence laboratory “Labex G-EAU-THERMIE PROFONDE” (University of Strasbourg). It was funded by the French National Research Agency, as part of the French “Investments for the future” program, by the Energie Baden-Württemberg AG (EnBW), the French institution CNRS, and by the French-German University (DFH-UFA). We wish to thank the ECOGI joint venture and the Électricité de Strasbourg – Géothermie company (ESG) for sharing data. We are grateful to N. Cuenot (EEIG “Heat Mining”) for sharing his experience on the Soultz raw seismic data and to A. Genter for fruitful discussions on the Soultz experiments. We also thank L. and C. Dorbath for providing the seismic data catalogues and sharing their knowledge on the datasets.

## References

- Bailleux, P., E. Schill, J.-B. Edel, and G. Mauri (2013), Localization of temperature anomalies in the Upper Rhine Graben: insights from geophysics and neotectonic activity, *International Geology Review*, 55, doi:10.1080/00206814.2013.794914.
- Bardainne, T., and E. Gaucher (2010), Constrained tomography of realistic velocity models in microseismic monitoring using calibration shots, *Geophysical Prospecting*, 58(5), 739–753, doi:10.1111/j.1365-2478.2010.00912.x.
- Baria, R., J. Baumgärtner, A. Gérard, and J. Garnisch (2000), The european HDR programme: main targets and results of the deepening of the well GPK2 to 5000 m.
- Baumgärtner, J., A. Gérard, R. Baria, and J. Garnisch (2000), Progress at the European HDR project at Soultz-sous-Forêts: preliminary results from the deepening of the well GPK2 to 5000 m.
- Calò, M., C. Dorbath, F. H. Cornet, and N. Cuenot (2011), Large-scale aseismic motion identified through 4-D P-wave tomography, *Geophysical Journal International*, 186(3), 1295–1314, doi:10.1111/j.1365-246X.2011.05108.x.
- Charl ty, J., N. Cuenot, C. Dorbath, and L. Dorbath (2006), Tomographic study of the seismic velocity at the Soultz-sous-For ts EGS/HDR site, *Geothermics*, 35(5-6), 532–543, doi:10.1016/j.geothermics.2006.10.002.
- Charl ty, J., N. Cuenot, L. Dorbath, C. Dorbath, H. Haessler, and M. Frogneux (2007), Large earthquakes during hydraulic stimulations at the geothermal site of Soultz-sous-For ts, *Int J Rock Mech Min*, 44(8), 1091–1105, doi:10.1016/j.ijrmms.2007.06.003.
- Cornet, F. H., T. B rard, and S. Bourouis (2007), How close to failure is a granite rock mass at a 5 km depth?, *Int J Rock Mech Min*, 44(1), 47–66, doi:10.1016/j.ijrmms.2006.04.008.
- Cuenot, N. (2009), R ponse du granite fractur  de Soultz-sous-For ts   des injections massives de fluide: Analyse de la microsismicit  induite et du r gime de contraintes, Ph.D., University of Strasbourg.
- Cuenot, N., C. Dorbath, and L. Dorbath (2008), Analysis of the microseismicity induced by fluid injections at the EGS site of Soultz-sous-For ts (Alsace, France): Implications for the characterization of the geothermal reservoir properties, *Pure Appl. Geophys.*, 165(5), 797–828, doi:10.1007/s00024-008-0335-7.
- Dorbath, L., N. Cuenot, A. Genter, and M. Frogneux (2009), Seismic response of the fractured and faulted granite of Soultz-sous-For ts (France) to 5 km deep massive water injections, *Geophys J Int*, 177(2), 653–675, doi:10.1111/j.1365-246X.2009.04030.x.
- Dyer, B. C. (2001), Soultz GPK2 stimulation June/July 2000, *Semore Seismic Report*, S. Seismic monitoring report.
- Gaucher, E. (1998), Comportement hydrom canique d’un massif fractur  : apport de la microsismicit  induite. Application au site g othermique de Soultz-sous-For ts (Hydro-mechanical behaviour of a fractured rock mass: induced microseismicity contribution. Application to the Soultz-sous-For ts geothermal site), Ph.D. Thesis, U. P. 7, Paris.
- Gaucher, E. (2013), Why the seismicity induced in Soultz-sous-For ts and Gross Schoenebeck enhanced geothermal fields are so different?
- Gaucher, E., X. Kinnaert, U. Achauer, and T. Kohl (Eds.) (2016), *Propagation of Velocity Model Errors in Earthquake Absolute Locations: Application to the Rittershoffen Geothermal Field*.
- Genter, A., K. Evans, N. Cuenot, D. Fritsch, and B. Sanjuan (2010), Contribution of the exploration of deep crystalline fractured reservoir of Soultz to the knowledge of enhanced geothermal systems (EGS), *Comptes Rendus Geoscience*, 342(7-8), 502–516, doi:10.1016/j.crte.2010.01.006.
- G rard, A., and O. Kappelmeyer (1987), The Soultz-sous-For ts project: proceedings of the first EEC/US workshop on Geothermal Hot Dry Rocks Technology, *Geothermics, special issue*, 393–399.

- Held, S., A. Genter, T. Kohl, T. Kölbel, J. Sausse, and M. Schoenball (2014), Economic evaluation of geothermal reservoir performance through modeling the complexity of the operating EGS in Soultz-sous-Forêts, *Geothermics*, 51(0), 270–280, doi:10.1016/j.geothermics.2014.01.016.
- Kinnaert, X., E. Gaucher, U. Achauer, and T. Kohl (2016), Modelling earthquake location errors at a reservoir scale: a case study in the Upper Rhine Graben, *Geophysical Journal International*, 206(2), 861–879.
- Kohl, T., and T. Mégel (2007), Predictive modeling of reservoir response to hydraulic stimulations at the European EGS site Soultz-sous-Forêts, *Int J Rock Mech Min*, 44(8), 1118–1131, doi:10.1016/j.ijrmms.2007.07.022.
- Kwiatek, G., M. Bohnhoff, G. Dresen, A. Schulze, T. Schulte, G. Zimmermann, and E. Huenges (2010), Microseismicity induced during fluid-injection: A case study from the geothermal site at Groß Schönebeck, North German Basin, *Acta Geophys.*, 58(6), 995–1020, doi:10.2478/s11600-010-0032-7.
- Lomax, A. (2011), *NonLinLoc: Probabilistic, Non-Linear, Global-Search Earthquake Location in 3D media*, ALomax Scientific.
- Lomax, A., A. Michelini, and A. Curtis (2009), Earthquake location , Direct, Global-Searc Methods, in *Encyclopedia of Complexity and Systems Science*, edited by R. A. Meyers, pp. 2449–2473, Springer New York.
- Megies, T., and J. Wassermann (2014), Microseismicity observed at a non-pressure-stimulated geothermal power plant, *Geothermics*, 52(0), 36–49, doi:10.1016/j.geothermics.2014.01.002.
- Place, J., M. Diraison, C. Naville, Y. Géraud, M. Schaming, and C. Dezayes (2010), Decoupling of deformation in the Upper Rhine Graben sediments. Seismic reflection and diffraction on 3-component Vertical Seismic Profiling (Soultz-sous-Forêts area), *Comptes Rendus Geoscience*, 342(7-8), 575–586, doi:10.1016/j.crte.2010.01.001.
- Podvin, P., and I. Lecomte (1991), Finite difference computation of traveltimes in very contrasted velocity models: a massively parallel approach and its associated tools, *Geophys J Int*, 105(1), 271–284, doi:10.1111/j.1365-246X.1991.tb03461.x.
- Sausse, J., C. Dezayes, L. Dorbath, A. Genter, and J. Place (2010), 3D model of fracture zones at Soultz-sous-Forêts based on geological data, image logs, induced microseismicity and vertical seismic profiles, *Comptes Rendus Geoscience*, 342(7-8), 531–545, doi:10.1016/j.crte.2010.01.011.
- Schill, E., A. Genter, N. Cuenot, and T. Kohl (submitted), Compiling hydraulic performance history at the Soultz EGS reservoirs from stimulation and long-term circulation tests, *Geothermics*.
- Schnaebele, R. (1948), *Monographie géologique du champ pétrolifère de Pechelbronn*, Mémoire du Service de la Carte Géologique d’Alsace et de Lorraine, Strasbourg.
- Tarantola, A., and B. Valette (1982), Inverse problems = quest for information, *Journal of Geophysics*, 50, 159–170.
- Tukey, J. W. (1977), *Exploratory Data Analysis*, 503 pp., *Behavioral Science*, Addison-Wesley, Reading, MA.
- Wentzel, F., and J.-P. Brun (1991), A deep Reflection Seismic Line across theNorthern Rhine Graben, *Earth and Planetary Science Letters*, 104, 140–150.
- Wittlinger, G., G. Herquel, and T. Nakache (1993), Earthquake location in strongly heterogeneous media, *Geophys J Int*, 115(3), 759–777, doi:10.1111/j.1365-246X.1993.tb01

---

# 5 Modelling earthquake location errors at a reservoir scale: a case study in the Upper Rhine Graben

X. Kinnaert<sup>1,2\*</sup>, E. Gaucher<sup>1</sup>, U. Achauer<sup>2</sup> and T. Kohl<sup>1</sup>

<sup>1</sup>: Division of Geothermal Research, Institute of Applied Geosciences, Karlsruhe Institute of Technology, Adenauerring 20b, Geb 50.40., D-76131 Karlsruhe, Germany.

<sup>2</sup>: EOST-IPGS UMR7516, 5 rue René Descartes, F-67000 Strasbourg, France.

\*Corresponding author: Email: xavier.kinnaert@kit.edu, Phone: +49 721 608 45223, Fax: +49 721 608 45228.

## Abstract

Earthquake absolute location errors which can be encountered in an underground reservoir are investigated. In such an exploitation context, earthquake hypocentre errors can have an impact on the field development and economic consequences. The approach using state-of-the-art techniques covers both the location uncertainty and the location inaccuracy – or bias – problematics. It consists, first, in creating a 3D synthetic seismic cloud of events in the reservoir and calculating the seismic travel times to a monitoring network assuming certain propagation conditions. In a second phase, the earthquakes are relocated with assumptions different from the initial conditions. Finally, the initial and relocated hypocentres are compared. As a result, location errors driven by the seismic onset time picking uncertainties and inaccuracies are quantified in 3D. Effects induced by erroneous assumptions associated with the velocity model are also modelled. In particular, 1D velocity model uncertainties, a local 3D perturbation of the velocity and a 3D geo-structural model are considered. The present approach is applied to the site of Rittershoffen (Alsace, France), which is one of the deep geothermal fields existing in the Upper Rhine Graben. This example allows setting realistic scenarios based on the knowledge of the site. In that case, the zone of interest, monitored by an existing seismic network, ranges between 1 and 5 km depth in a radius of 2 km around a geothermal well. Well log data provided a reference 1D velocity model used for the synthetic earthquake relocation. The 3D analysis highlights the role played by the seismic network coverage and the velocity model in the amplitude and orientation of the location



uncertainties and inaccuracies at sub-surface levels. The location errors are neither isotropic nor aleatoric in the zone of interest. This suggests that although location inaccuracies may be smaller than location uncertainties, both quantities can have a cumulative effect. Besides, small velocity uncertainties applied to the whole 1D profile can lead to large increase of the location uncertainties. However, local variations of the velocity field around the well may have negligible effects that would make such a feature undetectable with an absolute location method. Although the reference 1D velocity model was built from well log data, the results show that it is not a good representative of a more realistic 3D model including a fault and its associated block shift. The amplitude and distribution of the induced location inaccuracies are such that the positioning and the orientation of features delineated by seismicity are distorted and may be difficult to correctly interpret.

**Key words:** Location inaccuracy; Location uncertainty; Velocity model; Geothermal field; EGS; Rittershoffen.

## 5.1 Introduction

Earthquake hypocentres constitute a unique source of information for understanding the physical processes at the origin of earthquakes, describing the sub-surface and quantifying earthquake seismic hazard. It is the primary attribute of an earthquake without which other characteristics such as occurrence time, seismic moment, magnitude or focal mechanism cannot be determined. The merging of these individual properties into catalogues allows investigating the space-time interactions between earthquakes or the dynamic and spatial scale of the seismic ruptures. Tectonic interpretation or fault identification using the spatial distribution of earthquakes is also the purpose of many studies. However, earthquake location errors exist and need to be properly quantified for reliable result interpretation.

The earthquake location error can be described as the combination of two quantities: the location inaccuracy and the location imprecision. The latter will be confused with the *a posteriori* location uncertainties that are directly linked to the uncertainties which are taken into account during the location process (e.g. Tarantola, 2005). Typically, *a priori* picking uncertainties of seismic body-waves are integrated in the inverse problem and lead to *a posteriori* location uncertainties which are therefore part of the location result. On the contrary, the location inaccuracy is defined as the wrong positioning of the earthquake hypocentre due to all effects that have been ignored in the inverse problem, either for practical reasons or because of a lack of knowledge. These simplifications of the reality introduce systematic errors or bias in the computation of the earthquake location. In most cases, the use

of a velocity model not representative of the effective seismic propagation medium would lead to earthquake location inaccuracies (Pavlis, 1986; Bardainne and Gaucher, 2010; Husen *et al.*, 2013).

The earthquake hypocentres together with their associated errors determine the scale at which the sub-surface can be investigated. The use of earthquake hypocentres as direct markers of geological structures illustrates this. For example, if uncertainties of several tens of kilometres are suitable to describe subduction zones at 200 km depth (e.g. Pegler and Das, 1998), they are inadequate for local scale studies covering areas smaller than  $10 \text{ km} \times 10 \text{ km}$ . Interpretation of the interaction between on-going activity and geological structures in mines may require earthquake location errors of the order of a few metres (e.g. Kwiatek *et al.*, 2010, Plenkers *et al.*, 2010). To assess the efficiency of successive hydraulic fracturing stages for enhanced oil and gas recovery, micro-earthquake location errors smaller than 25 m are often necessary (e.g. Bardainne and Gaucher, 2010). Megies and Wassermann (2014) show that, in a geothermal field, depth uncertainties larger than 500 m may be problematic for unequivocal interpretation of the structures and physical processes at the origin of the earthquakes induced at ca. 5 km depth. These examples emphasize that, generally, more than one order of magnitude between earthquake location errors and description of earthquake-based spatial features is necessary for valuable use of the information.

In this work, we focus on uncertainties and inaccuracies of absolute location of earthquakes in underground reservoirs. Therefore, relative location algorithms of earthquakes based on double-differences (e.g. Waldhauser and Ellsworth, 2000) or master-slave events (e.g. Fréchet, 1985, Poupinet *et al.*, 1985) are not considered, although they often constitute a further step to better constrain hypocentres of clustered earthquakes. Location techniques based on waveform stacking and migration from dense array recordings (Kao and Shan, 2004; Gharti *et al.*, 2010; Drew *et al.*, 2013; Grigoli *et al.*, 2013) are not examined either, despite used routinely in hydraulic fracturing monitoring for oil and gas fields. The modelling of the hypocentre errors associated with these location methods would differ from the one we apply here and remains beyond the scope of this work.

It is common practice to deploy seismic networks over underground reservoirs in applications such as geothermal energy production, oil and gas production, underground storage or mining. In these cases, the monitored volume is typically of the order of  $10 \times 10 \times 10 \text{ km}^3$ . Within these industrial contexts, earthquake location errors may have a major impact on the field development and economic consequences. In particular, experience in the geothermal domain shows that induced seismicity always contributed to the identification of faults in the

reservoir (Sausse *et al.*, 2010; Kraft and Deichmann, 2014; Edwards *et al.*, 2015; Frietsch *et al.*, 2015). In many cases, this led to optimize the positioning of several wells, and sometimes to evaluate the field economic performances (e.g. Held *et al.*, 2014).

The understanding of the physical processes at the origin of the induced seismicity in geothermal contexts greatly increased with the observation and analysis of this phenomena (Cornet *et al.*, 2007; Lengliné *et al.*, 2014; Zang *et al.*, 2014; Gaucher *et al.*, 2015b), as well as the development of forecasting and mitigation approaches (GEISER, 2013; Gaucher *et al.*, 2015a). In the domain of enhanced oil and gas recovery similar use of recorded seismicity is often made. However, to our knowledge, only few studies provide, model or discuss earthquake location errors (e.g. Pavlis, 1986; Lomax *et al.*, 2009; Husen and Hardebeck, 2010), especially at such a spatial scale and with respect to inaccuracies (or bias). Earthquake locations are usually provided with uncertainties but without inaccuracies, which, by definition, must be evaluated separately from the standard location algorithm. Yet, it remains of importance to quantify them because they may be much larger than the location uncertainties. In other words, the location uncertainty domain may not contain the true earthquake location and is therefore not sufficient to correctly interpret the earthquake locations. Since inaccuracy implies that the real earthquake location is known, only synthetic models may be considered, unless a few controlled seismic sources have known locations (Bardainne and Gaucher, 2010; Husen *et al.*, 2013). Consequently, dedicated procedures, which are relatively time consuming and which require *a priori* knowledge to deliver beneficial results, must be developed. Our approach is described in the next section. This lack of *a priori* modelling of the earthquake location uncertainties and inaccuracies in reservoir contexts motivated this work and its application to the Rittershoffen (France) geothermal field. This site is located in the Upper Rhine Graben (URG) and surrounded by several other enhanced geothermal systems (EGS) like Soultz-sous-Forêts (France), Landau, Insheim and Bruchsal (all in Germany). Hence, although the quantitative results will be related to the Rittershoffen site, the existing or future geothermal fields in the URG could benefit from the general conclusions.

The paper is organized as follows: in section 5.2, we first recall the general problem of absolute earthquake location in 3D and then present the multi-step approach based on state-of-the-art techniques that we applied to model the location errors. The case study is described in section 5.3 which gives the basic information necessary to apply the methodology (geothermal field context, seismic monitoring configuration and reference seismic velocity model). In section 5.4, realistic scenarios for seismic wave picking and velocity model errors

are applied to model the associated hypocentre location errors. Each case is presented and discussed before giving concluding remarks and perspectives to the work.

## 5.2 Methodology

### 5.2.1 Earthquake absolute location

The earthquake absolute location is a classical nonlinear problem in geophysics, whose objective is to minimize discrepancies between seismological observations – presently only seismic wave onset times – and the solution of the forward problem, in a given physical system, for a given space-time source. The minimization process is referred to as the inverse problem, whereas the modelling of the observations is referred to as the forward problem (Tarantola, 2005). Accordingly, the earthquake hypocentre and origin time depend, among others, on the seismic onset times and associated uncertainties (i.e. the observations), on the velocity model (i.e. the physical system), and on the location algorithm applied (i.e. the minimization process).

In practice, the earthquake location numerical code NonLinLoc (NLL) developed by Lomax *et al.* (2000) was used in the process of modelling the location errors. This code, which is widely used in the seismological community, has several advantages. First, it keeps the non-linearity of the location inverse problem. Second, it is able to locate earthquakes in 3D velocity models, like we intend to do; and third, it is appropriate to a reservoir scale. Thanks to a Bayesian formalism, the location probability density of an earthquake hypocentre can be estimated everywhere in the location zone expected to include the event. The absolute location method proposed by Wittlinger *et al.* (1993) and implemented in NLL is applied. It combines the travel time computation algorithm of Podvin and Lecomte (1991) to solve the forward problem, with the least-square formalism of Tarantola and Valette (1982) to define the misfit function and to compute the location probability density function (PDF). Accordingly, the PDF  $\sigma$  at location  $\mathbf{X}$  is defined by:

$$\sigma(\mathbf{X}) = K \cdot \exp \left\{ -\frac{1}{2} \left( [\tilde{\mathbf{T}}_{Obs} - \tilde{\mathbf{T}}_{Calc}(\mathbf{X})]^t \cdot \mathbf{C}^{-1} \cdot [\tilde{\mathbf{T}}_{Obs} - \tilde{\mathbf{T}}_{Calc}(\mathbf{X})] \right) \right\} \quad (1)$$

with  $K$  a normalizing constant,  $\tilde{\mathbf{T}}_{Obs}$  the vector of the observed arrival times minus their weighted mean,  $\tilde{\mathbf{T}}_{Calc}$  the vector of the computed arrival times minus their weighted mean, and  $\mathbf{C}^{-1}$  the weight matrix. The  $t$  superscript indicates the transpose operation.

The  $\tilde{\mathbf{T}}_{Calc}$  vector is obtained by the Podvin and Lecomte (1991) numerical code which solves the Eikonal equation using the Huygen's principle and a finite-difference approximation. This numerical code computes the travel times between a seismic sensor and any source located on a Cartesian grid, for the first arrivals of the body-waves. It works in any type of seismic velocity model, in particular in strongly heterogeneous 3D models, without losing its robustness. Therefore, it is well adapted to the reservoir scale and to velocity models we wish to consider. We do not include in the weight matrix  $\mathbf{C}^{-1}$  any factor due to incorrect theoretical computation of the travel times by the Podvin and Lecomte (1991) code. This is justified by the fact that only this travel time computation code will be applied throughout the study (see sub-section 5.2.2). However, the  $\mathbf{C}^{-1}$  diagonal matrix contains the inverse of the uncertainties (standard deviations) of the observed arrivals times  $\mathbf{T}_{Obs}$  which are independent from each other (see sub-section 5.4.1 for details).

The earthquake hypocentre is located where the PDF is the highest, in other words where the misfit function (right term in brackets in eq. 1) is the smallest. From the determination of the PDF in the location zone, the true *a posteriori* earthquake location uncertainty is available in the 3D space. Assuming a Gaussian distribution of the PDF around the best location, the location uncertainty can be described by the so-called confidence ellipsoid which includes all grid points of confidence level larger than 68.3%. The analysis of the confidence ellipsoid using principal components gives the expected location (gravity centre of the grid-point distribution) and the three orientations and lengths of the uncertainty orthogonal axes (Lomax *et al.*, 2000). In the following, the location uncertainty will be quantified by the half-length of the largest confidence ellipsoid axis and, therefore, the location should be understood within  $\pm$  the uncertainty length.

Because  $\tilde{\mathbf{T}}_{Calc}$  is calculated once for a given velocity model, with this formalism, the earthquake location uncertainties do not contain any factor associated with the errors in the velocity model. This explains why uncertainties and inaccuracies have to be discriminated although they both contribute to the earthquake location error. We will see in sub-section 5.4.2.1 that the formalism may be adapted under specific assumptions to integrate velocity model uncertainties into location uncertainties.

To guarantee an earthquake hypocentre associated with the best absolute fit and a correct spatial estimate of the *a posteriori* location uncertainties, eq. 1 is calculated for all grid-points in the location zone (i.e. grid-search option). Once the hypocentre has been obtained, the earthquake origin time can be computed since it is equal to the weighted mean of the observed arrival times minus the computed ones (Moser *et al.*, 1992).

For several reasons, commonly used linearized iterative methods such as Hypo71 (Lee and Lahr, 1975), Hypoinverse (Klein, 1978) or Hypoellipse (Lahr, 1999) have not been retained to perform the analysis. Although they allow fast earthquake location, the linearization of the location inverse problem around an estimated initial solution was considered as a possibly too strong assumption with regards to the seismic network coverage. Moreover, we did not want to be limited to 1D velocity-depth models for the different configurations we intend to investigate. However, few characteristics of these linearized iterative methods will be reproduced to examine their effects on the location errors. In particular, the use of observed seismic arrival times rounded at 10 ms and the use of 1D velocity-depth models will be shown for Rittershoffen.

Interested readers can find more details about the absolute location of earthquakes in seismological books (e.g. Lee and Stewart, 1981, Chap. 6; Lay and Wallace, 1995, Chap. 6), or in Lomax *et al.* (2009), Husen and Hardebeck (2010) and Pavlis (1986) for problematics closer to ours.

**5.2.2 Synthetic modelling**

In order to quantify earthquake location errors (inaccuracies and uncertainties), a multi-step approach is applied (Figure 5-1). In short, it consists in 1) defining synthetic earthquake hypocentres and computing, in a given velocity model, the associated seismic arrival times at the seismic stations of a network (the synthetic modelling step), 2) relocating the earthquake hypocentres using the simulated times but after perturbing the initial conditions (the relocation step), and 3) comparing the relocated hypocentres with the initial ones.

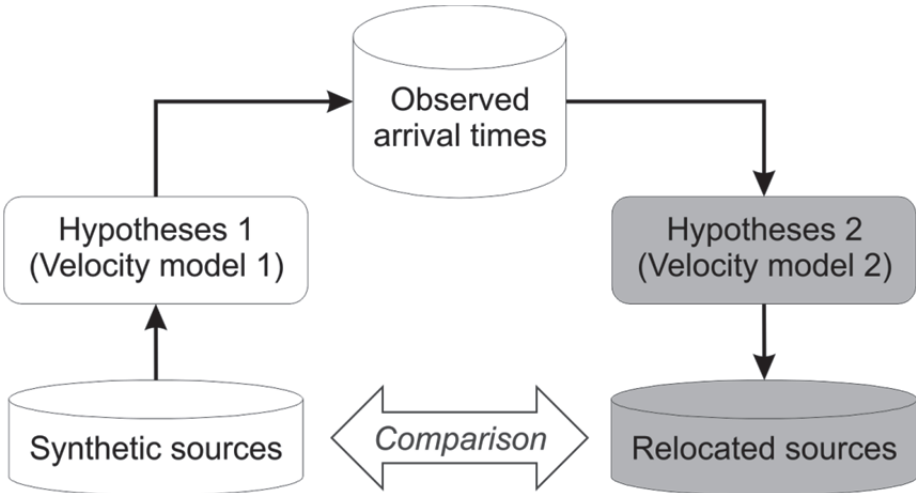


Figure 5-1: Schematic of the multi-step approach applied to model earthquake location errors.

In the synthetic modelling step, the sources are positioned in the sub-surface, where they are expected to occur within the reservoir. Then, the arrival times of the P- and S-waves corresponding to the synthetic sources and observed on the seismic network are computed in a given velocity model. This model is supposed to represent the reality of the seismic wave propagation in the Earth. Therefore, the associated travel times will be taken as the observed arrival times at the seismic network and used to relocate the synthetic earthquakes. As presented in detail in sub-section 5.4.2, several models will be simulated. Each model may represent a reality of the sub-surface associated with an *a priori* information. For the same reasons as described previously, the numerical code of Podvin and Lecomte (1991) is applied at this step to compute the seismic travel times.

The next step of the methodology consists in relocating the earthquakes from the synthetic arrival times, which were previously generated, by applying the NLL standard location code described in the previous sub-section. Therefore, it represents a real processing flow, especially as the initial hypotheses will be changed to mimic the intrinsic lack of knowledge of the reality. One unique velocity model will be used throughout the study to relocate the synthetic earthquakes. This model is a 1D depth-velocity model consisting of a series of horizontal layers of constant P- and S-wave velocities. Such a flat-layer model geometry is applied because it is used in a vast majority of real cases even at a local scale (e.g. Dorbath *et al.*, 2009; Bönnemann *et al.*, 2010; Maurer *et al.*, 2015). This is sometimes justified by the lack of information available to better characterize the sub-surface velocities, but it is also a convenient way to quickly obtain earthquake locations because these model geometries are easy to handle in linearized location numerical codes, especially in real-time processing software. This is precisely the effects of such simplifications that we want to quantify, especially when *a priori* information gives evidences that it may not apply.

Once the synthetic earthquake relocation is obtained, it is compared to the initial location to quantify the location error. In the error, we distinguish the location inaccuracy from the location uncertainty. The former is defined as the spatial distance separating the initial source hypocentre with the relocated one. The latter corresponds to the spatial domain delimited by the event relocation probability at the 68.3% confidence level. This level is chosen to allow comparison with the widely used standard deviation output by many location numerical codes.

## 5.3 Case study: Rittershoffen geothermal field

### 5.3.1 Geological settings

The about 300 km long Upper Rhine Graben (URG) is part of the European Cenozoic rift system, which extends over more than 1000 km in Central Europe (Ziegler, 1992; Schumacher, 2002). The deep geothermal field of Rittershoffen (Alsace, France) is located at the western margin of the NE-SW-striking central segment of the URG. The geological settings in Rittershoffen are rather comparable with those described for the geothermal field of Soultz-sous-Forêts (Dezayes *et al.*, 2011), which is located about 6 km to the NW (Figure 5-2). Polyphase reactivations of a complex pattern of Late Variscan and Permo-Carboniferous crustal discontinuities (Schumacher, 2002; Ziegler *et al.*, 2006) and intense Cenozoic faulting during evolution of the URG resulted in complex sub-surface structures. Hence, several graben and horst structures which dissect the approximately 2000-m thick Mesozoic and Cenozoic succession are delimited by synthetic and antithetic faults, predominantly N-S to NNE-SSW striking (Figure 5-3). The granitic basement is highly fractured and faulted and, at its uppermost part below the boundary to the overlying sediments, it shows distinct indications of alteration and probably represents a former erosional discordance (Genter, 1989). Sub-surface fluid flow along permeable fault zones under an extensional or transtensional stress state probably explains the occurrence of large scale convection cells and positive heat anomalies in the whole area (Pribnow and Schellschmidt, 2000; Baillieux *et al.*, 2013). Such anomalies contribute to the deep exploitation of this renewable energy resource in several active fields such as Landau, Insheim, Bruchsal (all in Germany) or Soultz-sous-Forêts (France) and furthermore highlight the geothermal potential in this part of the URG (Meixner *et al.*, 2016).

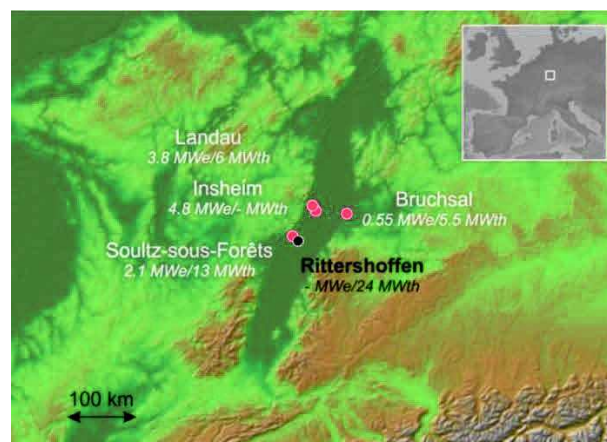


Figure 5-2: General view of the Upper Rhine Graben and of the deep geothermal fields (red circles) close to Rittershoffen (black circle).



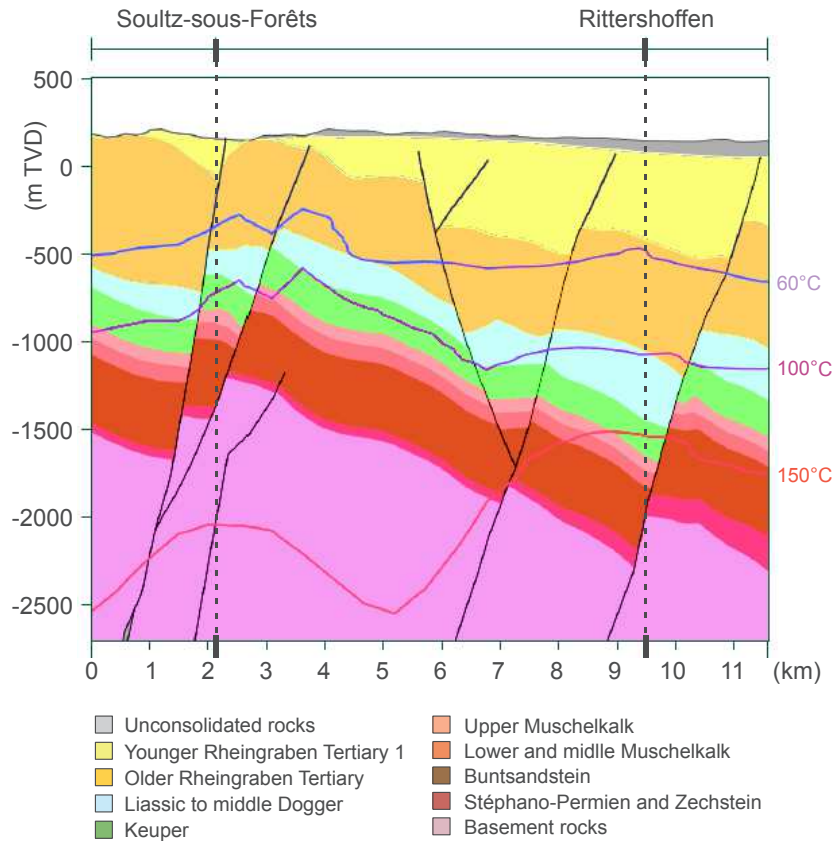


Figure 5-3: Vertical cross-section of the geological structure between Soultz-sous-Forêts and Rittershoffen geothermal fields. (Adapted from GeORG Project Team (2015)).

### 5.3.2 Field development and induced seismicity

Together with the acquisition of new geophysical data, the long hydrocarbon production history and the proximity of the Soultz-sous-Forêts EGS field contributed to the detailed characterization of the Rittershoffen sub-surface and the field development plan. The site benefits from one of the largest thermal gradient observed in the URG and temperatures of approximately 165°C were measured at 1800 m depth (Baujard *et al.*, 2014). Unlike the Soultz-sous-Forêts geothermal field, but like the Landau and the Insheim fields, the Triassic sandstone and the underlying Paleozoic granite constitute the exploited reservoir formations at Rittershoffen. To increase the chance to access permeable zones, the normal fault delimiting the two blocks below Rittershoffen was targeted by the geothermal doublet (Figure 5-3). This normal fault, which is approximately oriented N-S and dipping 60°W, accounts for approximately 200 m vertical shift. Both wells of the doublet are drilled down to ca. 2400 m mean-sea-level, that is 200 m below the Buntsandstein – granite interface.

To enhance the connectivity between GRT1 and the reservoir, several stimulations were carried out in 2013 (Baujard *et al.*, 2014). All stimulations induced seismicity which was

recorded by a surface seismic network. Several hundreds of events were detected and located, all with local magnitude smaller than  $M_L=1.6$  (Maurer *et al.*, 2015). Most of the seismicity is located in the south-west of GRT1 and centred close to the bottom of the hole at ca. 2500 m depth. The seismic cloud is roughly oriented N-S to NNE-SSW and is approximately 2 km long, 1 km wide and 2 km high (Maurer *et al.*, 2015).

Accordingly, to model the earthquake location errors, we will generally distribute the synthetic earthquake hypocentres in a cube of approximately 4 km side centred on the GRT1 open-hole mid-depth. The sources will be regularly spaced either in the 3D volume, or on several planes included in the volume (see grey boxes and segments in Figure 5-4). The detailed synthetic source positions will be presented in each of the examined scenarios.

### 5.3.3 Seismic monitoring network

The paper focuses on the period covering the chemical and mechanical stimulations of the well GRT1 which was carried out in June 2013 (Baujard *et al.*, 2014). The seismic network taken as reference for the location error analysis is made of 12 permanent and 5 temporary stations actively monitoring at that time (Maurer *et al.*, 2015). Among the 12 permanent stations, 7 have three-component short-period seismometers (L-4C-3D) and the remaining have a vertical short-period seismometer only (L-4C). The signal is sampled either at 100 Hz or at 150 Hz. All temporary stations have three-component short-period seismometers (L-4C-3D) whose signal is sampled at 300Hz. As shown in Figure 5-4, this network only covers the northern part of GRT1, and the associated effect on the earthquake location errors will be determined. Permitting issues prevented from deploying seismic stations in the southern part of GRT1 before the stimulation. Among the 17 active stations, the furthest two (GUNS and LAMP) are discarded from the analysis. According to N. Cuenot (pers. comm., 2015), the signal to noise ratio of the recorded induced seismicity at these stations was too low to enable body-wave picking and to include them in the location process. So, it was decided to keep the same assumption for the synthetic test. We further assumed that the synthetic P-wave arrival times could be used for all remaining 15 stations but that the S-wave arrivals could be used only for the 12 three-component stations. Hence, the P- and S-wave arrival times are always used in the (re)location process.

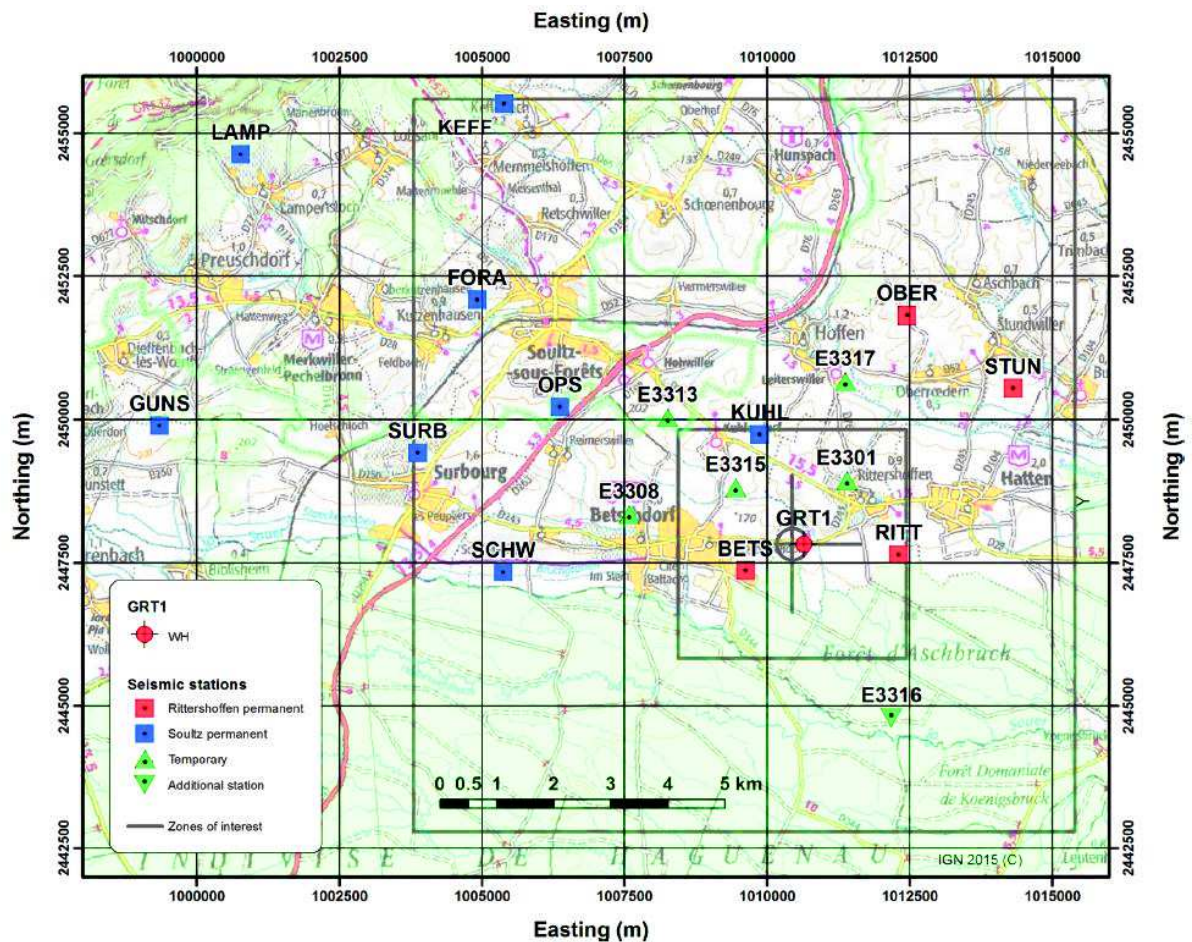


Figure 5-4: Map of the seismic network deployed at Rittershoffen. The Soultz-sous-Forêts permanent stations (blue squares), the Rittershoffen permanent stations (red squares) and the temporary stations (green triangles) are shown as well as GRT1 wellhead (red crossed circle). Station E3316 (reversed green triangle) was unavailable during the period of interest and is used only in sub-section 5.4.3. The largest rectangle delimits the velocity model zone used in this study. The smallest rectangle delimits the area in which the seismic sources are simulated; the two segments are the projections of the vertical sections of simulated sources. The projection of the zone with perturbed velocity (see sub-section 5.4.2.1) is shown as a grey circle. All coordinates are in Lambert II extended system.

This configuration did not change during the stimulation of GRT1 and is used over the whole study. However, more seismic stations were deployed afterwards and the effect of adding one surface station (E3316) in the southern part of the network (Figure 5-4) is discussed in the sub-section 5.4.3.

### 5.3.4 Seismic velocity model

At Rittershoffen, a 1D velocity-depth profile was created from several measurements taken in the well GRT1. This model, which was used to process the induced seismicity (Maurer *et al.*, 2015), is considered as the 1D reference model in the study and will always be used for relocating the synthetic sources. The P-wave interval velocities were computed from a zero offset VSP for the principal stratigraphic layers which were identified from the geological log

of the well (Aichholzer *et al.*, 2015). Then, using a compression- and shear-velocity log, the  $V_p/V_s$  ratio was averaged within each layer from a three-component sonic log performed in GRT-1 and applied to obtain the S-wave velocity profile. Figure 5-5 shows the P- and S-wave velocity profiles at Rittersshoffen.

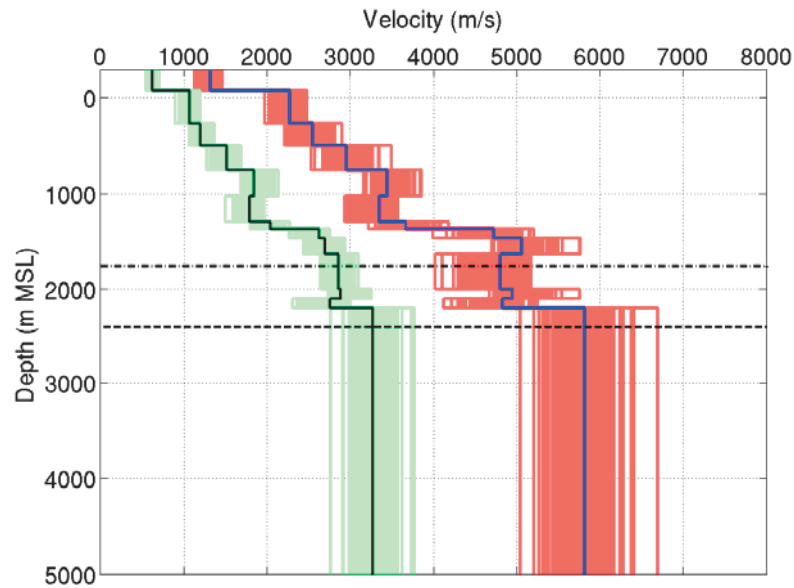


Figure 5-5: Profiles of the reference P-wave (blue curve) and S-wave (black curve) velocities at Rittersshoffen overlaying the 150 random profiles for the P-wave (red curves) and the S-wave (green curves) velocities (see sub-section 5.4.2.1 for details). The bottom depth of the well GRT1 (horizontal dashed line) and the upper depth of the injection zone (horizontal dotted-dashed line) are also shown.

Within this 13-layers model, the P-wave velocities range between 1320 m/s at surface and 5815 m/s in the granitic formation, and the S-wave velocities between 620 m/s at surface and 3275 m/s in the granitic formation. The  $V_p/V_s$  ratio varies between layers, from 1.68 to 2.12, the highest values being observed for the tertiary formations. Three embedded low-velocity layers exist for the depth intervals 1025 – 1300 m, 1630 – 2000 m and 2100 – 2200 m. Two large velocity contrasts are also observed at the top of the Lias layer (1365 m) and at the top of the granite (2200 m).

In the NLL location numerical code, this 1D velocity model is discretized on a 10-m mesh size in the East, North and depth directions.

## 5.4 Results and discussions

In this section, we present several scenarios applied to investigate the location uncertainties and inaccuracies, which could be expected at Rittersshoffen, based on the reference seismic network. Several effects are examined: first the seismic wave picking uncertainties and inaccuracies, and secondly the velocity model uncertainties and inaccuracies, for a few

realistic scenarios. For all scenarios, the reference 1D velocity model is used to relocate the synthetic earthquakes.

For clarity purpose, we used the GRT1 wellhead (1010653.18 m East, 2447831.75 m North, Lambert II extended) as the geographical origin for the latitude and longitude presentation of the results. Unless specified, the depth is a true vertical depth from mean-sea-level given in meter.

## 5.4.1 Location errors driven by the seismic onset time

### 5.4.1.1 Picking uncertainties

Earthquake hypocentre errors may be due to a variety of effects. First, the effect of the arrival time uncertainties on the amplitude and geometry of the hypocentre uncertainties, in the reference velocity model, using the reference seismic network, has to be quantified. Accordingly, the 1D-velocity model is used both for the synthetic modelling step and the relocation step. The only difference between both steps is the introduction of uncertainties in the synthetic arrival times. Consequently, no location inaccuracy is expected, which means that the hypocentre is positioned at the initial source location.

The P- and S-wave arrival times were given uncertainty values from manual picking of several seismograms observed by the network during the stimulation of GRT1 (N. Cuenot, pers. comm., 2015). For the 8 stations the closest to GRT1 (BETS, RITT, KUHL, E3301, E3308, E3313, E3315, E3317, see Figure 5-4), P- and S-picking uncertainties were set to  $\pm 20$  ms, and for the 7 remaining stations (FORA, KEFF, OBER, OPS, SCHW, STUN, SURB, see Figure 5-4), they were set to  $\pm 50$  ms. So, no picking uncertainty difference was noticed between the P- and the S-wave arrivals. These picking uncertainties constitute the matrix  $\mathbf{C}$  of eq. 1 and will apply in the rest of the study. The synthetic sources were placed every 200 m in the 3D cube centred at the bottom of the GRT1 well.

Figure 5-6 shows a 3D view of the relocation uncertainties at the 68.3% and 99.7% confidence levels, for a subset of 27 sources around GRT1 well separated by 1200 m. These levels are often used and correspond to one and three standard deviations respectively. As observed, most of the uncertainties at these confidence levels look ellipsoidal and their shape can be simply described by three orthogonal directions and three lengths (e.g. Lomax *et al.*, 2009). This also means that the uncertainties can be assumed Gaussian distributed around the highest probability location. To check whether the confidence ellipsoid quantifies correctly the uncertainties, we compared the hypocentre relocation with the expected location (i.e. the gravity centre of the distribution of all grid points included in the 68.3% confidence level, see

sub-section 5.2.1) for all synthetic sources, and we assumed that similar values were enough to validate the hypothesis. For 86% of the cases, the median and the 75% percentile of the location discrepancies are below the 10-m mesh size thereby negligible. However, median discrepancies up to 30 m (and 40 m for the third quartile) exist for sources located close to the large velocity contrasts at 1400 m and 2200 m depth, as could be expected (e.g. Lomax *et al.*, 2009). Increase of the distortion of the uncertainties from a Gaussian distribution is also observed when moving southward from GRT1, because the seismic network does not cover this zone. Hence, although we will assume in the following that the confidence ellipsoid of the location uncertainty is reliable in most of the volume below Rittershoffen, it is important to keep in mind that this is not correct close to the high velocity contrasts at 1400 m and 2200 m depth (Figure 5-5) and southward from GRT-1.

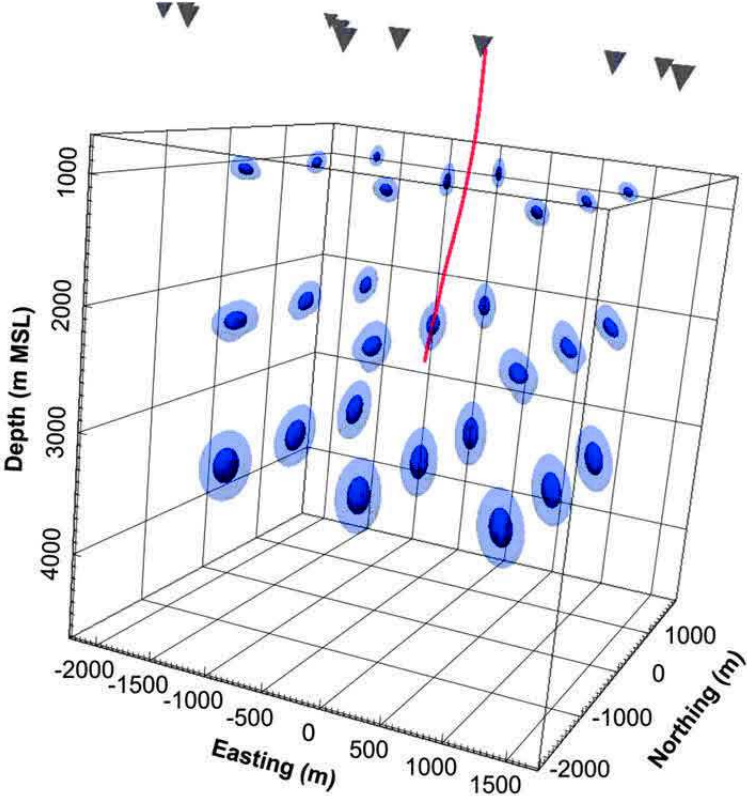


Figure 5-6: 3D view of the relocation uncertainties at 68.3% (dark blue) and 99.7% (light blue) confidence levels of 27 sources distributed around GRT1 well (red curve). Part of the seismic stations is also displayed (grey cones).

Figure 5-7 shows a horizontal section, at the bottom of the well GRT1 (2414 m), of the length of the largest axis of the 68.3% confidence ellipsoid. In the rest of the paper, this quantity will be associated with the location uncertainty. As observed, the uncertainty increases towards south and east of the GRT1 well. Such a horizontal variability is kept over depth (Figure 5-8 bottom).

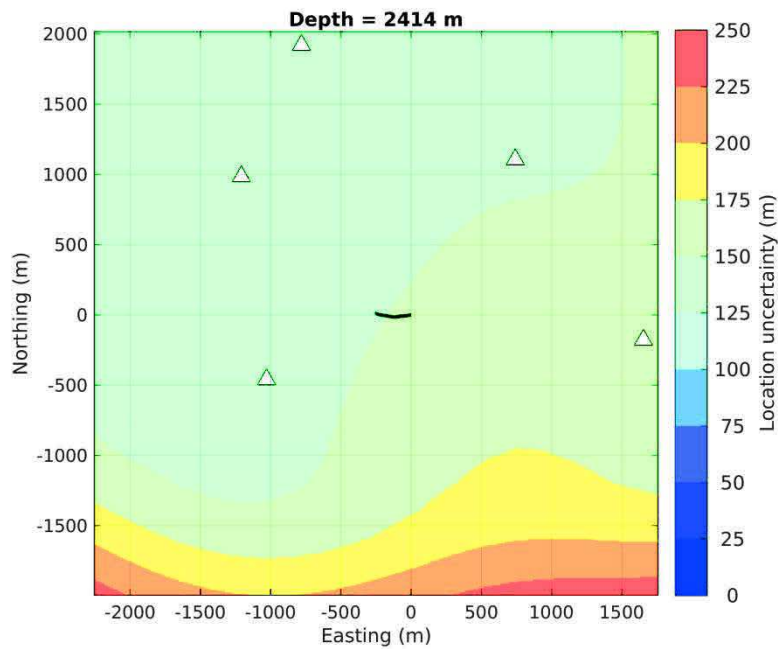


Figure 5-7: Horizontal section of the location uncertainty at 2414 m. The stations above the location zone are displayed (white triangles) as well as the GRT1 well trajectory (black curve).

Boxplots of the uncertainty variation as a function of latitude, longitude and depth (Figure 5-8) emphasize these spatial variations for the set of sources in the 3D volume. From a median value of 140 m north of GRT1, the uncertainty increases up to 190 m at 2 km south of GRT1. Uncertainty also slightly increases towards east: from 140 m to 150 m. However, as shown by the results as a function of depth, the uncertainty variations depend mainly on the earthquake depth. Starting from about 50 m 2 km above GRT1 bottom hole, the location uncertainties increase to 150 m at the top of the granite (at approximately 2500 m, close to GRT1 bottom hole) and then remain almost constant. At the depth of the stimulated zone (2089 m), the uncertainty represents about 6% of the distance to the surface. The orientation of the uncertainty is also anisotropic (but not shown). It roughly points towards the KUHL station, which is located about 4 km NNW from GRT1 well-head (see Figure 5-4), with an inclination between 40 and 45°. Consequently, for a given confidence level, the rough tendency for the hypocentre location is to either become deeper away from GRT1 or shallower closer to GRT1.

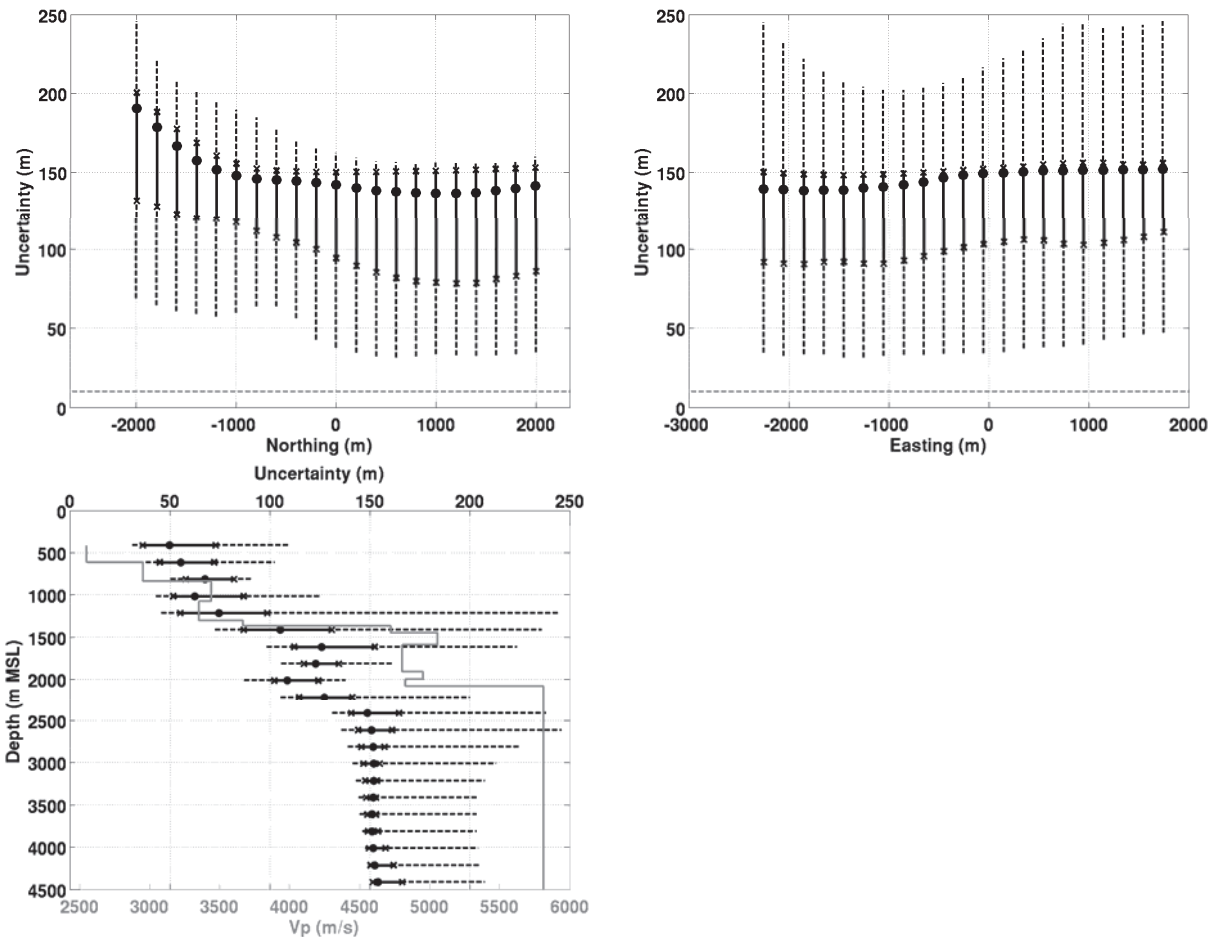


Figure 5-8: Boxplots of the location uncertainties as a function of latitude (top left), longitude (top right) and depth (bottom left). The uncertainties median (points), 25<sup>th</sup> and 75<sup>th</sup> percentiles (crosses), and range (dotted segment) are shown. The 10-m relocation-mesh size is displayed (grey dashed-line) as reference.

All seismic stations used for the analysis are located north of GRT1 or at similar longitude, with a higher station density in the western part of the investigated zone. Such a seismic coverage explains very well the spatial distribution of the uncertainties both in amplitude and direction. The uncertainty variation with depth is also consistent with the lack of down-hole station and with the strong velocity contrasts: the more south, and/or the more east and/or the deeper the earthquake sources are from the GRT1 well-head, the larger are the uncertainties.

To conclude, this analysis shows that even in the correct velocity model, with realistic picking uncertainties and with optimistic use of all 15 stations of the network, earthquake location uncertainties of minimum 150 m are to be expected in the granite (from 2400 m) and of approximately 50 m at 400 m depth.

#### 5.4.1.2 Picking precision

As mentioned previously, many linearized iterative algorithms work with initial seismic arrival times of 10 ms precision. We wish to investigate here whether or not what can be viewed as a random rounding of the arrival times at the stations plays a role in the hypocentre



inaccuracy, at the spatial scale of the Rittershoffen field (i.e. few kilometres on surface and a depth around 2.5 km).

To examine this effect, synthetic sources were placed every 200 m in the 3D cube centred at the mid-depth of the GRT1 open-hole section. Then, between the synthetic modelling step and the relocation step, nothing was changed but the P and S travel times which were rounded to the closest 10 ms.

The relocation of the synthetic sources using NLL leads to inaccuracies, which may exceed the 10-m relocation-mesh size. The larger inaccuracies are observed to the south and to the east of GRT1, as well as in depth and, therefore, have a distribution comparable to the one of the relocation uncertainties.

Figure 5-9 displays the horizontal, depth and total location inaccuracies as a function of the latitude. As observed, no relevant depth variation is observed since the median, 25<sup>th</sup> and 75<sup>th</sup> percentiles of the inaccuracies remain all within the relocation-mesh size (10 m). The median of the horizontal inaccuracy slightly decreases from South to North but is still smaller than 10 m. In fact, however, values larger than the mesh size are observed only when total inaccuracy is considered. Then, from approximately 12 m 2 km north of GRT1 the median inaccuracies increase to 15 m 2 km south of GRT1. The 75<sup>th</sup> percentile also increases from 15 m to 20 m. These largest values remain, however, relatively small; but, considering the range, distances between synthetic and relocated hypocentres may reach 45 m. Figure 5-9 also displays the variation of the location inaccuracies as a function of depth, independently from the latitude and longitude. Inaccuracies increase with depth and the median becomes larger than the mesh size below the first strong velocity contrast, at about 1400 m depth. The median inaccuracy can reach 18 m, 2 km below the GRT1 injection zone and the 75<sup>th</sup> percentile, 20 m.

When locating using only the P-wave arrival time, all other things remaining similar, the inaccuracies were multiplied by a factor of 2 to 3, the spatial distribution being unchanged.

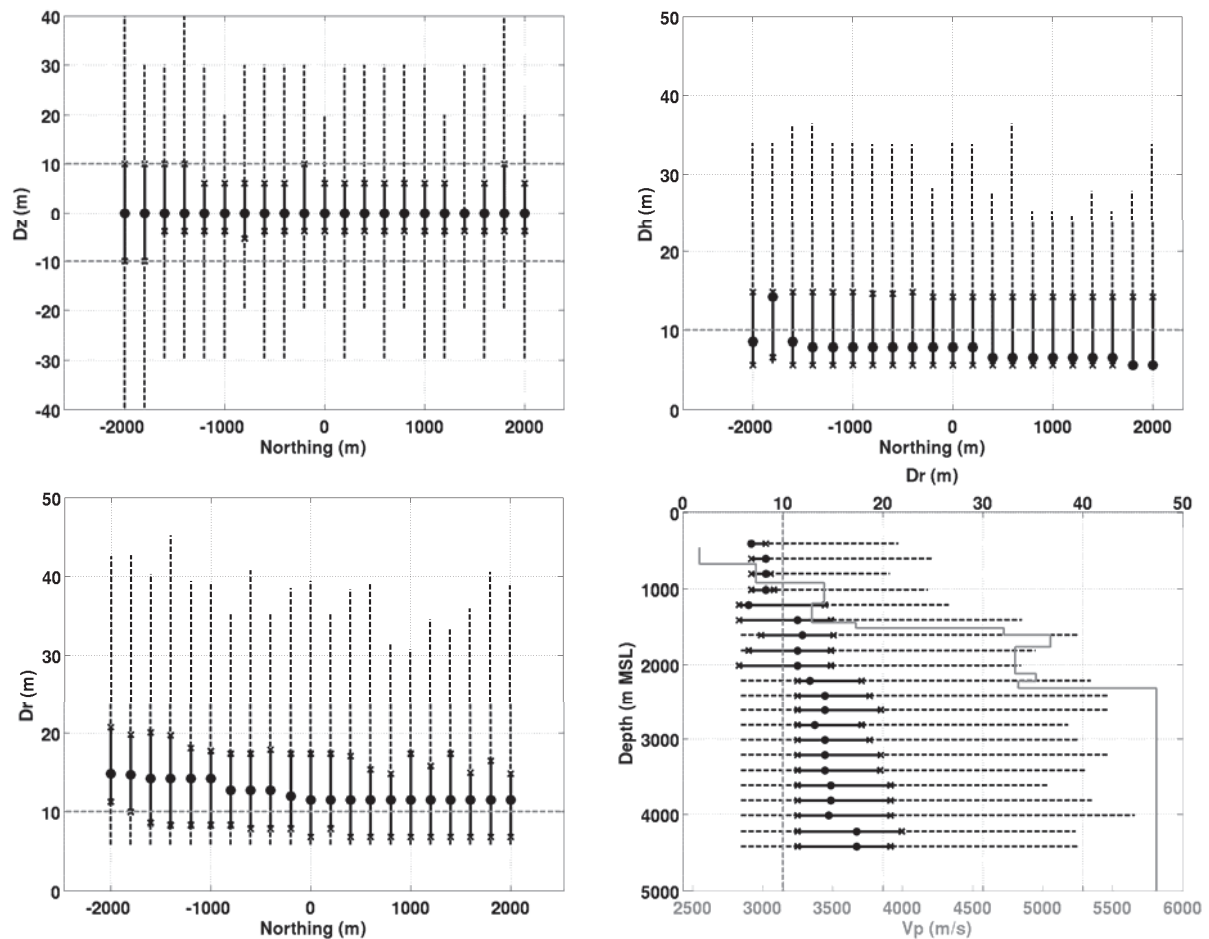


Figure 5-9: Boxplots of the depth (top-left), the horizontal (top-right) and the total (bottom left) location inaccuracies of the synthetic earthquakes as a function of the latitude, and location inaccuracies as a function of depth (bottom right). On this last subplot, the 1D velocity profile is shown in grey. The relocations were computed by NLL using the P- and S-waves arrivals rounded at the closest 10 ms. For details on the symbols see Figure 5-8.

To conclude, for the case of Rittershoffen, rounding the P- and S-wave arrival times at 10 ms can lead to inaccuracies of the order of 10 m to 20 m, with a maximum of 45 m. From 1400 m depth, the largest bias is approximately 40 m. The detailed study highlighted that despite relatively small, these inaccuracies are not isotropic, neither in depth nor in latitude. Their spatial distribution, which depends on the network coverage and on the velocity model, is similar to the distribution of the location uncertainties, which remain similar to those presented in the previous sub-section. As a consequence, the resulting location inaccuracies should be added to the location uncertainties rather than randomly included inside the location uncertainties (although the latter are larger). There is a cumulative effect in the location error due to the 10-ms picking accuracy.

## 5.4.2 Location errors driven by the velocity model

Velocity model errors lead to earthquake location inaccuracies, which may be so large that the true earthquake location may even not be included in the relocation uncertainties (Bardainne and Gaucher, 2010; Gesret *et al.*, 2015). Such an effect may be dramatic for interpretation when location uncertainty is mistaken for location error. In this sub-section, we model the effects induced by three different types of velocity uncertainties and inaccuracies which could be encountered at Rittershoffen. First, we introduce uncertainties in the original 1D velocity profile; second, the velocity model is perturbed in 3D around the stimulated zone; and third, a fault and its associated velocity shift are introduced leading to another 3D model. One after each other, these models will represent the real Earth in which the synthetic travel times will be calculated. However, in each case, the relocation will be computed in the initial 1D velocity model still considered as the reference (Figure 5-5).

### 5.4.2.1 1D velocity model uncertainty

The 1D velocity model proposed for Rittershoffen (see sub-section 5.3.4) is certainly not perfect beyond the hypothesis of the intrinsic lateral invariability. It has been created by merging information from the GRT1 Z-VSP for the P-wave velocity, and the GRT1 sonic log, for the  $V_p/V_s$  ratio, which are not error free measurements and which do not characterize the ground properties at similar spatial scale. In particular, the sonic log provides velocities which can differ from the Z-VSP and which deviate notably from their moving average over depth. To model the uncertainty in the 1D velocity profile, 150  $V_p$  and  $V_s$  profiles were generated by randomly drawing values of a Gaussian distribution with 5% standard deviation, centred on the original velocities (Figure 5-5). This 5% level is chosen because almost all velocity values measured by the sonic log fall within the interval defined by plus or minus three times this standard deviation. The random variations were taken independent per seismic phase and per layer (whose depth remained unchanged), but only those preserving the increase or the decrease of velocities between two layers were retained. The depths of the layers were kept unchanged because they are well constrained from the chrono-stratigraphic log of the GRT1 borehole (Aichholzer *et al.*, 2015).

Assuming that the numerous velocity profiles correctly sample the density distribution of the real Rittershoffen one, they can be used in a probabilistic framework to propagate the velocity model uncertainty to the earthquake location uncertainty (Gesret *et al.*, 2015). According to the Bayesian formalism developed by Gesret *et al.* (2015), the probability density distribution of the earthquake location is equal to the sum of the probability density distributions

computed within each velocity profile. In such a formalism, the propagation of the picking uncertainties (as per eq. 1) is also kept; hence, the final hypocentre location and its uncertainty depend on both the velocity and the picking uncertainties. This approach, in which the non-linearity of the location problem is kept, provides a final relocation uncertainty domain always including the real location.

In practice, the synthetic modelling step is carried out in each of the 150 perturbed velocity profiles (for the P- and S-waves) and the probability density function of the earthquake location computed within the initial 1D velocity profile using the grid-search algorithm of NLL. The maximum of the PDF resulting from their summation gives the hypocentre relocation and the 68.3% confidence level, their uncertainty. Two vertical planes of synthetic sources have been created, one in the N-S direction and one in the E-W direction, both crossing the bottom of GRT1 well. The N-S direction corresponds roughly to the direction of the initially located earthquakes in the area (Maurer *et al.*, 2015) and to the direction of the main horizontal stress (Cornet *et al.*, 2007). Each plane contains  $9 \times 9$  sources spaced by 300 m. During the relocation step, the reference seismic network and the P- and S-wave arrival times with their reference uncertainties are used.

Figure 5-10 gives a 3D view of the relocation uncertainties at 68.3% confidence level for each of the 81 sources of the E-W and N-S vertical planes. The associated volumes correspond roughly to ellipsoids in the granitic formation, deeper than 2200 m; however, this is less valid for the sedimentary cover in which several velocity contrasts exist and are potentially emphasized during the randomization process. Such an observation is consistent with the one made considering no velocity model variation (see sub-section 5.4.1) but the effect is strengthened. Nevertheless, to simplify the description of the location uncertainties due to velocity model uncertainties, we will suppose that the confidence ellipsoids are good enough representatives. The introduction of 5% uncertainty in the velocity model leads to larger variations of the earthquake hypocentre uncertainties compared to the fixed-model case. Location uncertainties up to 650 m are observed, which is more than 2.5 times larger (Figure 5-11) than the ones in sub-section 5.4.1.1. As previously observed, the deeper, the more east and the more south the events are of the well GRT1, the larger are the uncertainties.

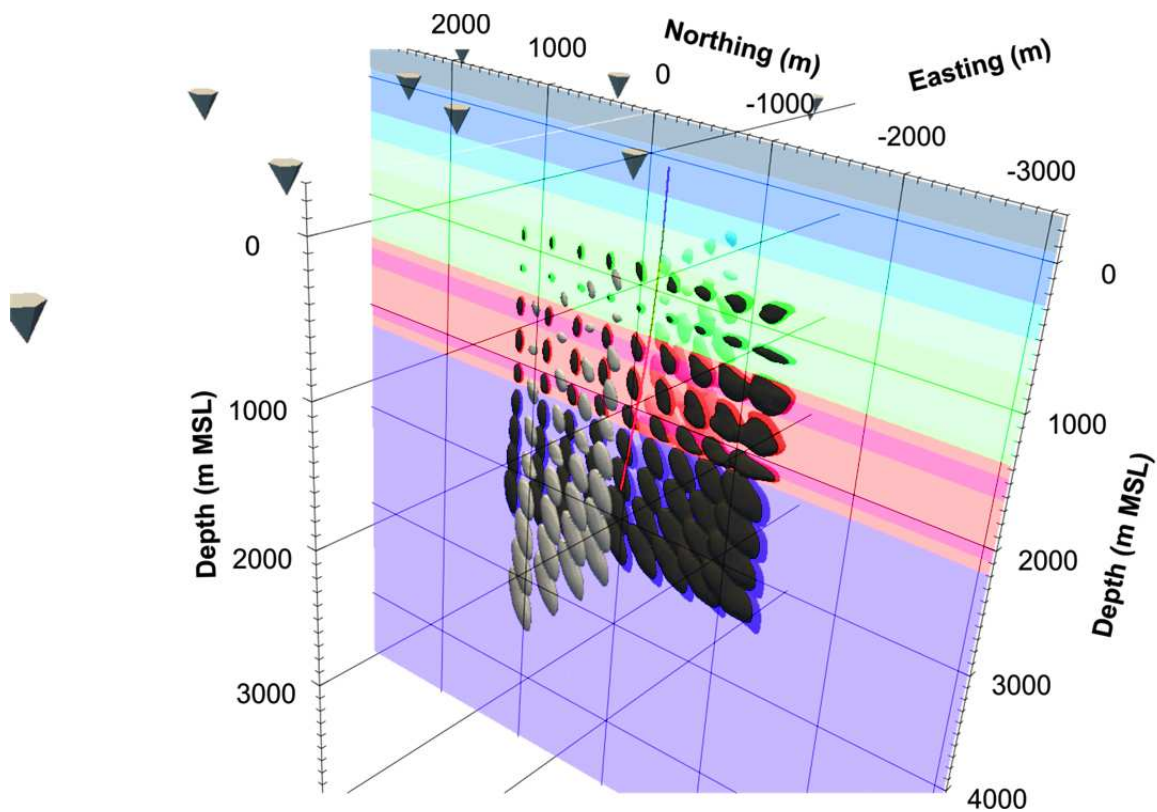


Figure 5-10: 3D view of the relocation uncertainties at 68.3% confidence levels for the 81 sources distributed every 300 m in the E-W vertical plane (light grey) and in the N-S vertical plane (dark grey) around GRT1 well (red curve). Part of the seismic stations is also displayed (grey cones) and the initial 1D velocity model is shown as a N-S vertical section.

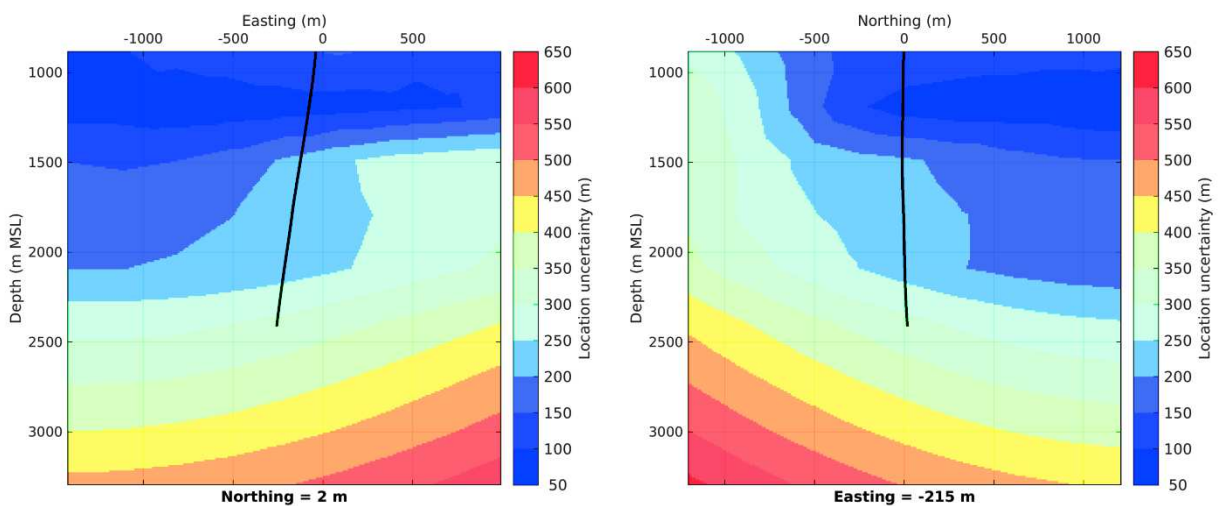


Figure 5-11: Vertical section at 2 m North (left) and 215 m West (right) of the largest location uncertainty interpolated on a 10-m mesh. The GRT1 well trajectory is displayed (black curve).

The perturbations of the initial 1D-velocity model also introduce inaccuracies of the hypocentre relocations. As a matter of fact, despite the initial model is randomly perturbed according to a Gaussian distribution, the non-linearity of the location problem with regards to the velocity models leads to hypocentre relocations different from the original locations. In the sediments, these inaccuracies (median value for the  $2 \times 81$  sources) are of the order of

10 m to 20 m but can reach 60 m in the granitic formation, and a maximum inaccuracy of 155 m is observed. In all of these cases, however, the inaccuracies are lower than the associated uncertainties. No systematic difference between the initial and the relocated hypocentres is observed along depth. However, it exists along the longitude and latitude and is, once again, spatially distributed like the uncertainties along these directions.

To conclude, Gaussian perturbation of the Rittershoffen initial velocity profile by 5% can lead to more than 250% increase of the location uncertainty and displacement of the original hypocentre. In the granitic formation, uncertainties in the range of 200 m to 650 m may be expected, which is not negligible with regards to the depth of the investigated zone: 2200 m to 3300 m.

#### **5.4.2.2 Local 3D perturbation of the initial velocity model**

In this second case, variation of the initial 1D velocity model is applied to the area around the injection zone of the GRT1 well. This zone may be seen as a volume in which the seismic velocity properties may change due to fluid injection. It is known that seismic velocities may differ between dry and fluid saturated rock samples, but also by varying the effective stress of rock samples (Spencer and Nur, 1976; Lockner *et al.*, 1977; Stanchits *et al.*, 2003). In the Soultz-sous-Forêts enhanced geothermal system, Calò *et al.* (2011) highlighted P-wave seismic velocity decreases of up to 10% during massive water injection, at 5 km depth, into the granite. This example illustrates our motivation to perform the present test and to quantify the effects of such localized variations on the seismic event absolute locations.

Therefore, over the 650 m depth interval of the GRT1 fluid injection and within a radius of 325 m around the well, the P- and S-wave velocities were decreased by a factor of 10%, whatever the geological formation was (granite, Buntsandstein and Muschelkalk). The velocity perturbed zone corresponds to a low-velocity cylinder embedded in the original 1D model and the velocity model representative of the real Earth becomes 3D. Synthetic sources are located on two vertical planes, which are crossing GRT1 at the average injection depth, one striking N-S and one striking E-W. The sources are distributed on a regular 40-m mesh including the perturbed zone and are relocated on a 20-m mesh.

Figure 5-12 shows the displacements of the earthquake locations induced by the use of the 1D velocity model instead of the perturbed 3D model. Both vertical planes are presented. As observed, the largest location inaccuracies occur in the depth range corresponding to the deeper half of the perturbed velocity zone, below the top of the granite. Moving away from the perturbed zone, the inaccuracies decrease. Events in the western part are located at the west of their initial position whereas events in the eastern part are located more to the East.

Similar relative behaviour exists for the events on the N-S vertical plane. Hence, earthquake relocations have a tendency to move away from their original locations relatively to the centre of the perturbed zone. We also observe higher inaccuracies in the eastern and southern parts than in the western and northern parts. All these effects can be well explained by the seismic coverage and the seismic ray bending, as for the earthquakes inaccuracies above the perturbed zone, which result from the propagation of refracted seismic waves in the inaccurate velocity model.

The median of the horizontal location inaccuracy can reach almost 40 m for the E-W plane (Figure 5-13), and is larger than 20 m (the relocation-mesh size) in the deeper half of the perturbed velocity zone. A maximum of 55 m horizontal shift is observed. For the N-S plane, the median is smaller but the largest uncertainty can reach 85 m. In most cases, the vertical inaccuracy is smaller than the horizontal one, whatever the vertical plane is, and in 50% of the cases they are not significant taking into account the mesh size. Locally, however, inaccuracies up to 75 m exist.

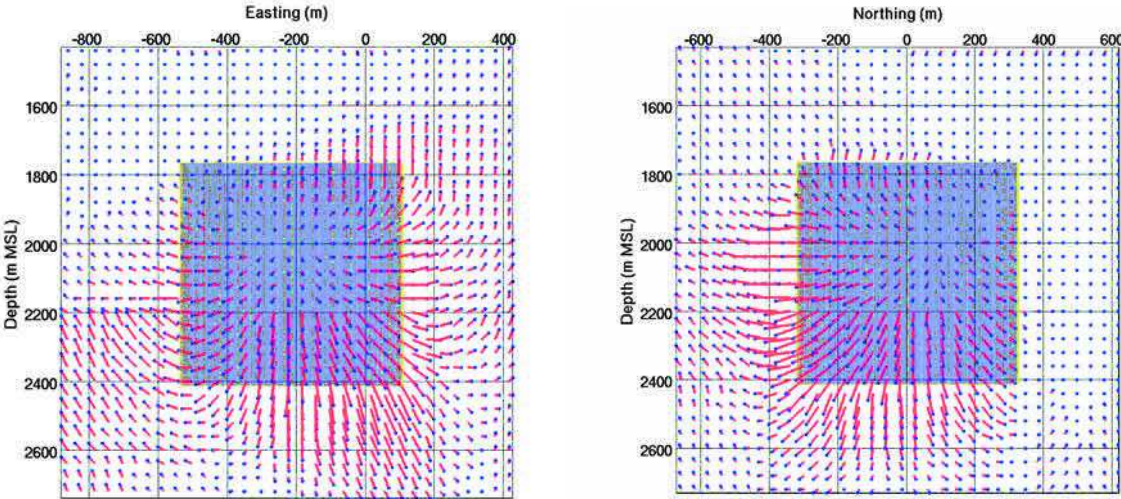


Figure 5-12: Projection of the initial locations and of the relocations of the synthetic earthquake hypocentres for the vertical E-W plane (left) and for the vertical N-S plane (right). The relocated hypocentres (blue points) should be shifted along the red line to come back to their initial location. The shadowed area represents the perturbed velocity zone.

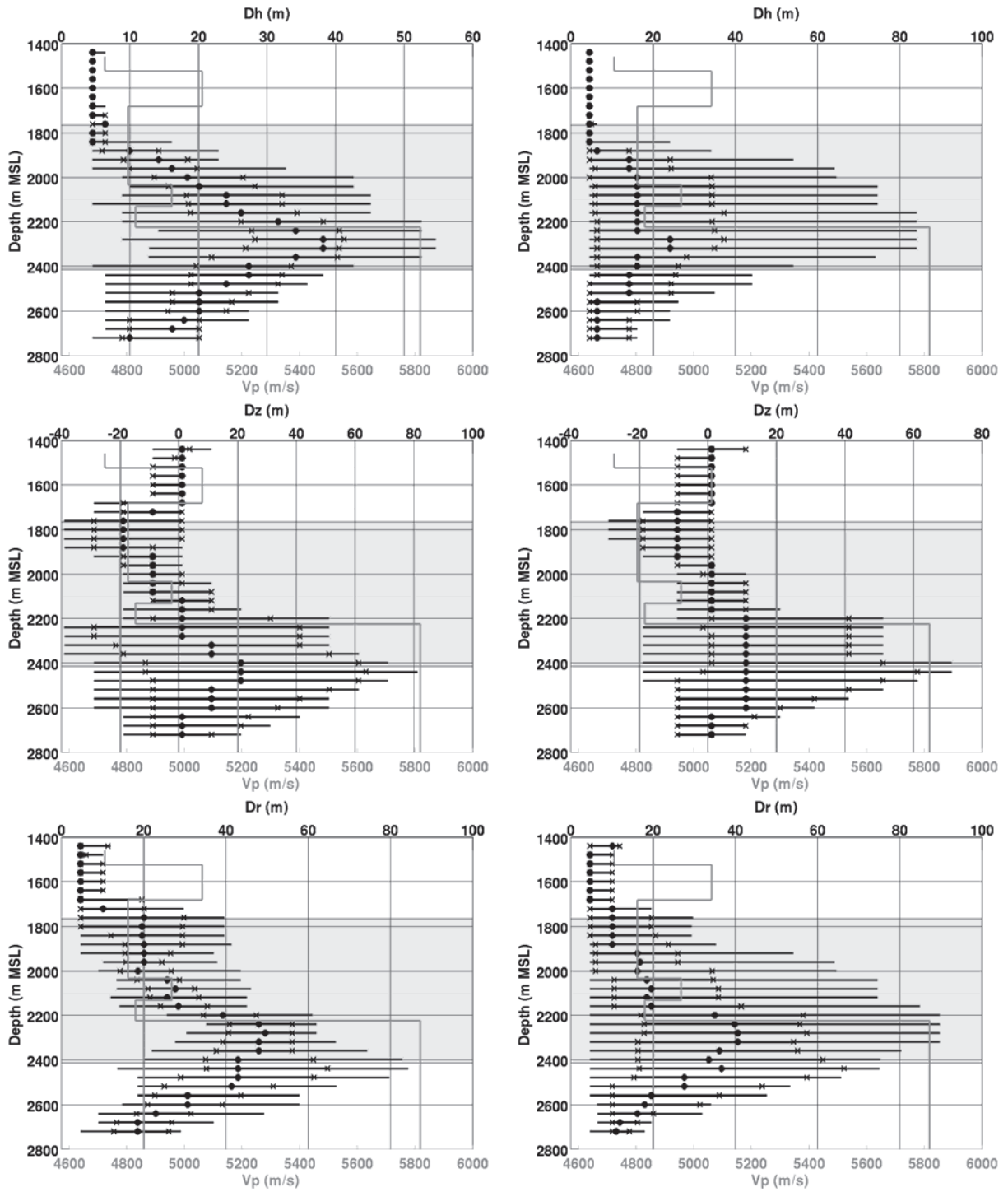


Figure 5-13: Boxplots of the relocation inaccuracies for the seismic sources located on the E-W vertical plane (left column) and on the N-S vertical plane (right column). The horizontal (top row), vertical (middle row) and total (bottom row) relocation inaccuracies as a function of the event depth are presented. The vertical grey lines at  $\pm 20$  m indicate the mesh-size of the relocation model, the 1D velocity profile is also displayed as a grey curve. For details on the symbols see Figure 5-8.

No significant differences are observed between the length and the orientation of the relocation uncertainties in this perturbed velocity test compared to the unperturbed velocity model (sub-section 5.4.1).



This test highlights that a decrease of 10% both in  $V_p$  and  $V_s$ , in a localized zone around the well GRT1, is difficult to detect from the absolute location of earthquakes. We stress here that we are only considering absolute locations and that further modelling should be carried out to quantify the effects associated with relative location techniques (outside the scope of this work). The resulting inaccuracies are one order of magnitude smaller than the location uncertainties and have no systematic trends which would notably change the shape of the vertical planes. Besides, the average P- and S-waves time residuals at the seismic stations after relocation in the perturbed model are all smaller than  $2 \text{ ms} \pm 4 \text{ ms}$ , for the events, on both planes. In other words, the time variations induced by the 10% velocity decrease inclusion would be very difficult if not impossible to detect using absolute location techniques because they are smaller than the picking uncertainties. Furthermore, because of their similar amplitudes, the inaccuracies induced by this local velocity decrease or by the use of 10 ms arrival-time precisions may be mistaken (see sub-section 5.4.1.2). Finally, since the average residuals are smaller than their associated uncertainties, it does not make any difference by applying the corresponding station corrections to improve the event relocations.

Testing a  $V_p$  and  $V_s$  decrease of 20% instead of 10% led to location inaccuracies distributed similarly but with larger amplitudes. Despite larger, the inaccuracies remain smaller than the location uncertainties and the time residual still smaller than the picking uncertainties. The effect of fluid injection on the decrease of the P- and S-wave velocities is generally not the same and may be associated with a reduction of the  $V_p/V_s$  ratio. Accordingly, we also tested 10% and 5% decreases of the P- and S-wave velocities respectively. This corresponds to approximately 5% decrease of the  $V_p/V_s$  ratio. In such a case, the location inaccuracies are very small and the median over depth remains almost smaller or of the order of the mesh. Consequently, the perturbed velocity zone associated with each of these configurations would also be undetected from absolute location of earthquakes.

#### **5.4.2.3 Geo-structural effect: 3D velocity model with a fault**

Heat exploitation at Rittershoffen was motivated by the presence of an unusual high temperature anomaly and a fault which could drive geothermal fluids (see sub-section 5.3.1, Figure 5-3). For these reasons, the well GRT1 was drilled to cross the major fault below surface. This fault separates, from the granitic formation up to the Tertiary formations, two blocks of the graben which are vertically shifted by 200 m. Consequently, although assuming a flat velocity model built from data acquired in the well GRT1 is locally representative, this is certainly not the case away from the well.

To investigate the effect of this structural setting on the earthquake locations, a 3D velocity model was built for Rittershoffen. A N-S fault dipping  $60^{\circ}$ W and crossing the well at 2200 m was included. According to the existing seismic profiles, this is an acceptable planar representation of the fault, which surface is obviously more complex. The initial 1D-velocity profile was kept for the western block of the fault but was shifted 200 m upward for the eastern block. So, the eastern block is on average faster than the western block.

Four planar surfaces with synthetic events were created. Two of them are vertical, one striking N-S the other one striking E-W, another one is horizontal, and the three of them cross GRT1 at 2089 m depth (injection range mid-depth). The last planar surface containing synthetic sources is the fault plane. For all planar surfaces, the synthetic sources are positioned on a 50-m squared mesh of 2400 m side length and centred on the injection point. As usual, to quantify the absolute location errors, the synthetic modelling was performed in the 3D velocity model and the relocation computed in the reference 1D velocity model.

On Figure 5-14, the four initial planar surfaces are displayed with the four associated surfaces obtained after hypocentre relocation. One can first note that, since the location inaccuracies are varying in direction and in amplitude, the initial planar surfaces become curved surfaces. The sources initially located on the fault (Figure 5-14, top) are systematically shifted towards East, slightly down and slightly southward for the sources located north of GRT1 well and northward for those located south of GRT1 well. This observation is consistent with the results obtained by Pavlis (1986) for a comparable simulation of a two-blocks velocity model in the Morgan Hill area (California). The median horizontal shift dominated by the eastern shift varies between 300 and 350 m. The median depth shift varies from 55 m for the deepest sources to 200 m for the shallowest. Despite these spatial inaccuracies, the average azimuth and dip of the relocated source surface are similar to the initial planar surface. However, a more complex transformation is observed for the three other surfaces of synthetic sources which are not parallel to the fault. In these cases, the initial planes are deformed in a continuous manner which depends on the initial source locations, but the fault plane and the associated block shift are neither delineated nor directly visible in the results. For the horizontal plane at 2089 m (Figure 5-14, top), with increasing Easting coordinate of the synthetic sources the eastern shift increases, and the initial southward shift becomes a northward shift. The eastern shift is however dominating and the median horizontal location inaccuracies vary from 250 to 350 m from the western to the eastern side of the plane (Figure 5-15). Still from West to East, the depth difference between the relocated and the initial sources decreases from 230 to -30 m (Figure 5-15), which means that, although the sources

are relocated deeper than expected on the western side of the plane, they are shallower on the eastern side. The sources of the E-W vertical plane (Figure 5-14, bottom) are relocated eastward from their original position with increasing shifts from the upper side of the original plane to the lower one. An original southward shift from the western side of the E-W plane becomes a northward shift at the eastern side of the plane. This change always occurs to the east of the modelled fault but for smaller easting coordinates as depth increases. The median of the horizontal inaccuracies ranges between 250 and 320 m. With regards to the depth, the relocated events are deeper and deeper than expected as a function of depth for the upper-western part of the plane but are shallower for the lower-eastern part (located to the east of the fault). Median depth inaccuracies range from -90 to 240 m. At last, the N-S vertical plane (Figure 5-14, bottom) moves eastward by a larger offset at depth. A southward-down shift from the upper-northern corner of the N-S plane becomes a northward-up shift at the lower-southern corner of the plane. Therefore, the median of the horizontal inaccuracies increases regularly with depth from 200 m in the sediments to 400 m in the granite and the vertical inaccuracies from -50 m in the bedrock to 230 m in the sediments (Figure 5-15).

To summarize the inaccuracy results, not considering the fault and the associated block shift leads to systematically locate the earthquakes eastward from expected when the 1D velocity model built from GRT1 well data is used. The offsets are in average close to 350 m. Moreover, the sources at the N-W-upper corner of the investigated zone are relocated deeper and more southward than originally but this tendency is reversed when considering sources located at the east of the fault. However, the fault position is not associated with a sharp variation of the location inaccuracies. In general, the inaccuracies are enhanced with the depth. Since the inaccuracies are variable in space, sources initially distributed on planar surfaces are relocated on curved surfaces. This means that planar features delineated by earthquakes are deformed. In other words, the azimuth and dip directions of such features are not kept constant (except for sources distributed on the fault).

Figure 5-14 also displays the location uncertainties associated with the relocated sources (colour scale of the planes). They range between 50 and 250 m and are bigger but still of the order of magnitude of the uncertainties observed in the original 1D velocity model, both in amplitude and in spatial distribution (see sub-section 5.4.1).

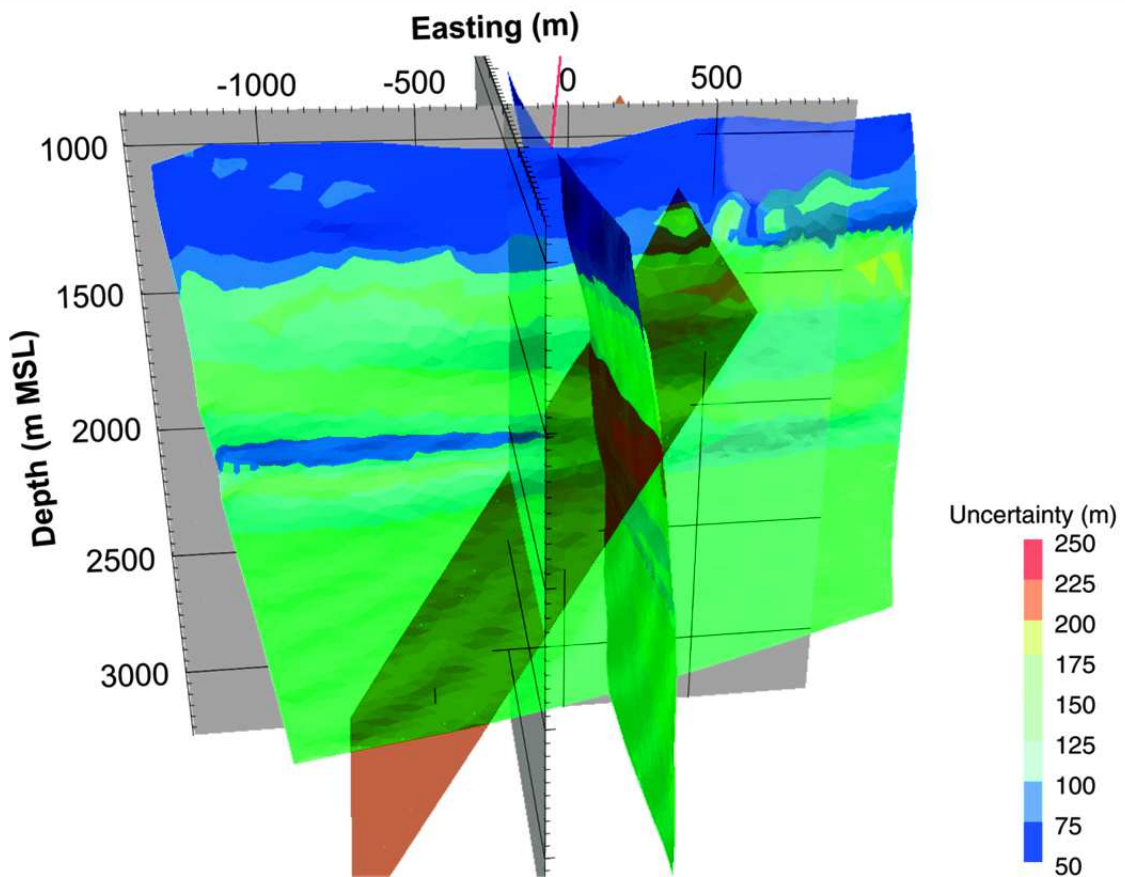
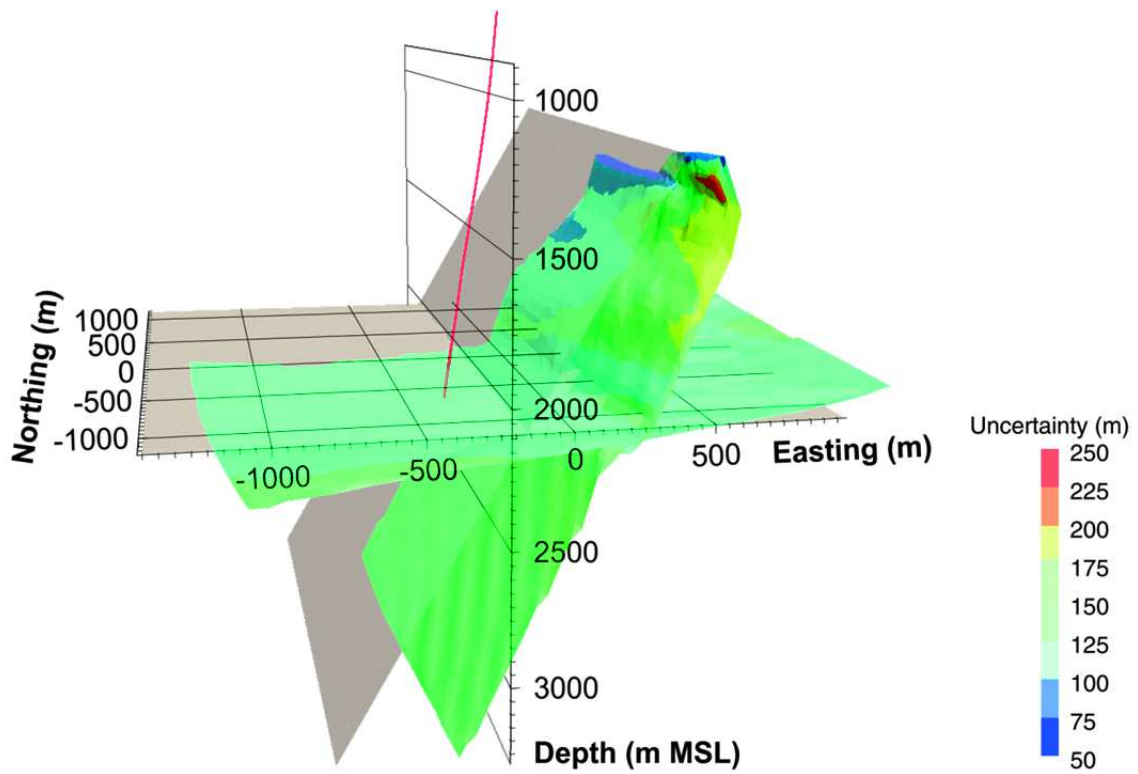


Figure 5-14: 3D view of the relocation of the synthetic events initially located on the horizontal plane and along the fault (top) and on the N-S and E-W vertical plane (bottom). The initial locations were on the grey planes whereas the relocations are on the coloured planes. The colour scale is associated with the largest uncertainty value which varies between 50 m and 250 m. The location of the fault is shown by the brown plane (bottom).

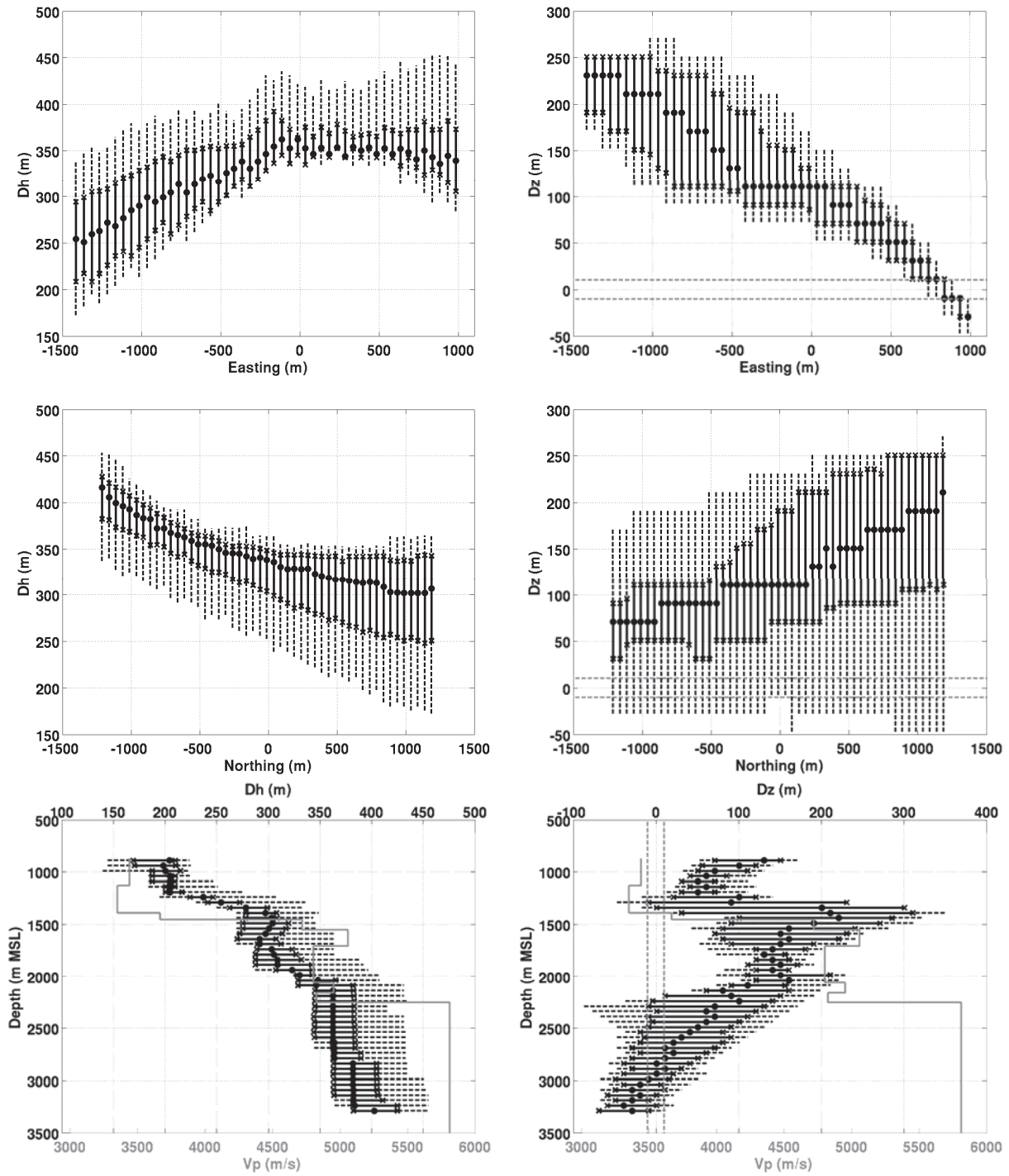


Figure 5-15: Boxplots of the horizontal (left column) and vertical (right column) inaccuracies for the horizontal plane along East (top row) and along North (middle row) and for the N-S vertical plane along depth (bottom row). For details on the symbols see Figure 5-8.

To conclude, this test clearly shows the very strong location bias induced by neglecting the fault and the associated shifted blocks at Rittershoffen for events initially located within a radius of at least 1200 m around the injection point. The location inaccuracies, of the order of 200 – 400 m, are larger than the location uncertainties which vary between 50 and 250 m. Consequently, they dominate and cannot be considered as included in the location

uncertainties. As shown, inaccuracy values and directions vary in space in a continuous manner although eastward shift is dominating. This prevents from applying a systematic and constant correction factor to the relocated hypocentres, although a westward shift of minimum 200 m could be used. This also makes difficult the delineation of the fault separating the two blocks. Moreover, expected delineation of seismic events in any direction or on any plane would be deformed in most cases and, as a consequence, spatial interpretation should be revised. This anisotropic bias is controlled by the fault geometry and the block shift as well as the coverage of the network.

This test shows that the reference 1D velocity model built from GRT1 well data is not representative of the 3D model with the fault and it quantifies the induced errors. It does not seek for the best 1D velocity model which would be representative of the 3D model with the fault; or, in other words, for the 1D velocity model minimizing the location errors. This work would imply a travel-time tomography which is a domain we do not consider here.

### **5.4.3 Addition of one surface station**

The previous discussions apply to the seismic network which was monitoring during the seismogenic phase of the GRT1 hydraulic stimulation. As shown, the network, which is mainly deployed North-West from the well, has a strong impact on the analysed earthquake hypocentre errors. Here, we shortly present and discuss the principal effects of adding one surface station.

To keep a realistic approach, the chosen supplementary station, E3316 (Figure 5-4), is taken from the temporary network installed after the stimulation of the GRT1 well and before the drilling of the GRT2 well. It is located in the forest, approximately 3 km SSE from the GRT1 well, on the eastern block delimited by the fault described in sub-section 5.4.2.3. Therefore, the seismic network coverage of the zone of interest is improved. All origins of location error investigated in the previous two sub-sections were also applied to this extended network and the processing flow remained the same. We focus, however, on the main results and their differences with those of the 15-station network.

At station E3316, the P- and S-picking uncertainties were set to  $\pm 20$  ms, like the other temporary stations. Following the approach described in sub-section 5.4.1.1, Figure 5-16 shows, as presented in Figure 5-7, a horizontal section of the location uncertainty, at 2414 m, driven by the picking uncertainties in the reference 1D velocity model. The section illustrates the general variation of the spatial distribution of the uncertainties which becomes more homogeneous horizontally; the depth distribution being still controlled by the layered velocity

model. Boxplot analysis of the uncertainties calculated in the volume delimited by  $\pm 2$  km around the well highlights a reduction of the location uncertainties, between the 16-station and the 15-station networks, which reaches approximately 20 m in the granite. These results show the interest of adding one surface station to diminish the location uncertainties and to get more uniform uncertainty distributions, at least horizontally. The other tested configurations, which are considering different velocity models between the synthetic modelling phase and the relocation phase, also agree with this conclusion.

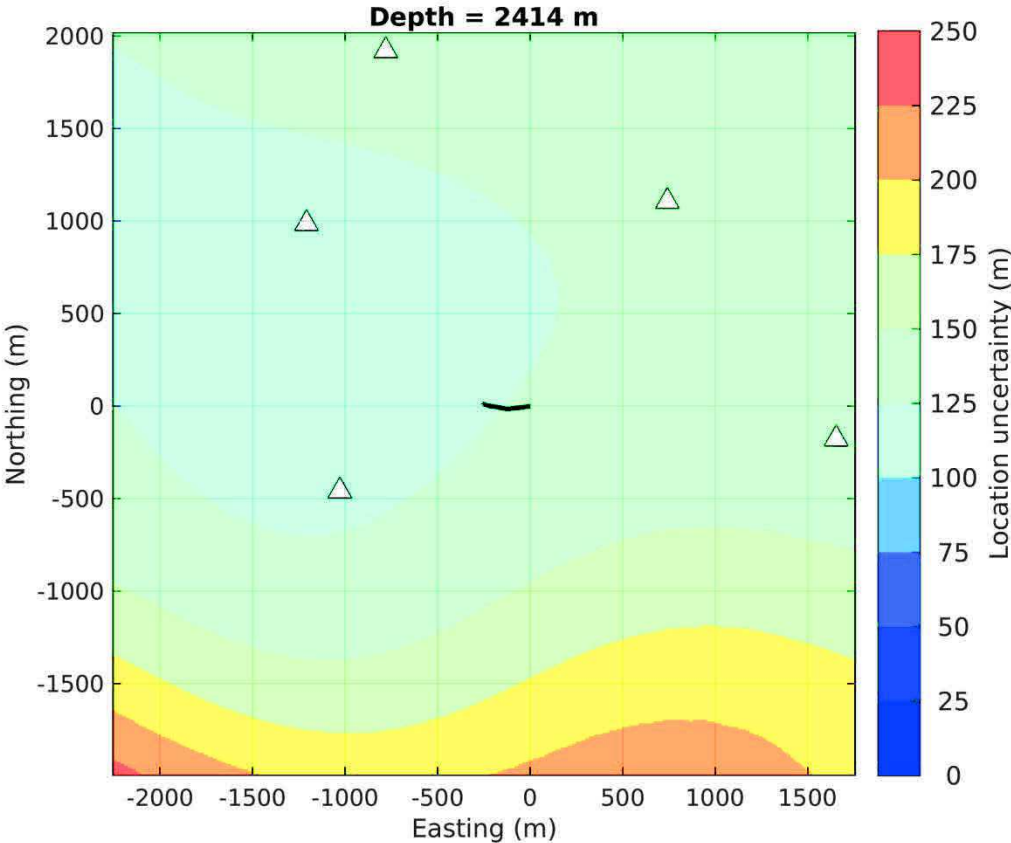


Figure 5-16: Horizontal section of the location uncertainty at 2414 m using the 16-station network. The stations above the location zone are displayed (white triangles) as well as the GRT1 well trajectory (black curve). Same display as Figure 5-7.

The addition of the station in the test investigating the effect of the 1D velocity model uncertainty (see sub-section 5.4.2.1) reduces the corresponding location inaccuracies by maximum 50 m, in the granitic formation. However, an opposite effect is observed when considering the 3D velocity model with the fault (see sub-section 5.4.2.3). In that case, an increase of the location inaccuracies is observed. Figure 5-17 presents 3D views of the relocation of the synthetic events initially located on the four tested source planes, with similar point of views and colour scale than in Figure 5-14. The median horizontal shift which

was ranging between 200 m and 350 m with the 15-station network is now ranging between 250 m and 425 m. Besides, the vertical median inaccuracies vary between -30 m and 275 m. So, the inaccuracies have increased and the planes are still distorted, thus preventing from direct interpretation of seismicity alignments in terms of location, azimuth and dip of major structures. This apparent contradictory behaviour between the impact of the 1D velocity model uncertainty and that of the model with the fault can be explained. In the latter case, the addition of the station E3316 located in the eastern block delimited by the fault is strongly in contradiction with the assumed 1D velocity model used to relocate the synthetic earthquakes. As a matter of fact the seismic ray paths between one event and the station E3316 will be very different in the 1D model and in the 3D model with the fault. Therefore, this station alone brings a lot of inconsistency in the (least-square) inverse problem since the associated seismic arrival times are outliers with regards to most of the other observed times. A more detailed study, outside the scope of this work, should be conducted to see if this effect may be counter balanced by adding more and more stations to the southern and eastern parts of the monitored area.



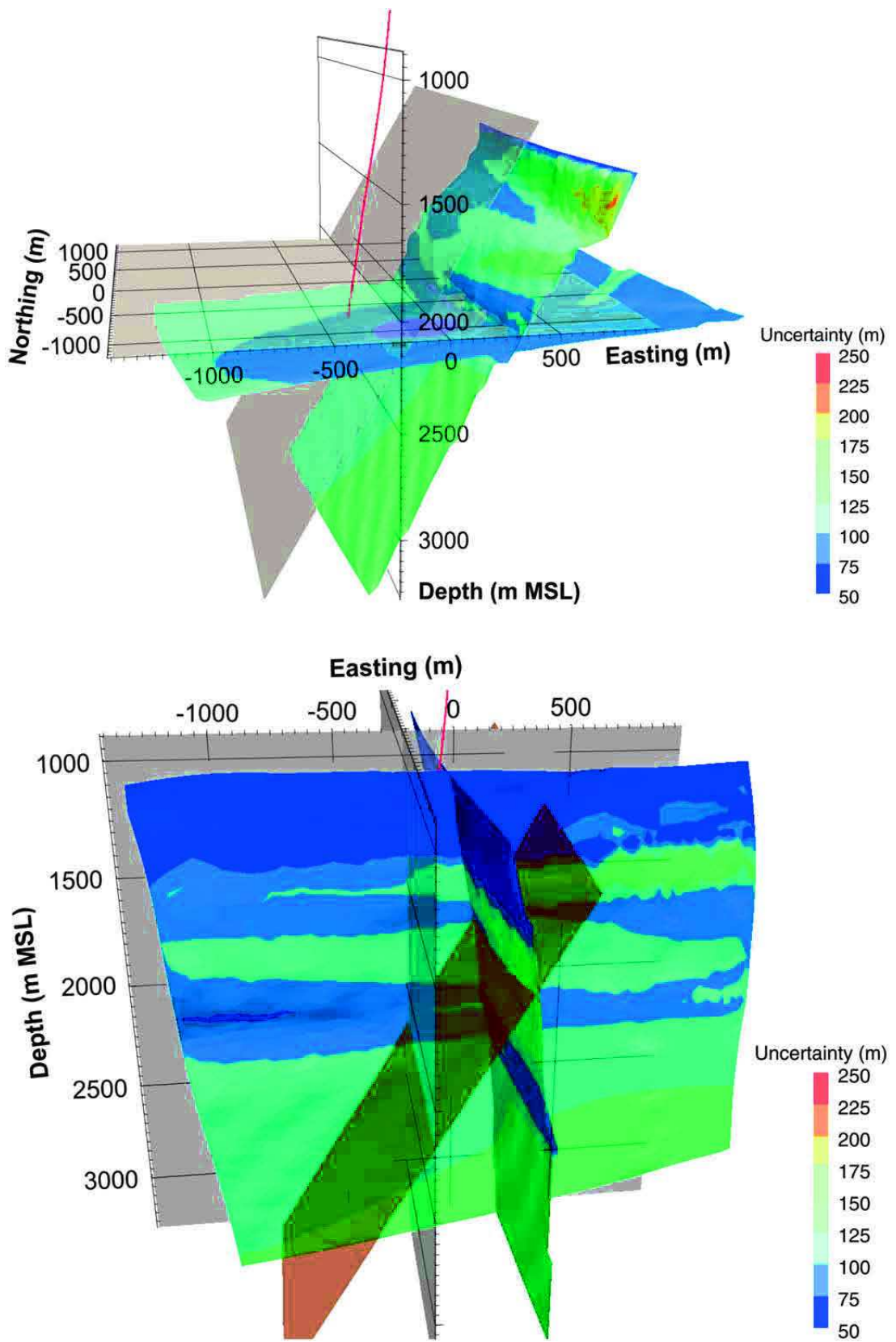


Figure 5-17: 3D view of the relocation, by the 16-station network, of the synthetic events initially located on the horizontal plane and along the fault (top) and on the N-S and E-W vertical plane (bottom). The initial locations were on the grey planes whereas the relocations are on the coloured planes. The colour scale is associated with the largest uncertainty value which varies between 50 m and 250 m. The location of the fault is shown by the brown plane (bottom). Same display as Figure 5-14.

## 5.5 Conclusions and outlook

In this paper, the impact of several factors on the absolute location of earthquakes in a reservoir was investigated. The methodology, which used state-of-the-art techniques, consisted in relocating synthetic hypocentres under hypotheses different from the data modelling step, and comparing the initial and relocated hypocentres. Hence, the effects of the P- and S-wave onset time uncertainties and inaccuracies were examined as well as the effects of the velocity model uncertainties and inaccuracies. In particular, we looked at the location errors driven by using a 1D velocity model instead of several 1D or 3D velocity models. The analysis was applied to the Rittershoffen geothermal field, where seismicity was induced between 1000 m and 5000 m, under the seismic monitoring conditions existing during the chemical and mechanical stimulations of the well GRT1. The 3D analysis of the location uncertainties and inaccuracies covers a zone of a couple of kilometres around the open-hole section of the well.

At Rittershoffen, in an ideal case where, firstly, a 1D velocity model is well representative of the propagation medium, and secondly, the P- and S-wave pickings and their uncertainties are representative of the recorded induced seismicity, the earthquakes location uncertainties will range between 50 m at 400 m depth and 150 m from 2400 m depth (in the granitic formation). The coverage of the seismic network, which is deployed in the north of the GRT1 well, controls the spatial distribution of the uncertainties in amplitude and direction. This layout leads to uncertainties roughly pointing towards the KUHL station, which is located about 4 km NNW from GRT1 well-head. Although a picking precision of 10 ms leads to inaccuracies smaller than the uncertainties, their similar spatial distribution have a cumulative effect and the location inaccuracy cannot be totally considered as contained in the uncertainty. Such an effect would be typical of the use of a location algorithm requiring 10 ms picking precision as input. The location errors driven by the hypotheses associated with the velocity model may be very large. As shown, only 5% uncertainty in the reference 1D velocity profile of Rittershoffen can multiply by a factor of 2.5 the uncertainties of the ideal case, thus leading to uncertainties up to 650 m in the granite at 3200 m. On the contrary, decreasing by 10% the P- and S-velocities in the neighbourhood of the GRT1 open-hole section has negligible effect and makes such a feature undetectable with an absolute location method. Not considering the Rittershoffen fault and the associated block shift in the velocity model induces very strong location biases, larger than the uncertainties. Although the reference 1D velocity model is based on well data and centred on the zone of interest, it is not a good representative of the 3D model with the fault and does not minimize the location errors. While the location

uncertainties range between 50 and 250 m, the expected sources are shifted by 200 to 400 m, mainly eastward. The location inaccuracies, however, vary continuously in space, thus making difficult any reliable interpretation of directions or surfaces delineated by the located seismicity.

As emphasized, the location errors driven by the velocity model may be dominating at the considered reservoir scale. This confirms the common sense which recommends using any *a priori* information to better constrain the initial velocity model or to define its uncertainties, which can be later integrated into the location uncertainty. The 3D analysis of the results highlighted that the location errors are neither aleatoric nor isotropic but clearly driven by the seismic network coverage and the velocity model. This suggests that although location inaccuracies may be smaller than location uncertainties, both quantities may have a cumulative effect.

The test consisting of adding one surface station to the network in an area so far uncovered by the seismic network showed that the location uncertainties are reduced, as may be expected. However, it also highlighted that the hypocentre inaccuracies can, on the contrary, increase due to the addition of inconsistency between the real Earth and its model. This underlines once more the distinction which must be made between imprecision and inaccuracy.

In this study, we did not perform an exhaustive analysis of all parameters which could influence the earthquake location at Rittershoffen. We focused on those which are usually not taken into account during standard location processing because they require synthetic modelling; in particular the discrepancies between the velocity model and the real seismic propagation medium. Moreover, we selected scenarios which looked the most relevant with regards to the *a priori* information available for Rittershoffen. To allow clear identification of each effect, the associated hypotheses for relocating the earthquakes were changed one by one. However, among numerous other options, it could be reasonable, for example, to jointly consider uncertainties of the 1D velocity profile and the inclusion of the fault. When studying the location errors driven by erroneous assumptions on the velocity models, we did not seek for a better velocity model which would minimize the location errors. This work, which would imply travel-time tomography, could constitute a future analysis.

For Rittershoffen, the quantitative results of this study can constitute an *a priori* knowledge useful for interpretation or processing of seismological data. Nearby geothermal fields such as Landau, Insheim, Bruchsal (all in Germany) or Soultz-sous-Forêts (France) have geological settings very similar to Rittershoffen geothermal reservoir. To some extent the present results can be used in these contexts, in particular at the Landau and the Insheim fields where

seismicity was induced and for which the Triassic sandstone and the Paleozoic granite also constitute the reservoir. At Soultz-sous-Forêts, the geothermal reservoirs were developed deeper into the granite (below 3500 m); however, major faults also delimit lifted blocks which lead to velocity contrasts in the 1400 m-thickness sedimentary cover. Several geothermal fields in the URG are currently under development or explored and can benefit from the present study. Since the described methodology is independent from the induced seismicity recorded at the site, it can also help in quantifying the location capabilities of a given network at a given site, even prior to the network deployment.

The earthquake hypocentre constitutes the primary attribute of a seismic event. Error of this attribute on the determination of secondary ones should be investigated in future works. The impact on the focal mechanisms, which are used to better describe the reservoir structure, is of special interest. Finally, the present work focused on quantifying errors of earthquake absolute locations. The extensive use of relative location methods to obtain earthquake hypocentres indicates that adapting and applying the developed methodology to this processing frame is necessary.

#### Acknowledgments

This work was conducted in the framework of the excellence laboratory “Labex G-EAU-THERMIE PROFONDE” (University of Strasbourg). It was funded by the French National Research Agency, as part of the French “Investments for the future” program, by the Energie Baden-Württemberg AG (EnBW), and by the French-German University (DFH-UFA). We wish to thank the ECOGI joint venture and the Électricité de Strasbourg – Géothermie company (ESG) for sharing data. We are grateful to V. Maurer, A. Genter and C. Baujard (ESG) for numerous discussions about this work, to N. Cuenot (EEIG “Heat Mining”) for sharing his experience on the Rittershoffen raw seismic data, and to J. Schmittbuhl (EOST, Strasbourg University/CNRS) for a fruitful review of an early version of the manuscript. The authors would like to thank F. Grigoli and T. Plenefisch for their valuable comments and suggestions for the improvement of the manuscript.

#### References

- Aichholzer, C., Düringer, P., Orciani, S. & Genter, A., 2015. New stratigraphic interpretation of the twenty-eight-year old GPK-1 geothermal well of Soultz-sous-Forêts (Upper Rhine Graben, France). in 4th European Geothermal Workshop, Strasbourg, France, Oct. 19-20.
- Baillieux, P., Schill, E., Edel, J.-B. & Mauri, G., 2013. Localization of temperature anomalies in the Upper Rhine Graben: insights from geophysics and neotectonic activity, *International Geology Review*, **55**(14), 1744-1762, doi: 10.1080/00206814.2013.794914.
- Bardainne, T. & Gaucher, E., 2010. Constrained tomography of realistic velocity models in microseismic monitoring using calibration shots, *Geophysical Prospecting*, **58**(5), 739-753, doi: 10.1111/j.1365-2478.2010.00912.x.
- Baujard, C., Genter, A., Maurer, V., Dalmais, E., Graff, J.-J. & Schmittbuhl, J., 2014. The ECOGI EGS project in Rittershoffen, France. in *GRC 38th annual meeting*, Portland, OR, USA, 28 Sep.-1 Oct.
- Bönnemann, C., Schmidt, B., Ritter, J., Gestermann, N., Plenefisch, T., Wegler, U., Schulz, R., Heidebach, O., Erbas, K., Baisch, S., Rother, E., Hauffe, P., Baumgärtner, J., Hettkamp, T., Rogulic, B., Teza, D., Baria, R., Fritschen, R., Pettitt, W. & Andrews, J., 2010. Das seismische Ereignis bei Landau vom 15. August 2009, in *Abschlussbericht der Expertengruppe „Seismisches Risiko bei hydrothermalen Geothermie“*, pp. 55, Hannover.
- Calò, M., Dorbath, C., Cornet, F.H. & Cuenot, N., 2011. Large-scale aseismic motion identified through 4-D P-wave tomography, *Geophysical Journal International*, **186**(3), 1295-1314, doi: 10.1111/j.1365-246X.2011.05108.x.

- Cornet, F.H., Bérard, T. & Bourouis, S., 2007. How close to failure is a granite rock mass at a 5 km depth?, *International Journal of Rock Mechanics and Mining Sciences*, **44**(1), 47-66, doi: 10.1016/j.ijrmms.2006.04.008.
- Dezayes, C., Beccaletto, L., Oliviero, G., Baillieux, P., Capar, L. & Schill, E., 2011. 3-D visualization of a fractured geothermal field: The example of the EGS Soultz site (Northern Upper Rhine Graben). in *36th Workshop on Geothermal Reservoir Engineering*, Stanford University, Stanford, California, Jan. 31 - Feb. 2, 2011.
- Dorbath, L., Cuenot, N., Genter, A. & Frogneux, M., 2009. Seismic response of the fractured and faulted granite of Soultz-sous-Forêts (France) to 5 km deep massive water injections, *Geophysical Journal International*, **177**(2), 653-675, doi: 10.1111/j.1365-246X.2009.04030.x.
- Drew, J., White, R.S., Tilmann, F. & Tarasewicz, J., 2013. Coalescence microseismic mapping, *Geophysical Journal International*, **195**(3), 1773-1785, doi: 10.1093/gji/ggt331.
- Edwards, B., Kraft, T., Cauzzi, C., Kästli, P. & Wiemer, S., 2015. Seismic monitoring and analysis of deep geothermal projects in St Gallen and Basel, Switzerland, *Geophysical Journal International*, **201**(2), 1022-1039, doi: 10.1093/gji/ggv059.
- Fréchet, J., 1985. Sismogénèse et doublets sismiques, Thèse d'État, Université J. Fourier, Grenoble.
- Frietsch, M., Groos, J. & Ritter, J.R., 2015. Detection and Delineation of a Fracture Zone with Observation of Seismic Shear Wave Anisotropy in the Upper Rhine Graben, SW Germany, *Pure and Applied Geophysics*, **172**(2), 267-282, doi: 10.1007/s00024-014-0899-3.
- Gaucher, E., Schoenball, M., Heidbach, O., Zang, A., Fokker, P.A., van Wees, J.-D. & Kohl, T., 2015a. Induced seismicity in geothermal reservoirs: A review of forecasting approaches, *Renewable and Sustainable Energy Reviews*, **52**(1473-1490), doi: 10.1016/j.rser.2015.08.026.
- Gaucher, E., Schoenball, M., Heidbach, O., Zang, A., Fokker, P.A., van Wees, J.-D. & Kohl, T., 2015b. Induced seismicity in geothermal reservoirs: Physical processes and key parameters. in *World Geothermal Congress*, Melbourne, Australia, 20-24 April 2015.
- GEISER, 2013. Geothermal Engineering Integrating Mitigation of Induced Seismicity in Reservoirs, Final Reports, <http://www.geiser-fp7.fr/ReferenceDocuments/Pages/ReferenceDocuments.aspx>.
- Genter, A., 1989. Géothermie Roches Chaudes Sèches: le granite de Soultz-sous-Forêts (Bas-Rhin, France), Université d'Orléans/BRGM, Orléans.
- GeORG Project Team, 2015. INTERREG IV Upper Rhine - Geopotentials of the deep Upper Rhine Graben, <http://maps.geopotenziale.eu/?app=georg&lang=en>.
- Gesret, A., Desassis, N., Noble, M., Romary, T. & Maisons, C., 2015. Propagation of the velocity model uncertainties to the seismic event location, *Geophysical Journal International*, **200**(1), 52-66, doi: 10.1093/gji/ggu374.
- Gharti, H.N., Oye, V., Roth, M. & Kuhn, D., 2010. Automated microearthquake location using envelope stacking and robust global optimization, *Geophysics*, **75**(4), MA27-MA46, doi: 10.1190/1.3432784.
- Grigoli, F., Cesca, S., Vassallo, M. & Dahm, T., 2013. Automated Seismic Event Location by Travel-Time Stacking: An Application to Mining Induced Seismicity, *Seismological Research Letters*, **84**(4), 666-677, doi: 10.1785/0220120191.
- Held, S., Genter, A., Kohl, T., Kölbl, T., Sausse, J. & Schoenball, M., 2014. Economic evaluation of geothermal reservoir performance through modeling the complexity of the operating EGS in Soultz-sous-Forêts, *Geothermics*, **51**(0), 270-280, doi: 10.1016/j.geothermics.2014.01.016.
- Husen, S. & Hardebeck, J.L., 2010. Earthquake location accuracy. in *Community Online Resource for Statistical Seismicity Analysis*.
- Husen, S., Kissling, E. & Deschanden, A., 2013. Induced seismicity during the construction of the Gotthard Base Tunnel, Switzerland: hypocenter locations and source dimensions, *Journal of Seismology*, **17**(1), 63-81, doi: 10.1007/s10950-012-9313-8.
- Kao, H. & Shan, S.-J., 2004. The Source-Scanning Algorithm: mapping the distribution of seismic sources in time and space, *Geophysical Journal International*, **157**(2), 589-594, doi: 10.1111/j.1365-246X.2004.02276.x.
- Klein, F.W., 1978. Hypocenter location program HYPOINVERSE. Part 1. User's guide to versions 1,2,3 and 4, in *U.S. Geological Survey, Open-file report 78-694*, pp. 113.
- Kraft, T. & Deichmann, N., 2014. High-precision relocation and focal mechanism of the injection-induced seismicity at the Basel EGS, *Geothermics*, **52**(0), 59-73, doi: 10.1016/j.geothermics.2014.05.014.
- Kwiatak, G., Plenkers, K., Nakatani, M., Yabe, Y., Dresen, G. & JAGUARS-Group, 2010. Frequency-Magnitude Characteristics Down to Magnitude -4.4 for Induced Seismicity Recorded at Mponeng Gold Mine, South Africa, *Bulletin of the Seismological Society of America*, **100**(3), 1165-1173, doi: 10.1785/0120090277.
- Lahr, J., C., 1999. HYPOELLIPSE: A Computer Program for Determining Local Earthquake Hypocentral Parameters, Magnitude, and First-Motion Pattern, in *U.S. Geological Survey, Open-File Report 99-23, Version 1.1*, pp. 119.
- Lay, C. & Wallace, T.C., 1995. *Modern Global Seismology*, edn, Vol., Academic Press, San Diego.

- Lee, W.H.K. & Lahr, J., C., 1975. HYPO71 (revised): a computer program for determining hypocenter, magnitude, and first motion patterns of local earthquakes, in *U.S. Geological Survey, Open-File Report 75-311*, pp. 116.
- Lee, W.H.K. & Stewart, S.W., 1981. *Principles and applications of microearthquake networks*, edn, Vol. Advances in Geophysics, Supplement No. 2, Academic Press, New York.
- Lengliné, O., Lamourette, L., Vivin, L., Cuenot, N. & Schmittbuhl, J., 2014. Fluid-induced earthquakes with variable stress drop, *Journal of Geophysical Research: Solid Earth*, 2014JB011282, doi: 10.1002/2014jb011282.
- Lockner, D.A., Walsh, J.B. & Byerlee, J.D., 1977. Changes in seismic velocity and attenuation during deformation of granite, *Journal of Geophysical Research*, **82**(33), 5374-5378, doi: 10.1029/JB082i033p05374.
- Lomax, A., Michelini, A. & Curtis, A., 2009. Earthquake location, direct, global-search methods, in *Encyclopedia of Complexity and Systems Science*, pp. 2449-2473, ed. Meyers, R. A. Springer New York, doi: 10.1007/978-0-387-30440-3\_150.
- Lomax, A., Virieux, J., Volant, P. & Berge-Thierry, C., 2000. 5 Probabilistic Earthquake Location in 3D and Layered Models, in *Advances in Seismic Event Location*, pp. 101-134, eds. Thurber, C. & Rabinowitz, N. Springer Netherlands, doi: 10.1007/978-94-015-9536-0\_5.
- Maurer, V., Cuenot, N., Gaucher, E., Grunberg, M., Vergne, J., Wodling, H., Lehujeur, M. & Schmittbuhl, J., 2015. Seismic monitoring of the Rittershoffen EGS project (Alsace, France). in *World Geothermal Congress*, Melbourne, Australia, 20-24 April 2015.
- Megies, T. & Wassermann, J., 2014. Microseismicity observed at a non-pressure-stimulated geothermal power plant, *Geothermics*, **52**(0), 36-49, doi: 10.1016/j.geothermics.2014.01.002.
- Meixner, J., Schill, E., Grimmer, J.C., Gaucher, E., Kohl, T. & Klingler, P., 2016. Structural control of geothermal reservoirs in extensional tectonic settings: An example from the Upper Rhine Graben, *Journal of Structural Geology*, **82**(1-15), doi: <http://dx.doi.org/10.1016/j.jsg.2015.11.003>.
- Moser, T.J., van Eck, T. & Nolet, G., 1992. Hypocenter determination in strongly heterogeneous Earth models using the shortest path method, *Journal of Geophysical Research: Solid Earth*, **97**(B5), 6563-6572, doi: 10.1029/91jb03176.
- Pavlis, G.L., 1986. Appraising earthquake hypocenter location errors: A complete, practical approach for single-event locations, *Bulletin of the Seismological Society of America*, **76**(6), 1699-1717.
- Pegler, G. & Das, S., 1998. An enhanced image of the Pamir-Hindu Kush seismic zone from relocated earthquake hypocentres, *Geophysical Journal International*, **134**(2), 573-595, doi: 10.1046/j.1365-246x.1998.00582.x.
- Plenkens, K., Kwiatek, G., Nakatani, M., Dresen, G. & Group, t.J., 2010. Observation of Seismic Events with Frequencies  $f > 25$  kHz at Mponeng Deep Gold Mine, South Africa, *Seismological Research Letters*, **81**(3), 467-479, doi: 10.1785/gssrl.81.3.467.
- Podvin, P. & Lecomte, I., 1991. Finite difference computation of traveltimes in very contrasted velocity models: a massively parallel approach and its associated tools, *Geophysical Journal International*, **105**(1), 271-284, doi: 10.1111/j.1365-246X.1991.tb03461.x.
- Poupinet, G., Fréchet, J., Ellsworth, W.L., Frémont, M.J. & Glangaud, F., 1985. Doublet analysis: improved accuracy for earthquake prediction studies, *Earthq. Predict. Res.*, **1**(147-159).
- Pribnow, D. & Schellschmidt, R., 2000. Thermal tracking of upper crustal fluid flow in the Rhine graben, *Geophysical Research Letters*, **27**(13), 1957-1960, doi: 10.1029/2000gl008494.
- Sausse, J., Dezayes, C., Dorbath, L., Genter, A. & Place, J., 2010. 3D model of fracture zones at Soultz-sous-Forêts based on geological data, image logs, induced microseismicity and vertical seismic profiles, *Comptes Rendus Geoscience*, **342**(7-8), 531-545, doi: 10.1016/j.crte.2010.01.011.
- Schumacher, M.E., 2002. Upper Rhine Graben: Role of preexisting structures during rift evolution, *Tectonics*, **21**(1), 6-1-6-17, doi: 10.1029/2001TC900022.
- Spencer, J.W. & Nur, A.M., 1976. The effects of pressure, temperature, and pore water on velocities in westerly granite, *Journal of Geophysical Research*, **81**(5), 899-904, doi: 10.1029/JB081i005p00899.
- Stanchits, S.A., Lockner, D.A. & Ponomarev, A.V., 2003. Anisotropic Changes in P-Wave Velocity and Attenuation during Deformation and Fluid Infiltration of Granite, *Bulletin of the Seismological Society of America*, **93**(4), 1803-1822, doi: 10.1785/0120020101.
- Tarantola, A., 2005. *Inverse problem theory and methods for model parameter estimation*, edn, Vol., Society for Industrial and Applied Mathematics, Philadelphia.
- Tarantola, A. & Valette, B., 1982. Inverse problems = quest for information, *Journal of Geophysics*, **50**(159-170).
- Waldhauser, F. & Ellsworth, W.L., 2000. A double-difference earthquake location algorithm: Method and application to the Northern Hayward fault, California, *Bulletin of the Seismological Society of America*, **90**(6), 1353-1368.
- Wittlinger, G., Herquel, G. & Nakache, T., 1993. Earthquake location in strongly heterogeneous media, *Geophysical Journal International*, **115**(3), 759-777, doi: 10.1111/j.1365-246X.1993.tb01491.x.

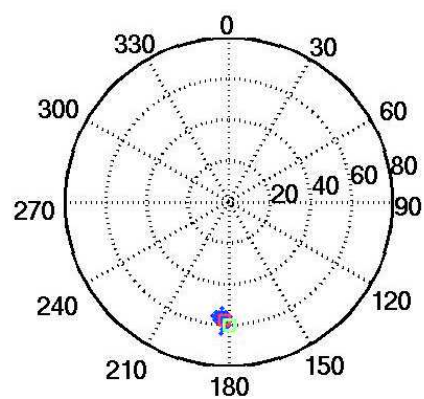
- Zang, A., Oye, V., Jousset, P., Deichmann, N., Gritto, R., McGarr, A., Majer, E. & Bruhn, D., 2014. Analysis of induced seismicity in geothermal reservoirs – An overview, *Geothermics*, **52**(0), 6-21, doi: 10.1016/j.geothermics.2014.06.005.
- Ziegler, P.A., 1992. European Cenozoic rift system, *Tectonophysics*, **208**(1–3), 91-111, doi: 10.1016/0040-1951(92)90338-7.
- Ziegler, P.A., Schumacher, M.E., Dèzes, P., Van Wees, J.-D. & Cloetingh, S., 2006. Post-Variscan evolution of the lithosphere in the area of the European Cenozoic Rift System, *Geological Society, London, Memoirs*, **32**(1), 97-112, doi: 10.1144/gsl.mem.2006.032.01.06.





## THIRD PART:

### Focal mechanism errors



Distribution of strike and dip angles of focal mechanisms calculated from observations from the complete network at Rittershoffen.

In this part, expected focal mechanism errors are calculated for different cases according to the Rittershoffen geothermal site and summarised in a paper (chapter 6). The effects on focal mechanism solutions of an incomplete seismic coverage as well as the effect of water injection are investigated.

# 6 Modelling focal mechanism errors of seismicity induced at Rittershoffen geothermal field (Alsace, France)

X. Kinnaert<sup>1,2\*</sup>, E. Gaucher<sup>1</sup>, T. Kohl<sup>1</sup> and U. Achauer<sup>2</sup>

<sup>1</sup> Karlsruhe Institute of Technology, Institute of Applied Geosciences, Geothermal Research, Karlsruhe, Germany

<sup>2</sup> EOST-IPGS UMR7516, Strasbourg, France

xavier.kinnaert@kit.edu

## Abstract

The determination of focal mechanisms of earthquakes induced in geothermal fields is of primary interest for reservoir characterization. For example, parameters like fault identification, faulting regime and stress field may be derived from it. The impact of a few parameters on the earthquake focal-mechanism determination is investigated using a three-step approach. First, synthetic waveforms are created for double-couple sources whose strike, dip and rake are consistent with the fault plane on which they are located. From the synthetic waveforms generated on the network, the polarity of P-waves and the amplitudes of P- and S-waves are measured to constitute the observed data. In the second step, the polarities and amplitude ratios are inverted to compute the focal mechanisms, once the earthquake was located. However, to represent the lack of knowledge or simplifications, the initial velocity model is replaced for this inversion. In the last step, the focal mechanisms obtained are compared with the original ones.

The method is applied to the deep geothermal site of Rittershoffen (France). In 2013, a massive water injection was performed at approximately 2.5 km depth to enhance the GRT1 well productivity. Induced seismicity was recorded by a surface network installed in several steps. After discussing the capabilities of the seismic network to estimate the focal mechanisms in a perfect case, we investigate the impact of approximating a 3D velocity model including a fault and a shifted block by a 1D velocity model. For each case, results using only polarities or polarities and amplitude ratios are compared.

The angular inaccuracies associated with the slip vector determination are usually smaller than the corresponding uncertainties or of the same order. The addition of amplitude ratios data only affect the focal mechanism of sources located in a low velocity zone and the impact of an incorrect velocity model can only be seen on focal mechanism uncertainties.

**Key words:** EGS, fault plane, inaccuracy, uncertainty, velocity model error

## 6.1 Introduction

In geothermal applications, the determination of focal mechanisms (FMs) of natural or induced earthquakes is of primary interest. This parameter may be used to identify and characterize active faults and fractures of the reservoir, and to build fracture networks (Koepke *et al.*, 2016). It is also of major interest for geomechanical interpretation and stress-field analysis (Schoenball *et al.*, 2014). The FM is a secondary attribute of an earthquake in the sense that it is usually determined once the earthquake hypocentre (the first attribute) has been located. Accordingly, FM determination is neither independent from the earthquake location nor from the errors in location. Hence, quantifying the error associated with the determination of FM is of interest to properly interpret the associated results..

The earthquake FM error can be described as the combination of the FM inaccuracy and the FM uncertainty. The FM uncertainties are directly linked to the uncertainties which are taken into account during the inversion process (Tarantola, 2005). Typically, *a priori* take-off angle or polarity uncertainties contribute to *a posteriori* FM uncertainties (Hardebeck and Shearer, 2002). On the other hand FM inaccuracies are commonly due to the lack of knowledge of the sub-surface or its simplification. For example, a bad location of the earthquake or/and a wrong velocity model would induce a wrong take-off angle which would lead to an incorrect slip vector (Hardebeck and Shearer, 2003). The quantification of FM uncertainties is nowadays common and several software can provide them (e.g. Hardebeck and Shearer, 2003; Snoke 2003). On the contrary, the quantification of the FM inaccuracy requires a special procedure.

This work focuses on the quantification of FM inaccuracies and uncertainties of earthquakes in the context of the Rittershoffen (France) deep geothermal field. It follows the study of Kinnaert *et al.* (2016) performed on the same site and dedicated to the quantification of errors of earthquake absolute location at this site. This work investigates the impact of velocity

model errors on the FM inaccuracies and uncertainties as well as their relationship with the seismic monitoring network design.

## 6.2 Methodology

To quantify the seismic event FM uncertainties and inaccuracies, a three-step method is applied. During the synthetic modelling step, seismic waveforms are created at the position of different seismic sensors for sources distributed on a plane and for a fixed double-couple FM. In this step, the assumptions are supposed to represent the reality of the sub-surface. The waveforms are computed using the finite-difference method of Virieux (1984; 1986) implemented in the SOFI3D software (Bohlen, 2002). Then, the polarities of the P-wave are determined directly from the waveforms associated with the vertical component of the sensors. On 3C-sensors, P- and S-wave amplitudes are determined in a window around the arrival as the maximum 3D-amplitude. The 3D-amplitude is defined as the square root of the sum of the squares of the amplitudes recorded by each component of the sensor. In the second step, the polarities and amplitude ratios obtained are considered as observations and are used to (re-)compute the FM of the synthetic seismic events. Nevertheless, the velocity model is changed compared to the model used during the synthetic modelling step, and different seismic network designs are also used. The FM determination is carried out by the HASH software (Hardebeck and Shearer, 2002; 2003) which uses a grid-search method over the strike, dip and rake angles defining the FM from modelled azimuth and take-off angles at the source focus. These later are obtained from the NonLinLoc package (Lomax, 2011), which is also used to relocate the earthquake in the changed velocity model (Kinnaert *et al.*, 2016). The HASH software has the advantage to provide uncertainties associated with the FM and to handle FM determination with or without observation of amplitude ratios. The uncertainties are given as two angles deviating from the slip vectors of the obtained fault plane and auxiliary plane of the best FM. The maximum angle is considered as the uncertainty. In the third and last step, the slip vectors of the obtained FMs are compared with those of the initial FM. The angle differences between the initial slip vectors and the computed ones (for the best FM) is calculated, and minimum difference is taken as the inaccuracy for each acceptable FM.

## 6.3 The Rittershoffen geothermal site

### 6.3.1 Geological settings

The Rittershoffen geothermal site is located in the Upper Rhine Graben (URG), in France. The geological and structural settings of the shallow sub-surface in the URG are well known due to earlier investigations from the oil industry (Schnaebele, 1948). Seismic profiles provided good knowledge of the sedimentary cover in the Rittershoffen area and highlighted numerous horst and grabens structures (Wentzel and Brun, 1991). The presence of fracture networks in the sub-surface and of thermal anomalies (Bailleux *et al.*, 2013) makes the URG a suitable place for geothermal development.

At Rittershoffen, the reservoir was developed at ~2500 m depth, at the interface between tertiary sediment layers and the granitic basement. The site benefits from one of the highest temperature gradient in the URG and the temperature reaches ~165°C at 1800 m depth (Baujard *et al.*, 2014). A major normal fault peculiar to the Rittershoffen geological structure was targeted by the two wells constituting the doublet. In the well GRT1, this fault is observed at a depth of ~2.4 km, 200 m deeper than the sediment/granite interface. The fault is oriented nearly NS, dips 60°W, and account for a vertical shift of 200 m.

### 6.3.2 Seismicity induced by GRT1 stimulation

In 2013, the well GRT1 was stimulated many times and induced several hundredths of unfelt micro-earthquakes all with local magnitude  $M_l < 1.6$  (Maurer *et al.*, 2015). The seismicity was recorded by surface seismic stations. It is located along a N-S to NNE-SSW direction within a zone extending 2 km to the north, 1 km to the east and 2 km in depth (Maurer *et al.*, 2015), and centred in the proximity of GRT1 bottom hole. The expected location errors for this seismic cloud were investigated using synthetic locations (Kinnaert *et al.*, 2016).

### 6.3.3 Velocity models

#### 6.3.3.1 1D velocity model

A 1D velocity profile was derived from different data measured in the well GRT1 at Rittershoffen (Figure 6-1). This model was used to process the induced seismicity and its errors (Maurer *et al.*, 2015; Kinnaert *et al.*, 2016). It will be considered here as the reference velocity model. In this layered model, the P-wave velocity ranges between 1320 m.s<sup>-1</sup> and

5815 m.s<sup>-1</sup>, the S-wave velocity varies between 620 m.s<sup>-1</sup> and 3275 m.s<sup>-1</sup>. The Vp/Vs ratio varies between 1.68 and 2.12. The profile presents three embedded low-velocity layers and two large velocity contrasts (at 1365 m and 2200 m corresponding to the Lias layer and the top of the granite respectively).

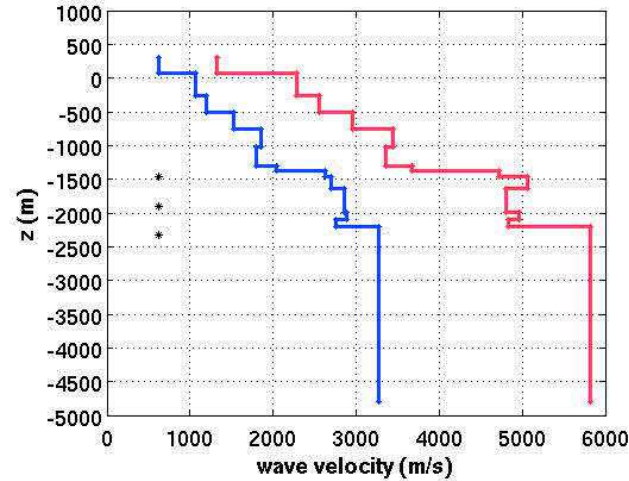


Figure 6-1: P- (red) and S- (blue) reference velocity profiles. The black stars indicate the depths of the synthetic sources.

### 6.3.3.2 3D velocity model

The major fault at Rittershoffen was targeted by the two wells of the geothermal doublet. It is oriented NS and is dipping 60° to the west. This is also a normal fault which exhibit 200 m vertical shift. Accordingly, we build a 3D-velocity model which consists in shifting the 1D-velocity profile along the fault. Hence, in the eastern block, the average velocity is higher than on the western block. This 3D model will be used as representative of the true Earth and was used in previous studies (Gaucher *et al.*, 2016; Kinnaert *et al.*, 2016).

### 6.3.4 Seismic monitoring networks

The earthquakes induced by the stimulation of the well GRT1 were recorded by 12 permanent and 5 temporary stations (Maurer *et al.*, 2015) (Figure 6-2). The 5 temporary stations have 3C-sensors and a sampling rate of 300 Hz. Among the permanent stations, sampling at 100 or 150 Hz, 7 have 3C-sensors whereas the others have only a vertical sensor. Among them, 2 stations were not used because the signal-to-noise ratio was too low to allow picking (N. Cuenot private communication, 2015). This network is called Net15 is the following. To increase the seismic network coverage, 24 temporary stations were installed before the drilling of the well GRT2. Their characteristics are similar to those of the 5 temporary sensors previously described. This larger network is called Net41 in the following.

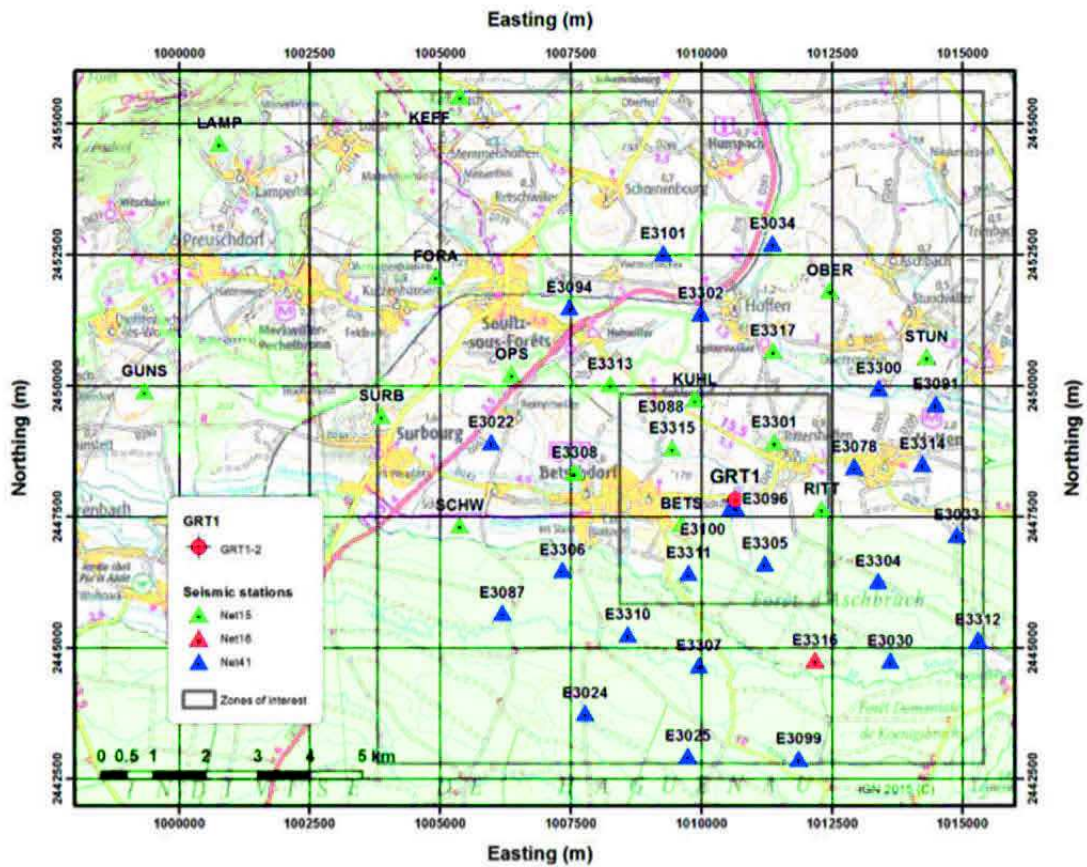


Figure 6-2: Geometry of the seismic networks monitoring seismicity at Rittershoffen geothermal field. The Net15 seismic network (green triangles) monitored the stimulations of GRT1 well in 2013. The Net16 network contains all stations from Net15 and an additional temporary station, E3316 (red triangle). The whole Net41 seismic network was installed before the drilling of GRT2 in 2014 and consists of the Net16 with the additional stations represented by blue triangles. The GRT1 well-head (red crossed circle), is also displayed. All coordinates are given in Lambert II extended system.

### 6.3.5 Synthetic event hypocentres

To investigate the FM errors, nine hypocentres were simulated on the fault plane which crosses the GRT1 well at 2089 m depth. Three by three sources are regularly distributed every 500 m in the north-south and along dip directions of the plane. Hence, the central source is located at the well and on the fault. With regards to the velocity model, the three deeper sources are located in the granite, the three intermediate sources in the low  $V_p$  velocity zone in the sediments, and the shallower sources close to the shallower high velocity contrast (Figure 6-1).



## 6.4 Results and Discussion

### 6.4.1 Reliability of the methodology

To test the methodology, we computed the FM of the central source using the denser seismic monitoring network, Net41, which has a good azimuthal coverage (see Figure 6-2), first in a homogeneous velocity model and in the reference 1D velocity model (Figure 6-3).

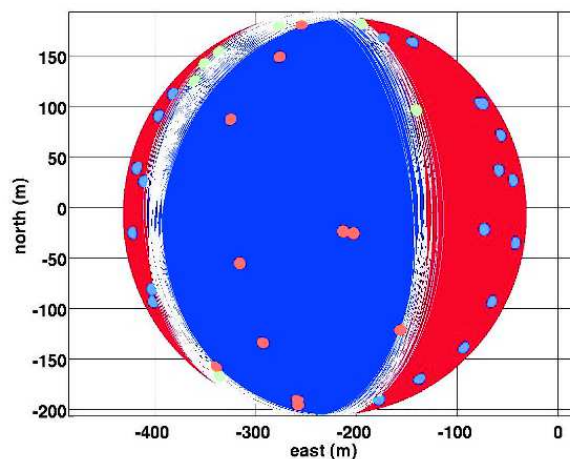


Figure 6-3: Upper view of the beachball of the best focal mechanism for the central source. Solution obtained in the 1D reference velocity model, from P-wave polarities on Net41. The white lines show all acceptable FMs. The circles show the polarities observed at the different seismic stations according to their azimuth and take-off angles: green for undetermined, blue for positive, orange for negative.

Neither in the homogeneous model nor in the reference 1D model do the inaccuracies exceed  $12^\circ$  from the expected normal faulting FM ( $180^\circ$  strike,  $60^\circ$  dip,  $-90^\circ$  rake). An inaccuracy of  $\sim 3^\circ$  is obtained for the best FM. The obtained uncertainty is around  $6^\circ$ . These results are the same considering the use of the polarities only or the polarities and amplitude ratios.

These tests prove the reliability of the proposed method which was then used for more complex studies.

### 6.4.2 Network effect in 3D velocity model

We investigate the effect of the lay-out of the seismic network which was monitoring the GRT1 stimulation, Net15, on the retrieval of the original FMs. This is of specific interest because there is a seismic coverage gap south of the well. To do so, we invert the FM in the 3D velocity model, which was also used to create the synthetic waveforms. Hence, the synthetic source location and take-off angle calculations were done in the 3D model. This

study provides the minimal FM errors which can be obtained at Rittershoffen during GRT1 stimulation.

Figure 6-4 shows the angular inaccuracy of the normal vectors of all acceptable FMs compared to the normal vector of the original FM as well as the angular inaccuracy of the mean normal vector.

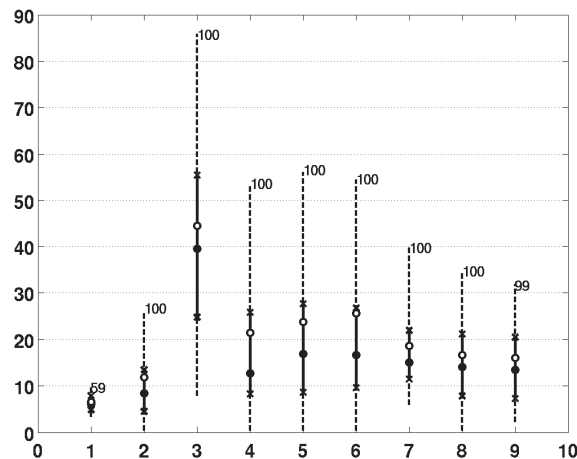


Figure 6-4: Boxplot representation (Tukey, 1977) of the angular inaccuracy (in degrees) of the slip vector of the acceptable focal mechanisms obtained using P-wave polarities measured on Net15. Each boxplot shows the inaccuracies for one source. The first three correspond to the shallowest sources and the last three to the deepest ones. For each triplet, the northern source is shown first. Each boxplot shows the median (full disk), the first and third quartiles (crosses) and the range (dashed line) of the angular discrepancies between both fault plane normals. The angular inaccuracy for the mean normal vector is shown by the unfilled disk and the number of FMs used to perform the statistics is written above each boxplot.

The angular inaccuracy of the mean vector varies between 5 and 45° (Figure 6-4). Apart from the shallowest-southern and the deepest-northern sources, the original solution always belongs to the range of possible solutions. Except for the shallowest-southern source, which shows the highest mean vector inaccuracy, 45°, all other sources have mean vector within ~25° from the original one. It seems that inaccuracies for the southern sources decrease with depth in values and in range. From ~45° for the shallowest source, the mean vector inaccuracy decreases to less than 30° at intermediate depth and to less than 20° for the deepest source. The maximum inaccuracy decreases from ~85° to ~35°. Apart from the shallowest-southern source, it looks like the angular inaccuracies are smaller for the deepest and the shallowest sources than for sources at intermediate depth.

One also has to mention that the inaccuracy associated with the mean normal vector usually do not fit with the median of the inaccuracies, the latter being always smaller. This means that the set of acceptable FMs are not equally distributed around that corresponding to the mean vector.

On the other hand, the inaccuracies associated with the strike, and dip angles defining the fault plane were studied separately for each acceptable FM of each source (Figure 6-5).

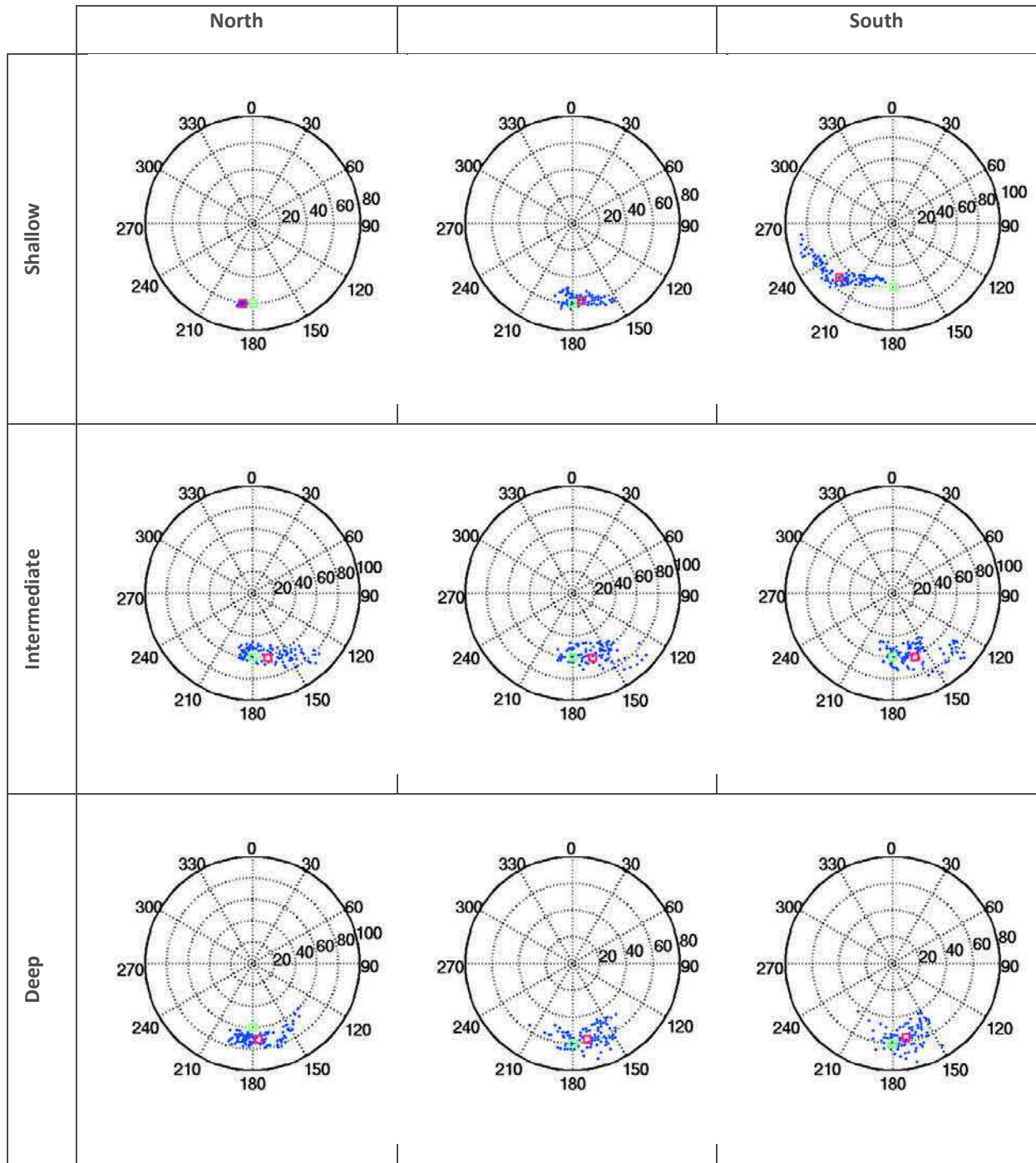


Figure 6-5: Polar representation of strike and dip angles for all acceptable FMs. The mean and the original fault plane solutions are represented by the red and green squares respectively. Rows of the table correspond to source depth whereas columns correspond to source latitude (north-left, south-right).

For seven cases over nine, the mean vector from all acceptable FMs and the vector associated with the original FM, the azimuthal inaccuracy is negative. The two exceptions are the northern and southern shallowest sources. This strike inaccuracy is usually in the range  $[-45^\circ, 30^\circ]$  with the major part of acceptable FMs in the interval  $[-30^\circ, 15^\circ]$ . Nevertheless, the set of

acceptable strikes vary according to the source location. However, no spatial and regular variation of the dip discrepancies as a function of the source location seems to appear.

To conclude, with the Net15, the same original fault plane could be interpreted as multiple plane solutions depending on the source location, if the focal mechanisms inaccuracies and uncertainties are not taken into account, and even in a correct velocity model.

### 6.4.3 Effect of a wrong velocity model

As shown by Kinnaert *et al.* (2016), locating in the 1D velocity model instead of locating in the 3D fault model (assuming the latter is representative of the true Earth) may lead to location inaccuracies up to 300-400 m. Here, we investigate the further impact these assumptions could bring into the FM determination.

For the modelling step, the 3D velocity model was taken as the reference and the waveforms and arrival times computed in it. Then, in the inversion step, the 1D velocity model was used first to relocate the sources, as proposed by Kinnaert *et al.* (2016), and to compute the azimuth and take-off angles from the computed hypocentre. Hence, the waveforms represent the reality of the sub-surface whereas the source locations and the emergence angles at the sources account for the bias introduced in the inverse problem.

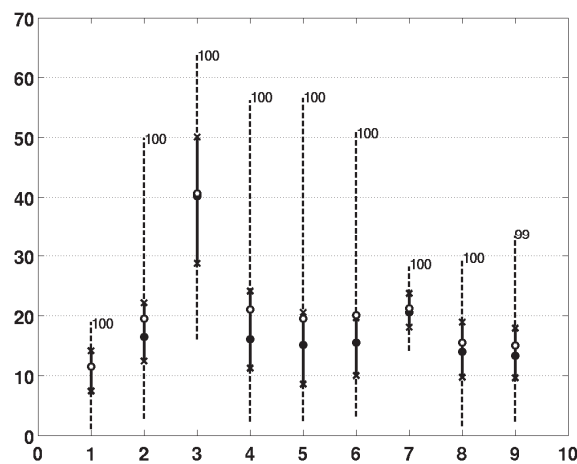


Figure 6-6: Angular inaccuracy (in degrees) of the slips of the acceptable fault plane solutions, which were determined by the P-wave polarities measured on Net15 in the 3D to 1D velocity model. See Figure 6-4 for symbol details.

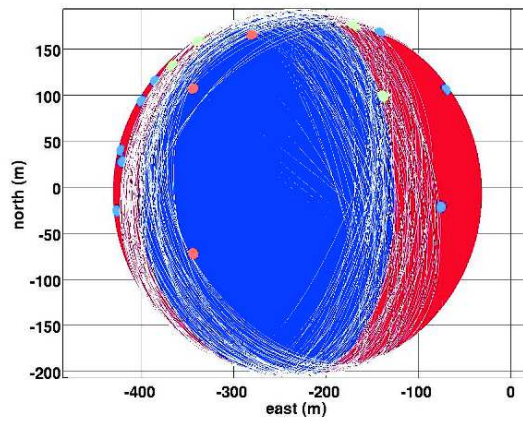


Figure 6-7: Upper view of the beachball of the best focal mechanism for the central source. Solution determined by the P-wave polarities and amplitude ratios measured on Net15 in the 3D to 1D velocity model. Same representation as in Figure 6-3

The results on angular inaccuracies are shown in Figure 6-6, for the case where only the P-wave polarities were used, and the focal mechanism obtained for the central source is represented in Figure 6-7, for the case where both the P-wave polarities and the amplitude ratios were used. The angular inaccuracies are not very different from the inaccuracies observed in the previous 3D model perfect case (Figure 6-6 vs Figure 6-4). One can however notice that the original fault plane is no more in the range of the possible solutions, for all considered sources. Furthermore, the inaccuracies of the two shallowest-northern sources are increased by about  $5^\circ$ .

## 6.5 Conclusion

In this paper, we mainly focused on the development of a technique to quantify focal mechanism uncertainties and inaccuracies at a geothermal reservoir scale. This technique was firstly validated on simple cases and then applied on a real case to study the impact of a velocity model simplification on focal mechanism determination.

Hence, it was shown that, at Rittershoffen geothermal field, the determination of the focal mechanisms for the seismicity induced during the GRT1 stimulation, may be inaccurate, in average, by  $5^\circ$  to  $45^\circ$  with uncertainties of around  $5^\circ$  to  $30^\circ$  if polarities are used and with uncertainties up to  $40^\circ$  when polarities and amplitude ratios are used. These effects are resulting from the finite coverage of the monitoring network only. In addition, assuming a 1D velocity model instead of the 3D fault model can lead to inaccuracies between  $10^\circ$  and  $40^\circ$  for the mean focal mechanism and uncertainties between  $10^\circ$  and  $35^\circ$ . These results suggest that, with the network monitoring during the GRT1 stimulation, multiple sources located on the same original fault plane could be interpreted as belonging to different ones according to their

determined FMs, especially if the focal mechanisms inaccuracies and uncertainties are not taken into account, and even in a correct velocity model.

## References

- Bailleux P., Schill E., Edel J.-B. and Mauri G. 2013. Localization of temperature anomalies in the Upper Rhine Graben: insights from geophysics and neotectonic activity. *International Geology Review* **55**.
- Baujard C., Villadangos G., Genter A., Graff J.-J., Schmittbuhl J. and Maurer V. 2014. The ECOGI geothermal project in the framework of a regional development of geothermal energy in the Upper Rhine Valley, 74<sup>th</sup> annual meeting of the German Geophysical Society (DGG), Karlsruhe, 10-13 March.
- Bohlen T. 2002. Parallel 3-D viscoelastic finite difference seismic modelling. *Computers & Geosciences* **28** (8), 887–899.
- Gaucher E., Kinnaert X., Achauer U. and Kohl T. (eds.). 2016. *Propagation of Velocity Model Errors in Earthquake Absolute Locations: Application to the Rittershoffen Geothermal Field*, 41<sup>st</sup> Workshop on Geothermal Reservoir Engineering, Stanford University, Stanford.
- Hardebeck J.L. and Shearer P.M. HASH: A FORTRAN Program for Computing Earthquake First-Motion Focal Mechanisms-v1.2-January 31, 2008.
- Hardebeck J.L. and Shearer P.M. 2002. A New Method for Determining First-Motion Focal Mechanisms. *Bulletin of the Seismological Society of America* **92** (6), 2264–2276.
- Hardebeck J.L. and Shearer P.M. 2003. Using S/P Amplitude Ratios to Constrain the Focal Mechanisms of Small Earthquakes. *Bulletin of the Seismological Society of America* **93** (6), 2434–2444.
- Kinnaert X., Gaucher E., Achauer U. and Kohl T. 2016. Modelling earthquake location errors at a reservoir scale: a case study in the Upper Rhine Graben. *Geophysical Journal International* **206** (2), 861–879.
- Koepke R., Gaucher E., Meixner J. and Kohl T. A method to interpret induced seismicity clouds as a fracture network. In: *EGC 2016, 19-23 septembre, Strasbourg*.
- Lomax A. 2011. *NonLinLoc: Probabilistic, Non-Linear, Global-Search Earthquake Location in 3D media*. ALomax Scientific.
- Maurer V., Cuenot N., Gaucher E., Grunberg M., Vergne J., Wodling H., Lehujuer M. and Schmittbuhl J. 2015. Seismic monitoring of the Rittershoffen EGS project (Alsace, France): World Geothermal Congress.
- Schnaebelen R. 1948. *Monographie géologique du champ pétrolifère de Pechelbronn*. Mémoire du Service de la Carte Géologique d'Alsace et de Lorraine.
- Schoenball M., Dorbath L., Gaucher E., Wellmann J.F. and Kohl T. 2014. Change of stress regime during geothermal reservoir stimulation. *Geophysical Research Letters* **41** (4), 1163–1170.
- Snoke J.A. 2003. FOCMEC: focal mechanism determinations. *International Handbook of Earthquake and Engineering Seismology* **85**.
- Tarantola A. (ed.). 2005. *Inverse problem theory and methods for model parameter estimation*. Society for Industrial and Applied Mathematics.
- Tukey J.W. 1977. *Exploratory Data Analysis*. Addison-Wesley. ISBN 0201076160.
- Virieux J. 1984. SH-wave propagation in heterogeneous media: Velocity-stress finite-difference method. *GEOPHYSICS* **49** (11), 1933–1942.
- Virieux J. 1986. P-SV wave propagation in heterogeneous media: Velocity-stress finite-difference method. *GEOPHYSICS* **51** (4), 889–901.
- Wentzel F. and Brun J.-P. 1991. A deep Reflection Seismic Line across the Northern Rhine Graben. *Earth and Planetary Science Letters* **104**, 140–150.

## Acknowledgment

This work was conducted in the framework of the excellence laboratory “Labex G-EAU-THERMIE PROFONDE” (University of Strasbourg). It was funded by the French National Research Agency, as part of the French “Investments for the future” program, by the Energie Baden-Württemberg AG (EnBW), the French institution CNRS, and by the French-German University (DFH-UFA).

## **FOURTH PART:**

### **Discussion, Conclusion and Outlooks**

# 7 Discussion, conclusion

## 7.1 Gaussian distribution of the hypocentre PDF

To simplify the analysis of the location uncertainty, the probability density function (PDF) related to the hypocentre was assumed to be Gaussian. The uncertainty was then defined as the half-length of the longest axis of the PDF at a confidence level of 68.3%. The representation of Gaussian distribution is an ellipsoid and hence determining the length of its longest axis is quite an easy task. To check the reliability of this assumption, two outputs provided by NonLinLoc were compared: the location obtained by the grid-search method and the location obtained for the expectation of a Gaussian distribution like described in *Lomax et al.* [2000]. The differences obtained in the case of location done for the GRT1 stimulation at Rittershoffen are displayed as boxplots in Figure 7-1.

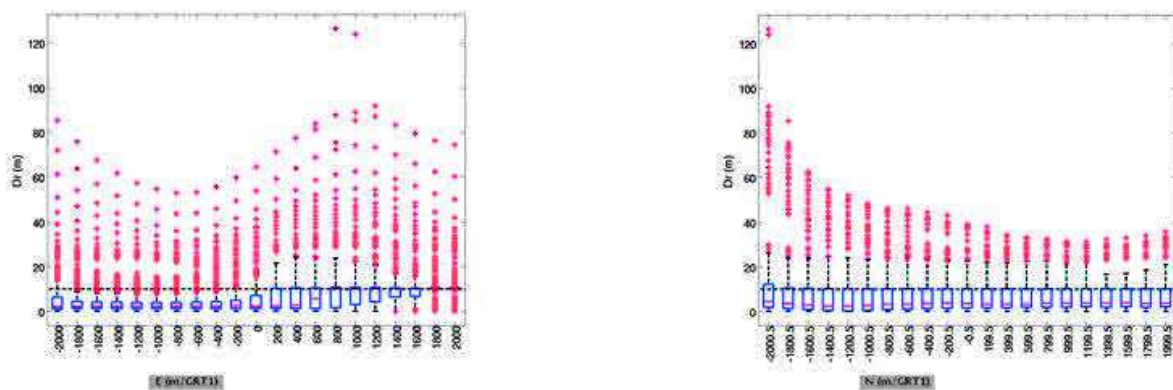


Figure 7-1 : Differences between locations performed with the grid-search method and expected location assuming a Gaussian distribution of the PDF. The boxplots are formed with the median value (red line), the first and third quartiles (extrema of the blue boxes) and the UIF and LIF (extrema of the vertical dashed lines). Outliers are represented by red crosses. The dashed gray line corresponds to the mesh size used for the location process.

Excepting for the most southern sources, 75% of the distances between the most probable hypocentre and the center of the 68,3% confidence volume obtained assuming a Gaussian PDF (in this case, the hypocentre is the centre of the ellipsoid) are smaller than the mesh used during the location process. Hence, it can be assumed that the PDF associated with the earthquake location has Gaussian distribution.



## 7.2 Impact of a calibration shot on earthquake location

As shown in sub-section 5.4.2.3, determining earthquakes hypocentre in an incorrect velocity model leads to strong inaccuracies (a misfit of 300 to 350 m to the East was found for Rittershoffen). Hence, possibilities to minimise this location inaccuracy were investigated. A common method to reach this goal is to perform a calibration shot and apply station corrections. The method relies on the recording of an explosion with well known location. The “calibration shot” method has already been used in many works. For example, *Toksöz et al.* [2000] used the Agri Dam explosion to calibrate the eastern Turkey broadband seismic network. In that study, the explosion was considered as the calibration shot. The method was also applied in the Colorado as a control test [*Raleigh et al.*, 1976]. At a smaller scale, a calibration shot was performed for some EGS to maximize the location of hypocentres detected for its stimulation [*Foulger and Julian*, 2014]. In our synthetic analysis, we adapt the standard procedure as follow. First, the travel-times are computed between station and this source in the model representative of the real Earth. Then, the travel-times between this source and the same seismic sensors are calculated in the incorrect velocity model. By differencing both travel-times, we get times-delays for each station and each phase. Those time corrections – which can be either positive or negative - are applied to the measured travel-times before locating the earthquakes.

In the present work, the synthetic calibration shot was assumed to be performed in the GRT1 well at mid-depth of its open-hole section (section 5.3). The travel-times for P- and S-waves were firstly calculated using the 3D velocity model describing a simplified fault (sub-section 5.4.2.3). The travel-times for the same stations and the same seismic event were then calculated again in the 1D reference velocity model (sub-section 5.3.4). By subtracting these travel-times to the ones obtained for the 3D model, we got the station corrections in time for each sensor and each associated phase(s). In the next step, all synthetic events initially located along a fault plane (sub-section 5.4.2.3) were relocated. We firstly took the travel-times obtained in the 3D model describing the fault and then the seismic events were relocated in the 1D velocity model but taking the station corrections into account. The provided locations were then compared to the initial synthetic positions. In the last step, the location inaccuracies obtained in this study were compared to the inaccuracies obtained for the study without taking the station corrections into account.

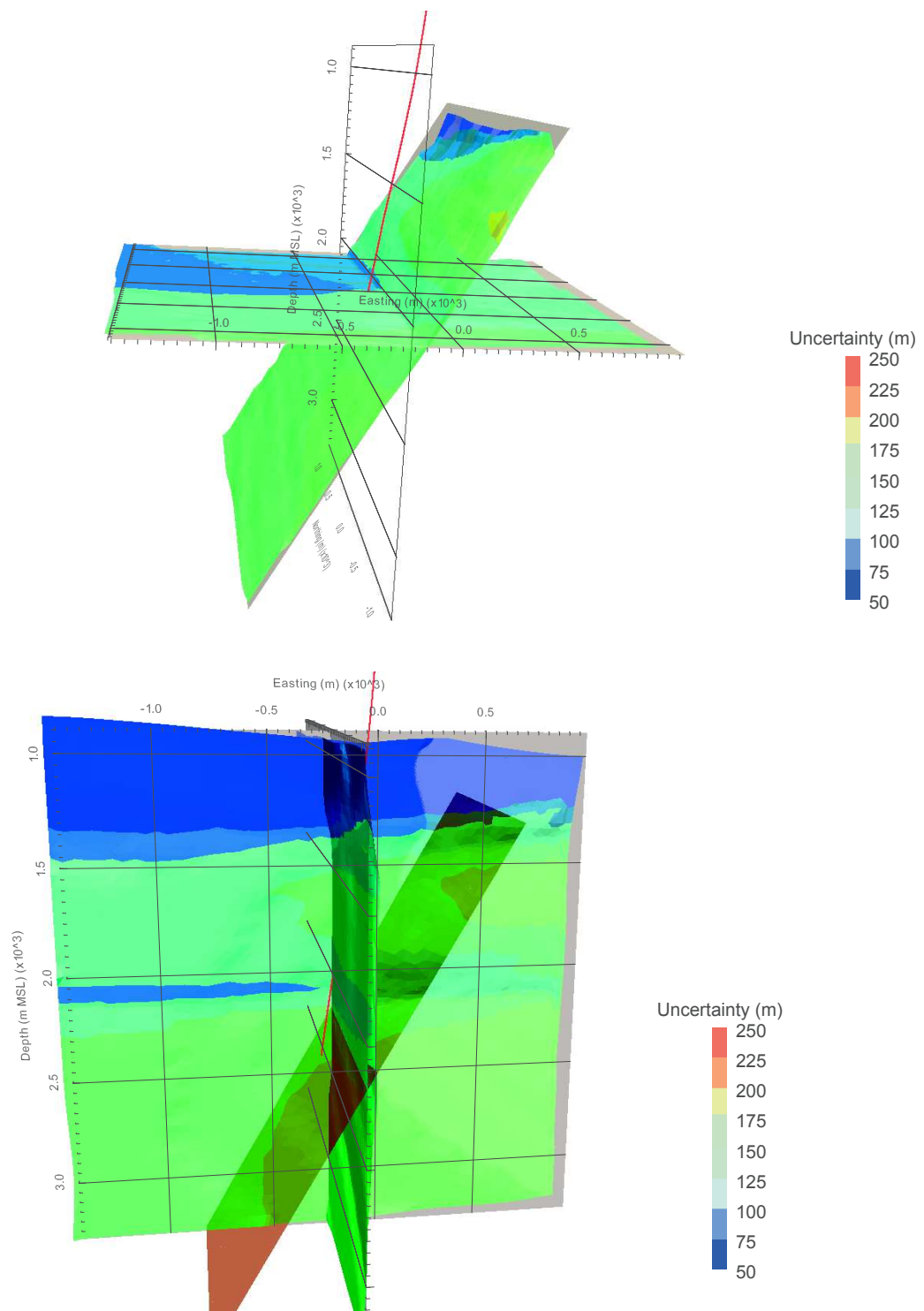


Figure 7-2 : Distribution of uncertainties and inaccuracies obtained after applying the station correction during the inversion process. Results for sources initially placed along the fault, on a horizontal plane, on a N-S vertical plane and on a E-W vertical plane are shown.

Since all synthetic events were located too much to the East and too deep (see Figure 5-17), it was expected that the “calibration shot” method would improve all locations along the fault. By comparing Figure 5-17 and Figure 7-2 we can easily note an improvement of the event absolute relocation when applying the station corrections obtained after a calibration shot. The location uncertainties (colour scale on both Figure 5-17 and Figure 7-2) are not distributed

exactly the same way, but their ranges are similar. Median values between 120 and 170 m roughly and a maximum value up to a bit less than 200 m are obtained for locations computed using the travel-times corrections whereas they could somewhere be a bit larger, up to 250 m, when the station corrections are applied.

Statistics on inaccuracies obtained after applying the station corrections shows horizontal misfits of about 30 to 80 m (median value). Like the horizontal inaccuracies, the vertical ones are not isotropically distributed. The highest vertical inaccuracies are seen for the case of sources initially located along the fault in the shallowest part. They reach a median value of about 65 m. The largest horizontal inaccuracies, of about 95 m, are noted in the Eastern part of the horizontal plane of sources. Once more we could see the impact of the seismic coverage (Figure 5-4).

Hence the application of station corrections obtained after a single calibration shot procedure improves earthquake location. Location inaccuracies may be decreased by a factor of 6 to 10 according to the initial location of the hypocentre. Since the inaccuracies were decreased to values smaller than the location uncertainties, the ellipsoid related to the PDF of the location should contain the real hypocentre. Therefore, one can assume that the calibration shot is a nice way to correct for location bias.

The choice of the calibration shot emplacement is another important parameter. If the calibration shot was positioned where the location inaccuracies were already low, the location would not have improved such a way. On the other hand, it is expected that the location improvement would not be so significant if the seismic network coverage was better in the South and East directions. A study with different seismic coverages should be performed to investigate this aspect but it is not the scope of the presented work. Nevertheless, it is really advised to perform a calibration shot before locating earthquakes in a reservoir.

### **7.3 Impact of the seismic coverage on focal mechanisms**

The goal of chapter 6 was to quantify the uncertainties and inaccuracies on the focal mechanism due to an incorrect model used to represent the sub-surface. This section aims at quantifying the impact of the seismic coverage. For that the same focal mechanisms were computed for observations coming from each of the two networks (Net15 and Net41, see sub-section 6.3.4) separately. The focal mechanisms were firstly calculated, assuming that the model of the sub-surface was correct in order to get the minimal uncertainties and inaccuracies. Hence, the 3D model is used for the observations and to calculate the take-off

angles and the event location. Nine sources are placed along the fault: the first three at shallow depth and the last three are the deeper. At a common depth, the smallest number on the x-axis represents the northern source and the biggest the southern one.

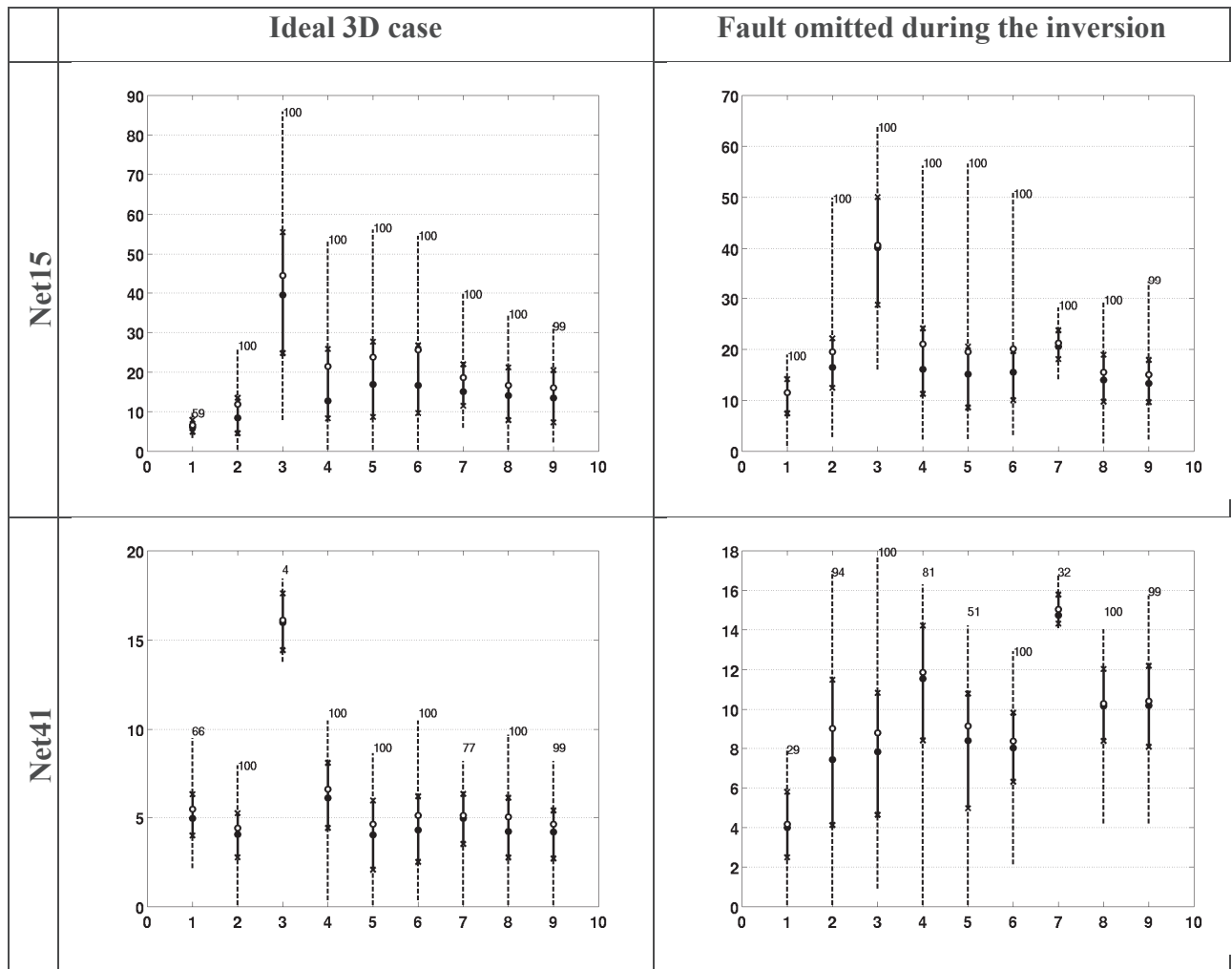


Figure 7-3: The angular inaccuracy for focal mechanisms obtained with Net15 (top) and Net41 (bottom) is presented as boxplots. The median (black disk), the first and third quartiles (crosses) and the range (dashed line) form the boxplot. The focal mechanism inaccuracy associated with the mean vector associated with the associated boxplot is shown (white disk) and the number of focal mechanisms used to carry out the statistics is written near the associated boxplot. The results are shown for the ideal case (left panels) and when the fault was omitted in the model (right panels).

As expected, a better azimuthal coverage of the studied area by the seismic network decreases the angular inaccuracy associated with the focal mechanism. The FM associated with the mean slip vector computed with polarities from Net41 is more accurate than  $7^\circ$  (Figure 7-3 bottom left) except for the southern shallow source ( $\sim 17^\circ$  of angular inaccuracy). For the same conditions, but inverting only observations from Net15, angular inaccuracies in the interval  $[5^\circ; 28^\circ]$  (and  $45^\circ$  for the southern shallow source) are obtained (Figure 7-3 top left).. Except for the shallowest southern source, median values in the interval  $[5^\circ, 20^\circ]$  are found for focal mechanisms calculated with observations from Net15 and the third quartile (Q3) does not exceed  $30^\circ$  (Figure 7-3). The median angular inaccuracies computed for Net 41

range between  $3^\circ$  and  $7^\circ$ . Hence, the accuracy of the FM may be improved by a factor of 4 if observations are provided by the whole Net41 instead of the Net15. Furthermore, the spatial distribution of the angular inaccuracy seems different than for the Net15 network.

As done for Net15 (sub-section 6.4.3), the impact of the omission of the fault in the inversion process was investigated for Net41. Some unexpected variations of the angular inaccuracy are noted. Actually, for the Net15 (Figure 7-3 top panels), the angular inaccuracy increases for the two northern shallow sources while omitting the fault in the model. This increase may reach  $\sim 10^\circ$ . For the other sources however the inaccuracy of the FM is unchanged or decreases. On the contrary, for the Net41, the angular inaccuracy of the FM is usually larger when omitting the fault: it only decreases for the northern and southern sources at the shallowest depth. Usually  $5^\circ$  can be added to the initial inaccuracy computed for the 3D model and even  $10^\circ$  for the deepest northern source. One could hypothesize that the effect due to the bad seismic coverage of Net15 is partly compensated by the impact of the incorrect sub-surface model. On the contrary, since the coverage of Net41 is quite good, an incorrect model of the sub-surface will have stronger negative impact on the FM. Nevertheless, contrarily to results obtained on the hypocentres [Gaucher *et al.*, 2016], the FM inaccuracies remain smaller for Net41 than for Net15 if an incorrect 1D model of sub-surface is considered instead of a 3D model.

To detail the angular inaccuracy and uncertainty, azimuth and dip of the acceptable FMs were compared to the azimuth and dip of the initial fault plane respectively. The study was performed for both Net15 and Net41 in the ideal case as well as in the case simulating the omission of the fault in the velocity model. Figure 7-4 shows the distribution of strike and dips associated with all acceptable FMs (blue dots) for each of the nine sources using polarities, take-off angles and hypocentres calculated in the ideal 3D case with observations from Net41.

For all sources at shallow and intermediate depth, the dip associated with the fault plane of the mean vector (red square) is always slightly smaller than (or equal to for the northern shallowest source) the dip of the initial fault plane (green squares, Figure 7-4 top and middle panels). On the contrary, it is slightly higher than the initial one for sources at depth (bottom panels). The obtained azimuths are a bit larger than the initial one. This means that the recomputed fault planes are oriented NNE-SSW instead of N-S. The recomputed fault plane associated with the initial fault plane is more horizontal for the shallowest sources and more vertical for the deepest sources. Nevertheless, one has to mention that the azimuthal and dip inaccuracies of the FM associated with the mean vector does not exceed  $5^\circ$  excepted for the shallowest northern source for which the obtained azimuth is  $200^\circ$  instead of  $180^\circ$ .

One also has to mention that except for this source the initial fault plane is contained in the cloud representing the set of acceptable solutions.

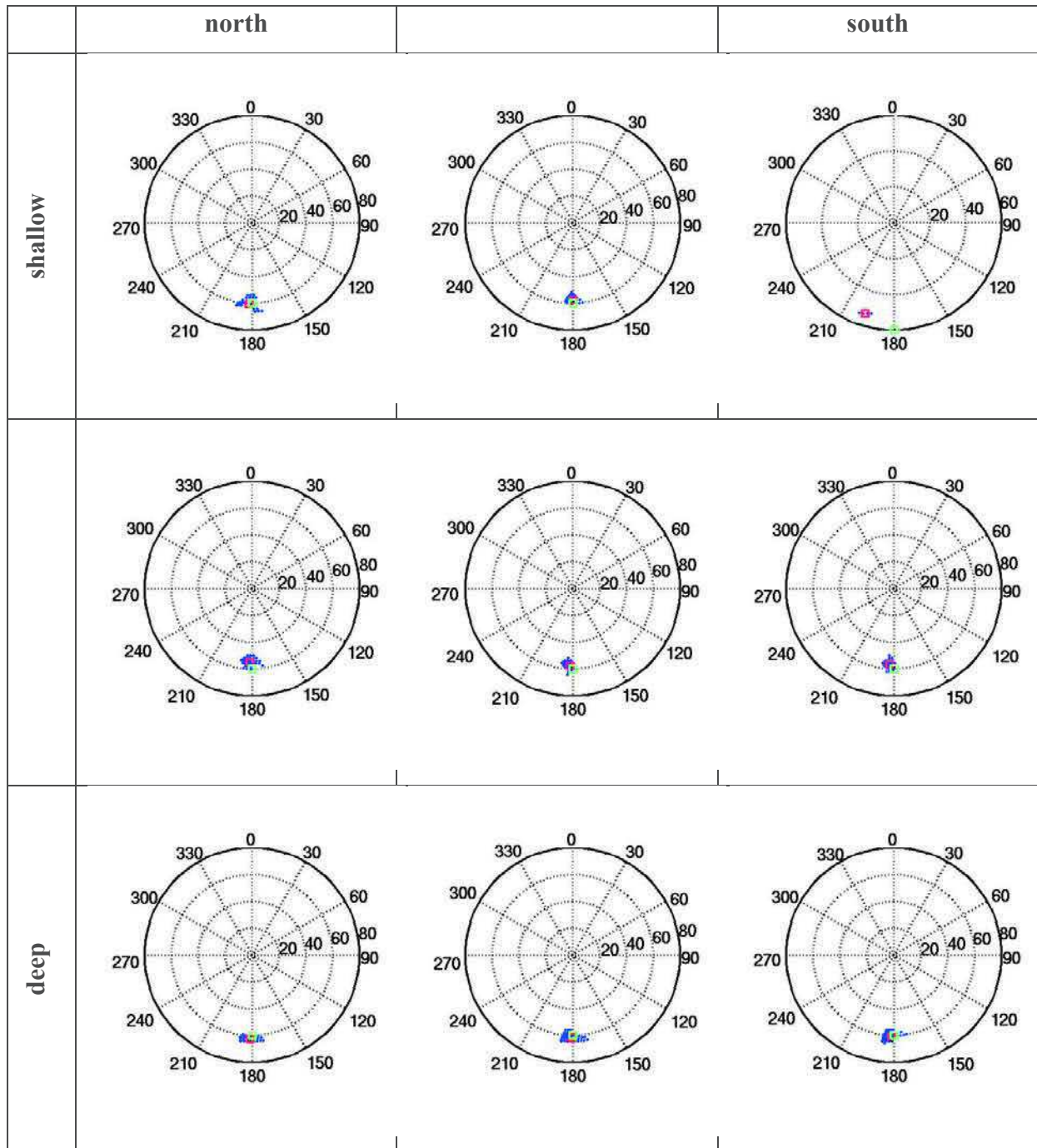


Figure 7-4: Polar representation of the set of fault planes associated with the acceptable focal mechanisms obtained by HASH software (blue dots) from polarities of the Net41. Each circle corresponds to a dip interval whereas each section to a 30° interval of azimuth. The initial (green square) fault plane is displayed as well as the fault plane associated with the mean slip vector (red square).

The same manipulations made on results obtained when omitting the fault during the inversion process show a small deterioration of the results (Figure 7-3 right panels, Figure 7-5).

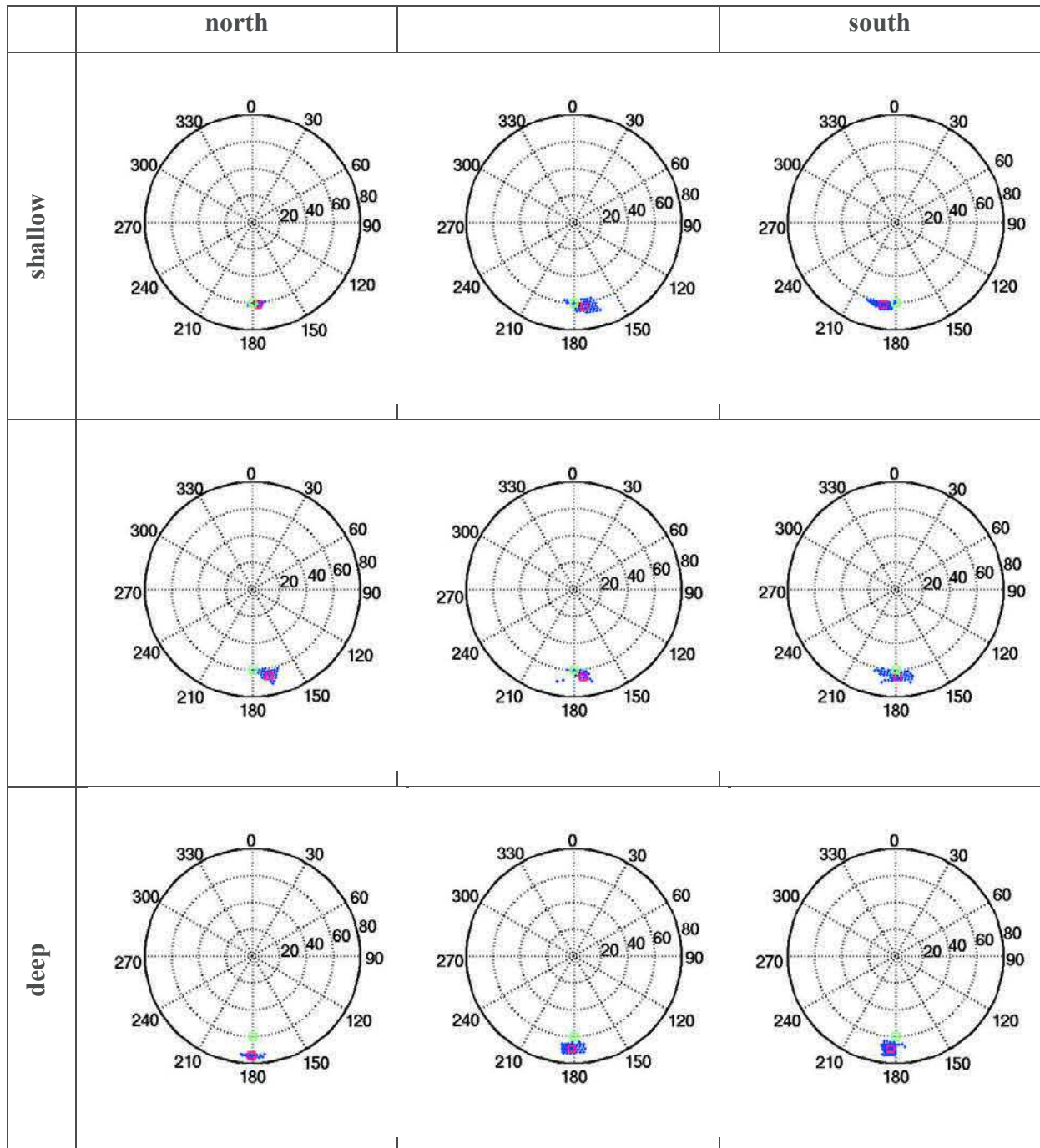


Figure 7-5: Same figure as Figure 7-4 but for FMs obtained when the fault is omitted in the inversion process.

The azimuth of the FM associated with the mean vector is always smaller for fault planes calculated when omitting the fault (Figure 7-5) than for the ideal 3D case (Figure 7-4). Consequently, except for the shallowest southern source, for which the azimuth even decreased is still  $190^\circ$ , and for the deepest sources, which azimuths do not appear affected by the omission of the fault, the obtained fault planes are now oriented NNW-SSE instead of N-S. The azimuth inaccuracy of the mean slip vector may reach  $10^\circ$ . The study of the dip angle associated with the mean slip vector leads to the conclusion that omitting the fault provides

more vertical fault planes than reality: the dips are 5 to 10° larger in that case than in the ideal 3D case. Moreover, for all sources in depth, the initial fault plane is not included in the set of acceptable FMs obtained by the inversion. Therefore, the interpretation deriving from the focal mechanisms might conclude in the presence of several and mis-oriented fault planes where only one exists.

On the other hand, and contrarily to hypocentre determination, focal mechanisms are always improved by a better seismic coverage. The azimuth and dip inaccuracies of FM are always smaller for the results of Net41 (Figure 7-3 bottom panels) than for the results of Net15 (Figure 7-3 top panels) in the ideal 3D case as well as in the case simulating the fault omission.

#### **7.4 Impact of the use of amplitude ratios S/P on focal mechanisms**

In sections 6.4 and 7.3, the focal mechanism (FM) inaccuracies and uncertainties were computed for focal mechanisms obtained using P-wave polarities only. Nevertheless, as explained in the theory part (sub-section 2.3.3.3), the FM may be calculated from a combination of P-wave polarities and P/S amplitude ratios. A comparison of the angular inaccuracies resulting from both inversions - with and without the amplitude ratios - is shown in Figure 7-6.

Probably due to the low number of simulated sources, one can not conclude on the improvement or the deterioration of the FM by adding the amplitude ratios in the input of the inversions for the case of Rittershoffen geothermal reservoir.



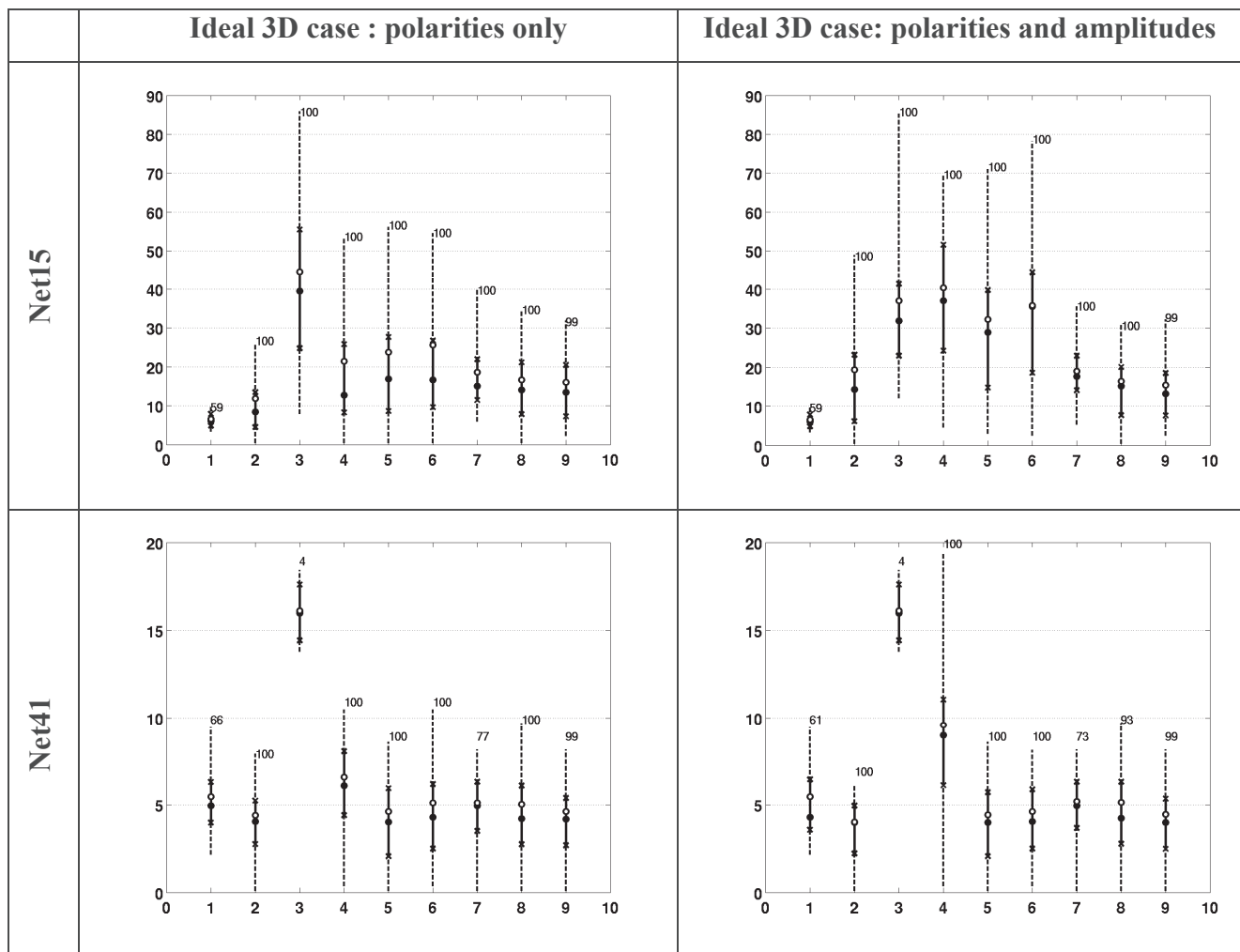


Figure 7-6 : The angular inaccuracy for focal mechanisms obtained with Net15 (top) and Net41 (bottom) is presented as boxplots. The median (black disk), the first and third quartiles (crosses) and the range (dashed line) form the boxplot. The focal mechanism inaccuracy associated with the mean vector is shown (white disk) and the number of focal mechanisms used to carry out the statistics is written near the associated boxplot. The results are shown for the ideal case when using (right panels) or not (left panels) the amplitudes ratios in the inversion.

## 7.5 Main discussion and conclusion

The proposed topic was focused on the determination of hypocentres and focal mechanisms errors. The aim was to distinguish between inaccuracies and uncertainties for both of them. Usually, seismic studies take care of uncertainties but do not deal with inaccuracies. Nevertheless, as shown through this Ph.D., the inaccuracies are sometimes as strong as or larger than the uncertainties. Here derived (mis-)interpretations on sub-surface design and characteristics were also studied. To reach our goal, a three-step method was developed. In the first step, the forward problem is solved to carry out synthetic data (arrival-times, waveforms). These sets of data are used as observations to solve the inverse problem in the second step. To mimic the common biases and uncertainties found in standard seismological studies, hypotheses made during the synthetic modelling step are modified before performing

the inversion (typically picking uncertainties are added, the velocity model may be changed...).

The synthetic arrival-times calculation and the inversion to carry out the hypocentre were performed using the same finite-difference method [*Podvin and Lecomte*, 1991]. Therefore, no bias is included due to different methodologies. On the other hand, two different finite-differences techniques were used in the study to determine FM errors. The method of *Virieux* [1984] was used to create the synthetic waveforms whereas the take-off angles necessary to compute for the focal mechanisms were obtained by the method of *Podvin and Lecomte* [1991]. Hence, simple tests were carried out to validate the methodology presented in section 6.2. Since only small inaccuracies ( $\sim 1$  or  $2^\circ$ ) were obtained for the focal mechanism calculated during these tests, it was concluded that the methodology was suitable for our goal.

Through this Ph.D., the impact of the seismic coverage and of the velocity model on hypocentre uncertainties was quantified. The computed uncertainties were decreased by a factor of two when observations from a down-hole network were added to the ones from a surface network (e.g sub-section 4.4.1). This decrease may be explained by the proximity of the down-hole sensors to the sources and by the chosen picking uncertainties which were smaller for the down-hole stations ( $\pm 5$  ms) than for the surface ones ( $\pm 15$  ms). Furthermore, the azimuthal coverage of the monitoring seismic network was proved to play an important role on location uncertainty values and its spatial distribution. This can be explained by the spatial coverage of the seismic rays [*Aki and Richards*, 2009]. In Rittershoffen, when the monitoring network covers only the northern part of the studied area, the location uncertainty at around 2400 m depth (injection depth) increases from 130 m in the north to 225 m in the south. By adding only one station in the SE, those uncertainties are decreased by 25 to 50 m. The precision of the arrival-time input catalogue and of the velocity model has negligible impact on hypocentre uncertainties. Nonetheless, using the probabilistic method developed by *Gesret et al.* [2015], the model uncertainties usually leading to location inaccuracies are introduced in the location uncertainties. By applying this technique at Rittershoffen, the location uncertainties were multiplied by a factor 2 to 3 leading to highest value around 650 m of uncertainties. This means that the PDF of the 68.3% confidence level may cover more than 25% of the vertical distance between the induced event and the surface.

Contrarily to location uncertainties, hypocentre inaccuracies are strongly affected by biases in the velocity model. Neglecting a normal fault dipping  $60^\circ$ W and presenting a vertical shift of 200 m in the velocity model at Rittershoffen, leads to horizontal bias up to 350 m toward east

and vertical bias up to 200 m for sources initially placed along the fault. Moreover, the anisotropic spatial variation of the hypocentre inaccuracies may lead to a distorted interpretation of the planar structure such as faults. This may lead to a wrong design interpretation of the sub-surface. Furthermore, the addition of one station to the seismic network increases the location inaccuracy if the location is performed in an incorrect velocity model. The median horizontal shift reaches 425 m and the vertical bias  $\sim 275$  m. The impact is expected to be even stronger by adding more stations since more “incorrect” information is added to the inverse problem formulation [Gaucher *et al.*, 2016]. Hence, improving the seismic coverage by adding sensors will certainly decrease the location uncertainties but may also lead to more biased hypocentres. The increase of location inaccuracies was also noted when using down-hole sensors. This may be explained by the proximity of the sensors to the sources. Hence, it is worth writing that using only hypocentres to image the fracture in the sub-surface is not advised if its correct model cannot be used in the inversion. But, since the real model of the sub-surface is usually unknown, performing the kind of studies carried out here should help for further investigations.

To correct from hypocentre inaccuracies, a common method is to use a calibration shot and compute the arrival-times correction at the different stations. Its efficiency is proven by the test carried out for Rittershoffen hypocentre determination (section 7.2). After the correction of arrival-times with the delays obtained by the calibration shot, the location biases were divided by a factor of 6 for the horizontal location and a factor of 3 to 5 for the vertical location. The interpreted structures from the obtained hypocentres are roughly not distorted compared to the ones used to create the synthetic observations (section 7.2). The technique of the calibration shot is hence very advised before computing for hypocentre determination.

Hypocentre biases might also be due to arrival-times precision used in the input catalogue or to a massive water injection modifying the velocity profile. Nevertheless, the inaccuracies computed for these cases are usually smaller than the uncertainties associated with the same location. Accordingly, the PDF might cover the wrong location due to these simplifications. Hence, the impact will not be seen by absolute location techniques even if the P- and S-wave velocities are stronger decreased, up to 20%, in the injection zone.

As well as for location uncertainty does the improvement of the seismic coverage decrease the focal mechanism (FM) uncertainty. From about 10 to 60° with data from Net15, the uncertainty associated with the same FM are reduced to 2 to 10° with data from Net41 in the ideal 3D case. The variation of azimuth between the ideal 3D case and the case of fault

omission is opposite if we consider results from Net15 and results from Net41. Actually, the azimuths of the mean vector are higher in the ideal 3D case for Net41 but lower if we consider the results from Net15. The dip angle is always increased comparing results from the case of fault omission to the ideal 3D case for Net41 even if the variation is not isotropic. On the contrary, the dip may increase or decrease for the same comparisons with results from Net15, according to the source location. Nevertheless, contrarily to earthquake location inaccuracies, angular inaccuracies are always smaller for Net41 than for Net15, even in the case simulating the omission of the fault. Hence, one should always use data from the complete Net41 when available to compute the FMs. Unfortunately this network was not installed during the stimulation of the well GRT1. The FMs obtained for this stimulation should consequently be interpreted according to the possible inaccuracies and uncertainties provided for Net15 in Figure 7-3.

Nevertheless, for more consistency in the interpretations, one should pursue the investigations with more sources (in this preliminary study only 9 sources positioned along the fault and separated by 500 m were used) to be able to apply statistics and to look at a more reliable spatial distribution of the focal mechanism uncertainty and inaccuracy.

## 8 Outlooks

The study was focused on absolute location error. Nevertheless, the impact of relative techniques [*Poupinet et al.*, 1984; *Waldhauser and Ellsworth*, 2000] on location uncertainties and inaccuracies may be a very interesting topic since nowadays many hypocentres are computed with them. At that aim, *Michelini and Lomax* [2004] studied the effect of velocity model errors on double-difference [*Waldhauser and Ellsworth*, 2000] hypocentre determination. They showed that a good velocity model is still mandatory for high resolution hypocentre computation. Because the relative location techniques are usually known to carry out more accurate hypocentres than the absolute techniques, one can wonder if the location inaccuracies are still larger than the location uncertainties. In other words, the question is to determine if the obtained PDF will contain the inaccuracy or not. Part of that work has already been carried out for simulated location in Bohemia [*Bouchaala et al.*, 2013] but not for geothermal systems. The time precision of the input catalogue for the relative hypocentre determination might be of great interest because seismic catalogues of arrival-times always have a precision. The work presented here was focused on hypocentre computation using arrival-time inversions. Nonetheless, similar method can be developed for location techniques using full-waveforms. The advantage of these techniques is that they directly use the observed seismograms or their derivatives. But the choice of the window for searching for the maximum amplitude is crucial [*Langet et al.*, 2014].

One step further, the impact of these location errors (from absolute or relative technique) on the reservoir design might be investigated. This task may be performed by looking for the impact of location errors on tomography. The impact for classical, absolute tomography techniques such as *Thurber's* [*Thurber*, 1983] or relative tomography techniques like TomoDD [*Zhang and Thurber*, 2003] should be carried out.

Another topic might be to investigate the impact of these hypocentres inaccuracies on the risk mitigation for economical purposes.

The impact of the hypocentre errors on focal mechanism was carried out. The global angular inaccuracies and uncertainties but also the separated inaccuracies on the strike, dip, and rake defining the focal mechanism were investigated. To get the spatial distribution of the

inaccuracies and uncertainties, the technique should be applied on more seismic events –either by their number or by the different focal mechanisms- to perform statistics. To pursue the investigation, the effect of these inaccuracies and uncertainties on stress-field inversion should be of primary interest. For example, *Schoenball et al.* [2014] used the stress-field to design the fractures and their modifications during a stimulation. An interesting topic should be to determine the impact of stress-field errors on the final design.

Our methodology was applied on two geothermal sites (Soultz-sous-Forêts and Rittershoffen) for hypocentre errors determination and only on Rittershoffen site for focal mechanism errors computation. Nonetheless, similar sites may benefit from the technique provided that the *a priori* knowledge of their sub-surface is sufficient and that they have the scale of a reservoir (several kilometres).

## 9 References

- Agemar, T., R. Schnellschmidt, and R. Schulz (2012), Subsurface Temperature Distribution of Germany., *Geothermics*, *44*, 65–77.
- Aki, K., and P. G. Richards (2009), *Quantitative Seismology, Theory and Methods*, 2nd ed., 704 pp., University Science Books, Mill Valley.
- Angelier, J. (1984), Tectonic analysis of fault slip data sets, *Journal of Geophysical Research: Solid Earth*, *89*(B7), 5835–5848.
- Aquilina, L., H. Pauwels, A. Genter, and C. Fouillac (1997), Water-rock interaction processes in the Triassic sandstone and the granitic basement of the Rhine Graben: Geochemical investigation of a geothermal reservoir, *Geochimica et cosmochimica acta*, *61*(20), 4281–4295.
- Aster, R. C., P. M. Shearer, and J. Berger (1990), Quantitative measurements of shear wave polarizations at the Anza seismic network, southern California: implications for shear wave splitting and earthquake prediction, *Journal of Geophysical Research*, *95*, 12449–12473.
- Bailleux, P., E. Schill, J.-B. Edel, and G. Mauri (2013), Localization of temperature anomalies in the Upper Rhine Graben: insights from geophysics and neotectonic activity, *International Geology Review*, *55*(14), 1744–1762, doi:10.1080/00206814.2013.794914.
- Baker, T., R. Granat, and R. W. Clayton (2005), Real-time Earthquake Location Using Kirchhoff Reconstruction, *Bull. Seismol. Soc. Amer.*, *95*(2), 699–707, doi:10.1785/0120040123.
- Bao, H., J. Bielak, O. Ghattas, L. F. Kallivokas, D. R. O'Hallaron, J. R. Shewchuk, and J. Xu (1998), Large-scale simulation of elastic wave propagation in heterogeneous media on parallel computers, *Computer methods in applied mechanics and engineering*, *152*(1), 85–102.
- Baria, R., J. Baumgärtner, A. Gérard, R. Jung, and J. Garnish (1999), European HDR research programme at Soultz-sous-Forêts (France) 1987–1996, *Geothermics*, *28*(4–5), 655–669, doi:10.1016/s0375-6505(99)00036-x.
- Båth, M. (1961), Polarization of transverse seismic waves, *Geophysical Journal International*, *4*(Supplement 1), 106–123.
- Baujard, C., A. Genter, V. Maurer, J.-J. Graff and E. Dalmais (2015), ECOGI, a new deep EGS project in Alsace, Rhine Graben, France, *Proceeding in World Geothermal Congress 2015*, Melbourne, Australia, April 19-25 2015.
- Baumgärtner, J., R. Jung, A. Gérard, R. Baria, and J. D. Garnish (1996), The European HDR project at Soultz-sous-Forêts: Stimulation of the second deep well and first circulation experiments, pp. 267–274.
- Baumgärtner, J., and C. Lerch (2013), Geothermal 2.0: The Insheim geothermal power plant, the second generation of geothermal power plants in the Upper Rhine Graben, *Third European Geothermal Review*, Mainz, Germany, June 24-26 2013.
- Bayes, T. (1958), Essay towards solving a problem in the doctrine of chances, *Bometrika*, *45*, 298–315.
- Bérard, T., and F. H. Cornet (2003), Evidence of thermally induced borehole elongation: a case study at Soultz, France, *Int J Rock Mech Min*, *40*(7–8), 1121–1140, doi:10.1016/S1365-1609(03)00118-7.
- Berenger, J.-P. (1994), A perfectly matched layer for the absorption of electromagnetic waves, *Journal of Computational Physics*, *114*(2), 185–200, doi:10.1006/jcph.1994.1159.
- Bergerat, F. (1985), Déformations cassantes et champs de contraintes tertiaires dans la plateforme européenne, Ph.D., Université Pierre et Marie Curie, Paris VI, Paris.
- Billings, S. D. (1994), Simulated annealing for earthquake location, *GJI*, *118*, 1143–1146.
- Bohlen, T. (2002), Parallel 3-D viscoelastic finite difference seismic modelling, *Computers & Geosciences*, *28*(8), 887–899, doi:10.1016/S0098-3004(02)00006-7.
- Bohlen, T., D. de Nil, D. Köhn, and S. Jetschny (2012), *SOFI3D - Seismic modeling with finite differences 3D - acoustic and viscoelastic version*, Karlsruhe GPI, Germany.

- Bohlen, T., and E. H. Saenger (2006), Accuracy of heterogeneous staggered-grid finite-difference modeling of Rayleigh waves, *GEOPHYSICS*, 71(4), T109-T115, doi:10.1190/1.2213051.
- Bonjer, K. P., C. Gelbke, R. Gilg, D. Rouland, D. Mayer-Rosa, and B. Massinon (1984), Seismicity and dynamics of the Upper Rhine Graben, *Journal of Geophysics*, 55, 1–12.
- Bouchaala, F., V. Vavryčuk, and T. Fischer (2013), Accuracy of the master-event and double-difference locations: synthetic tests and application to seismicity in West Bohemia, Czech Republic, *Journal of Seismology*, 17(3), 841–859, doi:10.1007/s10950-013-9357-4.
- Bouchon, M. (1981), A simple method to calculate Green's functions for elastic layered media, *Bulletin of the Seismological Society of America*, 71(4), 959–971.
- Bouchon, M. (2003), A Review of the Discrete Wavenumber Method: Pure and applied geophysics, *Pure appl. geophys.*, 160(3-4), 445–465, doi:10.1007/PL00012545.
- Bromley, C. J., and E. L. Majer (Eds.) (2012), *Geothermal induced seismicity - risks and rewards*.
- Brumbaugh, D. (1979), Classical focal mechanism techniques for body waves: Geophysical surveys, *Geophysical Surveys*, 3(4), 297–329, doi:10.1007/BF01449754.
- Byerly, P. (1926), The Montana Earthquake of June 28 1925 GMCT, *BSSA*, 16, 209–263.
- Carvalho, J., L. V. Barros, and J. Zahradník (2016), Focal mechanisms and moment magnitudes of micro-earthquakes in central Brazil by waveform inversion with quality assessment and inference of the local stress field, *Journal of South American Earth Sciences*, 71, 333–343.
- Cerjan, C., D. Kosloff, R. Kosloff, and M. Reshef (1985), A nonreflecting boundary condition for discrete acoustic and elastic wave equations, *GEOPHYSICS*, 50(4), 705–708, doi:10.1190/1.1441945.
- Charl y, J., N. Cuenot, L. Dorbath, C. Dorbath, H. Haessler, and M. Frogneux (2007), Large earthquakes during hydraulic stimulations at the geothermal site of Soultz-sous-For ts, *Int J Rock Mech Min*, 44(8), 1091–1105, doi:10.1016/j.ijrmms.2007.06.003.
- Cheng, A. H.-D., and D. T. Cheng (2005), Heritage and early history of the boundary element method, *Engineering Analysis with Boundary Elements*, 29(3), 268–302.
- Chew, W. C., and Q. H. Liu (1996), Perfectly matched layers for elastodynamics: a new absorbing boundary condition, *Journal of Computational Acoustics*, 4(04), 341–359.
- Christoffersson, A., E. S. Husebye, and S. F. Ingate (1988), Wavefield decomposition using ML-probabilities in modelling single-site 3-component records, *Geophysical Journal International*, 93(2), 197–213.
- Christopher C. Paige, and Michael A. Saunders (1982), LSQR: An Algorithm for Sparse Linear Equations and Sparse Least Squares, *ACM Trans. Math. Softw.*, 8(1), 43–71, doi:10.1145/355984.355989.
- Clauser, C., and H. Villinger (1990), Analysis of conductive and convective heat transfer in a sedimentary basin, demonstrated for the Rheingraben, *Geophysical Journal International*, 100(3), 393–414.
- Collino, F., and P. B. Monk (1998), Optimizing the perfectly matched layer, *Computer methods in applied mechanics and engineering*, 164(1), 157–171.
- Courant, R., K. Friedrichs, and H. Lewy (1928),  ber die partiellen Differenzengleichungen der mathematischen Physik, *Mathematische Annalen*, 100(1), 32–74.
- Coutant, O. (1990), Program of numerical Simulation AXITRA, Laboratoire de G ophysique Interne et Tectonophysique, Universit  Joseph Fourier, Grenoble, France.
- Cuenot, N., J. Charl y, L. Dorbath, and H. Haessler (2006), Faulting mechanisms and stress regime at the European HDR site of Soultz-sous-For ts, France, *Geothermics*, 35(5-6), 561–575, doi:10.1016/j.geothermics.2006.11.007.
- Cuenot, N., C. Dorbath, and L. Dorbath (2008), Analysis of the microseismicity induced by fluid injections at the EGS site of Soultz-sous-For ts (Alsace, France): Implications for the



- characterization of the geothermal reservoir properties, *Pure Appl. Geophys.*, 165(5), 797–828, doi:10.1007/s00024-008-0335-7.
- Deal, M. M., and G. Nolet (1996), Comment on ‘Estimation of resolution and covariance for large matrix inversions’ by J. Zhang and G. A. McMechan, *Geophysical Journal International*, 127(1), 245–250, doi:10.1111/j.1365-246X.1996.tb01548.x.
- Deichmann, N., and M. Garcia-Fernandez (1992), Rupture geometry from high-precision relative hypocentre locations of microearthquake clusters, *Geophys J Int*, 110, 501–517.
- Deichmann, N., and D. Giardini (2009), Earthquakes induced by the stimulation of an enhanced geothermal system below Basel (Switzerland), *Seismological Research Letters*, 80(5), 784–798, doi:10.1785/gssrl.80.5.784.
- Dezayes, C., A. Genter, and B. Valley (2010), Structure of the low permeable naturally fractured geothermal reservoir at Soultz, *Comptes Rendus Geoscience*, 342(7-8), 517–530, doi:10.1016/j.crte.2009.10.002.
- Dèzes, P., S. M. Schmid, and P. A. Ziegler (2004), Evolution of the European Cenozoic Rift System: interaction of the Alpine and Pyrenean orogens with their foreland lithosphere, *Tectonophysics*, 389(1), 1–33.
- Diaz, J., and P. Joly (2006), A time domain analysis of PML models in acoustics, *Computer methods in applied mechanics and engineering*, 195(29), 3820–3853.
- Dorbath, L., N. Cuenot, A. Genter, and M. Frogneux (2009), Seismic response of the fractured and faulted granite of Soultz-sous-Forêts (France) to 5 km deep massive water injections, *Geophys J Int*, 177(2), 653–675, doi:10.1111/j.1365-246X.2009.04030.x.
- Dose, T. (Ed.) (2006), *Geostatistical estimation of temperatures - an example from the Upper Rhine Graben*, DGMK Spring conference on Exploration and Production, Celle, Germany, April 20-21 2006.
- Dreger, D., R. Uhrhammer, M. Pasyanos, J. Franck, and B. Romanowicz (1998), Regional and far-regional earthquake locations and source parameters using sparse broadband networks: A test on the Ridgecrest sequence, *Bulletin of the Seismological Society of America*, 88(6), 1353–1362.
- Drew, J., R. S. White, F. Tilmann, and J. Tarasewicz (2013), Coalescence microseismic mapping, *Geophysical Journal International*, 195(3), 1773–1785, doi:10.1093/gji/ggt331.
- Drilleau, M., É. Beucler, A. Mocquet, O. Verhoeven, G. Moebis, G. Burgos, J.-P. Montagner, and P. Vacher (2013), A Bayesian approach to infer radial models of temperature and anisotropy in the transition zone from surface wave dispersion curves, *Geophysical Journal International*, 195(2), 1165–1183, doi:10.1093/gji/ggt284.
- Edel, J.-B., K. Schulmann, and Y. Rotstein (2007), The Variscan tectonic inheritance of the Upper Rhine Graben: evidence of reactivations in the Lias, Late Eocene-Oligocene up to the recent., *International Journal of Earth Sciences*, 96(2), 305–325, doi:10.1007/s00531-006-0092-8.
- Ekström, G. (2006), Global detection and location of seismic sources by using surface waves, *Bulletin of the Seismological Society of America*, 96(4A), 1201–1212.
- ES Geothermie, www.geothermie.es-groupe.fr, last visit of the web-site: July 10 2016.
- Expertengruppe (2010), Das sesimische Ereignis bei Landau vom 15. August 2009, [http://www.lgb.rlp.de/fileadmin/cd2009/images/content/endbericht\\_landau/Landau\\_Endbericht\\_101103\\_corr.pdf](http://www.lgb.rlp.de/fileadmin/cd2009/images/content/endbericht_landau/Landau_Endbericht_101103_corr.pdf), last visit of the web-site: July 5 2016.
- Flinn, E. A. (1965), Confidence regions and error determinations for seismic event location, *Reviews of Geophysics*, 3(1), 157–185, doi:10.1029/RG003i001p00157.
- Fojtíková, L., V. Vavryčuk, A. Cipciar, and J. Madarás (2010), Focal mechanisms of micro-earthquakes in the Dobrá Voda seismoactive area in the Malé Karpaty Mts. (Little Carpathians), Slovakia, *Tectonophysics*, 492(1–4), 213–229, doi:10.1016/j.tecto.2010.06.007.

- Foulger, G. R., and B. R. Julian (Eds.) (2014), *Maximizing earthquake hypocenter location accuracies in EGS stimulations*, Thirty-ninth Workshop on Geothermal Reservoir Engineering, Stanford University, Stanford, California, February 24-26 2014.
- Fréchet, J. (1985), *Sismogénèse et doublets sismiques*, Ph.D. thesis, U. J. Fourier, Grenoble, France.
- Frémont, M., and S. D. Malone (1987), High precision relative locations of earthquakes at Mount St. Helens, Washington, *Journal of Geophysical Research: Solid Earth*, 92(B10), 10223–10236.
- Frietsch, M., J. Groos, and J. R. Ritter (2015), Detection and Delineation of a Fracture Zone with Observation of Seismic Shear Wave Anisotropy in the Upper Rhine Graben, SW Germany, *Pure Appl. Geophys.*, 172(2), 267–282, doi:10.1007/s00024-014-0899-3.
- Frohlich, C., and J. Pulliam (1999), Single-station location of seismic events: a review and a plea for more research, *Physics of the Earth and Planetary Interiors*, 113(1–4), 277–291, doi:10.1016/S0031-9201(99)00055-2.
- G. Golub, and W. Kahan (1965), Calculating the Singular Values and Pseudo-Inverse of a Matrix, *Journal of the Society for Industrial and Applied Mathematics Series B Numerical Analysis*, 2(2), 205–224, doi:10.1137/0702016.
- Gajewski, D., and C. Prodehl (1987), Seismic refraction investigation of the Black-Forest, *Tectonophysics*, 141, 261–275.
- Gajewski, D., and E. Tessmer (2005), Reverse modelling for seismic event characterization, *Geophys J Int*, 163(1), 276–284, doi:10.1111/j.1365-246X.2005.02732.x.
- Gaßner, L., J. C. Groos, and J. R. R. Ritter (2014), Herdflächenanalys induzierter Seismizität in der Südpfalz: Reaktivierung präexistenter Bruchflächen und Spannungszustand, *Mainzer Geowiss. Mitt.*, 42, 195–214.
- Gaucher, E. (2016), Earthquake detection probability within a seismically quiet area. Application to the Bruchsal geothermal field, *Geophysical Prospecting*, 64(2), 268–286, doi:10.1111/1365-2478.12270.
- Gaucher, E., F. H. Cornet, and P. Bernard (1998), Induced seismicity analysis for structure identification and stress field determination, SPE/ISRM Rock mechnic in petroleum engineers, Trondheim, Norway, July 8-10 1998.
- Gaucher, E., A. Gesret, and M. Noble (in prep), A new Bayesian formulation integrating seismic-wave polarization in non-linear earthquake location.
- Gaucher, E., X. Kinnaert, U. Achauer, and T. Kohl (Eds.) (2016), *Propagation of Velocity Model Errors in Earthquake Absolute Locations: Application to the Rittershoffen Geothermal Field*, Forty-first Workshop on Geothermal Reservoir Engineering, Stanford University, Stanford, California, February 22-24 2016.
- Gaucher, E., M. Schoenball, O. Heidbach, A. Zang, P. A. Fokker, J.-D. van Wees, and T. Kohl (2015), Induced seismicity in geothermal reservoirs: A review of forecasting approaches, *Renewable and Sustainable Energy Reviews*, 52, 1473–1490, doi:10.1016/j.rser.2015.08.026.
- Geiger, L. (1912), Probability method for the determination of earthquake epicenters from the arrival time only, *Bulletin of St. Louis University*, 8(1), 60–71.
- Gelbke, C. (1978), Lokalisierung von Erdbeben in Medien mit beliebiger Geschwindigkeits-Tiefer-Verteilung unter Einschluss späterer Einsätze und die Hypozentren im Bereich des südlichen Oberrheingrabens von 1971-1975, Ph. D., University of Karlsruhe, Germany.
- Genter, A., K. Evans, N. Cuenot, D. Fritsch, and B. Sanjuan (2010), Contribution of the exploration of deep crystalline fractured reservoir of Soultz to the knowledge of enhanced geothermal systems (EGS), *Comptes Rendus Geoscience*, 342(7-8), 502–516, doi:10.1016/j.crte.2010.01.006.
- GeORG Project Team (2015), INTERREG IV Upper Rhine Graben - Geopotentials of the deep Upper Rhine Graben, <http://maps.geopotenziale.eu/?app=georg&lang=en>, last visit of the web-site: June 20 2016.

- Gephart, J. W. (1990), FMSI: A FORTRAN program for inverting fault/slickenside and earthquake focal mechanism data to obtain the regional stress tensor, *Computers & Geosciences*, 16(7), 953–989.
- Gérard, A., A. Genter, T. Kohl, P. Lutz, P. Rose, and F. Rummel (2006), The deep EGS (Enhanced Geothermal System) project at Soultz-sous-Forêts (Alsace, France), *Geothermics*, 35(5-6), 473–483.
- Gérard, A., and O. Kappelmeyer (1987), The Soultz-sous-Forêts project: proceedings of the first EEC/US workshop on Geothermal Hot Dry Rocks Technology, *Geothermics, special issue*, 393–399.
- Gesret, A., N. Desassis, M. Noble, T. Romary, and C. Maisons (2015), Propagation of the velocity model uncertainties to the seismic event location, *Geophys J Int*, 200(1), 52–66, doi:10.1093/gji/ggu374.
- Gharti, H. N., V. Oye, M. Roth, and D. Kuhn (2010), Automated microearthquake location using envelope stacking and robust global optimization, *GEOPHYSICS*, 75(4), MA27-MA46, doi:10.1190/1.3432784.
- Gholamy, A., and V. Kreinovich (Eds.) (2014), *Why Ricker wavelets are successful in processing seismic data: Towards a theoretical explanation*, Computational Intelligence for Engineering Solutions (CIES), 2014 IEEE Symposium on, 11-16.
- Giardini, D. (2009), Geothermal quake risks must be faced, *Nature*, 462(7275), 848–849, doi:10.1038/462848a.
- Gilks, W. R. (2005), *Markov chain monte carlo*, Wiley Online Library.
- Godano, M. (2009), Étude théorique sur le calcul des mécanismes au foyer dans un réservoir et application à la sismicité de la saline de Vauvert (Gard), Ph. D., Université de Nice-Sophia Antipolis UFR Sciences, Nice- Sophia antipolis.
- Godano, M., A. Pussacq, T. Bardainne, E. Gaucher, and M. Valette (2009a), Focal mechanism determination from few sensors - Application to the Arkema-Vauvert site, France.
- Godano, M., M. Regnier, A. Deschamps, T. Bardainne, and E. Gaucher (2009b), Focal mechanisms from sparse observations by nonlinear inversion of amplitudes: method and tests on synthetic and real data, *Bulletin of the Seismological Society of America*, 99(4), 2243–2264.
- Grigoli, F., S. Cesca, O. Amoroso, A. Emolo, A. Zollo, and T. Dahm (2013), Automated seismic event location by waveform coherence analysis, *Geophysical Journal International*, doi:10.1093/gji/ggt477.
- Gritto, R., J. E. Siegel, and W. W. Chan (Eds.) (2008), *One Dimensional versus Three-Dimensional Crustal Velocity Models for the Korean Peninsula*, 07 pp.
- Groos, J. C., J. R. R. Ritter, and R. Fritschen (2013), Untersuchung induzierter Erdbeben hinsichtlich ihrer Spürbarkeit und eventueller Schadenswirkung anhand der DIN 4150, *Bauingenieur*, 88, 374–384.
- Grund, M., J. C. Groos, and J. R. R. Ritter (2016), Fault Reactivation Analysis Using Microearthquake Clustering Based on Signal-to-Noise Weighted Waveform Similarity, *pure and applied geophysics*, 1–31.
- Hadamard, J. (1902), Sur les problèmes aux dérivées partielles et leur signification physique, *Princeton University Bulletin*.
- Hammersley, J. (2013), *Monte carlo methods*, Springer Science & Business Media.
- Hardebeck, J. L., and P. M. Shearer (2002), A New Method for Determining First-Motion Focal Mechanisms, *Bulletin of the Seismological Society of America*, 92(6), 2264–2276, doi:10.1785/0120010200.
- Hardebeck, J. L., and P. M. Shearer (2003), Using S/P Amplitude Ratios to Constrain the Focal Mechanisms of Small Earthquakes, *Bulletin of the Seismological Society of America*, 93(6), 2434–2444, doi:10.1785/0120020236.
- Häring, M. O., U. Schanz, F. Ladner, and B. C. Dyer (2008), Characterisation of the Basel 1 enhanced geothermal system, *Geothermics*, 37(5), 469–495, doi:10.1016/j.geothermics.2008.06.002.

- Hauber, L. (1993), Der südliche Rheingraben und seine geothermische Situation, *Bulletin der Vereinigung schweizerischer Petroleumgeologen und Petroleumingenieure*, 60(137), 53–69.
- Heidbach, O., A. Barth, P. Connolly, K. Fuchs, B. Müller, M. Tingay, J. Reinecker, B. Spencer, and F. Wenzel (2004), Stress maps in a minute: the 2004 World Stress Map release, *Eos, Transactions American Geophysical Union*, 85(49), 521–529.
- Heimlich, C., N. Gourmelen, F. Masson, J. Schmittbuhl, S.-W. Kim, and J. Azzola (2015), Uplift around the geothermal power plant of Landau (Germany) as observed by InSAR monitoring: Geothermal Energy, *Geotherm Energy*, 3(1), 1–12, doi:10.1186/s40517-014-0024-y.
- Herzberger, P., W. Muench, T. Koelbel, U. Bruchmann, P. Schlagermann, H. Hoetzel, L. Wolf, D. Rettenmaier, H. Steger, R. Zorn, P. Seibt, G.-U. Moellmann, M. Sauter, J. Ghergut, and T. Ptak (2010), The geothermal power plant Bruchsal, 1st ed.
- Hestenes, M. R., and E. Stiefel (1952), Methods of conjugate gradients for solving linear systems, *J R NBS*, 49, 409–436.
- Householder, A. S. (1955), Terminating and nonterminating iterations for solving linear systems, *Journal of the Society for Industrial and Applied Mathematics*, 3(2), 67–72.
- Husen, S., and J. L. Hardebeck (2010), Earthquake location accuracy: Community Online Resource for Statistical Seismicity Analysis, doi:10.5078/corssa-55815573.
- Husen, S., E. Kissling, N. Deichmann, S. Wiemer, D. Giardini, and M. Baer (2003), Probabilistic earthquake location in complex three-dimensional velocity models: Application to Switzerland, *Journal of Geophysical Research: Solid Earth*, 108(B2), 2077, doi:10.1029/2002jb001778.
- IEA (2011), Technology Roadmap, Geothermal Heat and Power, (None), 52 pp., I. E. Agency.
- Illies, J. H. (1978), Two stages Rhinegraben rifting, pp. 63–71.
- Ito, A. (1985), High resolution relative hypocenters of similar earthquakes by cross-spectral analysis method, *Journal of Physics of the Earth*, 33, 279–294.
- Jackson, D. D. (1972), Interpretation of Inaccurate, Insufficient and Inconsistent Data, *Geophysical Journal International*, 28(2), 97–109, doi:10.1111/j.1365-246X.1972.tb06115.x.
- Jaynes, E. T. (2003), *Probabilistic theory, the logic of science*, Cambridge University Press, Cambridge.
- Jeffreys, H. (1939), *Theory of probability*, Oxford University Press, Oxford.
- Jepsen, D. C., and B. L. Kennett (1990), Three-component analysis of regional seismograms, *Bulletin of the Seismological Society of America*, 80(6B), 2032–2052.
- Julià, J., A. A. Nyblade, R. Durrheim, L. Linzer, R. Gök, P. Dirks, and W. Walter (2009), Source Mechanisms of Mine-Related Seismicity, Savuka Mine, South Africa, *Bulletin of the Seismological Society of America*, 99(5), 2801–2814, doi:10.1785/0120080334.
- Julian, B. R., and G. R. Foulger (1996), Earthquake mechanisms from linear-programming inversion of seismic-wave amplitude ratios, *Bulletin of the Seismological Society of America*, 86(4), 972–980.
- Kao, H., and S. Shan (2007), Rapid identification of earthquake rupture plane using Source-Scanning Algorithm, *Geophys J Int*, 168(3), 1011–1020, doi:10.1111/j.1365-246X.2006.03271.x.
- Kao, H., and S.-J. Shan (2004), The Source-Scanning Algorithm: mapping the distribution of seismic sources in time and space, *Geophys J Int*, 157(2), 589–594, doi:10.1111/j.1365-246X.2004.02276.x.
- Kikuchi, M., and H. Kanamori (1991), Inversion of complex body waves—III, *Bulletin of the Seismological Society of America*, 81(6), 2335–2350.
- Kinnaert, X., E. Gaucher, U. Achauer, and T. Kohl (2016), Modelling earthquake location errors at a reservoir scale: a case study in the Upper Rhine Graben, *Geophysical Journal International*, 206(2), 861–879.
- Kinnaert, X., E. Gaucher, T. Kohl, and U. Achauer, The combination of surface and downhole seismic networks for earthquake location at the Soultz-sous-Forêts geothermal site (France), *Pure Appl. Geophys.*, submitted.

- Kinscher, J., P. Bernard, I. Contrucci, A. Mangeney, J. P. Pigué, and P. Bigarre (2015), Location of microseismic swarms induced by salt solution mining, *Geophysical Journal International*, 200(1), 337–362, doi:10.1093/gji/ggu396.
- Kirkpatrick, S., C. D. Gelatt, and M. P. Vecchi (1983), Optimization by Simulated Annealing, *Science*, 220, 671–680.
- Klein, F. W. (1994), Deep fault plane geometry inferred from multiplet relative relocation beneath the south flank of Kilauea, *Journal of Geophysical Research*, 99(B8), 15,375.
- Kohl, T., K. F. Evans, R. J. Hopkirk, and L. Rybach (1995), Coupled hydraulic, thermal and mechanical considerations for the simulation of hot dry rock reservoirs, *Geothermics*, 24(3), 345–359, doi:10.1016/0148-9062(96)87109-9.
- Komatitsch, D., C. Barnes, and J. Tromp (2000), Simulation of anisotropic wave propagation based upon a spectral element method, *GEOPHYSICS*, 65(4), 1251–1260.
- Komatitsch, D., and R. Martin (2007), An unsplit convolutional perfectly matched layer improved at grazing incidence for seismic wave equation, *GEOPHYSICS*, 72(5), SM155-SM167, doi:10.1190/1.2757586.
- Komatitsch, D., and J. Tromp (1999), Introduction to the spectral element method for three-dimensional seismic wave propagation, *Geophysical Journal International*, 139(3), 806–822.
- Komatitsch, D., and J. Tromp (2003), A perfectly matched layer absorbing boundary condition for the second-order seismic wave equation, *Geophysical Journal International*, 154(1), 146–153, doi:10.1046/j.1365-246X.2003.01950.x.
- Korsch, R. J., and A. Schäfer (1995), The Permo-Carboniferous Saar-Nahe Basin, south-west Germany and north-east France: basin formation and deformation in a strike-slip regime, *Geol. Rundsch.*(84), 293–318.
- Kuzuoglu, M., and R. Mittra (1996), Frequency dependence of the constitutive parameters of causal perfectly matched anisotropic absorbers, *Microwave and Guided Wave Letters, IEEE*, 6(12), 447–449.
- Lahr, John, C. (1999), HYPOELLIPSE: A Computer Program for Determining Local Earthquake Hypocentral Parameters, Magnitude, and First-Motion Pattern, *Open File Report 99-23, Version 1.1*, 119 pp.
- Lanczos, C. (1961), *Linear differential operators*, SIAM.
- Langet, N., A. Maggi, A. Michelini, and F. Brenguier (2014), Continuous Kurtosis-Based Migration for Seismic Event Detection and Location, with Application to Piton de la Fournaise Volcano, La Réunion, *Bull. Seismol. Soc. Amer.*, 104(1), 229–246, doi:10.1785/0120130107.
- Larroque, J. M., A. Etchecopar, and H. Philip (1987), Evidence for the permutation of stresses  $\sigma_1$  and  $\sigma_2$  in the Alpine foreland: the example of the Rhine graben, *Tectonophysics*, 144(4), 315–322, doi:10.1016/0040-1951(87)90299-X.
- Laubscher, H. (1992), Jura kinematics and the Molasse Basin, *Eclogae Geol. Helv.*, 67, 121–133.
- Lay, C., and T. C. Wallace (1995), *Modern Global Seismology*, Academic Press, San Diego.
- Lee, W., and J. C. Lahr (1975), HYPO71 (revised): a computer program for determining hypocenter magnitude and first motion patterns of local earthquakes, 116 pp., U. G. Survey.
- Lee, W. H. K., and S. W. Stewart (1981), *Principles and applications of microearthquake networks*, Academic Press.
- Levander, A. R. (1988), Fourth-order finite-difference P-SV seismograms, *GEOPHYSICS*, 53(11), 1425–1436, doi:10.1190/1.1442422.
- Levenberg, K. (1944), A method for the solution of certain nonlinear problems in least squares, *Quart. Appl. Math.*, 2, 164–168.
- Li, J., H. S. Kuleli, H. Zhang, and M. N. Toksöz (2011a), Focal mechanism determination of induced microearthquakes in an oil field using full waveforms from shallow and deep seismic networks, *GEOPHYSICS*, 76(6), WC87-WC101, doi:10.1190/geo2011-0030.1.

- Li, J., H. Zhang, H. Sadi Kuleli, and M. Nafi Toksoz (2011b), Focal mechanism determination using high-frequency waveform matching and its application to small magnitude induced earthquakes, *Geophysical Journal International*, 184(3), 1261–1274, doi:10.1111/j.1365-246X.2010.04903.x.
- Liu, Q.-H., and J. Tao (1997), The perfectly matched layer for acoustic waves in absorptive media, *The Journal of the Acoustical Society of America*, 102(4), 2072–2082, doi:10.1121/1.419657.
- Lomax, A. (2011), *NonLinLoc: Probabilistic, Non-Linear, Global-Search Earthquake Location in 3D media*, ALomax Scientific.
- Lomax, A., J. Virieux, P. Volant, and C. Berge-Thierry (2000), Probabilistic Earthquake Location in 3D and Layered Models, in *Advances in Seismic Event Location, Modern Approaches in Geophysics*, edited by C. Thurber and N. Rabinowitz, pp. 101–134, Springer Netherlands.
- Loohuis, J., and T. van Eck (1996), Simultaneous focal mechanism and stress tensor inversion using a genetic algorithm, *Physics and Chemistry of the Earth*, 21(4), 267–271, doi:10.1016/S0079-1946(97)00047-5.
- Lopes-Cardozo, G. G. O., and J. H. Behrmann (2006), Kinematic analysis of the Upper Rhine Graben boundary fault system, *Journal of Structural Geology*, 28(6), 1028–1039, doi:10.1016/j.jsg.2006.03.010.
- Lopes-Cardozo, G. G. O., and M. Granet (2005), A multi-scale approach to study the lithospheric structure of the southern Upper Rhine Graben: from seismic tomography through reflection seismics to surface geology, *International Journal of Earth Sciences*, 94(4), 615–620, doi:10.1007/s00531-005-0476-1.
- Maggi, A., and A. Michelini (2010), Waveloc - An algorithm for the detection and location of seismic sources within large, continuous waveform data volumes: The case of the l'aquila earthquake sequences, EGU, Vienna, Austria.
- Magotra, N., N. Ahmed, and E. Chael (1987), Seismic event detection and source location using single-station (three-component) data, *Bulletin of the Seismological Society of America*, 77(3), 958–971.
- Maurer, V., N. Cuenot, E. Gaucher, M. Grunberg, J. Vergne, H. Wodling, M. Lehujuer, and J. Schmittbuhl (2015), Seismic monitoring of the Rittershoffen EGS project (Alsace, France): World Geothermal Congress, Melbourne, Australia, April 19-25 2014.
- Mayer, G., P. M. Mai, T. Plenefisch, H. Echtler, E. Lüschen, V. Wehrle, B. Müller, K.-P. Bonjer, C. Prodehl, and K. Fuchs (1997), The deep crust of the Southern Rhine Graben: reflectivity and seismicity as images of dynamic processes, *Tectonophysics*, 275(1–3), 15–40, doi:10.1016/S0040-1951(97)00014-0.
- McMechan, G. A. (1982), Determination of source parameters by wavefield extrapolation, *Geophysical Journal of the Royal Astronomical Society*, 71(3), 613–628, doi:10.1111/j.1365-246X.1982.tb02788.x.
- Meixner, J. (2010), Diplomarbeit: Konzeptionelle hydrogeologische Modellansätze als Vorstudie für ein integriertes Standortmodell, KIT - Institut für Angewandte Geowissenschaften - Abteilung Hydrogeologie, Karlsruhe, Germany.
- Meixner, J., E. Schill, J. C. Grimmer, E. Gaucher, T. Kohl, and P. Klingler (2016), Structural control of geothermal reservoirs in extensional tectonic settings: An example from the Upper Rhine Graben, *Journal of Structural Geology*, 82, 1–15.
- Menke, W. (1999), Using waveform similarity to constrain earthquake locations, *Bulletin of the Seismological Society of America*, 89(4), 1143–1146.
- Menke, W. (2012), *Geophysical data analysis: discrete inverse theory*, Academic Press.
- Metropolis, N., A. W. Rosenbluth, M. N. Rosenbluth, A. H. Teller, and E. Teller (1953), Equation of State Calculations by Fast Computing Machines, *The Journal of Chemical Physics*, 21(6), 1087–1092, doi:10.1063/1.1699114.

- Metropolis, N., and S. Ulam (1949), The Monte Carlo Method, *Journal of the American Statistical Association*, 44(247), 335–341, doi:10.1080/01621459.1949.10483310.
- Michelini, A., and A. Lomax (2004), The effect of velocity structure errors on double-difference earthquake location, *Geophys Res Lett*, 31(9), doi:10.1029/2004gl019682.
- MOCZO, P., J. KRISTEK, and E. Bystrický (2001), Efficiency and optimization of the 3-D finite-difference modeling of seismic ground motion, *Journal of Computational Acoustics*, 9(02), 593–609.
- Moriya, H., K. Nakazato, H. Niitsuma, and R. Baria (2002), Detailed fracture system of the Soultz-sous-Forêts HDR field evaluated using microseismic multiplet analysis, *Pure Appl. Geophys.*, 159, 517–541.
- Mosegaard, K., and A. Tarantola (1995), Monte Carlo sampling of solutions to inverse problems, *J. Geophys. Res.*, 100(B7), 12431–12447, doi:10.1029/94JB03097.
- Moser, T. J., T. van Eck, and G. Nolet (1992), Hypocenter determination in strongly heterogeneous Earth models using the shortest path method, *Journal of Geophysical Research: Solid Earth*, 97(B5), 6563–6572, doi:10.1029/91jb03176.
- Nakano, H. (1923), Notes on the Nature of the Forces which Give Rise to the Earthquake Motions, *Cent. Meteor. Obs. Japan Seism. Bull.*, 1, 92–120.
- Natale, G. de (1994), Focal mechanism determination for volcanic microearthquakes, *Annali di Geofisica*, 37(6).
- Natale, G. de, A. Ferraro, and J. Virieux (1991), A probability method for local earthquake focal mechanisms, *Geophysical Research Letters*, 18(4), 613–616.
- Nolet, G. (1985), Solving and resolving inadequate and noise tomographic systems, *Journal of Computational Physics*, 61, 463–482.
- Patera, A. T. (1984), A spectral element method for fluid dynamics: laminar flow in a channel expansion, *Journal of Computational Physics*, 54(3), 468–488.
- Pavlis, G. L. (1986), Appraising earthquake hypocenter location errors: A complete, practical approach for single-event locations, *Bull. Seismol. Soc. Amer.*, 76(6), 1699–1717.
- Pavlis, G. L. (1992), Appraising relative earthquake location errors, *Bulletin of the Seismological Society of America*, 82(2), 836–859.
- Person, M., and G. Garven (1992), Hydrologic constraints on petroleum generation within continental rift basins: theory and application to the Rhine graben (1), *AAPG Bulletin*, 76(4), 468–488.
- Plenefisch, T., and K. P. Bonjer (1997), The stress field in the Rhine Graben area inferred from earthquake focal mechanisms and estimation of frictional parameters, *Tectonophysics*, 275(1–3), 71–97, doi:10.1016/s0040-1951(97)00016-4.
- Plenkens, K., J. R. Ritter, and M. Schindler (2013), Low signal-to-noise event detection based on waveform stacking and cross-correlation: application to a stimulation experiment, *J Seismol*, 17(1), 27–49, doi:10.1007/s10950-012-9284-9.
- Podvin, P., and I. Lecomte (1991), Finite difference computation of traveltimes in very contrasted velocity models: a massively parallel approach and its associated tools, *Geophys J Int*, 105(1), 271–284, doi:10.1111/j.1365-246X.1991.tb03461.x.
- Poupinet, G., W. L. Ellsworth, and J. Fréchet (1984), Monitoring velocity variations in the crust using earthquake doublets: an application to the Calaveras fault, California, *Journal of Geophysical Research*, 89, 5719–5731.
- Poupinet, G., J. Fréchet, W. L. Ellsworth, M. J. Frémont, and F. Glangaud (1985), Doublet analysis: improved accuracy for earthquake prediction studies, *Earthq. Predict. Res.*, 1, 147–159.
- Press, F. (1968), Earth models obtained by Monte Carlo inversion, *J. geophys. Res.*, 73(16), 5223–5234.
- Pribnow, D., and R. Schellschmidt (2000), Thermal tracking of upper crustal fluid flow in the Rhine graben., *Geophysical Research Letters*, 27(13), 1957–1960, doi:10.1029/2000GL008494.

- Rabinowitz, N., and A. Hofstetter (1992), A rapid algorithm for estimating fault plane solution using polarity-amplitude data: application of a non-linear programming approach, *Physics of the Earth and Planetary Interiors*, 73(3), 239–254.
- Raleigh, C. B., J. H. Healy, and J. D. Bredehoeft (1976), An experiment in earthquake control at Rangely, Colorado, *Science*, 191, 1230–1237.
- Ramm, A. G. (2006), *Inverse Problems: Mathematical and analytical techniques with applications to engineering*, Springer Science & Business Media B.V.
- Rau, R.-J., F. T. Wu, and T.-C. Shin (1996), Regional network focal mechanism determination using 3D velocity model and SH/P amplitude ratio, *Bulletin of the Seismological Society of America*, 86(5), 1270–1283.
- Reasenber, P., and D. H. Oppenheimer (1985), FPFIT, FPLOT and FPPAGE; Fortran computer programs for calculating and displaying earthquake fault-plane solutions, US Geological Survey.
- Ritter, J., M. Wagner, K. P. Bonjer, and B. Schmidt (2009), The 2005 Heidelberg and Speyer earthquakes and their relationship to active tectonics in the central Upper Rhine Graben, *International Journal of Earth Sciences*, 98(3), 697–705, doi:10.1007/s00531-007-0284-x.
- Ritter, J. R. R. (2011), Konzeptionelle Ansätze zur Überwachung induzierter Seismizität im Oberrheingraben im Rheinland Pfalz, *Mainzer Geowiss. Mitt.*, 39, 157–176.
- Rivera, L., and A. Cisternas (1990), Stress tensor and fault plane solutions for a population of earthquakes, *Bulletin of the Seismological Society of America*, 80(3), 600–614.
- Rotstein, Y., J. H. Behrmann, M. Lutz, G. Wirsing, and A. Luz (2005), Tectonic implications of transpression and transtension: Upper Rhine Graben, *Tectonics*, 24(6).
- Rotstein, Y., and M. Schaming (2011), The Upper Rhine Graben (URG) revisited: Miocene transtension and transpression account for the observed first-order structures, *Tectonics*, 30(3), doi:10.1029/2010tc002767.
- Rutledge, J. T., and W. S. Phillips (2002), A comparison of microseismicity induced by gel-proppant- and water-injected hydraulic fractures, Carthage Cotton Valley gas field, East Texas, *Internat. Mtg., Soc. Explor. Geophys., Expanded Abstracts*, 2393–2396.
- Sambridge, M. S., and B. L. N. Kennett (1986), A novel method of hypocentre location, *Geophysical Journal International*, 87(2), 679–697, doi:10.1111/j.1365-246X.1986.tb06644.x.
- Sanjuan, B., R. Millot, C. Dezayes, and M. Brach (2010), Main characteristics of the deep geothermal brine (5 km) at Soultz-sous-Forêts (France) determined using geochemical and tracer test data, *Comptes Rendus Geoscience*, 342(7-8), 546–559, doi:10.1016/j.crte.2009.10.009.
- Sausse, J., C. Dezayes, L. Dorbath, A. Genter, and J. Place (2010), 3D model of fracture zones at Soultz-sous-Forêts based on geological data, image logs, induced microseismicity and vertical seismic profiles, *Comptes Rendus Geoscience*, 342(7-8), 531–545, doi:10.1016/j.crte.2010.01.011.
- Schindler, M., J. Baumgärtner, T. Gandy, P. Hauffe, T. Hettkamp, H. Menzel, P. Penzkofer, D. Teza, T. Tischner, and G. Wahl (2010), Successful hydraulic stimulation techniques for electric power production in the Upper Rhine graben, Central Europe, 1st ed.
- Schnaebeler, R. (1948), *Monographie géologique du champ pétrolifère de Pechelbronn*, Mémoire du Service de la Carte Géologique d'Alsace et de Lorraine, Strasbourg, France.
- Schoenball, M., L. Dorbath, E. Gaucher, J. F. Wellmann, and T. Kohl (2014), Change of stress regime during geothermal reservoir stimulation, *Geophys Res Lett*, 41(4), 1163–1170, doi:10.1002/2013gl058514.
- Schumacher, M. E. (2002), Upper Rhine Graben: Role of preexisting structures during rift evolution, *Tectonics*, 21(1), 6-1-6-17, doi:10.1029/2001tc900022.
- Schweitzer, J., J. Fyen, S. Mykkeltveit, S. J. Gibbons, M. Pirli, D. Kühn, and T. Kvaerna (2011), Chapter 9: Seismic Arrays, in *New Manual of Seismological Observatory Practice (NMSOP-2)*, IASPEI, edited by P. Bormann, p. 80, GFZ German Research Centre for Geosciences, Potsdam, Germany.



- Sen, M. K., and P. L. Stoffa (2013), *Global optimization methods in geophysical inversion*, Cambridge University Press.
- Shearer, P. M. (2009), *Introduction to Seismology*, 2nd ed., Cambridge University Press.
- Šílený, J., and A. Milev (2008), Source mechanism of mining induced seismic events — Resolution of double couple and non double couple models, *The Monitoring of Induced Seismicity: Observations, Models and Interpretations*, 456(1–2), 3–15, doi:10.1016/j.tecto.2006.09.021.
- Snieder, R., and J. Trampert (2000), *Inverse problems in geophysics*, Utrecht University, Netherlands.
- Snoke, J. A. (2003), FOCMEC: focal mechanism determinations, *International Handbook of Earthquake and Engineering Seismology*, 85.
- Sokos, E., and J. Zahradník (2008), ISOLA: a Fortran code and a Matlab GUI to perform multiple point source inversion of seismic data, *Computers & Geosciences*, 34, 967–977.
- Sokos, E., and J. Zahradník (2013), Evaluating centroid-moment -tensor uncertainty in the new version of ISOLA software, *SRL*, 84, 656–665.
- Spakman, W., and G. Nolet (1988), Imaging algorithms, accuracy and resolution in delay time tomography, in *Mathematical Geophysics: A Survey of Recent Developments in Seismology and Geodynamics*, edited by N. J. Vlaar et al., pp. 155–187, Springer Netherlands, Dordrecht.
- Stein, S., and M. Wyss (2009), *An introduction to seismology, earthquakes, and earth structure*, John Wiley & Sons.
- Strang (1988), *Linear algebra and its applications*, Harbourt Brace Jovanovich Publishers, Fort Worth.
- Stussi, J. M., J. M. Cheilletz, J.-J. Royer, P. Chèvremont, and G. Féraud (2002), The hidden monzogranite of Soultz-sous-Forêts (Rhine Graben, France), *Mineralogy petrology and genesis Geol. France*, 1, 45–64.
- Tan, Y., and D. Helmberger (2007), A New Method for Determining Small Earthquake Source Parameters Using Short-Period P Waves, *Bulletin of the Seismological Society of America*, 97(4), 1176–1195, doi:10.1785/0120060251.
- Tarantola, A. (Ed.) (2005), *Inverse problem theory and methods for model parameter estimation*, 358 pp., Society for Industrial and Applied Mathematics, Philadelphia.
- Tarantola, A., and B. Valette (1982), Inverse problems = quest for information, *Journal of Geophysics*, 50, 159–170.
- Tarantola Albert (2005), *Inverse Problem Theory, and Methods for Model Parameter Estimation*, 2nd ed., Paris FR.
- Thurber, C., and N. Rabinowitz (Eds.) (2000), *Advances in Seismic Event Location, Modern Approaches in Geophysics*, Springer Netherlands.
- Thurber, C. H. (1983), Earthquake locations and three-dimensional crustal structure in the Coyote Lake Area, central California, *J. Geophys. Res.*, 88(B10), 8226–8236, doi:10.1029/JB088iB10p08226.
- Toksöz, M. N., H. S. Kuleli, C. A. Schultz, D. B. Harris, C. Gürbüz, D. Kalafat, and A. M. Isikara (2000), Calibration of regional seismic stations in the middle east with shots in Turkey, *Seismic Research Review*(24).
- Tukey, J. W. (1977), *Exploratory Data Analysis*, 503 pp., Behavioral Science, Addison-Wesley, Reading, MA.
- Valley, B., and K. F. Evans (2007), Stress state at Soultz-sous-Forêts to 5 km depth from wellbore failure and hydraulic observations, 1st ed.
- Vallina, A. U. (1999), *Principles of seismology*, Cambridge University Press.
- Villemin, T., and F. Bergerat (1987), L'évolution structurale du fossé rhénan au cours du Cénozoïque: un bilan de la déformation et des effets thermiques de l'extension, *Bulletin de la Société géologique de France*, 3, 245–255.

- Virieux, J. (1984), SH-wave propagation in heterogeneous media: Velocity-stress finite-difference method, *GEOPHYSICS*, 49(11), 1933–1942, doi:10.1190/1.1441605.
- Virieux, J. (1986), P-SV wave propagation in heterogeneous media: Velocity-stress finite-difference method, *GEOPHYSICS*, 51(4), 889–901, doi:10.1190/1.1442147.
- Waldhauser, F., and W. L. Ellsworth (2000), A double-difference earthquake location algorithm: Method and application to the Northern Hayward fault, California, *Bull. Seismol. Soc. Amer.*, 90(6), 1353–1368.
- Walsh, D., R. Arnold, and J. Townend (2009), A Bayesian approach to determining and parametrizing earthquake focal mechanisms, *Geophysical Journal International*, 176(1), 235–255, doi:10.1111/j.1365-246X.2008.03979.x.
- Wax, M., J. Sheinvald, and A. J. Weiss (1996), Detection and localization in colored noise via generalized least squares, *Signal Processing, IEEE Transactions on*, 44(7), 1734–1743.
- Wenke, A., H. Kreuter, W. Gall, S. Gutekunst, L. Rohrer, and Zühlke Rainer (2010), First steps in the development of a new geothermal field in the northern part of the Upper Rhine Graben, Germany.
- Wentzel, F., and J.-P. Brun (1991), A deep Reflection Seismic Line across the Northern Rhine Graben, *Earth and Planetary Science Letters*, 104, 140–150.
- Wiggins, R. A. (1972), The general linear inverse problem: Implication of surface waves and free oscillations for Earth structure, *Rev. Geophys.*, 10(1), 251–285, doi:10.1029/RG010i001p00251.
- Winton, S. C., and C. M. Rappaport (2000), Specifying PML conductivities by considering numerical reflection dependencies, *Antennas and Propagation, IEEE Transactions on*, 48(7), 1055–1063.
- Withers, M., R. Aster, and C. Young (1999), An automated local and regional seismic event detection and location system using waveform correlation, *Bull. Seismol. Soc. Amer.*, 89(3), 657–669.
- Wittlinger, G., G. Herquel, and T. Nakache (1993), Earthquake location in strongly heterogeneous media, *Geophys J Int*, 115(3), 759–777, doi:10.1111/j.1365-246X.1993.tb01491.x.
- Zeng, X., H. Zhang, X. Zhang, H. Wang, Y. Zhang, and Q. Liu (2014), Surface Microseismic Monitoring of Hydraulic Fracturing of a Shale-Gas Reservoir Using Short-Period and Broadband Seismic Sensors, *Seismological Research Letters*, 85(3), 668–677.
- Zhang, H., and C. H. Thurber (2003), Double-Difference Tomography: The Method and Its Application to the Hayward Fault, California, *Bull. Seismol. Soc. Amer.*, 93(5), 1875–1889, doi:10.1785/0120020190.
- Zhang, J., and G. A. McMechan (1995), Estimation of resolution and covariance for large matrix inversions, *Geophysical Journal International*, 121(2), 409–426, doi:10.1111/j.1365-246X.1995.tb05722.x.
- Zhao, L.-S., and D. V. Helmberger (1994), Source estimation from broadband regional seismograms, *Bulletin of the Seismological Society of America*, 84(1), 91–104.
- Ziegler, P. A. (1992), European Cenozoic rift system, *Tectonophysics*, 208, 91–111.
- Ziegler, P. A., and P. Dèzes (2007), Cenozoic uplift of Variscan Massifs in the Alpine foreland: timing and controlling mechanisms, *Global and Planetary Change*, 58(1), 237–269.
- Zoback, M. L. (1992), First and second order patterns of stress in the lithosphere: The World Stress Map Project, *JGR*, 97.
- Zollo, A., and P. Bernard (1989), S-wave polarization inversion of the 15 October 1979, 23: 19 Imperial valley aftershock: evidence for anisotropy and a simple source mechanism, *Geophys Res Lett*, 16, 1047–1050.
- Zollo, A., and P. Bernard (1991), Fault mechanisms from near-source data: joint inversion of S polarisations and P polarities, *Geophys J Int*, 104, 441–451.

# APPENDICES

# 10 Modelling seismic event location errors at the reservoir scale: application to the geothermal site of Soultz-sous-Forêts (Alsace, France)

X. Kinnaert<sup>1,2\*</sup>, E. Gaucher<sup>1\*</sup>, T. Kohl<sup>1</sup> and U. Achauer<sup>2</sup>

<sup>1</sup>: Division of Geothermal Research, Institute of Applied Geosciences, Karlsruhe Institute of Technology, Adenauerring 20b, Geb 50.40., D-76131 Karlsruhe, Germany.

<sup>2</sup>: EOST-IPGS UMR7516, 5 rue René Descartes, F-67000 Strasbourg, France.

\*Corresponding authors: [xavier.kinnaert@kit.edu](mailto:xavier.kinnaert@kit.edu), [emmanuel.gaucher@kit.edu](mailto:emmanuel.gaucher@kit.edu)

## Abstract

The location of earthquakes is of primary interest for seismic studies since many other characteristics of the seismic events and of the sub-surface are derived from it. We investigate the impact on the event absolute location errors of several parameters. In the location errors, we distinguish between location uncertainties and location inaccuracies.

A two-steps approach is applied to model these inaccuracies and uncertainties. In the first step, travel-times between synthetic earthquake locations and seismic receiver positions are calculated for body-waves. In the second step, the obtained travel-times are used as observed (picked) travel-times in the inverse problem formulation. However, several of the initial hypotheses are changed before location to represent the lack of knowledge or simplifications which are investigated.

The method is applied to the geothermal site of Soultz-sous-Forêts (Alsace, France). In 2000, a massive water injection was performed at approximately 5 km depth, in the granitic basement, to enhance the GPK2 well productivity. A down-hole and a surface networks recorded several thousands of induced micro-earthquakes.

In this work, we more specifically quantify the location variation due to the joint use of the down-hole and surface networks, or to the use of one of those networks alone. Besides the

description of the usual location uncertainties, the impact of the picking time precision in the input catalogue (at  $\pm 10$  ms) is investigated. Then, velocity model assumptions are modified to mimic the possible effect of a massive water injection and its impact on earthquake hypocentres.

The down-hole network is proven to be useful to decrease the location uncertainty obtained from the surface network alone, because of the increased coverage in depth. Nevertheless, the locations computed using this network may be more biased.

The proposed method and results could benefit to the geothermal fields developed in a similar context.

**Key words:** Location inaccuracy; Location uncertainty; Seismic coverage; Soultz; Geothermal field; EGS

## 10.1 Introduction

Because of the multiplicity of tasks requiring it, earthquake location is of primary interest for the geo-community. For example, it can be used either to determine other characteristic of the seismic source or to identify faults and fractures in the sub-surface (e.g. Frietsch *et al.*, 2015). The scale of the location errors however determines the scale at which results can be interpreted. For reservoir studies, location errors sometimes lower than 100 m may lead to misinterpretation of the sub-surface (Kinnaert *et al.*, 2016). Hence, the error associated with the earthquake location is of primary importance to obtain reliable result analysis and should always be investigated.

The earthquake location error can be described as the combination of the location inaccuracy and the location uncertainty. The location uncertainties are directly linked to the uncertainties which are taken into account during the location process (e.g. Tarantola, 2005). Typically, *a priori* picking uncertainties of seismic body-waves are integrated in the location inverse problem and contribute to *a posteriori* location uncertainties which are therefore part of the location result. On the contrary, the location inaccuracy is defined as the wrong positioning of the earthquake hypocentre due to all effects that have been ignored in the inverse problem. These simplifications of the reality introduce systematic errors, or bias, in the computation of the earthquake location. Usually, a velocity model not representative of the effective seismic propagation medium will lead to earthquake location inaccuracies (Pavlis, 1986; Husen *et al.*,

2013). Nevertheless, because of a lack of a-priori knowledge, the location inaccuracies cannot always be determined and are not often studied. This work focuses on location inaccuracies and uncertainties for absolute location.

The method is applied here on the well-known geothermal site of Soultz-sous-Forêt (France) for which many studies were done. In this paper, the main investigation concerns the impact of the seismic network design on the location inaccuracies and uncertainties. The method to quantify location inaccuracies and uncertainties is first described. Then, the Soultz geothermal site is presented. The impact of the different seismic coverages is quantified and the possible effect on sub-surface interpretation is discussed. The effect of picking time precision in a reference catalogue is also investigated. At last the velocity model is perturbed to mimic the impact of massive water injection.

## 10.2 Methodology

In order to get seismic event location uncertainties and inaccuracies, a two-steps method based on state-of-the-art techniques is applied.

During the synthetic modelling step, travel-times for body waves are calculated between synthetic sources and the position of different seismic sensors. In this first step, the assumptions are supposed to represent the reality of the sub-surface. The travel-times are computed using the finite-difference method of Podvin and Lecomte (1991) implemented in the NonLinLoc software (Lomax, 2011).

In the second step, the travel-times obtained in the synthetic modelling step are considered as observations and are used to (re-)locate the synthetic seismic event. Nevertheless, few modifications are introduced in the input data (velocity model, different seismic networks, time uncertainty and precision). The location is performed using the NonLinLoc software already mentioned and the grid-search method (Lomax *et al.*, 2009), which provides a complete Probability Density Function (PDF) of the event hypocentre. This software has the advantage to keep the non-linearity of the location inverse problem and to apply the Bayesian formalism proposed by Tarantola and Valette (1982) and methodology of Wittlinger *et al.* (1993), which allows the user to perform calculations in complicated models such as 3D structures.

For simplicity, we will define the location uncertainty as the half-length of the longest axis of the PDF for a 68.3 % confidence level, assuming a Gaussian posterior distribution (Lomax, 2011). The inaccuracy is obtained by comparing the hypocentre position obtained after the (re-)location process with the initial synthetic hypocentre of the source and corresponds to the Cartesian distance. Horizontal and vertical inaccuracies will also be discussed.

## **10.3 The Soultz-sous-Forêts geothermal site**

### **10.3.1 Geological settings**

The Soultz-sous-Forêts geothermal site is located in the Upper Rhine Graben (URG), in France. The geological and structural settings of the shallow sub-surface in the URG are well known due to earlier investigations from the oil industry (Schnaebele, 1948) and several seismic reflexion and refraction profiles. The profiles provided relatively good knowledge of the sedimentary cover in the Soultz area and highlighted the numerous horst and grabens typical of the URG (Wentzel and Brun, 1991).

Because of the presence of fracture networks in the sub-surface and thermal anomalies (Bailleux *et al.*, 2013) the URG is suitable for geothermal energy development. Besides Soultz, several deep geothermal sites exist (Landau, Insheim, Bruchsal) or are under development (Rittershoffen, Gross-Gerau).

At Soultz, two main reservoirs have been developed at around 3500 m and 5000 m depth in the granitic basement. Temperature reaches about 200°C (Baumgärtner *et al.*, 2000) in the deepest one. The highly fractured Paleozoic granitic basement is overlaid by about 1400 m of sediments from tertiary and quaternary eras (Genter *et al.*, 2010).

### **10.3.2 Seismicity induced in 2000**

In 2000, the well GPK2 was stimulated by a massive water injection which induced several thousands of micro-earthquakes (e.g. Cuenot *et al.*, 2008) recorded by both down-hole and surface seismic stations. Cuenot *et al.* (2008) were the first to combine the data from both networks to locate the induced seismicity. The obtained 7215 events were located in the granite, between 4000 and 5500 m depth (Cuenot *et al.*, 2008; Dorbath *et al.*, 2009). The seismic cloud is oriented N60E or N30W and referencing to GPK1 wellhead extended about -2.5 km to the North and about -1.5 km to the East with a rotation of about 30° counter-

clockwise. In the present paper, as in many other studies before ours, the earthquake catalogue resulting from the work of Cuenot *et al.* (2008) is used as a reference database.

### 10.3.3 Reference velocity model

The model used by and well-described in Cuenot *et al.* (2008) is here taken as a reference. Velocity model increases only as a function of depth (Figure 10-1) and no low-velocity-layer is included. The P-waves velocity is comprised between  $\sim 1800$  m/s in the shallowest sedimentary layer and  $\sim 5800$  m/s at the top of the non-altered granitic layer, which is located at  $\sim 1700$  m depth. The largest velocity contrast is observed at the sediment-altered granite interface, close to 1400 m depth. The S-wave velocity ranges from 860 m/s in the shallow sedimentary layer to  $\sim 3300$  m/s in the non-altered granitic basement. The  $V_p/V_s$  ratio is not constant over depth and varies between 1.75 in the granite and 2.15 for the shallowest sedimentary layer.

In our work, this model is always used to relocate the synthetic sources.

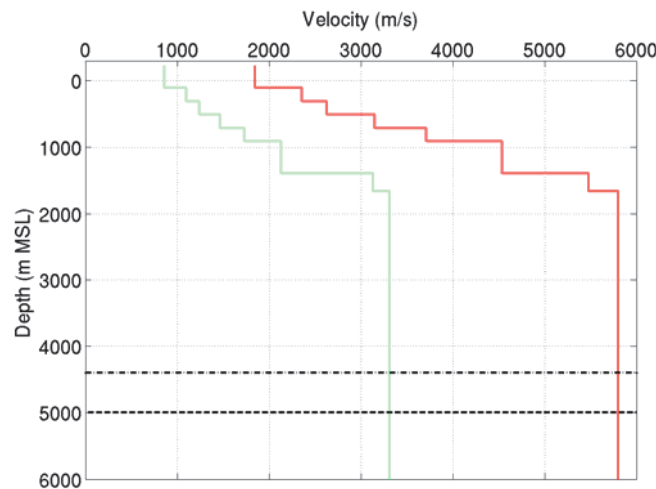


Figure 10-1: Reference P- (red curve) and S-wave (green curve) velocity profiles as described by Cuenot (2009, p.115). The shallower dashed line delimits the top of the deep injection zone during the GPK2 stimulation and the deeper dashed line delimits the bottom of GPK2.

### 10.3.4 Seismic monitoring network

In this paper, we deal with the seismic network used by Cuenot *et al.* (2008) to work out the reference picking catalogue and to locate the induced earthquakes of the GPK2 stimulation. This seismic network consisted of two main parts: a down-hole network and a surface



network. Three accelerometers with 4 components (in wells 4550, 4601 and OPS4 at ~1500 m depth) and 2 hydrophones (in wells EPS1 and GPK1 at ~2000 m and ~3500 m depth respectively) constitute the down-hole network (Dyer, 2001). Among them, the EPS1 sensor is not used in this study to mimic the lack of (reliable) picking at this station. The surface seismic network deployed before the stimulation was composed of eight vertical components sensors and nine 3C-sensors. However, to be still consistent with the reference processing catalogue, the three 3C-sensors of the ReNaSS seismic network were not used. One can note that one of the surface 3C-sensor (CARO) was installed near the GPK1 wellhead and thus right above the induced seismic cloud.

Three network combinations are used to locate the hypocentres in order to study the impact of the seismic coverage and more specifically of the down-hole network. Locations are computed with the observations from four down-hole sensors alone (red triangles in Figure 10-2). A network composed of 14 surface sensors (green triangles on Figure 10-2) alone gives a second set of hypocentres. The third network used here is simply the combination of both previous networks and is called the “combined network” in the following. Each of those three network combinations is used separately in all inversion cases investigated in the following.

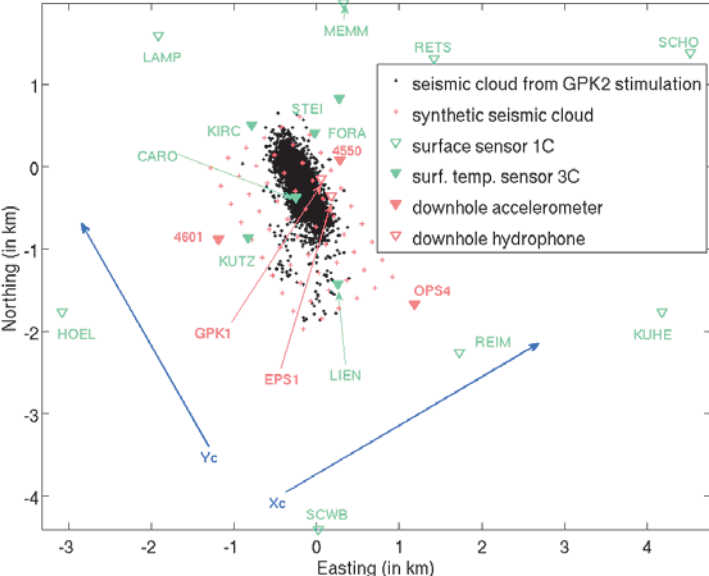


Figure 10-2: Geometry of the seismic networks monitoring during the stimulation of the well GPK2 in June-July 2000. The filled triangles stand for 3C-sensors whereas the empty symbols stand for mono-component geophones. Red and green triangles show the position of the down-hole and surface sensors respectively. The projections of the synthetic (crosses) and real (dots) seismic clouds (Cuenot, 2009) are also represented. The blue arrows show the  $X_c$  and  $Y_c$  axes used in this study, which correspond to a rotation of the original geographic system according to the main distribution of the seismic cloud. Easting and Northing are given relative to GPK1 well-head.

### **10.3.5 Synthetic event hypocentres**

To investigate the location errors, we created a synthetic seismic cloud (red crosses on Figure 10-2) representing the real one (black dots) obtained for the stimulation of GPK2. In the rotated system described by  $X_c$  and  $Y_c$  axes on Figure 10-2, the synthetic sources are distributed every 125 m in each direction. It extends from -1.125 to 0.125 km along  $X_c$  and from -1.625 to 0.625 km along  $Y_c$ . All coordinates are given referred to the GPK1 well-head in a system rotated  $30^\circ$  anti-clockwise. The real seismic events mainly cover the North-East quarter of the synthetic event zone. Hence, we will focus our interpretations on this part.

In the following sections either all sources in the described 3D grid or a set of three planes will be used. The extension of the planes is similar to the extension of the 3D grid and they all cut the well at the mid-point of the GPK2 open-hole section. Therefore, the horizontal plane is situated at a depth of 4529 m, a vertical plane oriented along  $X_c$  is 311 m south of GPK1 and one oriented along  $Y_c$  is 234 m west.

All depths given in this paper are true vertical depth from mean sea level (TVD MSL) unless specified differently. The reference system is also the rotated coordinate system defined by the  $X_c$ ,  $Y_c$  and vertical directions.

## **10.4 Results and discussion**

### **10.4.1 Location uncertainties**

To quantify location uncertainties, the only modification done between the synthetic modelling step and the location step is the addition of picking uncertainties to the travel-times. Hence, we used the reference layered velocity model, which is discretized on a 12.5 m mesh, for both steps. Picking uncertainty of 5 ms and 15 ms were implemented for down-hole stations and surface stations respectively. P- and S-waves uncertainties were taken similar. All sources of the 3D grid are relocated. The combined network, which was used to create the reference catalogue, is taken as a reference in our discussion.

In Figure 10-3 the evolution of location uncertainties along the two directions given by  $X_c$ ,  $Y_c$  and along depth is quantified using boxplots (Tukey, 1977). Our boxplots are formed with the median, the first (Q1) and third (Q3) quartiles, and the range defined by the minimum and

the maximum of the considered dataset. The Q1 (respectively the Q3) value is the threshold value for which 25 % of the dataset is lower (respectively higher). The location uncertainty obtained from the combined network increases almost linearly with increasing depth. The median reaches about 73 m at 5500 m and the maximum 77 m in the deepest part. Such an evolution is not seen along the Xc and Yc axes. The location uncertainty increases to the North and to the South along Xc from a point roughly corresponding to the latitude of the mid-point of GPK2 open-hole section. In the North-East part of the synthetic cloud, where most of the induced seismicity was located (Figure 10-2), the absolute locations can suffer uncertainties with a median ~65 m and a maximum Q3 ~70 m depending on the source depth. The obtained uncertainties are a bit smaller than the 80-100 m given as means by Cuenot *et al.* (2008).

Locating using the down-hole network alone leads to location uncertainties of the order of 65-95 m as a median value and a maximum uncertainty of about 105 m (Figure 10-4, left panels). Because of the depth of the sensors, their relative proximity to the synthetic seismic cloud and the relatively small picking uncertainties ( $\pm 5$  ms), the obtained locations are quite precise. On the contrary, locations calculated with the surface network alone lead to larger uncertainties. In the worst case, uncertainty of ~150 m is obtained (Figure 10-4, right panels). Comparing the location uncertainties from all networks, we suggest that the down-hole network has a strong influence on them. Furthermore, the down-hole network better constrains the location uncertainties in the South direction while the surface network better constrains the location uncertainties in the North along Yc. Finally, one can see that the down-hole network provides better depth control of the event hypocentres, especially for the shallower earthquakes.

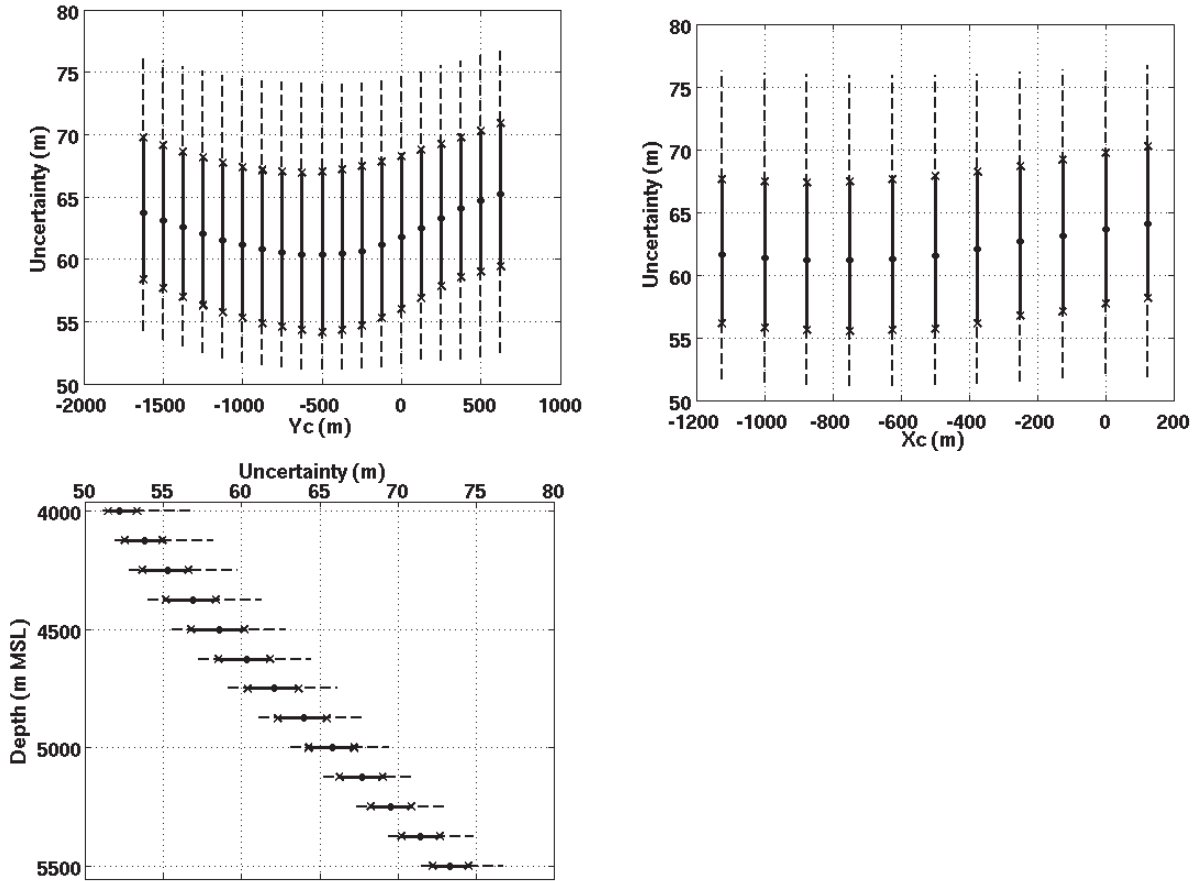


Figure 10-3 : Boxplots of the location uncertainties computed with the combination of the surface and the down-hole seismic networks. The variation with depth (bottom panel), along  $X_c$  (top right panel) and along  $Y_c$  (top left panel) are presented. The boxplots show the range of values (dashed lines), the first and third quartile (crosses) and the median (disk).

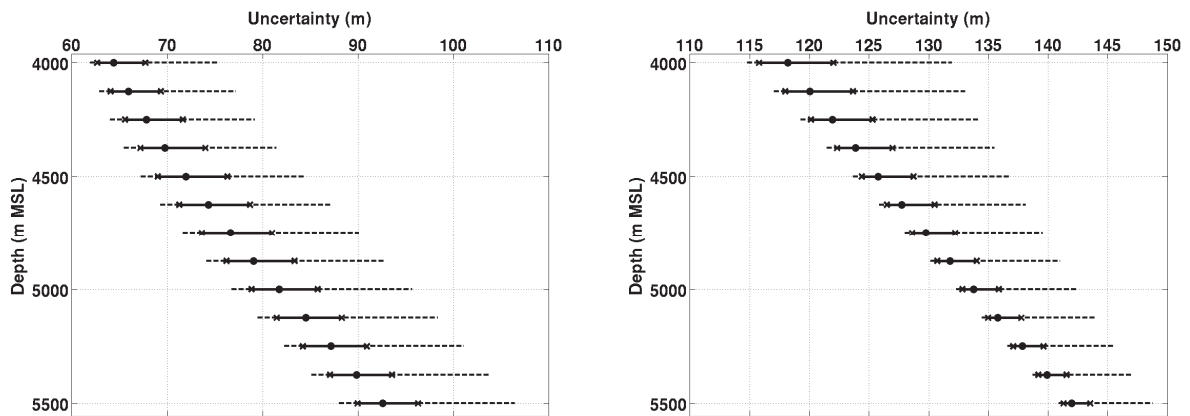


Figure 10-4: Uncertainties obtained with the down-hole network (left panel) and with the surface network (right panel). Boxplots symbols are the same as in Figure 10-3.

The amplitude and spatial distribution of the uncertainties described previously will remain very similar in the next studies of this paper.

## 10.4.2 Location errors due to inaccuracies in the input travel-times

Many software used for processing earthquake location as well as picking seismograms deal with input arrival-time picking accuracy rounded at 10 ms. Here, we quantify the possible effects at Soultz, where the induced seismicity was located using a reference catalogue with 10 ms as picking accuracy. In our method, we rounded at the nearest 10 ms the travel-times of the modelling step prior to location. All sources of the 3D grid are used. Both the synthetic modelling and the location were computed in the reference velocity model.

No significant vertical inaccuracy has been obtained in any direction and for all tested network: the absolute values of the first and third quartiles are always smaller than or equal to the mesh size used for the location process. For the combined network, observed inaccuracies are of the order of 15 to 30 m as median values with the smallest inaccuracies in Eastern and Southern part of the cubic modelled seismic cloud and for the shallowest events (Figure 10-5). A total bias of ~60m is obtained for the most inaccurate locations.

The location obtained using the down-hole network alone leads in general to global locations inaccuracies with median between 30 and 40 m showing similar variations as the horizontal inaccuracy. A bias up to 90-95 m can be found for the less accurate locations at depth and in the North part of the synthetic cloud. Hence, performing event location using the down-hole network alone does multiply the uncertainties and inaccuracies by a factor of about 1.5 as to compare to results obtained for the combined network.

Bias modelled for locations performed with the surface network alone are lower than the one obtained for the combined network. Global inaccuracies smaller than 20 m are found as a median case in all direction of the cubic cloud whereas the Q3 value does not exceed 30 m and a maximum bias of about 50 m is seen for the deepest sources and somewhere in the middle of the cubic cloud.

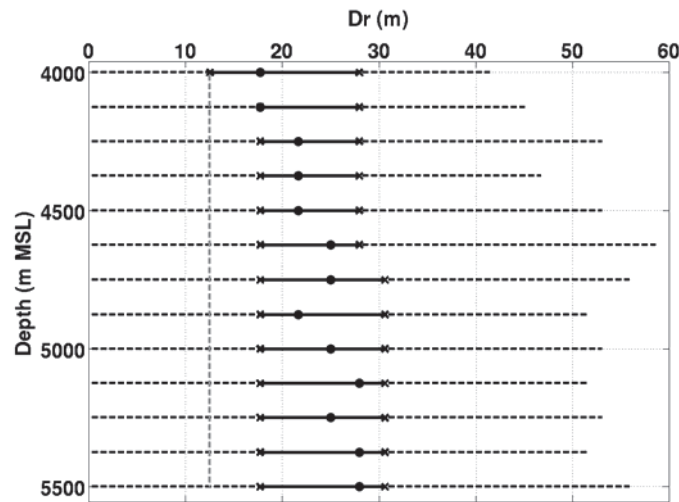


Figure 10-5 : Box-plots of the location inaccuracy along depth. The box-plots are formed like in Figure 10-3. The perpendicular dashed line accounts for the mesh size used for the location process.

As an explanation, let us consider the position of the different sensor relative to the source initial locations. The down-hole sensors are the nearest to the synthetic earthquakes. Therefore, the travel-times for any phase to arrive at the station is shorter than for the surface sensors. Consequently, rounding at 10 ms has a larger impact on the travel-times for the down-hole network than for the surface network. Hence, adding the down-hole sensors in the case of rounded picks adds stronger incorrect observations and consequently leads to larger bias.

### 10.4.3 Impact of the stimulation zone

The impact of a massive water injection is important for studies on induced seismicity due to well hydraulic stimulation or circulation tests. To model the effect of the fluid injection, we follow the synthetic test performed by Calò *et al.* (2011, Appendix A). At depths between 4030 and 5030m in a radius of 375 m around the mid-point of the open-hole section of the well GPK2, P- and S-waves propagate 10% and 5% slower respectively. In this part, the event locations are computed in the reference velocity but the travel-times were computed in the perturbed velocity model. The synthetic sources are distributed on the three orthogonal planes crossing GPK2 at the middle of the open-hole section.

No significant location inaccuracy is observed for any network for sources positioned shallower than the stimulated zone. The location inaccuracies are mainly horizontal since the vertical inaccuracies are always smaller than one grid-cell. Nevertheless, the results obtained for the combined network show a significant decrease of location accuracy (Figure 10-6 top panels). It increases through the injection zone and reaches about 100 m as median value of

horizontal bias at its bottom for sources situated on the vertical- $X_c$  plane. A maximum horizontal bias of about 150 m can be observed for these sources. When the sources were initially positioned on the vertical- $Y_c$  plane, the median horizontal inaccuracy can reach only 75 m in depth and the maximum is about 90 m. The events tend to be located away from their initial position in the direction opposite to the simulated stimulation zone. Interestingly, the origin times of the events are as accurate as for the ideal case.

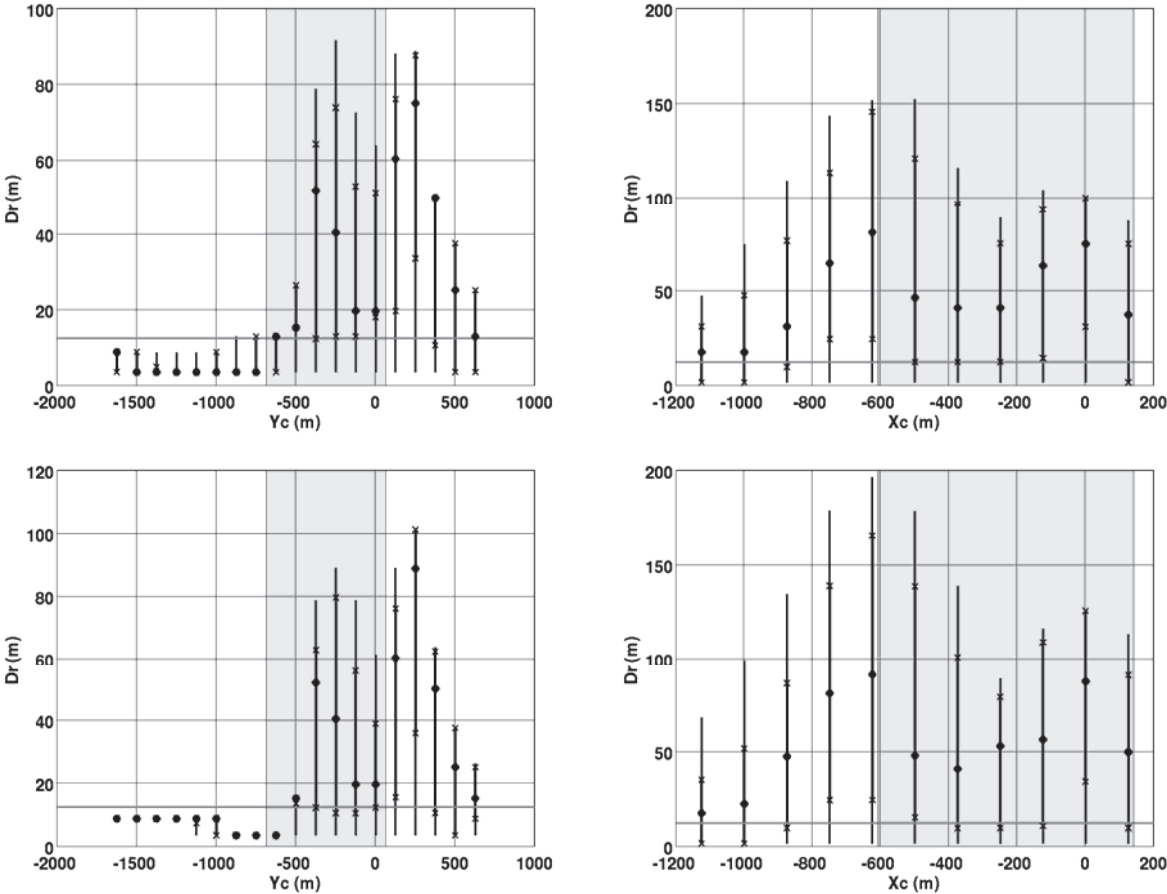


Figure 10-6: Boxplots showing total inaccuracies for location computed with the combined network (top panels) and the down-hole network alone (bottom) with data from a synthetic modelling in a profile with a LVZ. The locations were carried out in the reference velocity model. The location were computed for sources on vertical- $Y_c$  plane (left), vertical- $X_c$  plane (right) and horizontal plane (not shown). The perpendicular grey-line accounts for the mesh size used for the location and the shadowed zone corresponds to the simulated injection zone. The symbols concerning the boxplots are described in Figure 10-3.

For the locations computed with the surface network, the inaccuracies are of the same order as or smaller than the uncertainties. For location computed with the down-hole network (Figure 10-6 bottom panels), median inaccuracy of about 130 m, which is about 1.3 times the 95 m of the location uncertainty, can be observed in the deepest part of the  $X_c$ -vertical plane of sources. For the same source location, the combined network leads to  $\sim 110$  m inaccuracy, about 1.4 times the uncertainty. Furthermore, if we look at the inaccuracy variation along the  $X_c$  axis, the median value reaches 80 m, which is 1.25 times the median value of the uncertainty, in the Eastern part. The third quartiles difference is even larger than the “median difference” (120 m for the Q3 inaccuracy and “only” 75 m for the Q3 uncertainty). Taken the extreme values into account, the inaccuracies can be two times larger than the uncertainties for the combined network, leading to bias of about 150 m with uncertainties of about 75 m.

## 10.5 Conclusion and outlooks

In this paper, we mainly focused on the impact of several seismic network configurations on earthquake location errors, discriminating uncertainty from inaccuracy. The methodology was applied to a synthetic data-set representative of the seismicity induced during the stimulation of the GPK2 well at Soultz-sous-Forêts.

The combination of a surface and a down-hole network provides the most certain hypocentre locations, of the order of 55 m to 75 m in the denser part of the seismic cloud. This result is compatible with the estimates from Cuenot *et al.* (2008), however, we show that the uncertainty is not homogeneously distributed in space and is larger at the NE than at the SW and increases with depth. The implementation of the down-hole network allows decreasing by a factor of two the location uncertainties compared to those which would be obtained from the surface network only.

P- and S-wave arrival-times rounded at 10 ms, as written in the existing catalogue of observations, leads to location inaccuracy (mainly horizontal) up to 20-30 m for locations computed with the combined network. The picking inaccuracy generates stronger bias for sources which are deep or in the North-East part of the seismic cloud. Nevertheless, the location inaccuracies remain usually three times smaller than the location uncertainties and may be considered as negligible. The rounding effect induces location inaccuracies 50% larger with the down-hole network than with the surface network. Hence, the down-hole network is useful to diminish the location uncertainty but leads to stronger location bias. Due to some locations, it is worth mentioning that the absolute location should not be performed with a software or with catalogues using rounded travel-times at 10 ms for the case of Soultz.



The impact on event location of a P- and S-wave velocity decrease of 10 % and 5 % respectively in a low-velocity cylinder centred on the middle of the open-hole section of GPK2 was investigated. It was supposed to represent the effect due to the massive water injection carried out to stimulate the well in 2000. This does neither affect significantly the location uncertainty nor the vertical accuracy. Not taking into account the LVZ leads to significant location inaccuracies but usually not large enough to be extracted from the location uncertainty if we consider the median values. Unfortunately, bias larger than 100 m should be expected for location of event in the deep Eastern part using the combined network. This value is larger than the “only” 75 m of uncertainty. In that case, the real hypocentre won’t be in the PDF. Furthermore, the deterioration of the location accuracy is not isotropic. Moreover, the impact of the LVZ could be observed for some locations performed by the combined network or by the down-hole network but not for location computed by the surface network due to the larger location uncertainties.

All those conclusions are suitable for absolute location methods. Nevertheless, the improvement or deterioration brought by relative location methods should be also investigated since the latter become routinely used to locate earthquakes. The proposed methodology could be used in similar reservoir monitoring contexts to characterize the capabilities of the existing or expected seismicity in terms of reservoir description.

### **Acknowledgment**

This work was conducted in the framework of the excellence laboratory “Labex G-EAU-THERMIE PROFONDE” (University of Strasbourg). It was funded by the French National Research Agency, as part of the French “Investments for the future” program, by the Energie Baden-Württemberg AG (EnBW), the French institution CNRS, and by the French-German University (DFH-UFA). We wish to thank the ECOGI joint venture and the Électricité de Strasbourg – Géothermie company (ESG) for sharing data. We are grateful to N. Cuenot (EEIG “Heat Mining”) for sharing his experience on the Soultz raw seismic data and to A. Genter for fruitful discussions on the Soultz experiments. We also thank L. and C. Dorbath for providing the seismic data catalogues and sharing their knowledge on the datasets.

### **References**

- Bailleux, Paul; Schill, Eva; Edel, Jean-Bernard; Mauri, G. (2013): Localization of temperature anomalies in the Upper Rhine Graben. insights from geophysics and neotectonic activity. In *International Geology Review* 55. DOI: 10.1080/00206814.2013.794914.
- Baumgärtner, J.; Gérard, A.; Baria, R.; Garnisch, J. (2000): Progress at the European HDR project at Soultz-sous-Forêts. preliminary results from the deepening of the well GPK2 to 5000 m. In. SPE International Petroleum Conference and Exhibition. Villahermosa, Mexico.
- Calò, M.; Dorbath, C.; Cornet, F. H.; Cuenot, N. (2011): Large-scale aseismic motion identified through 4-D P-wave tomography. In *Geophys J Int* 186 (3), pp. 1295–1314. DOI: 10.1111/j.1365-246X.2011.05108.x.

- Cuenot, N. (2009): Réponse du granite fracturé de Soultz-sous-Forêts à des injections massives de fluide. Analyse de la microsismicité induite et du régime de contraintes. Strasbourg, University of.
- Cuenot, Nicolas; Dorbath, Catherine; Dorbath, Louis (2008): Analysis of the microseismicity induced by fluid injections at the EGS site of Soultz-sous-Forêts (Alsace, France). Implications for the characterization of the geothermal reservoir properties. In *Pure Appl. Geophys.* 165 (5), pp. 797–828. DOI: 10.1007/s00024-008-0335-7.
- Dorbath, Louis; Cuenot, Nicolas; Genter, Albert; Frogneux, Michel (2009): Seismic response of the fractured and faulted granite of Soultz-sous-Forêts (France) to 5 km deep massive water injections. In *Geophys J Int* 177 (2), pp. 653–675. DOI: 10.1111/j.1365-246X.2009.04030.x.
- Dyer, B. C. (2001): Soultz GPK2 stimulation June/July 2000. Seismic monitoring report, SOCOMINE (Semore Seismic Report).
- Frietsch, Michael; Groos, JörnC; Ritter, JoachimR R. (2015): Detection and Delineation of a Fracture Zone with Observation of Seismic Shear Wave Anisotropy in the Upper Rhine Graben, SW Germany. In *Pure Appl. Geophys.* 172 (2), pp. 267–282. DOI: 10.1007/s00024-014-0899-3.
- Genter, Albert; Evans, Keith; Cuenot, Nicolas; Fritsch, Daniel; Sanjuan, Bernard (2010): Contribution of the exploration of deep crystalline fractured reservoir of Soultz to the knowledge of enhanced geothermal systems (EGS). In *Comptes Rendus Geoscience* 342 (7-8), pp. 502–516. DOI: 10.1016/j.crte.2010.01.006.
- Husen, Stephan; Kissling, Edi; Deschwenden, Angela (2013): Induced seismicity during the construction of the Gotthard Base Tunnel, Switzerland. hypocenter locations and source dimensions. In *J Seismol* 17 (1), pp. 63–81. DOI: 10.1007/s10950-012-9313-8.
- Kinnaert, Xavier; Gaucher, Emmanuel; Achauer, Ulrich; Kohl, Thomas (2016): Modelling earthquake location errors at a reservoir scale: a case study in the Upper Rhine Graben. In *Geophys J Int* accepted.
- Lomax, Anthony (2011): NonLinLoc. Probabilistic, Non-Linear, Global-Search Earthquake Location in 3D media. Version CS6: ALomax Scientific.
- Lomax, Anthony; Michelini, Alberto; Curtis, Andrew (2009): Earthquake location, Direct, Global-Search Methods. In Robert A. Meyers (Ed.): *Encyclopedia of Complexity and Systems Science*: Springer New York, pp. 2449–2473.
- Pavlis, Gary L. (1986): Appraising earthquake hypocenter location errors. A complete, practical approach for single-event locations. In *Bull. Seismol. Soc. Amer.* 76 (6), pp. 1699–1717, checked on LU.
- Podvin, Pascal; Lecomte, Isabelle (1991): Finite difference computation of traveltimes in very contrasted velocity models. a massively parallel approach and its associated tools. In *Geophys J Int* 105 (1), pp. 271–284. DOI: 10.1111/j.1365-246X.1991.tb03461.x.
- Schnaebele, R. (1948): Monographie géologique du champ pétrolifère de Pechelbronn. Strasbourg: Mémoire du Service de la Carte Géologique d'Alsace et de Lorraine.
- Tarantola, A. (Ed.) (2005): *Inverse problem theory and methods for model parameter estimation*. Philadelphia: Society for Industrial and Applied Mathematics.
- Tarantola, A.; Valette, B. (1982): Inverse problems = quest for information. In *Journal of Geophysics* 50, pp. 159–170, checked on LU.
- Tukey, John W. (1977): *Exploratory Data Analysis*. Reading, MA: Addison-Wesley (Behavioral Science).
- Wentzel, Friedemann; Brun, Jean-Pierre (1991): A deep Reflection Seismic Line across the Northern Rhine Graben. In *Earth and Planetary Science Letters* 104, pp. 140–150.
- Wittlinger, G.; Herquel, G.; Nakache, T. (1993): Earthquake location in strongly heterogeneous media. In *Geophys J Int* 115 (3), pp. 759–777. DOI: 10.1111/j.1365-246X.1993.tb01491.x.



# Curriculum Vitae

## Personal information

Name Xavier Kinnaert  
Nationality French  
Date of Birth 14.04.1988 in Schiltigheim

## Education

Since 12/2012 PhD student of Prof. Thomas Kohl and Prof. Ulrich Achauer (cotutelle)  
In Div. of Geothermal Research, Institute of Applied Geosciences at  
Karlsruhe Institute of Technology (KIT), Germany  
And in Institute of Earth Physics in Strasbourg  
Specification: induced seismicity, estimation of errors and of their  
impact on reservoir modelling

09/2010 – 06/2012 2-year Master at University of Strasbourg (UdS), France  
Studies in Geology, Geophysics  
Thesis: "Imaging the Soultz-Sous-Forêts geothermic reservoir using  
noise tomography"  
Research project: "Archéologie sur le campus de l'UdS en utilisant des  
méthodes géophysiques"

09/2009 – 06/2010 1<sup>st</sup> year Master at University of Strasbourg (UdS), France  
Studies in theoretical physics  
Research project: "Bone tomodensitometry using gamma rays"

09/2006 – 06/2009 Bachelor at University of Strasbourg (UdS), France  
Studies in theoretical physics  
Research project: "Gamma ray and neutron propagation"

## Experience

07/2013 – 02/2016 Survey of signals recorded by a seismic network installed at Bruchsal

05/2011 – 06/2011 6-weeks voluntary internship at EOST in geophysics: preparing the master  
thesis

06/2009 – 07/2009 2-months voluntary internship in an astrophysics laboratory

## Publications

- Kinnaert X., Gaucher E., Kohl T., Achauer U., *The combination of surface and down-hole seismic networks for earthquake location at the Soultz-sous-Forêts geothermal site (France)*, Pure and Applied Geophysics, in prep
- Kinnaert X., Gaucher E., Kohl T., Achauer U., *Modelling earthquake location errors at a reservoir scale: a case study in the Upper Rhine Graben*, Geophysical Journal International, 2016, 206, 861-879, doi: 10.1093/gji/ggw184 (peer-reviewed)
- Gaucher E., Kinnaert X., Achauer U., Kohl T., *Propagation of Velocity Model Errors in Earthquake Absolute Locations: Application to the Rittershoffen Geothermal Field*, 41<sup>st</sup> Workshop on Geothermal Reservoir Engineering, Stanford, February 22-24 2016
- Calò M., Kinnaert X., Dorbath Catherine. *Procedure to construct three-dimensional models of geothermal areas using seismic noise cross-correlations: application to the Soultz-sous-Forêts enhanced geothermal site*. Geophysical Journal International, 2013, 194 (3), p. 1893-1899. ISSN 0956-540X (peer-reviewed)

## Presentations with abstract

Kinnaert X., Gaucher E., Kohl T., Achauer U., *Modelling seismic event location errors at the reservoir scale : application to the geothermal site of Soultz-sous-Forêts (Alsace, France)*, at 3<sup>rd</sup> EGC, Strasbourg, 19-23/09/2016 (poster, abstract accepted)

Kinnaert X., Gaucher E., Kohl T., Achauer U., *Modelling focal mechanism at the reservoir scale: application to the geothermal site Rittershoffen (Alsace, France)*, at 3<sup>rd</sup> EGC, Strasbourg, 19-23/09/2016 (oral presentation, abstract accepted)

Kinnaert X., Gaucher E., *Modelling earthquake location errors at Rittershoffen geothermal reservoir (France)*, 4<sup>th</sup> EGW 2015-10-19/20 Strasbourg (oral presentation)

Kinnaert X., Gaucher E., *Modelling location errors of the seismicity induced at Soultz-sous-Forêts*, 3<sup>rd</sup> EGW 2014-10-15/16 Karlsruhe (oral presentation)

Kinnaert X., Gaucher E., *Towards S-wave picking of seismicity induced by GPK2 stimulation at Soultz-sous-Forêt*, 2<sup>nd</sup> EGW Strasbourg, 2013-10-24/25 (poster)

Calò M., Kinnaert X., Dorbath C., *Imaging the geothermic reservoir of Soultz-Sous-Forêts using seismic noise tomography*, DGG, Karlsruhe 2012-11 (oral presentation)

# Declaration in lieu of oath

I herewith declare in lieu of oath that I have composed this thesis without any inadmissible help of a third party and without the use of aids other than those listed. The data and concepts that have been taken directly or indirectly from other sources have been acknowledged and referenced.

I further declare that I have followed the rules for ensuring proper scientific practice at the Karlsruhe Institute of Technology (KIT), passed on December 19<sup>th</sup>, 2012 by the executive committee of KIT.

This thesis has not been submitted, wholly or substantially, neither in this country nor abroad for another degree at any university or institute.

I have said nothing but the truth to the best of my knowledge, and I have not withheld any information.

Karlsruhe, July 14<sup>th</sup>, 2016

Xavier Kinnaert





## Zusammenfassung

Die korrekte Lokalisierung von induzierter Seismizität und den dazugehörigen Herdflächenlösungen sind sehr wichtige Parameter. So werden zum Beispiel die Verteilung der Erdbeben und die Orientierung ihrer Herdflächenlösungen dazu benutzt um in der Tiefe liegende Reservoirs zu lokalisieren und abzubilden. In dieser Doktorarbeit wird eine Technik vorgeschlagen um die methodisch bedingten Fehler zu quantifizieren. Mit dieser Methode werden die verschiedenen Fehlerquellen, die Unsicherheiten und die Fehler im Modell getrennt. Die Technik wird für die geothermischen Felder in Soultz und in Rittershoffen benutzt um den Einfluss verschiedener Parameter (Annahmen) auf die Lokalisierung der induzierten Seismizität zu bestimmen. Es wurde festgestellt, dass Bohrlochseismometer und eine gute azimutale Verteilung der seismischen Stationen die Unbestimmtheiten verkleinern. Die Geschwindigkeitsunbestimmtheiten, die durch eine Gauss-Verteilung mit 5% Fehler dargestellt werden, vervielfachen die Lokalisierungsungenauigkeiten um einen Faktor 2 bis 3. Eine ungenaue Kenntnis des Untergrunds oder die verwendete vereinfachte Darstellung der Geschwindigkeitsverhältnisse im Untergrund (notwendig um die synthetischen Rechnungen durchführen zu können) führen zu anisotropen Abweichungen und Fehlern in der Herdtiefe von bis zu 10%. Diese können die Interpretationen des Untergrunds deutlich verfälschen. Ein "calibration shot" kann diese Fehler korrigieren. Leider können die Fehler für die Herdflächenlösungen nicht in derselben Weise korrigiert werden. Es erscheint daher als keine gute Idee, ein Reservoir nur über die Lokalisierung von Erdbeben zu bestimmen. Eine Kombination mehrerer seismischer Methoden scheint angezeigt. Die hier besprochene Methode kann als Grundlage dienen für die Erkundung anderer (geothermischer) Reservoirs. Eine gute *a priori* Kenntnis über den Untergrund bleibt dabei unabdingbar.

Schlüsselwörter: Unbestimmtheiten, Ungenauigkeiten, induzierte Seismizität, seismische Lokalisierung, Herdflächenlösung

# Data processing of induced seismicity : estimation of errors and of their impact on geothermal reservoir models

## Résumé

La localisation de séismes induits ainsi que les mécanismes au foyer associés sont des outils fréquemment utilisés afin, entre autres, d'imager la structure d'un réservoir. Cette thèse présente une technique permettant de quantifier les erreurs associées à ces deux paramètres. Par cette méthode, incertitudes et imprécisions sont distinguées. La méthode a été appliquée aux sites de Soultz et de Rittershoffen pour étudier l'impact de plusieurs critères sur la localisation de la sismicité induite. Ainsi, il a été montré que l'utilisation de capteurs installés profondément dans des puits et qu'une bonne couverture sismique azimutale réduit sérieusement les incertitudes de localisation. Les incertitudes du modèle de vitesse, représentées par une distribution gaussienne des modèles avec un écart de 5% autour du modèle de référence, multiplient les incertitudes de localisation par un facteur 2 à 3. Des simplifications utilisées pour le calcul ou une mauvaise connaissance du milieu peuvent mener à des imprécisions de l'ordre de 10% spatialement non isotropes. Ainsi, les structures du sous-sol peuvent être déformées dans les interprétations. L'application d'un tir de calibration peut néanmoins corriger ce fait en grande partie. L'étude d'erreurs associées aux mécanismes au foyer ne semble cependant pas conduire aux mêmes conclusions. Le biais angulaire peut certes être augmenté par l'omission de la faille dans le modèle de vitesse, mais dans plusieurs cas il est le même que dans le cas idéal voire diminué. En outre, une meilleure couverture sismique améliorerait toujours le mécanisme au foyer obtenu. Ainsi, il n'est pas conseillé d'imager un réservoir en n'utilisant que la localisation de séismes, mais une combinaison de plusieurs paramètres sismiques pourrait s'avérer efficace. La méthode appliquée dans le cadre de cette thèse pourra servir pour d'autres sites à condition d'en avoir une bonne connaissance *a priori*.

Mots clés : imprécisions, incertitudes, sismicité induite, localisation de séisme, mécanisme au foyer

## Abstract

Induced seismicity location and focal mechanisms are commonly used to image the sub-surface design in reservoirs among other tasks. In this Ph.D. the inaccuracies and uncertainties on earthquake location and focal mechanisms are quantified using a three-step method. The technique is applied to the geothermal sites of Soultz and Rittershoffen to investigate the effect of several criteria on the earthquake location. A good azimuthal seismic coverage and the use of seismic down-hole sensors seriously decreases the location uncertainty. On the contrary, velocity model uncertainties, represented by a 5% Gaussian distribution of the velocity model around the reference model, will multiply location uncertainties by a factor of 2 to 3. An incorrect knowledge of the sub-surface or the simplifications performed before the earthquake location can lead to biases of 10% of the vertical distance separating the source and the stations with a non-isotropic spatial distribution. Hence the sub-surface design may be distorted in the interpretations. To prevent from that fact, the calibration shot method was proved to be efficient. The study on focal mechanism errors seems to lead to different conclusions. Obviously, the angular bias may be increased by neglecting the fault in the velocity. But, It may also be the same as or even smaller than the bias calculated for the case simulating a perfect knowledge of the medium of propagation. Furthermore a better seismic coverage always leads to smaller angular biases. Hence, it is worth advising to use more than only earthquake location in order to image a reservoir. Other geothermal sites and reservoirs may benefit from the method developed here.

Key words: uncertainties, inaccuracies, induced seismicity, earthquake location, focal mechanism